Nouveaux Développements en Interférométrie Photothermique et Lasers à Cascade Quantique à Grande Longueur d'Onde pour la Détection de Gaz

Raphaël Paegelow

Dissertation

Novel Developments in Photothermal Interferometry and Long-Wavelength Quantum Cascade Lasers for Gas Sensing

A thesis submitted for the degree of
Doctor of Technical Sciences (Dr. techn.)

at

Technische Universität Wien
Faculty of Technical Chemistry
Institute of Chemical Technologies and Analytics

under supervision of
Univ. Prof. Dr. Bernhard Lendl
Dr. Alexei N. Baranov

defended by
Davide Pinto

Vienna, 25.06.2024

THÈSE POUR OBTENIR LE GRADE DE DOCTEUR DE L'UNIVERSITÉ DE MONTPELLIER

Spécialité: Électronique

École doctorale: Information, Structures, Systèmes

Unité de recherche: Institut d'Électronique et des Systèmes – UMR 5214

En partenariat international avec TU Wien, Autriche

Novel Developments in Photothermal Interferometry and Long-Wavelength Quantum Cascade Lasers for Gas Sensing

Présentée par Davide PINTO
Le 25 Juin 2024

Sous la direction de Bernhard LENDL
et Alexeï BARANOV

Devant le jury composé de

Jérôme FAIST, Professeur, ETH Zürich, Suisse	Rapporteur
Ulrike WILLER, Maître de conférences, TU Clausthal, Allemagne	Rapporteur
Bernhard LENDL, Professeur, Institute of Analytical Chemistry, TU Wien, Autriche	Directeur de thèse
Alexeï BARANOV, Directeur de recherche, CNRS, IES, Université de Montpellier, France	Co-directeur de thèse

UNIVERSITÉ DE MONTPELLIER

To my parents

Acknowledgement

Looking back to the last four year, I cannot help but express my gratitude to all the people that I encountered along this path.

First of all, I must thank my main supervisor Bernhard for the constant support that I received during these years and for the many positive feedbacks to pursue my goals, especially when I was discouraged about my findings. I have to acknowledge also how you pushed me to disseminate my achievements in the countless conferences we attended. I probably travelled more with you than I did with my family.

I would also like to thank my co-supervisor Alexei for encouraging my scientific curiosity and for the many constructive discussions we had during my time in Montpellier and beyond. I particularly appreciated the way you always pushed me in experimenting new things and your positive attitude, especially when (quoting) *shit happened*. Thank you also for having me printed in the QCL-lab for future memory. I am sure I give my best impression.

Lastly, I would like to thank Ulrike and Jérôme for accepting to review this work and for taking your time to attend my defence in Vienna.

The following part is dedicated to the friends and people I met in this journey.

First, I need to thank Giovanna, my girlfriend, colleague and flatmate, for the infinite moments spent together during this PhD and for the memories that we built together. From the ritual morning coffee at Uni before starting every working day, to the endless scientific discussions we had at every hour of the day - especially in the night. You helped me to return to reality in many occasions when I felt lost in my thoughts, and you showed me a different way of approaching science, a more pragmatic way: this is a precious lesson that I learned collaborating with you. Without you, this PhD would have not been the same. I am glad we could conclude this path as we started it, together.

A giant 'thank you' goes to *mama* Pily, without whom I would not have completed this journey. Literally. I would have probably lost my student status at both Universities without you. Aside from your technical competence, I must acknowledge your human side, for being always present and promotive to solve any problem, for all the laughs we shared and the good memories across Europe. Thank you for everything you have done for me.

A huge thank goes to the whole CAVS team, for making my stay in Vienna so enjoyable. First, I need to thank the gas-lab people for sharing with me their knowledge and the daily struggles in the lab. Stefan for being such a supportive lab-mate and for the pizza stickers on my oscilloscope's knobs. Iskander for your lame jokes, but also for your scientific curiosity. I wish we could have worked together for longer. But please, stop drinking cappuccino with the pizza in the evening. Savda, for the happiness you brought with you in the lab, we needed your positive attitude. Also, it was a pleasure to share all the jokes on how short we are. I felt less alone. Giulia, for taking over my setup without being caught by the instinct to destroy it. The elder guys, Paul and Harald, for dedicating to

me their time when needed.

I must also thank the rest of the group - in no particular order - with whom I shared many unforgettable parties and experiences. Felix, for his contagious laugh and his incredible Italian impressions. Alicja, for always finding an opportunity to congratulate me on my culinary skills - I really started wondering whether I'm Italian or not. Ufuk, for your puns and in general for being a core presence in the CAVS group - I hope I could teach you the true recipe of the Italian caprese. Daniel, for opening the gates of TU-Wien for all of us and for being a respectable coffee-drinking rival - you earned that first place. Jesus, for his unconditional support during the last steps of this journey. Leo, for all the LabView tips and for helping me in fixing any tech-related problem when I asked, but also for the nice evening chats. Gustavo and Elizandra for being always positive and with a smile on your faces - it really helps to be surrounded by people like you. Georg, for being an infinite resource of knowledge in science and memology. Thank you for keeping your door open to everyone in the group, me included. Elisabeth, Shilpa, Nikolaus and Dominik for the nice chats during the lunch breaks. Many thanks to the old members of the group - Jakob, Catarina, Stefan, Karim and Andreas for the good times shared together in many parties and festivities. But also thanks to the new group members Miranda, Sebastian, Dani, Alex, Adea, Lena, Lisa and Margaux for cheering up the mood.

Special thanks to Mauro, for being a good friend and always a nice guest presence in our labs. I very much appreciated your pizza skills, the time together and the activities done in Vienna with the Italian community. In this regard, many thanks also to Stefania, Davide D., Nicola and Anna, for the beautiful memories we collected together: the European Championship, the Oktoberfest, the Escape room, birthday parties and many more.

I must also spend some words for the whole NanoMIR group in Montpellier, who welcomed me warmly in their lab.

I have to thank Michele, with whom I have shared the office, morning coffees, laughs, and many evenings together. I will always remember the 'king blue cheese', the Churros and Mimmo Modem's videos. When I felt alone, you and Iolanda brought a bit of Italy in my days. Daniel T., for being a loyal friend and the many thoughts and discussions we shared together. I really envy your explosive energy, and I always appreciated the way you bring joy to the people around you. Thanks also for the infinite tips you gave me in the cleanroom. I must also thank *tronca* Zayneb (otherwise you would kill me) for the support you gave me when I cried out for help and for the ease with which you got angry at everything I said or did. I know, though, that deep down you have a tender heart. A giant thank to Diba for being such a fun person and always brightening up the day at IES with her presence. I can still hear you laughing sometimes. In my nightmares. Thanks to Anis, as well, for all the laughs we shared and for that only time we went for an actual biking tour together - we have been very lazy, let's admit it. I must thank Julien and Pierre, the noisy office-neighbours, for the nice moments spent together in the corridors of the IES, and for convincing me to go to the gym. I'm still waiting for the results, not

your fault though. I thank Arianne and Kinjalk, for introducing me to the cleanroom activities. Also thanks to Guilherme, for your puns and jokes. I need to thank the heads of the group, Eric and Thierry, for their support during my stay in Montpellier and for making me feel part of the group. To Lolo, for your humble personality, your passion and dedication to science which is an inspiration to me. I must thank you for the way you used to mock me when my single frequency lasers looked more like Fabry-Pérot: proving you wrong has been my main source of motivation. Also the many French sentences you learned me, such as '*Qui peut le plus peut le moins*'. Finally, thanks for coming to my defence, even though I know you came to eat the taralli. A huge thank you to all the other members of the NanoMIR group I had the pleasure to meet: Aurore, Mike, Roland, Jean-Baptiste, Andres, Maeva, Audrey, Aurélie, Milan, Maxime, Salah, Matthias, Julien C., Basil and Tarek.

Finally, I would like to thank the people that I met at IRsweep and Sensirion during my internship. Even if for a short period, I felt very enriched by this experience and I had the chance to meet incredible scientists. In particular in the IRsweep team: again Jakob for supporting me with his dedication, which has always inspired me and for taking his time to arrange my arrival in Stäfa. I really enjoyed working together with you after so long. Markus G., for offering me a roof over my head in Stäfa and for being a nice flatmate, with whom I could share nice dinners, night runs and much more. Raphael H., Pierre, Pitt, Michele, Markus M., Kristina, Daniel H. and Daniel R. for making my stay at IRsweep so enjoyable, among terrace lunches and nice parties at Zürich lake. In the Sensirion team: Raphael B., my *Götti*, for his guidance and his friendship - I'm sorry if I desecrated the raclette cheese you gifted me. Manuel, Yannick and the whole Optics cluster team for the nice moments spent together.

A final acknowledgement goes to my parents, who always supported me with their presence even though we have been apart for the last four years. Vi dedico questo ringraziamento in italiano. Grazie per aver supportato e mai ostacolato le mie scelte, specialmente quelle più dolorose che comportano la nostra lontananza. Grazie per avermi spinto a perseguire i miei sogni e le mie ambizioni, con la giusta dose di positività, e per essere sempre stati al mio fianco nei momenti più difficili. Grazie per essere venuti a trovarmi, ovunque mi spostassi, facendomi sentire a casa. È un'abitudine che mi auguro non perdiate mai. I would also like to thank my brother Giuseppe for always being open to give me his valuable advice when I needed it most and for being a role model when it comes to pursuing a life-goal.

Finally, in the hope that I have not missed anyone, a huge thank you to all the people I have met along the way and who have helped to make my days better.

Abstract

The monitoring of gaseous compounds in trace concentrations is crucial across various fields, from industry to breath analysis. Continuous improvement of gas sensors is essential to meet diverse application needs. Optical sensors stand out for their fast and accurate results. Among these, laser-based sensors offer unprecedented sensitivities by targeting well resolved roto-vibrational transitions. Over the past few decades quantum cascade laser (QCL) technology has undergone significant developments with positive implications for spectroscopic analysis.

In this thesis, advancements in both photothermal interferometry and QCL sources are presented. The first part of this work is devoted to photothermal interferometry, an indirect approach in which thermal effects, photoinduced in the sample from an excitation source, are detected with a probe laser using an interferometric readout. This approach enables small sensing volumes and high sensitivity which scales with the optical power of the excitation source. Several interferometric arrangements can be employed. This work makes use of the Fabry-Pérot Interferometer (FPI), since it offers compactness, due to the close mirror spacing, and enhanced sensitivity arising from the finesse of the resonator. For real-case scenarios, two fundamental requirements must be fulfilled: spatial overlapping of the probe and excitation beams, between the mirrors of the FPI, and frequency tuning of the probe laser to the interferometric fringe. A diode laser (DL) source has been chosen as probe, for its cost-effectiveness, swift current tuning capabilities, and mature technology in the telecom region.

A model for the transduction properties of a DL coupled with the FPI in presence of sample excitation was derived. The model agreed with the experimental results, tested on the case of nitric oxide detection. A novel normalization scheme and locking method were developed for stable signal readout, compensating for system's drifts by self-referencing the measurement to the cavity quality. Detection limits of a few parts-per-million were achieved, leading to normalized noise equivalent absorptions on the order $\sim 10^{-6}$ W cm^{-1} Hz$^{-1/2}$. System's performance can be improved by lowering the noise level by balanced detection with a reference cavity.

The second part of this manuscript is focused on advancing the long-wavelength (LW) QCL technology, based on InAs/AlSb material system. The LW regime ($\lambda > 10$ µm), plays a pivotal role for the detection of organic compounds since they exhibit strong absorptions between 12.5 – 15 µm. Already existing wafer-growths have been used for the fabrication of tapered QCLs, emitting at 14 µm. The developed tapered waveguide aims to improve the available optical power, by enhancing the active volume in the resonant cavity. Tapered lasers with angles between 0° and 3° were fabricated and compared in terms of optical and electrical properties. A scaling of the optical power was observed with respect to the ridge device, up to a factor of 3 for the largest taper. Far-field intensity distribution was investigated to assess the beam quality factor. In most cases, a diffraction-limited

beam was observed, with appearance of side-lobes only for higher driving currents. Thin dielectric coatings are also presented to improve the optical power, with devices reaching peak powers of the order of 400 mW. Spectroscopic applications usually require single-frequency operation, which was demonstrated for all the tapered devices by fabrication of Bragg gratings in the upper cladding. Side-mode suppression ratios above 20 dB, in both pulsed and continuous wave operation have been achieved. Finally, the potential of long-wavelength QCLs for spectroscopic applications was explored in the context of classical absorption spectroscopy, in combination with a circular multi-pass cell and 2f-wavelength modulation spectroscopy for the detection of benzene and carbon dioxide. Detection limits of 200ppb and 9ppb were achieved for the two species, respectively, corresponding to a noise equivalent absorption of $8.8 \cdot 10^{-8}$ $\mathrm{cm}^{-1}\,\mathrm{Hz}^{-1/2}$.

Kurzfassung

Die Überwachung gasförmiger Verbindungen in Spurenkonzentrationen ist in verschiedenen Bereichen, von der Industrie bis zur Atemgasanalyse, von entscheidender Bedeutung. Eine kontinuierliche Verbesserung der Gassensoren ist unerlässlich, um den vielfältigen Anwendungsanforderungen gerecht zu werden. Optische Gassensoren zeichnen sich durch ihre Schnelligkeit und auch durch ihre Genauigkeit aus. Laserbasierte Gassensoren erreichen auch eine sehr hohe Empfindlichkeit, da sie auf gut aufgelöste fundamentale Rotationsschwingungsübergänge abzielen. In den letzten Jahrzehnten hat die Quantenkaskadenlaser (QCL)-Technologie bedeutende Entwicklungen durchlaufen, die sich nun positiv auf die Entwicklung von spektroskopischen Gassensoren auswirken.

In dieser Arbeit werden Fortschritte sowohl in der photothermischen Interferometrie als auch bei QCL-Quellen vorgestellt. Der erste Teil dieser Arbeit ist der photothermischen Interferometrie gewidmet, einem indirekten Messansatz, bei dem thermische Effekte, die in der Probe durch eine Anregungsquelle induziert werden. Diese Effekte werden mit einem zweiten Laser ausgelesen. Dieser Ansatz ermöglicht kleine Messvolumina und eine hohe Empfindlichkeit, die mit der optischen Leistung der Anregungsquelle skaliert. Es können verschiedene interferometrische Anordnungen verwendet werden. In dieser Arbeit wird das Fabry-Pérot-Interferometer (FPI) verwendet, welches aufgrund des geringen Spiegelabstands sehr kompakt ist und auch eine hohe Empfindlichkeit bietet, die mit der Güte des Interferometers skaliert. Für reale Szenarien müssen zwei grundlegende Anforderungen erfüllt werden: die räumliche Überlappung des Auslese- und des Anregungsstrahls zwischen den Spiegeln des FPIs und die Frequenzabstimmung des Ausleselasers auf einen Wendepunkt der Transmissionsfunktion des Interferometers. Als Ausleselaser wurde ein schnell abstimmbarer Diodenlaser (DL) ausgewählt, da dieser zum einen kostengünstig ist und auch auf einer ausgereiften Technologie aus dem Telekommunikationsbereich beruht.

Es wurde ein Modell für die Signalübertragungsfunktion eines mit dem FPI gekoppelten DL in Gegenwart einer photothermischen Probenanregung erstellt. Das Modell stimmte mit den experimentellen Ergebnissen sehr gut überein, wie am Beispiel der Messung von Stickstoffmonoxid auch gezeigt werden konnte. Im Zuge der Dissertation wurde eine neue Signalverarbeitungsmethode erarbeitet, die mögliche Drifts durch Normierung auf die aktuelle Empfindlichkeit des Interferometers kompensiert sowie eine robuste Messung möglich macht. Letzteres gelang durch Fixieren des Sondenlasers auf den Wendepunkt der Transferfunktion des Interferometers. Es wurden Nachweisgrenzen von einigen Teilen pro Million erreicht, was zu normalisierten rauschäquivalenten Absorptionen in der Größenordnung $\sim 10^{-6}$ $\mathrm{W\,cm^{-1}\,Hz^{-1/2}}$ führte. Die Leistung des Systems kann verbessert werden, indem der Rauschpegel durch eine parallel durchgeführte Messung an einem Referenzinterferometer mit differentiellen Datenauswertung gesenkt wird.

Der zweite Teil dieser Dissertation befasst sich mit der Weiterentwicklung der langwelligen (LW) QCL-Technologie, die auf dem InAs/AlSb-Materialsystem basiert. Der

LW-Bereich ($\lambda > 10$ µm) spielt eine entscheidende Rolle für den Nachweis organischer Verbindungen, da diese starke Absorptionen zwischen 12.5 - 15 µm aufweisen. Für die Herstellung von 'getaperten' QCLs, die bei 14 µm emittieren, wurden bereits bestehende Wafer-Lasermaterialien verwendet. Der entwickelte konische Wellenleiter zielt darauf ab, die verfügbare optische Leistung zu verbessern indem das aktive Volumen im Resonanzraum vergrößert wird. Es wurden konische Laser mit Winkeln zwischen 0° und 3° hergestellt und in Bezug auf die optischen und elektrischen Eigenschaften verglichen. Es wurde eine Skalierung der optischen Leistung bis zu einem Faktor 3 für die größte Verjüngung in Bezug auf das Ridge Device beobachtet. Die Intensitätsverteilung im Fernfeld wurde untersucht, um den Strahlqualitätsfaktor zu bewerten. In den meisten Fällen wurde ein beugungsbegrenzter Strahl beobachtet, wobei nur bei höheren Betriebsströmen Nebenmaxima auftraten. Es werden auch dünne dielektrische Beschichtungen zur Verbesserung der optischen Leistung verwendet, die Spitzenleistungen in der Größenordnung von 400 mW erreichten. Spektroskopische Anwendungen erfordern in der Regel eine streng monochromatische Emission, die für alle konischen Bauelemente nach Aufbringen von Bragg-Gittern auf das obere Lasermaterial auch nachgewiesen werden konnte. Sowohl im gepulsten als auch im Dauerstrichbetrieb wurden Seitenmodenunterdrückungswerte von über 20 dB erreicht. Schließlich wurde das Potenzial langwelliger QCLs für spektroskopische Anwendungen für den Nachweis von Benzol und Kohlendioxid untersucht. Dazu wurde eine zirkulare Multireflexionsabsorptionszelle und die 2f-Wellenlängenmodulationsspektroskopie zur Datenaufnahme verwendet. Es wurden Nachweisgrenzen von 200ppb bzw. 9ppb für die beiden Substanzen erreicht, was einer rauschäquivalenten Absorption von $8.8 \cdot 10^{-8}$ $\mathrm{cm}^{-1}\,\mathrm{Hz}^{-1/2}$ entspricht.

Résumé

La détection des gaz à très faibles concentrations est indispensable dans divers domaines, de l'industrie à la biologie. L'amélioration continue des capteurs de gaz est essentielle pour répondre aux diverses exigences des applications. Les capteurs optiques se distinguent par leur précision et la réaction rapide. Parmi ceux-ci, les capteurs laser offrent une sensibilité et une sélectivité sans précédent. Au cours de ces dernières décennies la technologie du laser à cascade quantique (QCL) a démontré des progrès significatifs très attractifs pour la spectroscopie. Cette thèse présente les avancées sur la spectroscopie photo-thermique et des sources QCL. La première partie du travail est consacrée à l'interférométrie photo-thermique, une méthode dans laquelle les effets thermiques, photoinduits dans l'échantillon par la source d'excitation, sont détectés avec une lecture interférométrique d'un laser sonde. Cette approche offre une possibilité d'utiliser de faibles volumes de détection et une sensibilité élevée, proportionnelle à la puissance de la source d'excitation. Un élément clé de cette technique est un interféromètre Fabry-Pérot (FPI), qui offre une compacité, en raison de l'espacement étroit des miroirs, et une sensibilité élevée. Pour les scénarios réels, deux conditions fondamentales doivent être remplies : un recouvrement spatial des faisceaux de la sonde et d'excitation, entre les miroirs du FPI, et l'ajustement de la fréquence du laser de la sonde à la frange interférométrique. Une diode laser (DL) a été choisie comme sonde, en raison de son accordabilité efficace par le courant et de son faible cout. Un modèle pour les propriétés de transduction d'un DL couplé au FPI en présence d'excitation de l'échantillon a été développé. Le modèle concordait avec les résultats expérimentaux, obtenus sur la détection de l'oxyde nitrique. Un nouveau schéma de normalisation et une nouvelle méthode de verrouillage ont été mis au point pour une lecture stable du signal, compensant les dérives du système en auto-référenciant la mesure à la qualité de la cavité FP. Des limites de détection de quelques ppm ont été atteintes, conduisant à des absorptions équivalentes de bruit normalisées de l'ordre de $\sim 10^{-6}$ $\mathrm{W\,cm^{-1}\,Hz^{-1/2}}$. La deuxième partie du manuscrit est consacrée à la technologie QCL à grande longueur d'onde (LW), basée sur le système de matériaux InAs/AlSb. La gamme spectrale choisie ($\lambda > 10$ µm) joue un rôle central dans la détection des composés organiques visés car ils présentent de fortes absorptions entre 12.5 et 15 µm. Des QCL effilés émettant autours de 14 µm ont été fabriqués à cet effet. Le guide d'onde effilé vise à améliorer la puissance optique disponible en augmentant le volume actif tout en conservant le régime d'émission monomode spatial, une caractéristique des lasers étroites. Des lasers à ruban evasé avec des angles compris entre 0° et 3° ont été fabriqués et étudiés. Une augmentation de la puissance optique a été obtenue par rapport au dispositif à ruban étroit, jusqu'à un facteur 3 pour le plus grand angle. Le profil du faisceau a été étudiée pour évaluer son facteur de qualité. Dans la plupart des cas, un faisceau limité par la diffraction a été observé. Des revêtements diélectriques minces ont été également déposés sur les facettes des lasers pour améliorer la puissance optique découplée, atteignant des

puissances de pointe de l'ordre de 400 mW. Les applications spectroscopiques nécessitent généralement un fonctionnement monomode spectrale, ce qui a été démontré pour tous les dispositifs par la fabrication de réseaux de diffraction dans la couche de confinement optique supérieur des lasers. Une suppression des modes latéraux supérieur à 20 dB a été atteint, à la fois en mode pulsé et en mode continu. Enfin, le potentiel des QCL à grande longueur d'onde pour des applications spectroscopiques a été exploré dans le cadre de l'absorption classique, en combinaison avec une cellule multi-passage pour la détection du benzène et du dioxyde de carbone. Des limites de détection de 200ppb et 9ppb ont été atteintes pour les deux espèces, respectivement, ce qui correspond à une absorption équivalente au bruit de $8.8 \cdot 10^{-8}$ $\mathrm{cm}^{-1}\,\mathrm{Hz}^{-1/2}$.

Contents

List of Figures

List of Tables

Abbreviations

AR ..... Anti reflection

ARHCF ..... Antiresonant hollow-core fiber

BTEX ..... Benzene, Toluene, Ethylbenzene, Xylene

CEAS ..... Cavity enhanced absorption spectroscopy

CEPAS ..... Cantilever enhanced photoacoustic spectroscopy

CRDS ..... Cavity ring down spectroscopy

CW ..... Continuous wave

DBR ..... Distributed Bragg reflector

DCS ..... Dual comb spectroscopy

DFB ..... Distributed feedback

DL ..... Diode laser

EBL ..... Electron beam lithography

EC ..... External cavity

ENBW ..... Equivalent noise bandwidth

FM ..... Frequency modulation

FPI ..... Fabry-Pérot interferometer

FSR ..... Free spectral range

FTIR ..... Fourier transform infrared spectroscopy

FWHM ..... Full-width at half-maximum

GEISA ..... Gestion et Etude des Informations Spectroscopiques Atmosphériques

HCF ..... Hollow core fiber

HITRAN ..... High-resolution transmission molecular absorption database

HPSDS ..... Heterodyne phase-sensitive dispersion spectroscopy

HR ..... High reflection

HWHM ..... Half-width at half-maximum

ICAPS ..... Interferometric cavity assisted photothermal spectroscopy

ICL ..... Interband cascade laser

IM ..... Intensity modulation

LIA ..... Lock-in amplifier

LIV ..... Light-current-voltage

LOD ..... Limit of detection

LOQ ..... Limit of quantification

LWIR ..... Long-wavelength infrared

MDL ..... Minimum detection limit

MOPA ..... Master-oscillator power-amplifier

NEA ..... Noise equivalent absorption

NEC ..... Noise equivalent concentration

NIR ..... Near infrared

NNEA ..... Normalized noise equivalent absorption

PAS ..... Photoacoustic spectroscopy

PNNL ..... Pacific Northwest National Laboratory

PTI ..... Photothermal interferometry

PTS ..... Photothermal spectroscopy

QCL ..... Quantum cascade laser

QEPAS ..... Quartz enhanced photoacoustic spectroscopy

RAM ..... Residual amplitude modulation

RT ..... Room temperature

SMSR ..... Side-mode suppression ratio

SNR ..... Signal-to-noise ratio

TDLAS ..... Tunable diode laser absorption spectroscopy

TEC ..... Thermoelectric controller

WMS ..... Wavelength modulation spectroscopy

Introduction

Laser trace-gas sensing is becoming a popular and attractive solution for a wide range of applications, including industrial process control [1], environmental and pollution monitoring [2], medical diagnostics [3] and scientific research. The advances and the commercialization of high-performance mid-IR laser sources have facilitated the development of ultra-sensitive spectrometers, since the strongest vibrational transitions occur in this spectral region. To date, more than 100 types of gas have been detected with laser spectroscopy, in different spectral regions [4].

Both metrological and productivity related aspects can be accessed more favourably with laser sources. Highly selective, fast and precise quantification of the gas species are only few of the benefits of laser spectrometers. Furthermore, the high throughput and non-destructive nature of the measurement permit real-time analysis, thereby enabling online monitoring.

The latest advances aim at miniaturizing the sensor, e.g. by integrating both the optical and the electronic part on a chip. [5]. The reduced interaction pathlength of the radiation with the analyte in the waveguide limits the sensor's sensitivity. Rather than measuring the properties of the transmitted beam, one can focus on the effects triggered in the sample as a consequence of the light absorption. This is the case with photoacoustic and photothermal spectroscopies, an ensemble of techniques that promise to advance laser-based spectrometers towards higher compactness. In particular, photothermal approaches have emerged only recently due to the difficulty of measuring the thermally-induced effects, but have undergone tremendous development reaching state-of-the-art sensitivities in compact sensing volumes compared to conventional direct absorption spectroscopies.

The majority of photothermal approaches are based on a dual-laser configuration, in which one laser is employed as an excitation source, while the other is used to probe the photoinduced effect. Among photothermal approaches, interferometric ones offer the highest sensitivity [6]. Miniaturized Fabry-Pérot interferometers have attracted particular attention for the development of compact and highly sensitive photothermal systems.

The performance of these systems is partially related to the quality of the excitation laser sources. High power and optimal beam quality are essential to generate strong, spatially confined thermal gradients. In the mid-IR, the InP-based technology has reached a high level of maturity. However, these devices are less performing in the long-wavelength

infrared (LWIR, $\lambda > 10$ µm) region and cannot operate under continuous-wave operation at room temperature, which is convenient for most spectroscopic applications. A solution was found in InAs-based lasers, due to the small electron effective mass of InAs. The smaller effective mass results in higher intersubband gain, and these devices were proven to operate in continuous wave at room temperature.

The importance of long-wavelength IR lies in the presence of very strong ring vibrations in aromatic molecules. The class of BTEX compounds (Benzene, Toulene, Ethylbenzene and Xylene) has gained considerable attention over the last decade, since they are an important part of volatile organic compounds (VOCs), mainly of industrial origin. VOCs are often environmental pollutants and some of them, such as benzene, are recognised as carcinogens, hence dangerous to human health. In LWIR, BTEX absorption features are readily distinguishable, allowing for highly selective measurement of these molecules. Furthermore, long-wavelength absorption bands are approximately two orders of magnitude more intense than their mid-IR counterparts at shorter wavelengths.

The aim of this work is to showcase the potential of both novel photothermal approaches, as compact and highly sensitive alternatives to the well-established direct absorption methods, and the capabilities of long-wavelength quantum cascade laser sources. The first part of this work focuses on the development of a photothermal interferometry system, based on a compact Fabry-Pérot interferometer. The second part encompasses the most recent advances on long-wavelength sources, concluding with a spectroscopic demonstration of benzene and carbon dioxide detection.

This thesis has been developed within the framework of the double doctorate program *Optaphi*, under the Marie Skłodowska-Curie actions. The scientific research was conducted at TU Wien (Austria) and at the Université de Montpellier (France). The manuscript is structured in six chapters, intended to provide a basic theoretical knowledge of laser spectroscopy methods, as well as fundamental concepts of quantum cascade laser sources.

Chapter 1 provides a comprehensive introduction to spectroscopic approaches, with a particular focus on those based on laser sources, which are relevant to this work. The chapter concludes with a discussion of the main definitions and metrics employed in laser-based gas sensors, which are essential for a spectroscopist.

Chapter 2 provides a detailed examination of photothermal spectroscopy, encompassing its phenomenology and common detection approaches. The chapter explains the generation of both acoustic and thermal effects, starting from a microscopic level and providing some exemplified solutions for modulated excitation sources. The chapter presents an analysis of the interferometric detection scheme, which is the relevant topic in this work. It then concludes with a review of the state-of-the-art of photothermal interferometry.

Chapter 3 discusses the basic principles of Interferometric Cavity Assisted Photothermal Spectroscopy (ICAPS in short). The objective of this chapter is to provide the interested reader with a comprehensive overview of the key considerations to build an ICAPS system. The developed ICAPS sensor is presented, by employing a diode laser as probe

source. The critical limitations imposed by the diode laser are addressed with a novel normalization and locking approach for robust sensing of nitric oxide. The scientific research presented in this chapter was carried out at TU Wien.

In Chapter 4 the fundamental concepts of quantum cascade lasers are presented. The chapter focuses on the challenges of long-wavelength sources, with the last advancements in terms of design and fabrication for high-performance devices. The chapter concludes by proposing the tapered waveguide as a possible solution for the inherent low optical power of LW-sources.

Chapter 5 addresses the solution proposed in the previous chapter from an experimental standpoint. The chapter analyses in detail the features of the fabricated tapered lasers, starting from the fabrication protocol and concluding with a full analysis of the electro-optical and far-field properties. Thin film coatings are also explored as a feasible approach. The chapter concludes with the demonstration of single frequency operation, for distributed feedback tapered devices. This work was conducted at the Université de Montpellier.

Chapter 6 concludes this dissertation providing a demonstration of the capabilities of LW-QCLs, using direct absorption in combination with wavelength modulation spectroscopy and a multipass cell for enhanced sensitivity. An experimental apparatus for the detection of carbon dioxide and benzene was built at TU Wien, by employing a LW-QCL source provided from the Université de Montpellier.

Chapter 1

Optical gas sensing

The accurate and selective detection of gaseous species is a critical task in modern society. The need for gas sensing arises from the necessity to monitor and control gas concentrations in numerous applications to ensure safety, compliance with environmental regulations, and process optimization. Gas sensors are used in a wide range of applications, some of which include:

- **environmental monitoring**, to assess air quality and detect pollutants such as carbon dioxide (CO_2), methane (CH_4), and nitrogen oxides (NO_x). This is crucial for tracking emissions, understanding environmental changes, and ensuring compliance with environmental regulations;
- **industrial processes**, where the concentration of certain gases or their production can be used as an indicator of the process quality, to enhance safety, and prevent leaks;
- **medical diagnostics**, by analyzing breath samples to detect biomarkers for various diseases. For instance, high levels of nitric oxide (NO) in exhaled breath are a sign of asthma, while volatile organic compounds (VOCs) are correlated with lung cancer [7];
- **food and agriculture**, where gas sensing is used to monitor gases in agricultural settings to ensure quality control in food packaging.

One of the main problem of the contemporary society lies in control and regulation of emissions in the atmosphere. The uncontrolled release of gaseous compounds profoundly impacted both air quality and our ecosystem, by depleting the ozone layer. It is undoubted that anthropogenic emissions are the main cause of such damages, which as a result is leading to climate change [8]. In conjunction with these world-wide effects comes air pollution, especially in urbanized areas, where the byproducts of industrial activities and engine combustion are dispersed in air. Several chemical species have been identified as dangerous to human health, if encountered at a sufficiently high concentration. Among

them, carbon monoxide (CO), sulfur dioxide (SO_2), nitrogen oxides, VOCs and many others are acknowledged as harmful to human health or play an important role in key atmospheric processes affecting the concentration of harmful substances. As with any other substance, the level of toxicity depends on the chemical compound and the task of identifying the tolerance levels to human health falls to specific agencies and institutions. Concentrations and exposure time are the most relevant parameters for human safety. Organizations such as the World Health Organization (WHO) and the Environmental Protection Agency (EPA) helped in defining worldwide guidelines for the management of air quality [9], [10]. Local governments also establish their own threshold levels. In Europe, numerous directives have been issued and compiled under the European Union Air Quality Standards framework [11].

For a gas sensor the requirements in terms of sensitivity are strictly application-dependent: in some cases, even the detection of part-per-billion (ppb) levels are needed, which is the case for chlorofluorocarbons concentrations in the atmosphere. These halogenated hydrocarbons can strongly alter the atmospheric chemistry at regional and global levels even at the part-per-trillion (ppt) level.

Some critical features of gas sensors that determine their effectiveness in various applications are:

- **dynamic range**, which defines the operative concentration range of the sensor. A wider dynamic range enables the sensor to detect gases across a broader spectrum of concentrations. A larger dynamic range enhances the sensor's versatility and applicability in diverse environments;
- **throughput**, which refers to its capacity to process measurements within a given time frame. For real-time monitoring and analysis applications, high throughput is essential;
- ***in situ* analysis**, namely the capability of monitoring gases directly at the site of interest, without the need for sample collection or transportation to a laboratory;
- **invasiveness**, which refers to the extent to which the measurement process disrupts the sample. Non-invasive sensing methods allow for measurements to be taken without physically altering the sample. In contrast, invasive methods may require the consumption of the sample. Minimizing invasiveness is important in applications where sample preservation or non-destructive analysis is desired.

1.1 Optical sensing over traditional approaches

In contrast with the traditional gas analysis techniques, analysed below, optical gas sensing offers all the aforementioned key properties, making it an extremely advantageous alternative.

Quantitative gas detection is traditionally performed by gas chromatographs (GC) and mass spectrometers (MS), or their combination (GC-MS). In gas chromatography, the chemical affinity of analyte molecules to a stationary phase (the chromatographic column) is exploited to separate each component under analysis. The mixture is carried by an inert carrier gas (typically helium, nitrogen, hydrogen or argon) which flows through the stationary phase. Every substance will be slowed down depending on its chemical affinity with the stationary phase. The separated components reach the detection stage, which may vary from one application to another. Some of the most used are: the thermal conductivity detector, which measure changes in thermal conductivity; flame ionization detector, which induces an ionization in the component via a hydrogen flame and measures electrically the produced ions; mass spectrometer, which identifies the component based on its mass/charge ratio. A great distinction among GC detectors is their destructive or not-destructive nature. The first class does not permit sample recovery, whereas the latter allows partial or full sample recovery. In general, gas chromatography is a widely used laboratory technique capable of reaching extremely low limits of detection, but the time needed for the sample separation precludes real-time measurements. A strong effort in achieving faster response times has pushed the limits of this technique in the last decades [12]. However, the fastest response times in the range of 1-60 s (hyper-fast separation) or below 1 s (ultra-fast separation), have been limited to demonstrative studies [13].

On the other hand, on a commercial level, small low-cost devices are widely used due to their compactness and cost-effectiveness on a large scale. Among them, the most diffused are pellistors, semiconductor gas sensors and electrochemical devices [14]. Pellistors are four-terminal devices based on a Wheatstone bridge circuit which includes two beads: one of these beads is treated with a catalyst, which lowers the ignition temperature of explosive gases. The heating coming from combustion events changes the conductivity of the catalyst-treated bead, resulting in an imbalanced voltage, from which the gas concentration can be retrieved [15]. However, pellistors suffer from drift at part per million (ppm) levels and can be subjected to poisoning, i.e. a change (partially reversible or irreversible) in sensor response due to chemical reactions between certain gases with the catalyst surface.

Semiconductor gas sensors are typically made by a porous assembly of n-type doped metal oxide semiconductors (MOS), typically SnO_2, In_2O_3 or WO_3. The crystals are often loaded with a foreign substance called sensitizer. When operated at adequate temperature in air, the resistor changes its resistance sharply on contact with a concentration of reducing or oxidizing gas [16]. However, there are many complex factors that affect the sensing properties. First, the selection of the oxide semiconductor and its fabrication method strongly influences its gas sensing properties. Donor density, crystallite size, porosity and so on, also affect the transduction efficiency. Finally, these gas sensors exhibit cross-response to other gases or humidity and suffer from drifts.

Optical gas sensors exploit a physical properties of many gases, namely electromagnetic

radiation absorption, analysed in detail in the next sections. The detection is based on the direct or indirect measurement of the molecules' absorption at a specific wavelength. In contrast to the slow-response of GC-methods, the optical absorption takes place on a femtosecond scale (10^{-15} s) and in many cases the sensor provides real-time measurement. The slow-drifts, which negatively affect MOS and pellistors, can be compensated in optical sensing by self-referencing the measurement to the incident intensity. In addition, optical methods allow in situ analysis and non-invasive detection, with high gas specificity, connected to the characteristic absorptions of the gas molecule, with little to none cross-response from other interfering analytes.

In this sense, optical gas sensing bridges the gap between lower cost sensors, with inferior performance, and high end laboratory approaches. Optical gas sensing encloses a wide variety of techniques which may fundamentally differ from one another. The common ground is that light triggers an absorption process which can be directly or indirectly measured. This branch of chemistry and physics, falls under the name of *spectroscopy*.

1.2 Principles of spectroscopy

In spectroscopy, the interaction between electromagnetic (EM) radiation and matter is investigated. The electromagnetic radiation corresponds to a harmonic wave travelling in space. The properties that undergo such oscillations are interconnected electric and magnetic fields. James Clerk Maxwell was the first scientist to mathematically describe the propagation of electromagnetic fields in vacuum, demonstrating that visible light encompasses only a portion of the electromagnetic spectrum. The fundamental relation that connects the number of oscillations per second - *frequency* (ν, expressed in cycles per second or Hz) - and the distance travelled in a full oscillation - *wavelength* (λ, expressed in m) - is the speed of the wave. For propagation in vacuum:

$$\lambda\nu = c \tag{1.1}$$

where c is the speed of light in vacuum. The way the electromagnetic radiation interacts with matter is strictly connected to the energy carried by the photon, which is proportional to the frequency of the wave. At a specific energy, a particular transition in the atom or molecule being present in gaseous, liquid or solid samples can be excited. Another way of expressing the wavelength, widely used in spectroscopy, is the *wavenumber* $\tilde{\nu}$, which corresponds to the reciprocal of the wavelength and is expressed in cm^{-1}. The way in which only specific frequencies of the spectrum interact with matter is difficult to understand without the notion of the quantization of energy. Until 1900, it was believed that matter could absorb (or emit) energy in a continuous way. However, such belief was in contradiction with experimental evidence. It was only when Max Plank introduced the idea of *quanta*, a discrete packet of energy, that experimental and theoretical predictions started

to match. According to Plank's theory, the energy of an oscillator is discontinuous and any change in its energy content can occur by means of a jump between two states. This new idea found a solution to the black body radiation problem, which until then according to the classical theory of the Rayleigh-Jeans law, led to the *ultraviolet catastrophe*. Five years later, in 1905 Albert Einstein proposed a similar description of quantized energy to describe the *photoelectric effect*. These early attempts to understand the microscopic world, known as the 'old quantum theory', led to the full development of *quantum mechanics* in the way we know it, by Niels Bohr, Erwin Schrödinger, Werner Heisenberg, Max Born, Paul Dirac and many others.

As a first simplification, the packet of electromagnetic energy also called a *photon* can be absorbed (or emitted) in a transition that involves two energy levels such that:

$$\Delta E = E_2 - E_1 = h\nu \tag{1.2}$$

where $h = 6.62607 \cdot 10^{-34}$ $\mathrm{m^2\,kg/s}$ is the Plank constant and E_1, E_2 are the energy levels. Only when the photon energy is resonant with the transition, the absorption can occur. The frequency of the transition (and hence, its energy) varies according to the stimulated phenomenon. The electromagnetic spectrum can be divided into various regions:

- Radiofrequency region: 10 m - 1 cm wavelength, it involves the reversal of spin of nuclei and electrons, which can be used for nuclear magnetic resonance and electron spin resonance spectroscopies;
- Microwave region: 1 cm - 1000 µm wavelength. The energy of microwaves excites the rotation modes of molecules and is used in rotational spectroscopy;
- Infrared region: 1000 µm - 750 nm wavelength. It is further divided into far-IR (1000 µm - 15 µm), mid-IR (15 µm - 2.5 µm) and near-IR (2.5 µm - 750 nm). The infrared region is responsible for roto-vibrational transitions and thus involves vibrational spectroscopy. Typically, most of the analytically relevant absorption happen in the mid-IR;
- UV-Visible region: 750 nm - 10 nm wavelength. It is used in UV-vis spectroscopy, and comprehends transitions of valence electrons;
- X-ray region: 10 nm - 100 pm wavelength. It involves inner electron transitions to the outer shells;
- γ-ray region: 100 pm - 10 pm wavelength. Involves energy transitions of inside nuclear particles (e.g. atomic nuclei).

The way in which the electromagnetic field can interact with a rotation or vibration mode of a molecule, is explained in more details in the next section. Such phenomenon opened the path to an ensemble of techniques for chemical analysis of gases, liquids and solid samples, proving to be an excellent tool for both qualitative and quantitative analysis.

1.3 Roto-vibrational transitions in gas molecules

A simple yet very effective description of the interaction between the electromagnetic field with a molecule comes from the model of a roto-vibrator, which is well represented by a diatomic molecule. Such result, even though some exception arise, can be generalized for polyatomic molecules and offer a precise description of the expected transition energies.

In order to be infrared active, the electric dipole of the molecule must change. This means that, homonuclear diatomic molecules will intrinsically be infrared inactive since the only vibration mode that such a molecule possesses will not cause any change in the dipole moment. This result has the important practical consequence that infrared spectroscopy can be performed in an open-path, since the atmospheric gas matrix is mainly composed of IR-inactive species (N_2, O_2, Ar). However, in some cases it is possible to observe infrared absorption in homonuclear molecules. It is the case of molecular hydrogen (H_2) absorption, which occurs as a consequence of tiny electric quadrupole and magnetic dipole transitions [17].

The molecule itself is formed as an effect of electron rearrangements of the two atoms when they get in close contact: the strength of such bond is an interplay between the repulsive Columbian forces of the positively charged nuclei and their negative electron 'clouds', and the attraction forces between each nuclei and the electrons of the other atom. Once the molecule is formed, the two atoms settle at an equilibrium distance. Bringing the atoms closer one another or pulling them apart requires energy, since repulsive and attractive forces will oppose to such action. The compression and extension of the bond behaves like a spring. Just like a system of two masses attached by a spring, also the bond will have an intrinsic vibrational frequency which depends on the mass of the system, or *reduced mass* ($\mu = m_1 m_2/(m_1 + m_2)$), and the force constant (k). In wavenumbers, this characteristic frequency reads:

$$\tilde{\omega}_{res} = \frac{1}{2\pi c}\sqrt{\frac{k}{\mu}} \tag{1.3}$$

In a real scenario, the potential energy as a function of the internuclear separation will not obey to a parabolic law (as it is for a harmonic oscillator), but needs a correction to describe the dissociation process, which takes place when the two atoms are pulled too far apart and the repulsion of the positively charged atom nuclei when both move closer together. An empirical expression was derived by Morse, from whom comes the Morse potential. The molecule is thus better represented by an anharmonic oscillator. In the quantum mechanical harmonic oscillator, the energy cannot be continuous but has to be quantized. It can be shown - by solving the Schrödinger equation assuming a parabolic potential - that the energy states (expressed in wavenumbers) are:

$$E_\nu = \left(\nu + \frac{1}{2}\right)\tilde{\omega}_{res} \tag{1.4}$$

where ν is an integer called *vibrational quantum number*. The two main results are that the lowest energy state ($\nu = 0$) doesn't have null energy, so a molecule can never be at rest. Also, in the harmonic oscillator model the energy levels are equispaced. By plugging the Morse potential in the Schrödinger equation, it comes out that the energy levels are no longer equispaced and their separation energy diminishes with ν, accumulating towards the dissociation state. Another fundamental difference in the solution of the two oscillators consists in the selection rules of the transition. For a harmonic oscillator, the selection rule $\Delta\nu = \pm 1$ applies, meaning that jumps of two or more states cannot take place. However, this is no longer true for the anharmonic oscillator, whose selection rules are $\Delta\nu = \pm 1, \pm 2, \pm 3 \ldots$, enabling the possibility of *overtone transitions*. The overtone transitions are statistically less probable, meaning they are weaker than the fundamental. Also, most of the transitions happen between the fundamental level as starting level, due to its occupancy relative to the other states. Since the typical separation energy is on the order of 10^3 cm^{-1}, at room temperature the occupancy of the first excited level can be obtained by the Maxwell-Boltzmann distribution, leading roughly to 1% of the ground state population. For sufficiently high temperatures, transitions between excited states can take place, leading to the formation of *hot bands*. Analysis of the transition strength between fundamental and hot bands is a common tool for the determination of the sample temperature.

Vibration is not the only motion that atoms in a molecule posses. In a molecule with N atoms, each atom contributes three degrees of freedom as its movement in space can be described by the three axis of the coordinate system. Thus, the total number of *degrees of freedom* is $3N$, as each atom is quite independent from the others. If we specify the translation of the molecule as a whole, we can make use of its center of mass, which can move along the three axis of the coordinate system without requiring the relative position of the atoms in the molecule to change, hence leaving $3N - 3$ degrees of freedom. The molecule can also rotate around three perpendicular axes: specification of these axes also requires 3 degrees of freedom leaving $3N - 6$ degrees of freedom ($3N - 5$ for linear molecules). Those modes corresponds to internal vibration modes. For instance, in a diatomic molecule ($N = 2$), which is necessarily linear, the vibrational mode will be only 1, the bond stretching.

As introduced in Section 1.2, rotational modes of molecules have energies that fall in the microwave region. The energy of those transitions is typically much smaller than vibrational energies, which in turn is much smaller than electronic transition energy. The importance of this evidence can be summarized in the Born-Oppenheimer approximation, which assumes the separation of electronic and nuclei wavefunctions, on the basis of the much higher mass of nuclei compared to electrons. We can assume the atoms coordinates to be frozen, while the electrons move. The same approximation, to some extent, applies for vibration and rotation motions. During a full rotation, we can expect to have approximately 10^3 vibrations. Hence, the total energy of the molecule can be written as:

$$E_{total} = E_{electronic} + E_{vibration} + E_{rotation} \tag{1.5}$$

which implies that electronic, vibrational and rotational energies are independent of each other. Clearly, this is only an approximation, which may be invalid under some conditions. This approximation is depicted in Fig. 1.1(a), showing the ground and excited electronic state of a molecule, each of them supporting vibrational and rotational levels. Another consequence of the Born-Oppenheimer approximation is that vibrational transitions produce a 'coarse structure' on top of electronic transitions, while rotational transitions produce a 'fine structure'. In this thesis, electronic transitions will not be discussed in detail. However, to comprehend the fine structure of vibrational spectra, a brief description of rotational transitions is needed.

Again, the simplest case is the rigid diatomic molecule, which can be depicted as a rotator. By the use of the Schrödinger equation, the rotational energy levels are readily obtained:

$$E_J = \frac{h}{8\pi^2 Ic} J(J+1) \quad \text{where } J = 0, 1, 2, \ldots \tag{1.6}$$

where E_J is the j-th energy levels in cm^{-1}, J is the *rotational quantum number* which assumes integer values and I is the moment of inertia of the molecule around the specified axis of rotation. As it can be seen from Eq. (1.6), the separation energy between two neighbouring states scales with J. The selection rules of the rigid diatomic rotator states that:

$$\Delta J = \pm 1 \tag{1.7}$$

and all the other transitions are forbidden. It is worth noting that, for rotational states, the energy states' occupancy probability is similar to that of the ground state level $J = 0$, and decays exponentially with increasing J. Nevertheless, each energy level is $(2J+1)$-fold degenerate, thus increasing the occupation probability of the J-state. The result is that the maximum population is found at intermediate J-values, producing the most intense peak absorption at some distance from the band center.

A more accurate model accounts for the distortion of the rotator length (bond length) as in more energetic rotations the length is stretched by the centrifugal force. Moreover, also the decoupling of rotational and vibrational energies is an approximation. If we consider both centrifugal distortion and the effect of the molecular vibration, we can calculate with great precision the frequency of rotational lines. The combination of vibration and rotational transitions gives the typical roto-vibrational branches in the mid-IR region. The simultaneous rotation and vibration of a diatomic molecule follows the selection rules:

$$\Delta\nu = \pm 1, \pm 2, \pm 3 \ldots \quad \Delta J = \pm 1 \quad \Delta J \neq 0$$

For $\Delta J = +1$, we have a set of transitions which form the R-branch, while for $\Delta J = -1$

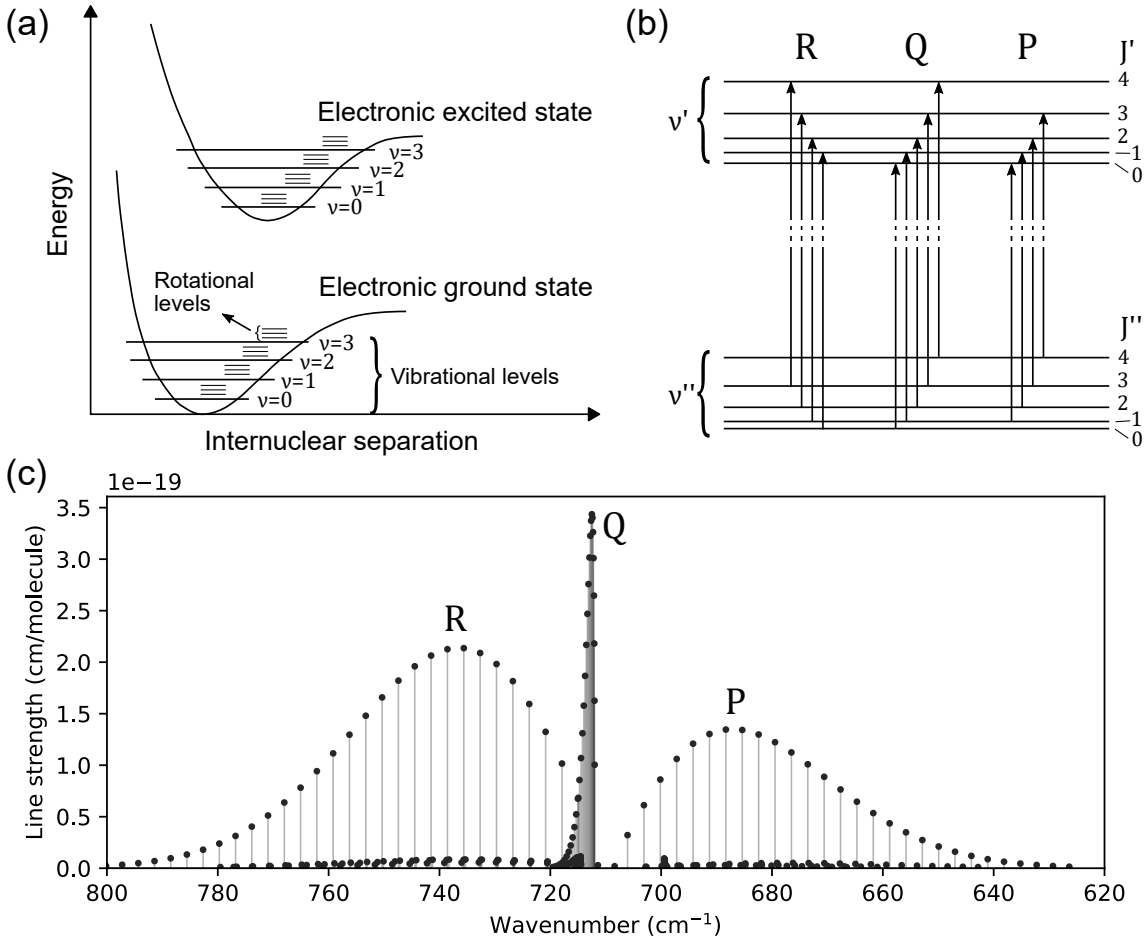

Figure 1.1: (a) Representation of the electronic ground and excited states, together with the Morse Potential. Each electronic state supports a set of vibrational levels (indicated with ν), which in turn held rotational states. (b) Roto-vibrational transitions in a simple system. The vibration transition $\nu'' = 0 \rightarrow \nu' = 1$ happens simultaneously with a rotation transition. The change in rotational quantum number $\Delta J = J' - J'' = 0, +1, -1$ gives rise to the Q, R and P-branches, respectively. (c) Simulated line strengths of HCN from the HITRAN2016 database [18], which displays all the three branches. The overlap of neighboring transitions (not displayed in the line strength of individual lines) in the Q-branch generates a very strong absorption.

the P-branch is formed. They appear as two set of lines almost symmetric around the wavenumber corresponding to the pure vibrational transition ($\Delta J = 0$). Surprisingly, the selection rule for the rotational transition depends on the direction of the vibrational transition ($\parallel$ or $\perp$ to the rotation axis). For perpendicular vibrations, the selection rule $\Delta J = 0$ is no longer forbidden and gives rise to the Q-branch, which is usually very intense since it is made by the superposition of many transitions with almost the same energy. In reality, those transitions do not posses the same energy, but their separation can be small enough to provide an overlap in the absorption. Line-broadening processes are responsible for this behavior, which will be explained in Section 1.4. In Fig. 1.1(b), a schematic for the formation of P-, Q- and R-branches is presented. The transition happens between the ground vibrational state ($\nu'' = 0$) to the first excited vibrational state ($\nu' = 1$).

Simultaneously, transitions between the rotational states of the ground vibrational level (J'') and the rotational states of the excited vibrational level (J') take place. Fig. 1.1(c) presents a simulation of the fundamental transitions of hydrogen cyanide (HCN) from the HITRAN database [18]. On the ordinate, the line strength (cm/molecule) is plotted as a function of the wavenumber.

1.4 Line parameters and broadening processes

The line strength (or intensity) is a measure of the probability of the transition (cm/molecule), and allows to predict the absorption that an individual line produces under certain conditions. If we denote the transition between two states $i \rightarrow j$, we can express the line strength as follows [19]:

$$S_{ij} = I_a \frac{A_{ij}}{8\pi c \tilde{\nu}_{ij}^2} \frac{g' e^{-c_2 E_i/T} \left(1 - e^{-c_2 \tilde{\nu}_{ij}/T}\right)}{Q(T)} \tag{1.8}$$

where I_a is the molecule isotopic abundance, $c_2 = hc/k_B$ ($k_B = 1.38065{\cdot}10^{-23}\ \mathrm{m^2\,kg\,s^{-2}\,K^{-1}}$ being the Boltzmann constant), A_{ij} is the Einstein coefficient for spontaneous emission ($\mathrm{s^{-1}}$), g' is the upper state statistical weight (or degeneracy factor), E_i is the lower state energy ($\mathrm{cm^{-1}}$), and $Q(T)$ is the total internal partition sum:

$$Q(T) = \sum_k g_k \exp\left(\frac{c_2 E_k}{T}\right) \tag{1.9}$$

which provides the molecule occupancy distribution among the possible energy states accounting for the sample temperature and the state degeneracy, according to Maxwell-Boltzmann distribution.

The line intensity as defined in Eq. (1.8) is often indicated as S_ν^N, indicating that it is proportional to the number N of absorbing molecules per unit volume. With the knowledge of the normalized line shape function $\Phi(\tilde{\nu}-\tilde{\nu}_0)$ ($1/\mathrm{cm^{-1}}$), the spectral absorption coefficient (α, expressed in $\mathrm{cm^{-1}}$) can be calculated:

$$\alpha(\tilde{\nu} - \tilde{\nu}_0) = S_\nu^N \Phi(\tilde{\nu} - \tilde{\nu}_0) N = \sigma(\tilde{\nu} - \tilde{\nu}_0) N \tag{1.10}$$

where the quantity $S_\nu^N \Phi(\tilde{\nu}-\tilde{\nu}_0)$ is also referred to as *cross-section*, $\sigma(\tilde{\nu}-\tilde{\nu}_0)$ ($\mathrm{cm^2}$/molecule). The absorption coefficient defines how planar monochromatic EM radiation exponentially decays within a medium, according to the well known Bouguer-Beer-Lambert law [20]:

$$I_T(\tilde{\nu}) = I_0(\tilde{\nu}) \exp[-\alpha(\tilde{\nu}) L] \tag{1.11}$$

being L the length of the optical absorption, and I_T and I_0 the transmitted and incident light intensities. The ratio between the transmitted and the incident radiation intensity

provides the *transmittance* ($T(\tilde{\nu})$) and its anti-logarithm gives the *absorbance* ($A(\tilde{\nu})$):

$$T(\tilde{\nu}) = \exp[-\alpha(\tilde{\nu})L] \tag{1.12}$$

$$A(\tilde{\nu}) = \alpha(\tilde{\nu})L \tag{1.13}$$

Absorbance allows to linearly relate the optical absorption of a substance with its concentration (contained within the absorption coefficient term). Such phenomenon is widely used in most spectroscopic instrumentation, and will be described more in detail in Section 1.6.

In Eq. (1.10), the effect of the normalized line shape function on the absorption coefficient is described. The knowledge of the line shape function, together with the absorbing specie number density N, and the transition line intensity, allows a full prediction of the sample's absorption coefficient.

So far, as per Eq. (1.8) we considered the transition between two discrete states as described by a specific energy. However, there are many reasons why a transition is never strictly monochromatic, leading to a distribution of transition energies.

1.4.1 Natural linewidth

The first, fundamental reason, lies in *Heisenberg uncertainty* principle which - in its energy-time relation - asserts that the uncertainty on the state energy (ΔE_i) and its lifetime (τ_i) are connected according to:

$$\Delta E_i \tau_i \gtrsim \frac{\hbar}{2} \tag{1.14}$$

where $\hbar = h/2\pi$. Hence, aside from the ground state which has an infinite lifetime, the upper-energy states will always be affected by an uncertainty. Assuming no other competing phenomenon, the spontaneous emission rate will define the lifetime of the molecule in the excited state. The Einstein's coefficient for spontaneous emission scales as $\tilde{\nu}^3$ for an electronic-dipole transition [21]. The direct implication is that roto-vibrational transition will have very small natural linewidths. If the lower state is not the ground state, it will also be affected by an uncertainty and the total transition linewidth will be defined by:

$$\delta\tilde{\nu}_n = \frac{1}{2\pi c}\sqrt{\frac{1}{\tau_i^2} + \frac{1}{\tau_j^2}} \tag{1.15}$$

Usually, the natural linewidth can only be measured for species at rest with respect to the observer, since Doppler effects will produce a much broader linewidth. A simple model for natural broadening assumes the atomic system as a damped oscillator and the resulting line shape will be described by a Lorentzian shape:

$$\Phi(\tilde{\nu}) = \frac{1}{2\pi}\frac{\delta\tilde{\nu}_n}{(\tilde{\nu} - \tilde{\nu}_0)^2 + (\delta\tilde{\nu}_n/2)^2} \tag{1.16}$$

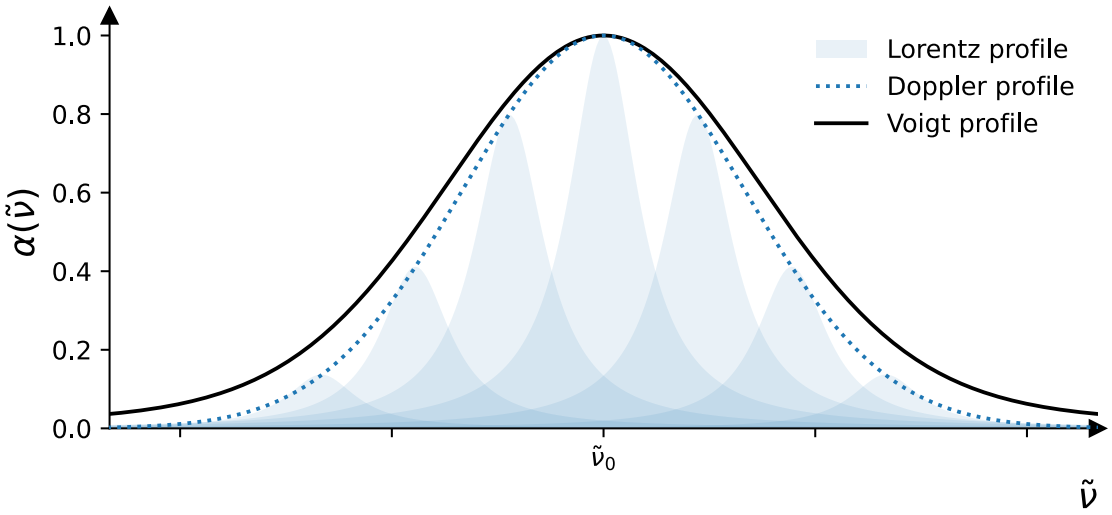

Figure 1.2: Voigt profile as a convolution of Lorentzian shapes (shaded areas), located at shifted absorption frequencies as an effect of collisional broadening. The location and intensity of the Lorentzian line follow the Doppler (Gauss) distribution of velocities in the sample.

1.4.2 Doppler broadening

One of the major contributions in gases at low pressures is the Doppler width, which is due to the Brownian motion of the absorbing molecules. This phenomenon happens if the molecule posses a velocity component in the direction of the absorbed electromagnetic field. Because of the velocity component (v_z) along the EM field propagation direction, the transition frequency will appear shifted to a new value $\delta\tilde{\nu}_a = \delta\tilde{\nu}(1 + v_z/c)$. The shift will be positive, for a molecule moving in the same direction of the field, and negative for a molecule in opposing motion. At the thermal equilibrium, the gas molecules follow a Maxwell velocity-distribution such that the resulting line shape will be:

$$\Phi(\tilde{\nu}) = \sqrt{\frac{\ln 2}{\pi\delta\tilde{\nu}_D^2}} \exp\left(-\frac{(\tilde{\nu}-\tilde{\nu}_0)^2 \ln 2}{\delta\tilde{\nu}_D^2}\right) \tag{1.17}$$

$$\text{with} \qquad \delta\tilde{\nu}_D^2 = \frac{\tilde{\nu}_0}{c}\sqrt{\frac{2N_A kT \ln 2}{M}} \tag{1.18}$$

where $\delta\tilde{\nu}_D$ is the Half-Width at Half-Maximum (HWHM) of the line shape Gaussian distribution, N_A is the Avogadro number (number of molecules per mole, $6.022 \cdot 10^{23}$ mol^{-1}), M is the molar mass of the gas specie. A more detailed description of Doppler broadening considers the finite lifetime of the transitions. The frequency response will be described by a Lorentzian shape, as per Eq. (1.16). Plugging this term into the Maxwell distribution of the molecule velocities leads to the convolution of Lorentzian and Gaussian profiles, called a *Voigt profile*. In Fig. 1.2, the formation of a Voigt profile as a convolution of the Lorentzian lines and the Doppler line is portrayed.

1.4.3 Collisional broadening

Collisional broadening happens as a consequence of collision with other molecules. By collision, we mean a mutual interaction between the two molecules which alters the energy states of both partners. If no internal energy is transferred between the two partners, the collision is termed elastic. On the other hand, if an energy transfer process happens, or the energy is converted into heat, the collision is termed inelastic. We will see in Chapter 2 how the latter can be efficiently exploited for trace gas sensing.

We can depict the collision process as a promoter of the excited molecule relaxation, which in turn induces a broadening of the excited state level as per Eq. (1.15). The total transition probability can be expressed as:

$$A_i = \frac{1}{\tau_{sp}} + ap_b \quad \text{with} \quad a = 2\sigma_i j \sqrt{\frac{2}{\pi \mu k T}} \tag{1.19}$$

being μ the reduced mass of the system. Hence, additionally to the natural linewidth, the term $\gamma_p = ap_b$ will be responsible of the *pressure broadening*. Inelastic collisions are responsible for the broadened line. On the other hand, elastic collisions do not change the amplitude of the *oscillator*, but change its phase and in turn its center frequency. In many cases, the line shape can still be described by a Lorentzian function:

$$\Phi(\tilde{\nu}) = \frac{C}{(\tilde{\nu} - \tilde{\nu}_0 - \Delta\tilde{\nu})^2 + (\delta\tilde{\nu}/2)^2} \tag{1.20}$$

where C is a normalization constant which depends on the linewidth, the line shift $\Delta\tilde{\nu} = N_B \bar{v} \sigma_s$ and the line broadening $\delta\tilde{\nu} = \delta\tilde{\nu}_n + N_B \bar{v} \sigma_b$, being N_B the number density of the collisional partner B, and σ_s, σ_b the collision cross sections for line shifts and broadening (elastic and inelastic collisions), while $\bar{v}$ is the mean relative velocity.

1.4.4 Collisional narrowing

In infrared and microwave ranges, collisions may sometimes cause a narrowing of the linewidth, also known as *Dicke narrowing* [22]. This phenomenon might happen when the lifetime of the excited state is longer than the mean time between successive collisions. If so, the mean free velocity of the molecule can be reduced by the many collisions, causing a smaller Doppler shift. Hence, if the Doppler broadening is the dominating effect, a reduction of the linewidth can be observed. Usually, such effect can be observed in a certain pressure range, above which pressure-broadening will dominate [23].

1.4.5 Homogeneous and inhomogeneous broadening

To summarize what have been explained so far, we can distinguish between homogeneous and inhomogeneous line broadening effects. A spectral line profile is said to be *homogeneously broadened* if the absorption probability as a function of the frequency is

equal for all the molecules of the sample that are in the same energy level. These line shapes can be described by a Lorentzian line shape. An example of homogeneous broadening is natural line broadening. On the other hand, if the molecules that experience the transition have a different probability at different frequencies of the absorbed field, we speak of *inhomogeneously broadened* line. An example of inhomogeneous broadening is the Doppler broadening, since molecules with different mean velocities along the field direction will experience a red or blue-shifted absorption and thus, the transition probability at a certain frequency will differ.

1.5 Fourier Transform Infrared Spectroscopy

Spectrometers are used to measure the absorption features of a sample, by resolving the light intensity passing through the sample at different wavelengths. The spectrometer consists of a radiation source, an optical system that allows interaction of the light with the investigated sample, a dispersion element (prism, or monochromator) and the detector. In the UV-Vis range, the separation of the wavelengths is achieved by means of monochromators, which are made up of slits and a dispersive element, mainly one or more gratings. The grating induces a spreading of the white light into its components, while the slit filters a narrow band of the incoming and/or exiting light. In most high-end spectrometers, the resolving power ($\lambda/\Delta\lambda$) of the instrument is enhanced by the use of multiple gratings, or a combination of a prism and a grating (Echelle monochromators). However, when it comes to the infrared region, a fundamental problem arises in how well the light can be dispersed. First, if using a dispersive optical element, normal dispersion is required in a wide IR range. Historically in the first generation of IR spectrometers, large NaCl prism were used, which required careful control over air humidity. Additionally, small scan ranges were possible with limited repeatability. The usage of gratings improved the quality of such spectrometers, leading to the second generation. However, it has to be noted that the resolving power of a grating is strictly wavelength dependent. Moreover, the physical separation of the gratings' lines scales with the λ, such that the lines density can strongly change. For instance, UV-Vis gratings can feature line densities up to 3000 l/mm. However, at $\lambda = 3$ µm, the line density goes down to 300 l/mm. For high spectral resolution, large gratings are required. Moreover, reaching the same spectral resolution in the full spectrum is difficult since the IR spans wavelength between 1 - 1000 µm. The greatest breakthrough happened with the third generation, when Fourier Transform Infrared Spectrometers (FTIR) were introduced. The main difference in FTIR spectrometers is the capability of recording all wavelengths at the same time, by only scanning a movable mirror. The operation principle of FTIR consists in passing the broadband light, produced by the source, through a Michelson interferometer and the sample compartment. The interferometer is made up of a beamsplitter and two mirrors, one static and one movable. The light is finally collected on top of a detector, at different positions

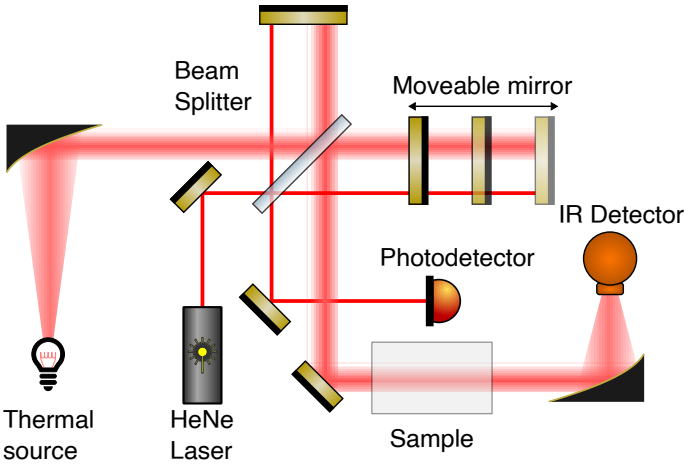

Figure 1.3: Experimental apparatus of an FTIR spectrometer.

of the movable mirror in the interferometer. By doing so, an optical path difference is achieved between the arms of the interferometer. The intensity of the light is recorded as a function of the optical path delay. When the arm are symmetrical, the retardation is null and every wavelength interferes constructively, generating a strong peak intensity. On the other hand, when a certain retardation is introduced, each wavelength will experience a different phase shift. The result of the superposition of each wavelength electric field into the detector, as a function of the mirror displacement, is called the *interferogram*. Since the mirror is displaced at a certain scan speed, the interference of the electric fields, oscillating in the THz domain, will produce an intensity modulation in the range of few kHz which can be detected by standard IR detectors. From the interferogram, a Discrete Inverse Fourier transformation is calculated to retrieve the light spectrum of the impinging broadband radiation as a whole. A typical experimental arrangement of an FTIR spectrometer is provided in Fig. 1.3.

The resolution of the FTIR spectrometer is limited by the maximum extent of the mirror displacement, such that $\delta_{\text{res}} = 1/\Delta L_{\text{max}}$. Resolution as little as 0.05 cm^{-1} are readily available by high-end spectrometers. Moreover, FTIR has many other advantages:

- **Multiplex or Fellgett advantage**: all the wavelengths are recorded at once, such that each point in the interferogram contains information of the full spectrum. Thus, in the equivalent time it takes to produce a spectrum in a dispersive instrument, FTIR can collect multiple interferograms that are averaged to produce a spectrum with a higher signal-to-noise ratio (SNR);

- **Jacquinot advantage**: also known as **Throughput advantage**, arise from the fact that in the FTIR spectrometer no slits are required as in dispersive spectrometers, which strongly reduce the area of the beam passing through the spectrometer. An interferometer can accept a circular cross section of the IR beam thus the amount of light passing the interferometer is significantly higher resulting in higher throughput;

- **Connes advantage**: the *precision advantage* of FTIR in terms of wavelength calibration comes from the internal referencing of the measurement via a HeNe laser co-aligned to the Michelson interferometer. A precise measurement of the mirror displacement can be attained simultaneously while recording the IR interferogram, by monitoring also the interferogram of the reference laser. Since a monochromatic source produces a pure sinusoid, sample points are captured very reliably every time the reference interferogram undergoes a zero-crossing. Exact knowledge of the laser's wavelength allows accurate determination of the optical path lengths while performing a scan.

Nowadays FTIR spectrometers are widely employed for routine operations and find their application in revealing the composition of solids, liquids, and gases. A common use for qualitative measurements is the identification of unknown materials and confirmation of production materials (incoming or outgoing). FTIR spectrometers also provide powerful solutions when quantitative information regarding several analytes in a given sample is required. FTIR provides valuable insight into both intermolecular and intramolecular interactions within a sample. For example, they can be used to study how molecules interact and orient themselves on surfaces, or to analyze the secondary structures of proteins. Beyond these specific interactions, FTIR spectra also offer access to latent properties of a sample that are not directly tied to the quantitative information of a single analyte. This capability allows for a broad range of applications, such as determining the octane number of fuels, identifying different varieties of wine, and diagnosing conditions like cancer. For the analysis of solids and liquids, resolutions above 1 cm^{-1} are sufficient to resolve the wide absorption bands, since the fine rotational structure is lost in condensed phases. On the other hand, resolving individual lines for gas-phase sample can be challenging and is limited to research-grade instruments. Higher resolutions are obtained for longer mirror displacements, hence the size of the instrument will also be connected to the capabilities of the same. For low resolutions, compact sizes are available, but it is not the case for resolutions higher than 0.1 cm^{-1}. This complicates the possibility of deploying this technology in the field.

While FTIR is a powerful technique for multicomponent analysis, thanks to the capability of surveying the whole infrared spectrum at once, it lacks in terms of sensitivity. This is especially true if compared to the most recent laser-based spectrometers, which on the other hand present a limited spectral coverage.

1.6 Methods in laser spectroscopy

Since their invention in the 1960s, lasers have undergone tremendous improvements. Laser applications have been extended to spectroscopy due to the numerous advantages that this light source provides compared to non-coherent sources like thermal emitters:

1. the high spectral power density of laser sources is always a desirable property, as it allows to work well above the detector noise level, improving the performance of the system;

2. the detection sensitivity increases with narrower spectral emissions (temporal coherence), since in many cases the sensitivity of the technique is defined by the spectral overlap of the emitted radiation and the absorption feature. The highest sensitivity is achieved when the spectral feature is larger than the emission spectrum of the source, which is the case in many situations for laser spectroscopy;

3. the high directionality (spatial coherence) of laser beams can be exploited to improve the interaction pathlength, leading to higher sensitivities as per Lambert-Beer equation (Eq. (1.11)). Multi-pass cells, as well as more complicated approaches such as cavity enhanced techniques can be employed to reach unmatched limits of detection;

4. the improved spectral resolution paves the path for metrological measurements, for the determination of line parameters, line shape profiles, even in sub-Doppler conditions or parameters of collisional processes, taking part in collisional broadening;

5. swift spectral tuning can be achieved for semiconductor based lasers by operating on the diode bias current;

6. wavelength stabilization techniques can be employed to lock the laser to the maximum of an absorption profile, or to external oscillators, reaching relative accuracies up to 10^{-8} or better;

7. the inherent polarization of laser sources can be exploited for samples that exhibit polarization-sensitive absorption, which is used in Faraday rotation spectroscopy;

8. the coherence of lasers allows to access the dispersion of the samples, with the advantage of an extended linearity - exploited in dispersion spectroscopy.

Semiconductor diode lasers are the most used type of lasers in chemical analysis, primarily because of their ease of wavelength tuning through temperature or bias current adjustment. Semiconductor diode lasers are a class of solid-state lasers, which are based on a semiconductor gain medium to convert injected charge carriers into photons. In the last decades, semiconductor lasers have garnered significant attention from the scientific community and have undergone substantial advancements. Semiconductor lasers comprehend a large variety of devices, which can be categorized mainly into diode lasers (DL), interband cascade lasers (ICL) and quantum cascade lasers (QCL). The main difference between these devices concerns the emission range, which is defined by the specific physics behind their architecture and material systems used for the gain medium. Diode lasers typically operate from the ultraviolet up to the near-infrared region, depending on the semiconductor used in their fabrication. In spectroscopic applications, diode lasers in the

near-infrared region are used to target less-efficient overtone transitions. Moving towards the mid-infrared, ICLs utilize a cascaded structure composed of multiple quantum wells to achieve efficient light emission. Emissions between 2.7 µm to 5.6 µm in continuous wave have been demonstrated [24], while at cryogenic temperatures emission up to 11 µm have been reported [25]. More recent work [26] has shown the capability of ICLs to emit under pulsed operation in the long-wavelength regime ($\lambda \approx 13.2$ µm).

Differently from interband cascade lasers, QCLs are a class of semiconductor lasers which exploits electronic intersubband transitions between confined levels in the conduction band. An extensive explanation will be dedicated to this specific laser class in Chapter 4. Typical QCL emission ranges from 2.6 µm up to the THz domain [27], [28]. They find application in high precision chemical sensing, medical diagnostics, and free-space optical communication due to their precision, versatility, and performance capabilities [29].

The following sections will deal with the main direct and indirect absorption approaches in laser sensing.

1.6.1 Direct methods in laser spectroscopy

By *direct absorption methods* we refer to those approaches which are based on the detection of transmitted photons upon interaction of an incident laser beam on an absorbing sample. The transmittance, as given by Eq. (1.12), decays exponentially with the absorption coefficient of the substance and the interaction pathlength. The same equation can be rewritten in terms of the sample concentration, as

$$T(\tilde{\nu}) = \exp(-\sigma(\tilde{\nu}) N_{tot} c L) \tag{1.21}$$

being N_{tot} the molecular number density at given pressure and temperature and c the concentration, usually expressed in parts-per-million (ppm) or parts-per-billion (ppb). The molecular number density is conveniently obtained from the ideal-gas law in the form of:

$$N_{tot} = \frac{p}{k_B T} = \frac{p}{T} \frac{L(T_S) T_S}{p_0} \tag{1.22}$$

where p and T are the pressure and absolute temperature of the sample, while in the last relation $L(T_S) = 2.68676 \cdot 10^{19}$ molecules/cm^3 is the Loschmidt number, $T_S = 273.15$K and $p_0 = 1$ atm. The relationship in Eq. (1.21) holds for multiple absorptive species, such that the absorption coefficient can be expressed as

$$\alpha(\tilde{\nu}) = \sum_{i=1}^{n} \sigma_i(\tilde{\nu}) N_{tot} c_i \tag{1.23}$$

making direct absorption a powerful tool for multi-specie analysis. One of the most known and applied direct approaches consists in swift tuning of a single diode laser line across

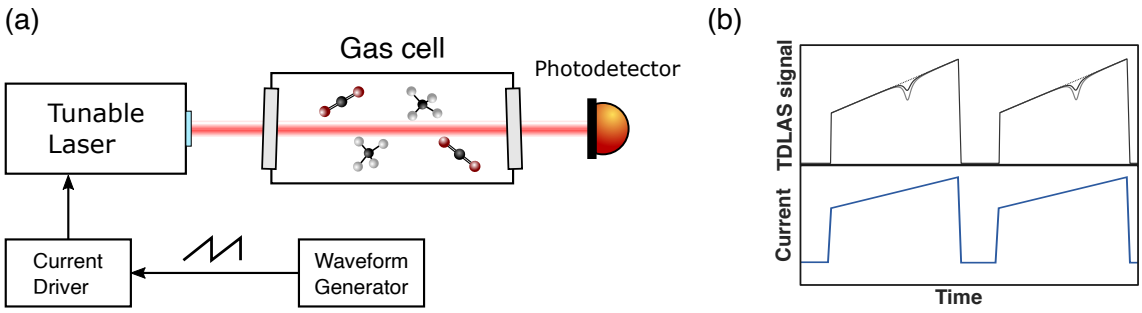

Figure 1.4: (a) Schematic of a TDLAS setup. A tunable diode laser is scanned via current-tuning across a spectroscopic feature, while the transmitted laser intensity is monitored by a photodiode. (b) The resulting TDLAS signal exhibit a dip in correspondence of the absorption line, on top of a rising background (represented in dotted line) typical of current tuned diode lasers. In light grey, the same absorption resulting by a higher concentration, or equivalently, by a longer interaction pathlength.

an atomic or molecular absorption. Such technique is often referred to as *Tunable Diode Laser Absorption Spectroscopy* (TDLAS).

1.6.1.1 Tunable Diode Laser Absorption Spectroscopy

In TDLAS, the use of a single frequency source ensures unambiguous assignment of the absorption lines. This greatly simplifies the system apparatus, since the employed laser source is assumed monochromatic and does not require any dispersive optical element. Nevertheless, the typical scanning range is limited to few cm^{-1}.

A schematic of a typical TDLAS setup is presented in Fig. 1.4(a). The diode laser is scanned via current tuning across an absorption line, while the transmitted laser intensity is monitored with a photodetector. As a reference, a background spectrum in absence of the absorbing analyte is needed, in order to compute the absorbance spectrum of the sample. The resulting TDLAS signal is presented in Fig. 1.4(b), where a dip in correspondence of the absorption feature is observed. Scanning rates in the kHz range allow to average many spectra in short time, increasing the SNR.

The main limitation of TDLAS comes from the need of measuring extremely low signals on top of a strong background. Several methods to improve the performance of TDLAS have been demonstrated, which either enhance the absorption features or are aimed to reduce the noise level. To improve the absorption of the analyte, one can exploit the high directionality of laser beams by increasing the interaction pathlength. Among such approaches, multipass cells and optical cavities are the most common. A multipass cell is a system composed by two or more mirrors, such that a laser beam can be reflected multiple times to enhance the interaction pathlength by a few orders of magnitude. Multipass cells come in various designs, including cylindrical, rectangular, and toroidal configurations. Common types of multipass cells include Pfund, White, Herriott, and circular cells. The design of a multipass cell requires careful attention of the geometry which influences optical stability, pathlength and easiness in the alignment, together with the choice of suitable

mirror curvatures and coatings. The management of stray light and interference fringes limits the minimum detectable absorption.

Another class of techniques, named *Cavity Enhanced Absorption Spectroscopy* (CEAS), increase the effective pathlength by making use of optical cavities. Similarly to multipass cells, optical cavities traps the light within two or more highly reflective mirrors. The substantial difference lies in the fact that the optical cavity generates a standing wave, behaving as a resonant element for the electromagnetic field. Depending on the quality of the mirrors, the light can travel equivalent pathlengths of several km. Common approaches include Cavity Ring Down Spectroscopy (CRDS), where the characteristic extinction time (ring-down time) of the intensity inside the cavity is measured and compared in presence and absence of an absorbing analyte. The presence of an absorber introduces additional losses in the cavity, decreasing the time needed for the photons to leak out of the cavity. Other techniques exploit optical feedback (OF-CEAS) from the cavity, to lock the frequency of the laser to one of the cavity's modes. For high quality cavities, the optical feedback reduces the laser emission linewidth compared with the free-running laser.

While the latter methods mainly address the interaction pathlength, another ensemble of techniques aims to reduce system noise. Such approaches are usually named *modulation techniques*, since they involve modulation of the laser light, either in terms of its amplitude or frequency. Modulation techniques can also be combined with multipass cell approaches and CEAS, such as for Noise-immune cavity-enhanced optical heterodyne molecular spectroscopy (NICE-OHMS). Since this work makes wide use of modulation approaches, a review of the main methods is provided in the following subsections.

1.6.1.2 Frequency modulation

Frequency modulation techniques were not directly designed for laser spectroscopy, but were taken from microwave spectroscopy. In frequency modulation techniques, the instantaneous frequency of the laser line is modulated in time either by applying a sinusoidal current-bias or by using external optical elements which introduce phase-shifts in the optical wave, such that:

$$\nu(t) = \nu_c + \Delta\nu \cos(2\pi\Omega t) \tag{1.24}$$

being ν_c the carrier (optical) frequency, $\Delta\nu$ the extent of the modulation and Ω the modulation frequency. The interaction of the sample with a modulated radiation field leads to the generation of a periodic signal at the modulation frequency, which can be selectively extrapolated by making use of frequency and phase-sensitive detectors (Lock-in amplifiers). The advantage of this detection scheme consists in the rejection of noise contributions that does not fall within the bandwidth of the phase-sensitive detector. Typically, the noise contribution of technical sources in the detection system can be almost completely suppressed at sufficiently high frequencies ($\Omega > 1$GHz), reaching the quantum

fluctuations of the laser source [30]. Electro-optic crystals or acousto-optic modulators can be used to achieve RF modulation frequencies, where the technical noise of the system is almost completely suppressed.

Historically, two families of techniques have always been identified under the name of *wavelength modulation* (WM) and *frequency modulation* (FM) spectroscopy. However, the technical difference is very subtle, since conceptually they are the same thing. Several authors provided a unified mathematical description of the phenomenon, which can be found in [31]. In both wavelength modulation and frequency modulation spectroscopy, the laser frequency is sinusoidally modulated over time as per Eq. (1.24). The sinusoidal modulation of the instantaneous frequency produces a similar effect on the time-dependent phase shift, such that the optical field can be described in its complex form as:

$$\begin{aligned} E(t) &= E_0 \exp\left[2\pi i \left(\nu_c t + \frac{\Delta\nu}{2\pi\Omega}\sin(2\pi\Omega t)t\right)\right] \\ &= E_0 \sum_{n=-\infty}^{+\infty} J_n(\beta)\exp[2\pi i(\nu_c + n\Omega)t] \end{aligned} \tag{1.25}$$

where $J_n(\beta)$ are the n-th order Bessel functions of the first kind computed at the modulation index $\beta = \Delta\nu/2\pi\Omega$. The representation via the Bessel function directly shows how, in the frequency domain, an infinite set of discrete frequencies appear separated by the modulation frequency Ω. All these frequency components, symmetric to the carrier, are called sidebands. The number of sidebands increases with the modulation index. The difference between WM and FM lies in the number of sidebands and their separation with respect to the spectroscopic feature ($\delta\nu$). In wavelength modulation [32], large modulation indexes are used ($\beta \gg 1$), but low modulation frequencies are employed such that the modulation frequency is small compared to the spectral feature ($\Omega \ll \delta\nu$). The result is a spectrum of closely spaced sidebands, where the dispersion information is lost, and the change in intensity over time is measured. Typically, the maximum frequency excursion $\Delta\nu$ determines the resolution in WMS, and values $\Delta\nu < \delta\nu$ are set to assure a derivative spectrum. Modulation frequencies on the order of few kHz are common. On the other hand, in FM the modulation frequency is so high that the sideband spacing is on the order of the spectroscopic feature, such that each sideband probes individually the absorption line. Also, the modulation index is kept low, in order to have the formation of only 2 sidebands. It appears obvious that the only difference between WM and FM is the frequency regime of the modulation.

The heuristic description for WM uses the formalism of the instantaneous frequency to evaluate the effect of the sample interaction with a 'slowly' modulated field [31]. If the absorption $\alpha(\nu)L \ll 0.05$ is assumed to be small [32], the transmitted intensity (as per Eq. (1.11)) can be expressed as $I_T = I_0(\nu)[1 - \alpha(\nu)L]$. Such expression holds for optically thin samples, which is the case for trace gas detection, where high sensitivities are desirable. Several mathematical formalism are possible to describe the phenomenon.

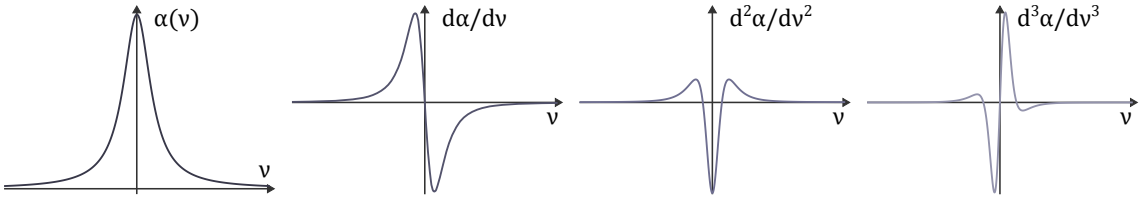

Figure 1.5: From the left, absorption of a Lorentzian line and its 1st, 2nd and 3rd derivative. In wavelength modulation spectroscopy, similar signals are obtained upon demodulation to the n-th harmonic.

By making use of the Taylor expansion around the carrier frequency one obtains:

$$I_T(\nu) = I_0 \left[1 - L \left(\alpha(\nu_c) + \left.\frac{d\alpha}{d\nu}\right|_{\nu_c} (\nu - \nu_c) + \frac{1}{2!}\left.\frac{d^2\alpha}{d\nu^2}\right|_{\nu_c} (\nu - \nu_c)^2 + \right.\right. \\ \left.\left. + \frac{1}{3!}\left.\frac{d^3\alpha}{d\nu^3}\right|_{\nu_c} (\nu - \nu_c)^3 + \cdots \right)\right] \tag{1.26}$$

and by substitution of Eq. (1.24) in Eq. (1.26), one gets:

$$I_T(\nu) = I_0 \left[1 - L \left(\alpha(\nu_c) + \left.\frac{d\alpha}{d\nu}\right|_{\nu_c} \Delta\nu \cos(2\pi\Omega t) + \frac{1}{2!}\left.\frac{d^2\alpha}{d\nu^2}\right|_{\nu_c} \Delta\nu^2 \cos^2(2\pi\Omega t) + \right.\right. \\ \left.\left. + \frac{1}{3!}\left.\frac{d^3\alpha}{d\nu^3}\right|_{\nu_c} \Delta\nu^3 \cos^3(2\pi\Omega t) + \cdots \right)\right] \tag{1.27}$$

The sinusoidal dependency of the instantaneous frequency causes the convergence of the Taylor series to the Fourier series. For some modulation depths $\Delta\nu$, such series might not converge, but in the assumption of small modulation depths, higher-order terms can be neglected. Lock-in amplifier based detection allows to retrieve a specific frequency component (in this case the modulation component, Ω) or one of its harmonics ($n\Omega$). The n-th harmonic signal will be then:

$$S_n(\nu) = \frac{1}{n!}\Delta\nu^n \left.\frac{d^n\alpha}{d\nu^n}\right|_{\nu_c} \tag{1.28}$$

Such result is only true in the limit of small modulation depths, since the effect of higher-order terms on the n-th term is negligible. However, in most experimental cases, the amplitude of a component has to be maximized to improve the signal-to-noise ratio. In this case, the modulation depth has to be almost comparable to the spectral feature extent. Arndt [33] showed the dependence of the first and second harmonic amplitude for a Lorentzian line. A maximum for the first harmonic signal is obtained for normalized modulation indexes $m = \Delta\nu/\Delta\nu_{\mathrm{HWHM}} = 2$. For the second harmonic signal, the maximum is achieved for $m \approx 2.2$ for Lorentzian, Gaussian and Voigt profiles [32]. In Fig. 1.5, the typical derivative shapes of a Lorentzian absorption feature are portrayed up to the 3rd derivative.

The model presented in Eq. (1.27) is not comprehensive of unwanted intensity modu-

lation components. In most cases where a diode laser is employed, it is advantageous to tune the laser's wavelength via current dithering with a sinusoidal signal. Current tuning induces both intensity and frequency modulation. The resulting effect is a distortion of the presented shapes by appearance of asymmetry and background signals.

Such a derivative-like approach showcases several advantages. First, the second harmonic signal is often used for the quantification of trace concentrations upon calibration of the system (2f-WMS). Contrary to the first harmonic, the second harmonic allows to remove slowly varying absorption features which might arise from optical components. Moreover, the first harmonic suffers from residual amplitude modulation (RAM) of the diode laser, which introduces an additional offset. The second harmonic signal, on the other hand, removes the offset and is often referred to as background free technique. An additional feature is the coincidence of its peak signal with the resonance absorption, which allows to introduce locking schemes to the peak. The most common is the use of the third-harmonic via a reference cell, since its central zero-crossing coincides with the resonance absorption. Similar locking concepts have been used in the context of this work and will be thoroughly discussed in Section 3.5.

1.6.1.3 Lock-in amplifier principles

Due to its extensive use in many spectroscopic applications, a dedicated description of the lock-in amplifier (LIA) operation principle is needed. The lock-in amplifier allows phase-sensitive detection by retrieving the in-phase and the quadrature component of a periodic signal, oscillating at a particular frequency Ω. The in-phase and quadrature component, often referred to as X- and Y-component are 90° phase-shifted, and the simultaneous knowledge of such quantities allows to retrieve the phase-shift of the measured signal with respect to the internal phase of the lock-in amplifier.

The operation of the lock-in amplifier is schematically shown in Fig. 1.6. The analog signal ($V_s(t)$), with all its frequency components is fed to the LIA. The LIA mixes (multiplies) this signal with a reference signal ($V_r(t)$) at the modulation frequency or one of its harmonics ($n\Omega$). The reference signal can be either generated from an internal oscillator by the lock-in amplifier, and used for the experiment purposes (such as modulation of a physical quantity), or can be obtained by an external reference port. In this case, a phase-locked loop (PLL) is used from the instrument to retrieve the external frequency component and its phase. The signal is multiplied with the reference and a 90° phase-shifted copy of it, such that both in-phase and quadrature components can be retrieved. Such instruments are defined double-phase lock-in amplifiers.

After multiplication with the reference signal, a low-pass filtering operation is performed. The filter order and time constant (τ) of the low-pass filter can be in many cases adjusted to optimize response time, noise-rejection performance and phase-shifts introduced by the lock-in. The result of this operation is the demodulated signal, which

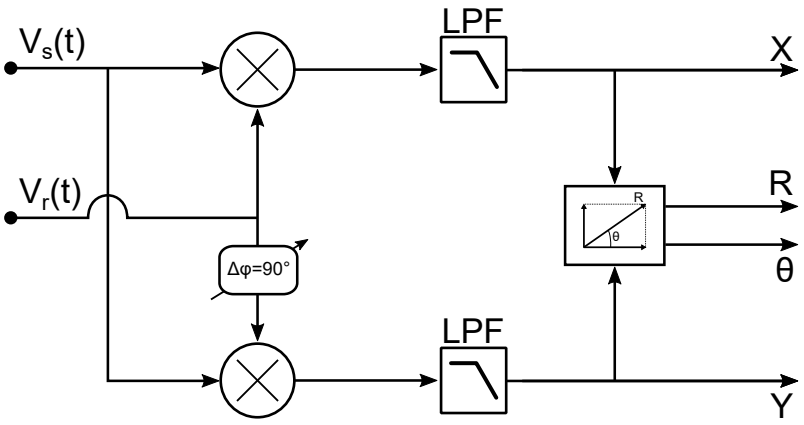

Figure 1.6: Block diagram of a double-phase lock-in amplifier.

is deprived from any high-frequency components and contains only the frequency components centred at the reference frequency, with a bandwidth defined by the low-pass filtering stage.

We can assume an oscillating signal at radial frequency ω_s with its noise components ω_n:

$$V_s(t) = A_s \cos(\omega_s t + \phi_s) + \sum_{\omega_n} A_n \cos(\omega_n t + \phi_n) \tag{1.29}$$

and a reference signal of frequency ω_r:

$$V_r(t) = A_r \cos(\omega_r t + \phi_r) \tag{1.30}$$

where A_s, A_n and A_r are the amplitudes of the signal, the noise component and the reference signal, while ϕ_s, ϕ_n, ϕ_r their phase. Upon mixing, we obtain:

$$\begin{aligned} V_s \times V_r = A_s A_r \cos(\omega_s t + \phi_s) \cos(\omega_r t + \phi_r) + \\ + A_r \cos(\omega_r t + \phi_r) \cdot \sum_{\omega_n} A_n \cos(\omega_n t + \phi_n) \end{aligned} \tag{1.31}$$

The product of the signal generates a beat note at frequency $\omega_s - \omega_r$ and a high frequency term $\omega_s + \omega_r$. The low-pass filter will suppress those fast oscillating components, except for the case in which $\omega_s = \omega_r$. In this case, the mixing downshifts the frequency spectrum of the signal by a quantity ω_r, such that the wanted component is now a DC-component. With this requirement ($\omega_r = \omega_s = \omega_n$), Eq. (1.31) becomes:

$$\begin{aligned} V_r \times V_s = \frac{1}{2} A_s A_r \left[\cos(2\omega_r t + \phi_s + \phi_r) + \cos(\phi_s - \phi_r)\right] + \\ + \frac{1}{2} A_n A_r \left[\cos(2\omega_r t + \phi_n + \phi_r) + \cos(\phi_n - \phi_r)\right] \end{aligned} \tag{1.32}$$

Finally, the filtering strips away the $2\omega_r$ component resulting in:

$$V_{PSD} = \frac{1}{2} A_s A_r \cos(\phi_s - \phi_r) + \frac{1}{2} A_n A_r \cos(\phi_n - \phi_r) \tag{1.33}$$

where usually the phase of the lock-in is adjusted such that $\phi_r = \phi_s$ and the output of the phase-sensitive detection corresponds to the in-phase component. The same calculations are performed for the quadrature component by using $V_r(t) = A_r \sin(\omega_r t + \phi_r)$. The magnitude ($R$) and phase ($\Theta$) of the signal are obtained by applying the relationships:

$$R = \sqrt{X^2 + Y^2} \tag{1.34}$$

$$\Theta = \text{atan2}\left(\frac{Y}{X}\right) \tag{1.35}$$

It should be noted that the choice of the low-pass filter settings are fundamental for proper demodulation. If too large bandwidths are selected, residual $2\omega_r$ components might affect the expected DC-output, leading to oscillations. At the same time, too narrow bandwidths have the detrimental effect of increasing the response time of the instrument, which is often avoided in sensing applications. Nowadays almost all lock-in amplifier make large use of digital signal processing. By doing so, the digitized signal can be multiplied by a pure reference (free of noise sources), and the filtering stage can be easily customized. For instance, infinite impulse response (IIR) or finite impulse response filter (FIR) can be applied, as well as more complicated filter designs such as Gaussian filtering. Digital lock-in amplifiers can even be implemented in dedicated circuits such as field-programmable gate arrays (FPGAs), which tend to be more stable over time [34], [35].

One last quantity that is worth discussing in LIAs applications is the equivalent noise bandwidth (ENBW). This quantity is often used to express the bandwidth of a detection system, and is defined as the bandwidth of a perfect rectangular filter that passes the same amount of power as the used filter. This quantity depends on the filter typology and settings. For a typical RC-filter as the one represented in Fig. 1.7(a), the filter time constant is defined by $\tau = RC$, while the filter order indicates how many identical RC-filters are cascaded. The transfer function of the n-th order RC-filter and the corresponding cutoff frequency $f_{(-3dB)}$ are expressed by:

$$H_n(\omega) = H_1(\omega)^n = \left(\frac{1}{1 + i\omega\tau}\right)^n \tag{1.36}$$

$$f_{(-3dB)} = f_c\sqrt{2^{\frac{1}{n}} - 1} \tag{1.37}$$

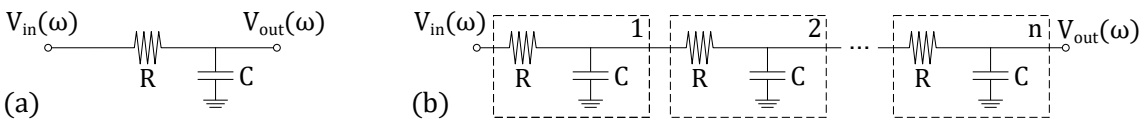

Figure 1.7: (a) Single stage and (b) n-stage RC filters.

where $f_c = 1/2\pi\tau$ is the cutoff frequency for a first-order filter. From the filter transfer function, it is possible to compute the equivalent noise bandwidth.

Acting as movable pass-band filters, lock-in amplifiers can also be used to assess system's noise, like a spectrum analyser. It should be noted though, that this is not their primary purpose. In summary, lock-in amplifiers are swiss-knives for spectroscopists and scientists, due to their capabilities of extracting periodic signals buried in noise. For the interested reader, many useful informations can be found in the whitepapers of LIA producers, including tips on how to optimize response time by using advanced filter settings [36].

1.6.1.4 Dispersion spectroscopy

In WMS, the differential absorption of the analysed sample is measured. However, many other approaches exploit the coherence of the laser source and can measure the phase delay of the radiation wave, induced by the sample anomalous dispersion in proximity of an absorption feature. Such techniques are usually termed *dispersion spectroscopies*. The relationship between a sample absorption coefficient and refractive index is provided by the Kramers-Kronig relations [37]. In the approximation of weakly absorbing samples, the sample's refractive index can be expressed as

$$n(\omega) = 1 + \frac{c}{\pi} \int_0^{+\infty} \frac{\alpha(\omega')}{\omega'^2 - \omega^2} \, d\omega' \tag{1.38}$$

By the same relationship, also the absorption can be retrieved with the knowledge of the refractive index. The measurement of the phase grants some advantages, among which the linear relationship between the dispersion spectrum and the sample concentration, which tends to saturate for conventional intensity measurements. Moreover, phase measurements can be immune to intensity fluctuations.

One of the first techniques to provide dispersion information was FM-spectroscopy, introduced by Bjorklund [38]. Two sidebands are generated via FM-modulation at very high frequencies, and their heterodyne signal with the carrier frequency is measured. In the absence of an absorption, the sidebands cancel each other out due to their 180° phase-shift, while in presence of an absorption this symmetry is perturbed. The in-phase and the quadrature component of the beatnote signal will be a measure of the absorption and dispersion ($\Delta\alpha$ and $\Delta\phi$ in Fig. 1.8(a)), respectively. Both absorption and dispersion are retrieved by intensity measurements and are therefore affected by intensity fluctuations.

Another approach, very similar to FM-modulation, consists in modulating the intensity (IM) of the radiation field at frequencies comparable to the width of the spectral feature. Such technique goes under the name of heterodyne phase-sensitive dispersion spectroscopy (HPSDS). In HPSDS, the two generated sidebands simultaneously probe the anomalous dispersion of the transition line. Being in phase with one another, the beatnote generated by each sideband and the carrier sums up, leading to maximized signals at the peak of the

transition. The phase-delay between the sidebands is extracted by measuring the phase of the beatnote. Many works showcased the capabilities of this technique, especially in the near-IR where intensity modulators are cost-effective and readily available [39]–[42]. The signal can be optimized by modifying the modulation frequency Ω, such that the largest extent of the anomalous dispersion is probed by the sidebands, as pictured in Fig. 1.8(b). However, the presence of residual frequency modulations on the modulated radiation field induce non-linearities and asymmetry in the detected signal. This occurs when the IM-modulation is provided by superimposing a radio-frequency component on the bias-current of the diode laser, as is mostly the case in mid-IR [40].

Wysocky et al. [43] in 2010 proposed a novel method which directly measures the sample induced dispersion. This techniques, known as chirped laser dispersion spectroscopy (CLaDS), relies on a single frequency laser that is frequency chirped across the spectroscopic feature. Single or dual sidebands are generated by means of an acousto-optical modulator (AOM). The beams are then combined in a Mach-Zehnder arrangement and the propagation through the sample compartment induces a slight effect on the propagation of the light wave. The beatnote frequency is demodulated and contains the information of the dispersion spectrum. The beatnote frequency shift is linearly dependent on the frequency chirp applied to the carrier frequency. For direct-CLaDS measurements, the nonlinear frequency chirping of the laser has to be characterized in advance, for instance by using an etalon in the optical path. Once this is done, a fitting procedure can be used to retrieve the information on the sample, just as in TDLAS. More complicated approaches can be used, for instance by using a chirped-modulation CLaDS - similar to WMS ap-

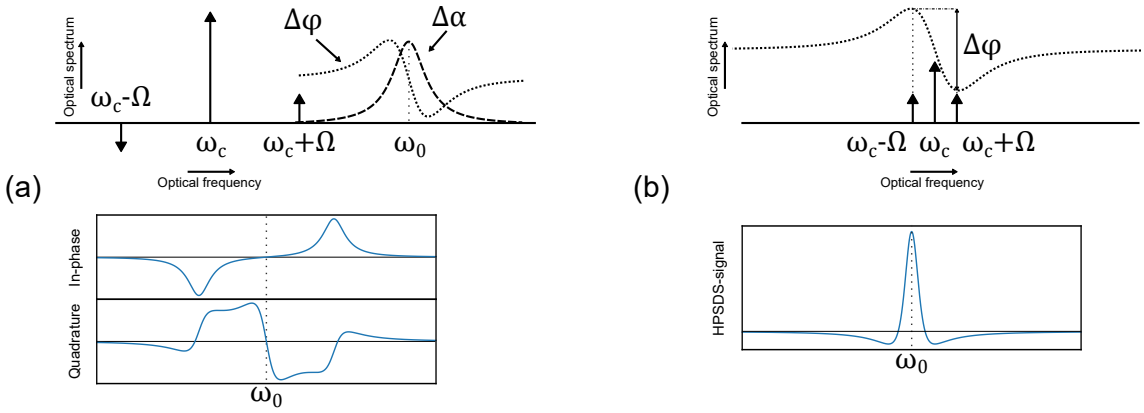

Figure 1.8: (a) Representation of a typical FM-spectroscopy experiment. The sideband separation from the carrier is larger than the spectroscopic feature, such that the spectroscopic feature is probed by each sideband individually. On the bottom, exemplary spectra from the in-phase and quadrature components (containing the absorption and dispersion information, respectively) retrieved by a demodulation at the beatnote frequency. (b) Schematic of HPSDS probing of the dispersion profile of a spectroscopic feature. The spacing between the sidebands is much lower than in FM-spectroscopy, and the initial phase difference between them is zero. On the bottom, an example of a HPSDS spectrum for a purely IM-modulated optical field.

proaches applied to TDLAS. In this case, a sinusoidal modulation is superimposed to the chirp, and harmonics detection of this sinusoidal modulation provides derivative spectra, just like in WMS. Although fundamentally different from WMS, also in CM-CLaDS an optimization of the modulation parameters is needed but more complex [44]. The added system complexity is compensated by the benefits of the technique, namely the possibility of measuring optically thick samples and the immunity to intensity fluctuations.

Dispersion spectroscopy has also been successfully applied for liquid-phase analysis [45], where the condition of optically thin samples is difficult to achieve, due to the technical limits in achievable pathlengths. In this case, external cavity QCLs (EC-QCLs) coupled with an interferometric detection allowed to convert the phase delay into an intensity fluctuation. Moreover, the use of a balanced detection rejects the intensity noise of the laser source, while the phase-delay measurement extends the linearity beyond the limit of Lambert-Beer saturation [46].

Among the cited techniques, a notable mention has to be spent for dual-comb spectroscopy, an emerging technique which has the capability of probing wide spectral regions at once, without the need of moving parts such as in external-cavity diode lasers or FTIRs. Both direct absorption and dispersion spectroscopy can be retrieved by this measurement, even though dispersion is rarely used for sensing.

1.6.1.5 Dual-comb spectroscopy

Optical frequency combs (OFCs) are pulsed laser sources that emit a broadband spectrum composed by a series of equispaced phase-locked spectral emission lines. The separation of the comb lines corresponds to the repetition frequency (f_{rep}) of the ultra-short pulses. The optical spectrum corresponds to an *optical frequency ruler*, where each line is located at a frequency $f_{\mathrm{n}} = \mathrm{n}f_{\mathrm{rep}} + f_{\mathrm{CEO}}$, where f_{CEO} is the carrier envelope offset frequency. Since their first introduction, frequency combs underwent a tremendous development and have been employed in a wide variety of sensing approaches. The most notable is the dual-comb spectrometer, in which two twin comb sources are beaten together to produce a multi-heterodyne spectrum. However, probing fundamental transitions in the mid-IR poses strong limits in the applicability of such systems, due to the need of a pair of coherent mode-locked lasers and frequency conversion stages (such as optical parametric oscillators). However, in 2012 electrically pumped quantum cascade lasers were first demonstrated [47], strongly simplifying those requirements. The main feature of QCL-based frequency combs lies in the fast recovery of the gain material, in the order of 1 ps, which is much shorter than the cavity round-trip time, on the order of $\sim$ 100 ps for 4.5 mm long cavity [48]. This feature prevents the generation of high-intensity pulses, typical of mode-locked frequency combs with saturable absorbers. Differently from mode-locked comb sources with amplitude modulation (AM), QCL-combs exhibit an FM behavior with a quasi-constant intensity. The proposed mechanism for FM phase locking is based on the

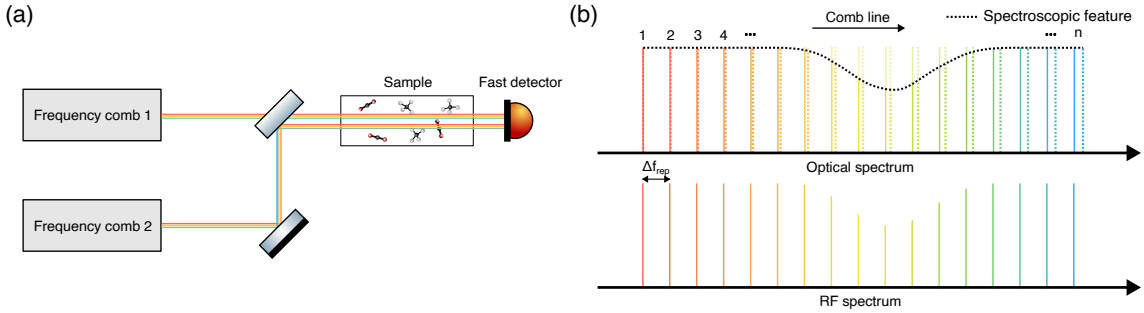

Figure 1.9: (a) Schematic of a dual-comb spectrometer in the amplitude-sensitive configuration. After passing through the sample and interacting with the spectral feature, shown at the top of panel (b), the beams are recombined on the photodetector to produce a multiheterodyne spectrum in the radiofrequency domain (bottom of panel (b)).

synergy between spatial hole burning to achieve broadband emission, Four-Wave Mixing (FWM) to ensure line equidistance and a suitable group velocity dispersion. FWM by itself is insufficient to produce sidebands in the spectrum of Fabry-Pérot resonators. The interested reader is referred to reviews that provide a clear and detailed description of the topic [49], [50].

The typical dual-comb spectroscopic schematic is shown in Fig. 1.9(a). In the schematic, only the *amplitude-sensitive* configuration is portrayed. In this configuration, both combs interact with the sample, leading to an improved sensitivity. In the second configuration, named *phase-sensitive* configuration, only one comb is passed through the sample, allowing to access both attenuation and phase-shift induced by the sample. As can be seen from Fig. 1.9(b), each line of the two OFCs, produces a beating in the RF-domain. The separation of the RF multiheterodyne spectrum corresponds to the difference in repetition frequency of the two combs ($\Delta f_{\mathrm{rep}} = f_{\mathrm{rep},1} - f_{\mathrm{rep},2}$). The beating is measured by recombining the beams on top of a fast photodetector. A beating between the lines of a same comb, or between non-coincident lines is also possible: they would however fall at frequencies $f > f_{\mathrm{rep},1(2)}$, usually much greater than the detector bandwidth, and are therefore not detectable. The resulting electric field superposition leads to an interferogram, like in FTIR spectroscopy. However, unlike Fourier spectrometers, several advantages are obtained. Firstly, no moving parts are employed since the interferogram is the result of the superposition of these optical sources. Secondly, the time resolution for the individual beat notes has to be

$$\tau > \frac{1}{\Delta f_{\mathrm{rep}}} \geq \frac{2n}{f_{\mathrm{rep}}} = \frac{2f_{\mathrm{span}}}{f_{\mathrm{rep}}^2} \tag{1.39}$$

In general, common values of f_{rep} are comprised between 50-250 MHz, and time-resolutions on the scale of the $\sim$ 1ms are usually obtained, with f_{span} between 100 to 400 cm^{-1}. In QCL-combs, instead, typical values of f_{rep} are in the tenths of GHz, leading to $\tau \sim$ 40ns. In practice, technical limitations increase this value to the µs scale. Compared to other comb-sources, the optical power of QCL-combs can span from 50 mW to 1 W [51], which is beneficial in highly absorbing samples or long-distance measurements. Finally, spectral

interleaving approaches [52] allows to achieve spectral resolutions orders of magnitude better than high-end FTIR spectrometers, higher than 10^{-4} cm^{-1}. Spectral coverage is currently limited to 50-100 cm^{-1}. However, the scientific community is investing significant effort in enhancing the emission bandwidth of such sources [53].

In summary, dual-comb spectroscopy is a promising approach which offers numerous advantages. Future perspectives may include on-chip integration, together with the emerging quantum cascade detectors [54], [55]. At the moment, dual-comb spectroscopy is still limited to specialized laboratories due to its high cost and its challenging technological requirements.

1.6.2 Indirect methods in laser spectroscopy

As described in Section 1.6.1.1, one of the major limitation of direct methods is the necessity of measuring tiny signals on top of large backgrounds. Approaches such as WMS, might help to reduce this effects, and with demodulation at second or higher harmonics, background free signals can be retrieved to a large extent. Nevertheless, in real-case scenarios, RAM components might still produce undesired backgrounds, thus preventing the technique from being truly 'background-free'. Rather than probing the transmitted photons, the effects arising in the sample as a consequence of photon absorption can be detected as well. When the photons are fully transmitted, no signal is generated, making these techniques inherently background-free. This ensemble of techniques are defined *indirect methods*, as opposed to the *direct* methodologies presented up to this point. A brief description of the most used techniques will follow in this section, while Chapter 2 will provide a focus on one of those, photothermal spectroscopy, as a novel and attractive alternative for the realization of miniaturized, rugged and portable gas sensing systems.

The 'indirect' probing of the absorbed radiation relies on different phenomena triggered by the photon absorption. The most known and widely spread approaches for chemical analysis are laser-induced fluorescence (LIF), photoacoustic spectroscopy (PAS) and photothermal spectroscopy (PTS).

1.6.2.1 Laser-induced fluorescence

Laser-induced fluorescence is a technique used in the visible and ultraviolet range, where electronic transitions occur. LIF can be applied to atoms, molecules, and radical species. The basic principle of LIF relies on the detection of spontaneous emission of photons after laser excitation. In the case of atoms, a photon with the same energy of the absorbed one is re-emitted after a characteristic time (the decay time of the unstable excited state). For molecules, instead, the energetic states are more complex due to the presence of roto-vibrational levels (as per Section 1.3), and many possible pathways can be followed leading to red-shifted emissions. When the excitation laser is scanned across a spectral range of interest, the fluorescence photons are collected on a photomultiplier tube,

giving the excitation spectrum. Under certain circumstances, the excitation spectrum corresponds to the absorption spectrum. While the excitation spectrum gives informations on the absorption pathways of the molecule, the opposite information, namely the emission properties, can be obtained by fixing the excitation laser and scanning the collected photon energies. Remarkable sensitivities have been obtained in the detection of organic molecules, down to the detection of single molecules [56]. Apart from quantitative measurement, LIF is very useful for the study of kinetic dynamics in the study of short-lived radical species, distribution of quantum states or combustion diagnostics, where a flame temperature can be retrieved from the fluorescence information (fluorescence thermometry) [57].

While being highly efficient with some molecules, the sensitivities of LIF cannot be extended to every analyte evenly. The number of emitted photons per each absorbed photon is given by the fluorescence quantum yield. Such quantity is dependent not only on the chemical specie, but also on the excitation wavelength. Competing processes such as collisional de-excitation or pre-dissociation are killers of the fluorescence yield. In this case, fluorescence is said to be 'quenched'. Collisional de-excitation is particularly important in the mid-IR. While being an effective method in the visible or UV range, fluorescence becomes much less effective in the mid-IR due to the longer radiative lifetimes, which are several orders of magnitude larger than those of excited electronic states. The competing collisional de-activation processes quench the fluorescence yield, with conversion of the energy to local heating of the sample.

In the mid-IR region, the dominating techniques are the ones that fully take advantage of collisional de-activation, namely photoacoustic and photothermal spectroscopies. As the upcoming chapter will demonstrate, photoacoustic and photothermal phenomena stem from common underlying processes. However, they mainly differ in the quantity that is probed.

1.6.2.2 Photoacoustic spectroscopy

As the name suggests, photoacoustic spectroscopy probes acoustic waves generated as an effect of modulated light absorption. The first spectroscopic arrangement of a PAS spectrometer dates back to 1938 from the work of Viengerov [58]. The advent of lasers has been a major catalyst in the development of this field. Kerr and Atwood [59] used for the first time a continuous-wave CO_2 laser as a radiation source to detect CO_2 in nitrogen. A breakthrough in the technique happened with the the work of Dewey at al. [60] and by Kamm [61], who employed a laser source modulated at the acoustic resonance frequency of the PA cell. Similarly to cavity-enhanced techniques, the acoustic cell behaves as a resonator for the pressure waves and its efficiency can be likewise quantified by the quality factor (Q-factor). The amplification of the acoustic wave leads to improvement factors of few orders of magnitude compared with the previous works. It is not surprising

that a crucial part of PAS detection is the cell, which can be accordingly engineered to optimize the sensitivity of the system. In general, the photoacoustic (and photothermal) signal scales inversely with the modulation frequency, suggesting that low modulation frequencies would be preferable. However, several noise sources show the characteristic 1/f frequency dependence, and better SNR are usually achieved in the kHz range. Two main operational modes can be distinguished, namely resonant and non-resonant mode. In the first case, the laser is modulated in order to match one of the eigenfrequencies of the acoustic cell, with the generation of a standing wave and amplification of the pressure wave. The position of the microphone is crucial in this approach, since it must probe the anti-nodes of the standing wave. In the latter mode, the modulation is lower than any natural resonance, and no standing-wave can be produced within the resonator.

Typical PAS cell geometries include excitation of longitudinal, radial and azimuthal modes. The most common approaches, reviewed in [62], comprise: simple pipe tubes for the excitation of longitudinal modes, sometimes with the presence of buffer volumes next to the optical windows to reduce the generation of background noise indistinguishable from the analyte signal; Helmholtz cells, where the microphone is placed in a separate chamber. This cell design provides limited enhancement factors due to loss mechanism in the cell; cavity resonators, whose eigenfrequencies strictly depend on the cavity geometry.

Combination with the aforementioned spectroscopic techniques is possible, in particular the use of multipass acoustic resonators [63], (optical) cavity-enhanced approaches [64], [65], wavelength modulation [66], or the use of dual-comb sources for broadband coherent detection [67], [68].

Some expedient can be employed to further push the sensitivity of PAS approaches. Reduction of fringes can be attained by exploiting the natural polarization of some laser sources, such as the inherent TM-polarization of quantum cascade lasers, by making use of Brewster windows. In more complex detection systems the use of reference microphones in combination with differential amplification optimizes environmental noise rejection. In other cases, specific transducers inherently immune to acoustic noise sources are used. This is the case for quartz-enhanced photoacoustic spectroscopy (QEPAS), a technique introduced by Kosterev and al. [69]. In QEPAS, the piezoelectric property of the quartz-tuning fork is used for the generation of an electric signal, as a consequence of the prong deformation. Quality factors on the orders of 10'000 are easily achievable. Its noise immunity comes from the fact that acoustic wavelength in air is typically larger than the prong separation, meaning that external acoustic noise will cause a symmetric deformation of the prongs, which is not a piezoelectrically active mode. Only acoustic sources capable of inducing an anti-symmetric deformation can generate a piezoelectric signal. Since its introduction in 2002, QEPAS has undergone significant development, reaching commercialization levels, and has been successfully applied for breath analysis [70], [71], and trace-gas detection down to the part-per-trillion (ppt) level [72], [73]. The interested reader is referred to the following reviews articles, encompassing the main challenges and

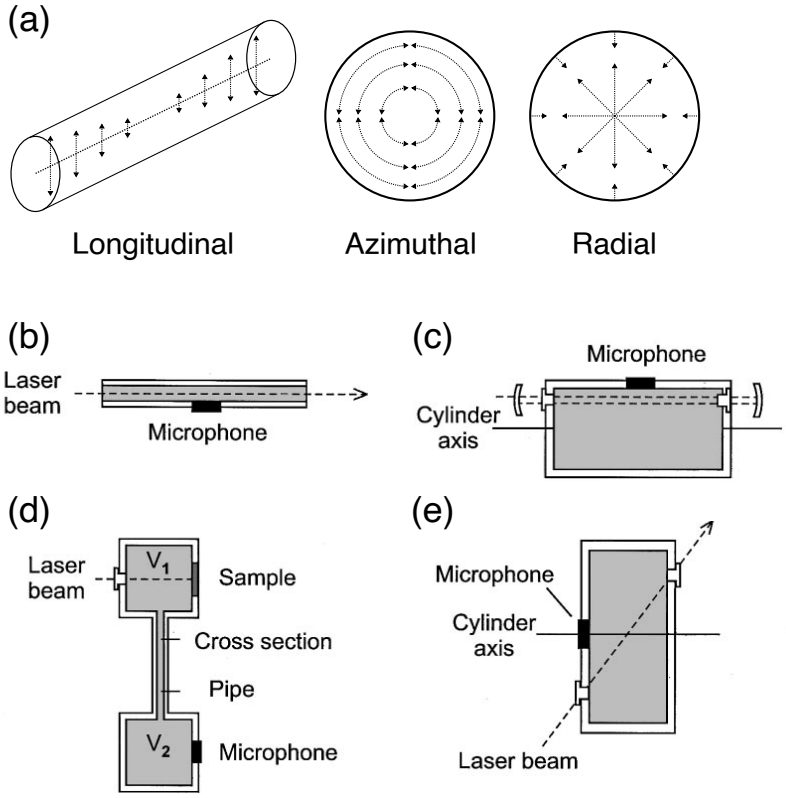

Figure 1.10: (a) Schematic of acoustic longitudinal, azimuthal and radial modes in cylindrical resonators. (b) Pipe resonator for excitation of longitudinal modes. (c) Multi-pass arrangement for asymmetric azimuthal modes in a cylinder. (d) Helmholz resonator with separate sample and detection chambers. (e) Arrangement for suppression of window noise. Adapted from [62].

benefits of QEPAS-sensing [74], [75].

Another valuable technique in the field of photoacoustic sensing is cantilever-enhanced photoacoustic spectroscopy (CEPAS) [76]. The main difference in CEPAS is the choice of a different mechanical resonator, namely a cantilever. The cantilever is not always operated in resonant mode. Non-resonant operation provides improved robustness at expenses of the sensitivity. The cantilevers can be fabricated by micro-electrical-mechanical system (MEMS) technologies, which can reduce size and cost of the overall system. Several readouts are possible, such as optical, by employing a quadrant photodiode (similarly to atomic force microscopy)[77], piezoelectric (as in QEPAS, but with a single prong) [78], piezoresistive [79] and capacitive [80]. State of the art sensitivities were achieved both in QEPAS and CEPAS, with the additional benefit of higher compactness.

The next chapter will provide an in-depth description of the photoacoustic and photothermal phenomena, exploring the latest advancement in this emerging technique.

1.7 Figure of merit of optical sensors

Comparing different techniques on the same common ground is often difficult due to the many parameters involved in the chosen experimental approach. For such reason, several metrics have been developed to compare the goodness of a method.

1.7.1 Detection limits metrics

The most notable figure of merit of a gas sensor is its minimum detection limit (MDL), which might differ depending on the used definition. The limit of detection (LOD) of a system is defined as the lowest concentration that can be measured with *statistical significance* [81]. Similarly, a limit of quantitation (LOQ) can be defined as the lowest concentration which can be quantified with acceptable accuracy. For linear sensors, as it is (almost) always the case, the sensor transfer function is a linear function $S = a \cdot c + b$, being S the sensor response, c the analyte concentration and a, b the coefficients of the linear relationship. With the knowledge of the transfer function, LOD and LOQ can be defined as:

$$\mathrm{LOD} = \frac{3\sigma_b}{a} \tag{1.40}$$

$$\mathrm{LOQ} = \frac{10\sigma_b}{a} \tag{1.41}$$

where σ_b is the standard deviation of the blank measurement (background). Those quantities are routinely used in analytical chemistry applications, and very often are disregarded by physicists. The latter tend to use the noise equivalent concentration (NEC) as a definition of the MDL, which as well appears in several forms. The most rigorous makes use of a calibration curve and corresponds to LOD/3, while another used form of it corresponds to the ratio between concentration and SNR (corresponding to a 2-point calibration curve, origin of the axes included). Both definitions correspond respectively to:

$$\mathrm{NEC} = \frac{\sigma_b}{a} \tag{1.42}$$

or

$$\mathrm{NEC} = \frac{c}{\mathrm{SNR}} \tag{1.43}$$

With the knowledge of the minimum detection limit, the *minimum detectable absorption coefficient* ($\alpha_{\min}$) can be estimated. It corresponds to the absorption coefficient that generates, for a 1 cm optical pathlength, a signal whose intensity is equal to the minimum detection limit:

$$\alpha_{\min} = \mathrm{MDL}\, N_{tot} \sigma_\nu \tag{1.44}$$

where σ_ν is the absorption peak cross-section and $N_{tot} = pN_A/RT$ from the ideal gas law.

The minimum detection limit and its minimum absorption coefficient, however, do

not provide any further information regarding the goodness of the used method. The MDL depends on the strength of the targeted absorption line, the bandwidth used for the measurement, and - in indirect approaches - on the excitation optical power, while $\alpha_{\min}$ normalizes only for the line-strength.

To remove the dependency on the detection bandwidth, the *noise equivalent absorption coefficient* (NEA, [$\mathrm{cm}^{-1}\,\mathrm{Hz}^{-1/2}$]) is used:

$$\mathrm{NEA} = \frac{\alpha_{\min}}{\sqrt{\Delta f}} \tag{1.45}$$

being Δf the equivalent noise bandwidth defined in Section 1.6.1.3. Finally, in indirect approaches the most useful metrics is the *normalized noise equivalent absorption* (NNEA, $\mathrm{W\,cm}^{-1}\,\mathrm{Hz}^{-1/2}$), which compensates the NEA based on the available excitation power (P_{exc}):

$$\mathrm{NNEA} = \frac{P_{exc}\alpha_{\min}}{\sqrt{\Delta f}} \tag{1.46}$$

1.7.2 Allan variance for long-term stability

While the NNEA describes the sensor performance on a short time scale, other measurements are required to characterize long-term drifts and establish the signal averaging limits. The commonly employed approach [82] consists in performing the Allan variance of time sequences of measurements to quantify the long-term stability of optical trace gas sensors. The Allan variance analysis is performed to determine the maximum achievable sensitivity by selecting the optimal integration time. Ideally, the signal from a perfectly stable system could be averaged infinitely. However, real systems are stable only for a limited time. The stability of a system is affected by thermal drifts of the laser source, moving fringes, mechanical instabilities and other factors [83].

Given a set of M time-series data $(y_1, \ldots, y_M)$ acquired with an integration time τ and a time delay Δt, the Allan variance is defined as:

$$\sigma_y^2(\tau) = \frac{1}{M}\sum_{k=1}^{M}\frac{1}{2}(y_{k+1} - y_k)^2 \tag{1.47}$$

Allan variance allows to study the noise components in the system, as the integration time has a specific dependency on the power spectral density of several noise sources. An example of the Allan deviation (square root of the variance) is presented in Fig. 1.11 for several noise sources. The dependency of the Allan deviation with respect to the integration time is also displayed by the dotted lines. In a real-case scenario, the combination of these noise sources produces regions of instability which limit the possible integration times.

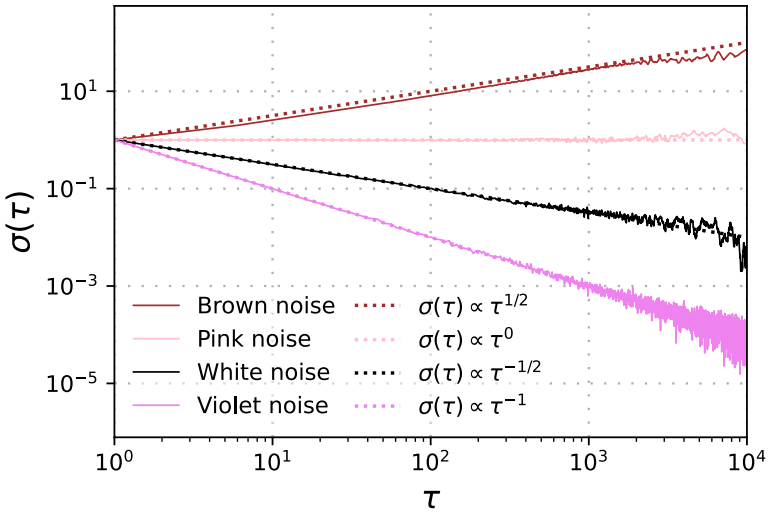

Figure 1.11: Example of an Allan deviation analysis over several simulated noise sources. Brownian, pink, white and violet noise sources are represented in terms of their Allan deviation as a function of the integration time. While white and violet noise can be reduced with longer integration times, that is not the case for pink and brown noise.

Chapter 2

Photothermal spectroscopy and methods for chemical sensing

Historically, the detection of photoacoustic effects happened well before than the first photothermal detections. Already in 1881, Bell realized that acoustic waves can be produced by the absorption of a periodically interrupted light beam, absorbed by a layer of thin material [84]. Moreover, this effect increased in intensity when the layer was dark in color, suggesting that such effect was connected to light absorption.

On the other hand, while the evidence of thermally induced effects is ubiquitous, the lack of appropriate instrumentation has limited interest in its applicability to chemical analysis. One glaring example of thermally-induced effects is the optical mirage effect. At least once during a hot summer day, everyone has experienced the shimmering appearance of the hot asphalt surface. The heat released from the hot surface generates a thermal gradient so that warm air in the vicinity of the asphalt expands, reducing its refractive index. In contrast, the overlying layer of cold air has a higher refractive index. The refractive index gradient deflects an incident light ray at an acute tangent angle, which is refracted upward to the observer: thus, the asphalt surface will appear almost 'reflecting', because of light rays coming from the sky to the surface. In a way, this effect is the basis of one class of photothermal approaches, namely *photothermal deflection spectroscopy*.

The first photothermal approach for chemical analysis appeared only in 1965 by Gordon et al. [85]. In this work, pure organic liquids and solids were placed in a laser cavity,

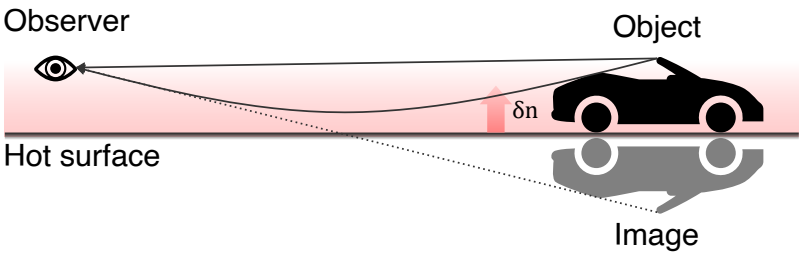

Figure 2.1: Schematic of the mirage effect.

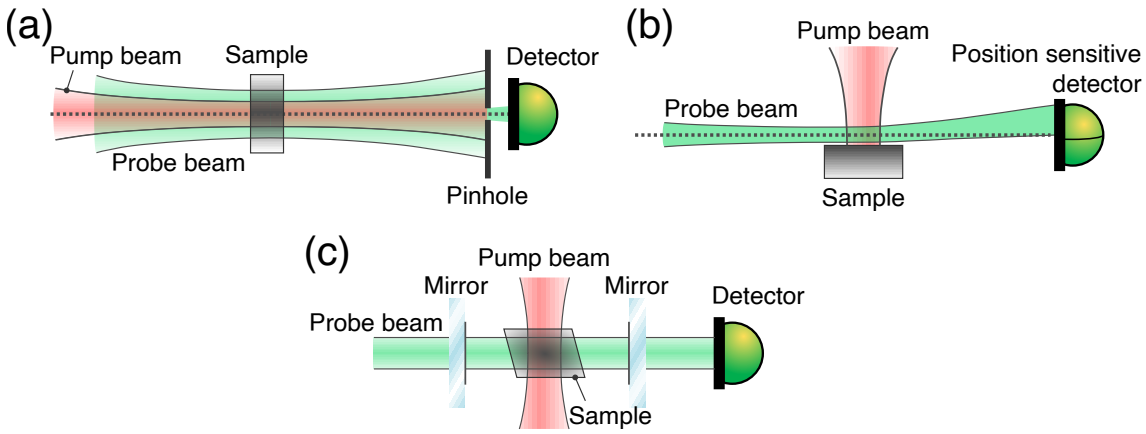

Figure 2.2: (a) Arrangement for a photothermal lensing system. The excitation beam induces the formation of a thermal lens in the sample, which causes the focusing or defocusing of the probe beam. The resulting beam is clipped by a pin-hole and collected on a photodetector. (b) Photothermal deflection measures the gradient in the refractive index. (c) Photothermal interferometry measures a change in the refractive index of the sample with an interferometric transduction. Adapted from [88].

causing a diverging beam as a consequence of the formation of a thermal lens. Usually, the thermal lens has a negative focal length, since most material posses a negative thermo-optic coefficient (their refractive index decreases with increasing temperature). This experimental approach can be considered the father of *photothermal lensing*. A few years later, McLean, Sica & Glass in 1968 [86] and Longaker & Litvak in 1969 [87] recognized that by making use of laser coherence, a more direct and sensitive measure of changes in refractive index was possible, leading to *photothermal interferometry*.

It is not surprising to notice that almost all PTS approaches employ laser technologies, explaining why such approaches are becoming more popular just recently. A typical arrangement of a photothermal spectroscopy setup requires a laser source for the excitation of the sample - though broadband or incoherent emitters such as light emitting diodes can be used [89] - and a second laser beam, used to probe the refractive index changes in the sample. A direct measurement of the temperature change is employed in photothermal calorimetry, or can be probed via infrared emission, in photothermal radiometry. However, these approaches are not very sensitive. The rise in temperature can be much more easily detected by exploiting the dependency of the refractive index on the temperature. Typical experimental arrangements are portrayed in Fig. 2.2. Photothermal lensing, in panel (a), measures the intensity of the probe beam after passing through a thermal lens, generated as an effect of the temperature gradient within the sample. Focusing or defocusing of the beam are dependent on the properties of the sample (its thermo-optic coefficient) and the probe beam parameters. For many materials, a diverging lens is photoinduced as an effect of the negative thermo-optic coefficient. In panel (b), a schematic of photothermal deflection is represented: the refractive index gradient of the air upon the hot sample's surface causes a bending of the light (just like in the mirage effect). The position of the beam can

be measured with a position sensitive detector. The stronger the displacement, the larger the refractive index gradient. Finally, in panel (c), one of the possible arrangements for photothermal interferometry is shown. In photothermal interferometry, the phase-shift induced by the refractive index change is transduced as a change in the transmitted intensity of the probe beam passing through the interferometer. Different configurations are possible: in collinear configurations, employed in Mach-Zehnder interferometers, the excitation and the probe beam travel along the same path to maximize the interaction pathlength. In transverse configuration, as the one proposed in Fig. 2.2(c), the interaction pathlength is restricted to the overlapping volume between the probe and the pump beam. The sensitivities of photothermal interferometric systems have proven to achieve astonishing results, with minimum detectable absorption coefficients on the order of 10^{-10} cm^{-1} [90]. Almost all kinds of interferometers have been used in photothermal interferometry, such as Mach-Zehnder [87], [90]–[93], Jamin [94], [95] and Fabry-Pérot interferometers [96], [97]. Among them, the Fabry-Pérot interferometer has the peculiarity of acting as an optical resonator, such that the probe beam interacts with the photo-excited volume multiple times before exiting the interferometer. This allows to reduce the dimension of the system, while preserving its sensitivity.

In the next section, the description of the generation of photoinduced effects is discussed from a theoretical point of view.

2.1 Description of the photoinduced effects

Photoacoustic and photothermal effects are two strictly interlaced phenomena which arise from the absorption of modulated light in the sample. The excitation and subsequent relaxation of the sample produces a local change in its thermophysical properties, such as temperature and density, which in turn generate pressure waves with the same periodicity of the excitation source.

The theoretical modelling of photothermal and photoacoustic generation has been presented by several authors, such as Morse & Ingard [98] or Bialkowski [88]. A brief description is given here to familiarise the reader with the main concepts. The process can be subdivided in three steps, summarized in Fig. 2.3:

1. Photon absorption and excitation of the molecule internal state;

2. Collisional de-activation with generation of the heat source;

3. Modification of the thermophysical properties of the system, with generation of a thermal field and an acoustic field.

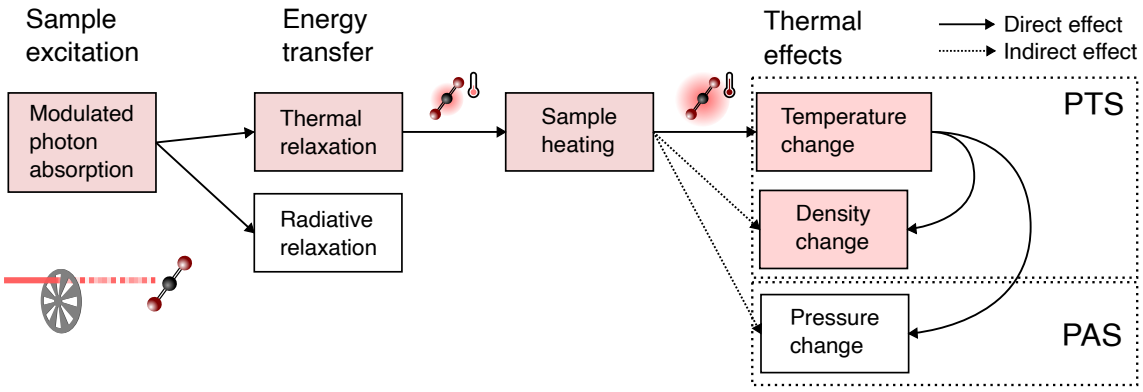

Figure 2.3: Block diagram of the photoacoustic and photothermal phenomena. Modulated photon absorption induces a periodic heat source by collisional de-activation of the molecules. The resulting increase in the sample temperature causes a modulated gas expansion, detected in PAS, and changes in the local density, probed in PTS.

2.1.1 Photon absorption and de-activation processes

Assume a ground and an excited state of energies E_0, E_1 with molecular densities $n_0(\mathbf{r}, t)$ and $n_1(\mathbf{r}, t)$, respectively, such that the energy difference $\Delta E = E_1 - E_0$ equals the photon energy $h\nu$. The optical excitation will populate the excited state. These molecules will eventually lose this energy, transitioning towards the ground state. Radiative processes, such as stimulated and spontaneous emission, and non-radiative pathways are responsible for the molecule de-activation. Non-radiative pathways happen as a consequence of molecular collision, causing an energy transfer between the excited state of the excited molecule and another mode of the collision partner. In this context, we define *relaxation* the energy transfer process to translational modes. Since we are dealing with the excitation of vibrational modes, we will consider the excited state as a higher vibrational level. Hence, the possible vibrational relaxation processes include vibrational to vibrational levels ($V-V$), vibrational to rotational levels ($V-R$) and vibrational to translational relaxation ($V-T$). $V-V$ equilibration consists in the energy exchange between the *excited* molecules and leads to vibrational level equilibration, following a Boltzmann distributions of the levels. This process is followed by the much slower $V-R/T$ relaxation (which includes $V-R$ and $V-T$ processes), which converts the absorbed energy into heat. In general, each vibrational excited state decays to the ground state at a rate roughly proportional to the exponential energy gap of the excited state:

$$\frac{1}{\tau} = \eta e^{-\Delta E/kT} \tag{2.1}$$

where τ is the relaxation time constant, η (s^{-1}) is the frequency of the energy transfer processes, and T is the equilibrium temperature. At standard temperature and pressure (300 K, 1 atm), typical relaxation times for the $V-R/T$ process are 10^{-5} sec, and depend upon the matrix composition and the analyte under investigation. Clearly, these rates are pressure and temperature dependent. Comparing radiative relaxation times, whose

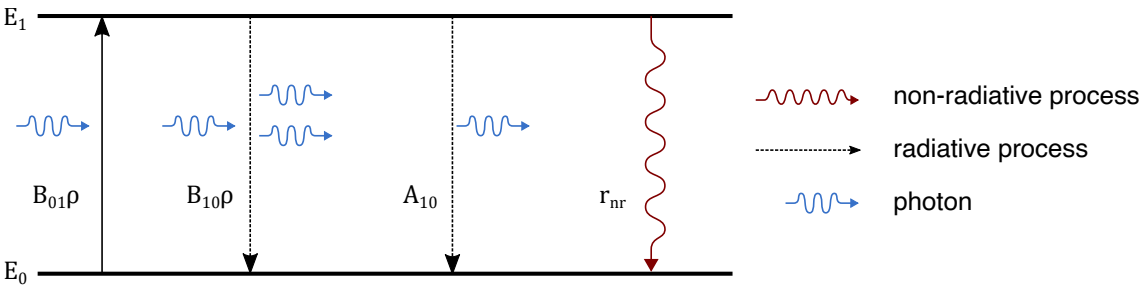

Figure 2.4: Schematic of the interaction of a two-level system with a radiation field. From left to right, absorption, stimulated emission, spontaneous emission and non-radiative relaxation are shown, respectively.

typical values are $10^{-1} - 10^{-3}$ sec, and non-radiative processes in the mid-infrared leads to the conclusion that non-radiative relaxation is the most efficient phenomenon.

Although photon excitation involves a set of transitions, and the energy structure of molecules can be quite complex, a simple model based on a two-level system is still effective in representing the kinetics of excitation and relaxation. The system can be described by a set of rate equations which relates the population and depopulation rates of the ground and the excited state. A schematic of the process is presented in Fig. 2.4.

By using the Einstein's coefficient for spontaneous emission (A_{10}, $[\mathrm{s}^{-1}]$), absorption (B_{01}, $[\mathrm{m}^3\,\mathrm{J}^{-1}\,\mathrm{s}^{-2}]$) and stimulated emission ($B_{10} = B_{01}$), the radiative transition rate can be expressed as:

$$r_r = \rho_\nu B_{01} + A_{10} \tag{2.2}$$

with ρ_ν being the source energy spectral density $[\mathrm{J\,Hz}^{-1}\,\mathrm{m}^{-3}]$ at ν, while the non-radiative rate is indicated by $r_{nr} = 1/\tau_{nr}$. Hence, the rate equation for the excited state population is expressed by:

$$\frac{dn_1}{dt} = \rho_\nu B_{10}(n_0 - n_1) - (A_{10} + r_{nr})n_1 \tag{2.3}$$

The total relaxation rate of the upper state is defined as the sum of the rates, such that the lifetime of the upper state (τ) is:

$$\tau^{-1} = \tau_r^{-1} + \tau_{nr}^{-1} \tag{2.4}$$

which inserted in Eq. (2.3) gives:

$$\frac{dn_1}{dt} = \rho_\nu B_{10}(n_0 - n_1) - \frac{n_1}{\tau} \tag{2.5}$$

The weak absorption hypothesis ($n_1 \ll n_0$) further simplifies the rate equation, leading to:

$$\frac{dn_1}{dt} = \rho_\nu B_{10} n_0 - \frac{n_1}{\tau} \tag{2.6}$$

The term $\rho_\nu B_{10}$ represents the optical absorption rate and can be more conveniently expressed as the product between the photon flux (Φ_0, $[\mathrm{m}^{-2}\,\mathrm{s}^{-1}]$) and the absorption cross section (σ_ν), introduced in Eq. (1.10):

$$\rho_\nu B_{10} = \Phi_0 \sigma_\nu \tag{2.7}$$

PAS and PTS however rely on the detection of a periodic effect, which would not result in the case of a constant photon flux. A more interesting result is obtained when considering a modulated photon flux in the form:

$$\Phi_0(\mathbf{r}, t) = \Phi_0(\mathbf{r})(1 + \delta e^{i\omega t}) \tag{2.8}$$

being δ the amplitude of the modulation and ω its radial frequency. Plugging Eq. (2.7) and Eq. (2.8) into Eq. (2.6) and solving for the population of the excited state, gives [99]:

$$n_1(t) = n_0 \sigma \Phi_0 \tau \left(1 + \frac{\delta}{\sqrt{1+\omega^2\tau^2}} e^{i(\omega t - \theta)}\right) \tag{2.9}$$

where $\theta = \tan^{-1}(\omega\tau)$ is the phase-shift between Φ_0 and n_1. In this solution, small optical intensities are considered, such that optical bleaching effects can be neglected. As expected, the excited state population features a steady state and a modulated component.

2.1.2 Heat source generation

As previously described, the molecules in the excited state eventually lose their energy with a time constant τ which in the case of roto-vibrational transitions is almost completely dominated by non-radiative relaxation processes ($\tau \approx \tau_{nr}$). Hence, the photon energy stored in the molecule upon excitation, is converted into heat. The heat rate generation $H(\mathbf{r}, t)$ $[\mathrm{J}\,\mathrm{s}^{-1}\,\mathrm{m}^{-3}]$ can be expressed as:

$$H(\mathbf{r}, t) = \frac{n_1(\mathbf{r}, t) E'}{\tau_{nr}} \tag{2.10}$$

where E' is the energy released during the relaxation (assumed to be the photon energy $h\nu$). The excited state population, as per Eq. (2.9), is composed of two terms, a time-independent and a time-dependent one. The first is responsible for a constant generation of heat, responsible of slow thermal drifts. The second-term, however, oscillates with the same frequency of the external light modulation, and is easy to measure via phase-sensitive detection (cfr. Section 1.6.1.3). Inserting Eq. (2.9) into Eq. (2.10), and keeping only the time-dependent term provides:

$$H(\mathbf{r}, t) = \frac{n_0 \sigma I_0(\mathbf{r}, t)}{\sqrt{1+\omega^2\tau^2}} \delta e^{i(\omega t - \theta)} \tag{2.11}$$

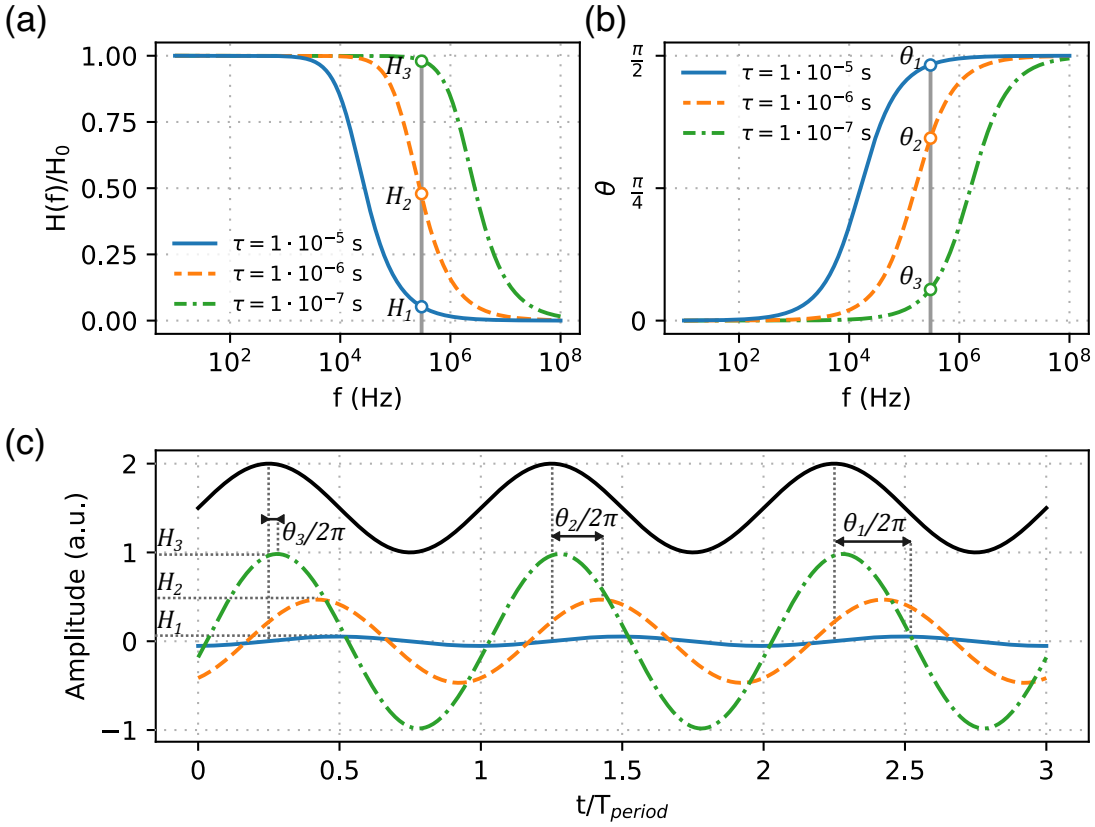

Figure 2.5: (a) Magnitude and (b) phase of the heat-response to a sinusoidal intensity modulation as a function of the modulation frequency for different relaxation time constants. (c) Time-evolution of the system for a set frequency of $3 \cdot 10^5$ Hz, for the same relaxation time constants presented in (a-b). In black, the modulated intensity excitation.

where the optical intensity $I_0 = \Phi_0 h\nu$ [W/m^2] has been introduced. This equation provides a fundamental result for indirect absorption spectroscopies, namely the influence of the relaxation rate on the entity of the photoinduced effect (which is assumed to be proportional to the generated heat). When the modulation frequency is slower than the relaxation rate, such that $\omega\tau \ll 1$, the amplitude of the photoinduced signal tends to its maximum value $H(\tau = 0) = H_0$. At the same time, no phase-shift between modulation and photoinduced signal is observed. On the other hand, when the modulation frequency and the relaxation rates are comparable, a drop in the amplitude of the signal is observed, with the limit $H(f \to \infty) = 0$, while a 90° phase-shift is observed. In Fig. 2.5(a-b), the magnitude of the heat source and its phase shift with respect to the intensity modulation are presented, for three different relaxation time constants of 10^{-5},10^{-6} and 10^{-7} sec. At a frequency of $3 \cdot 10^5$ Hz, each system responds differently both in terms of amplitude and phase. The time-response is shown in Fig. 2.5(c), which highlights the dramatic effect of the relaxation time.

It should be stressed in this context that in resonant PAS techniques, the modulation frequency of the laser source has to be tuned to a natural eigenfrequency of the mechanical resonator. If the resonance frequency is in the order of tenths of kHz, as it happens in

QEPAS for standard tuning forks with resonant frequency of $\sim$ 32 kHz, the approach does not allow full relaxation of the gas. In this case, relaxation promoters (i.e. molecules that increase the relaxation rate by introducing additional de-activation pathways) can be added to the gas mixture to enhance the photoacoustic signal. This is the case of water, which has been observed to promote the relaxation of small relaxing gases such as CO and NO [100], [101].

Nevertheless, if we consider the complicated scenario of gas mixtures, the energy transfer can lead to a kinetic cooling effect, where the thermal energy of the system is used to excite endothermic energy transfers, which subsequently relaxes with time constants so slow not to contribute to the photoacoustic effect. If the endothermic energy transfer is fast compared to the modulation frequency, it will result in a complete 180° phase-shift, partially canceling the PAS signal. Several works [102]–[104] described anomalous dependency of the PAS signal for varying humidity concentrations as an effect of kinetic cooling. In [104], the presence of water promoted the exothermic relaxation of the energy, completely out-of-phase with respect to the competitive kinetic cooling, arising from the endothermic energy transfer between CO and N_2. Hence, an anomalous dependency of the PAS signal with the humidity concentration was observed.

In summary, vibrational energy transfer phenomena complicate the interpretation of PAS spectra, and can introduce unwanted dependencies.

2.1.3 Generation of the thermal field and acoustic waves

The last relevant process arises from the modulated heat source presented in Eq. (2.11). The theoretical modeling of this process is well described by Bialkowski [88]. Several approximations are needed for an analytic solution of the involved differential equations. The natural tendency of the excited system to reach the equilibrium generates two types of hydrodynamic relaxation modes. The first kind are diffusive modes, which equilibrate the system through diffusive flux. The second kind are propagating modes, which transfer energy in the form of waves. These modes correspond to thermal diffusion (also referred to as thermal waves) and acoustic waves.

A general solution of the problem is obtained in the form of the Navier-Stokes equations, where small perturbations of the bulk thermodynamic parameters are introduced such that:

$$T(\mathbf{r},t) = T + \delta T(\mathbf{r},t) \tag{2.12}$$

$$\rho(\mathbf{r},t) = \rho + \delta\rho(\mathbf{r},t) \tag{2.13}$$

$$p(\mathbf{r},t) = p + \delta p(\mathbf{r},t) \tag{2.14}$$

$$\mathbf{u}(\mathbf{r},t) = \delta\mathbf{u}(\mathbf{r},t) \tag{2.15}$$

where T, ρ and p are the bulk temperature, density and pressure, while the flow velocity

$\mathbf{u} = 0$ since the fluid is considered at rest. With the aid of the continuity equation, the laws of momentum and energy conservation and the ideal gas law, one obtains the following equations:

$$\frac{\partial}{\partial t}\delta T(\mathbf{r},t) - D_T \nabla^2 \delta T(\mathbf{r},t) = \frac{H(\mathbf{r},t)}{\rho C_P} \tag{2.16}$$

$$\frac{1}{v^2}\left(\frac{\partial}{\partial t} - \Gamma_a \nabla^2\right)^2 \delta p(\mathbf{r},t) - \nabla^2 \delta p(\mathbf{r},t) = \frac{\beta}{C_P}\left(\frac{\partial}{\partial t} - \Gamma_a \nabla^2\right)^2 H(\mathbf{r},t) \tag{2.17}$$

where D_T [$\mathrm{m^2\,s^{-1}}$] is the thermal diffusivity, β [$\mathrm{K^{-1}}$] is the volumetric expansion coefficient, C_P [$\mathrm{J\,kg^{-1}\,K^{-1}}$] is the specific heat at constant pressure , Γ_a [$\mathrm{m^2\,s^{-1}}$] is the diffusive constant, and v is the sound velocity in the gas medium. Equation 2.16 corresponds to the thermal diffusion equation and its solution provides the evolution over space and time of the thermal field ($\delta T(\mathbf{r},t)$). Equation 2.17 has the form of a d'Alembert equation (wave equation), and describes the generation of pressure waves under periodic heat sources (right-hand side of the equation), by neglecting acoustic attenuation. Hence, the main difference between the two phenomena is that continuous excitation does not result in acoustic wave generation, but induces a constant thermal field.

Thermal diffusive solutions are probed in photothermal spectroscopy, along with possible interfering effects of the pressure waves. The latter are detected in photoacoustic spectroscopy, and if the pressure transducer is placed far enough from the excitation region, no interference from the photothermal effect is observed. Consequently, while photothermal effects are not measured in photoacoustic spectroscopy, this is not the case in the opposite situation. The second main distinction is that the acoustic waves are propagating relaxation modes, moving away from the excitation volume at the speed of sound; on the other hand, the diffusive mode is stationary in the sense that its maximum lies always at the same position.

2.1.3.1 Thermal diffusion equation solution

In the case where no boundaries are considered, a solution to the diffusion equation can be obtained using the Fourier-Laplace transform. If we can factorize the heat source $H(\mathbf{r},t) = H(x,y,z,t)$ into space- and time-dependent components:

$$H(\mathbf{r},t) = \Psi(t) S(x,y,z) \tag{2.18}$$

plugging this term into Eq. (2.16) yields the general solution:

$$\delta T(x,y,z,t) = \frac{1}{\rho C_P}\Psi(t) * \left[\frac{1}{(4\pi D_T t)^{3/2}} e^{-(x^2+y^2+z^2)/4D_T t}\right] \otimes S(x,y,z) \tag{2.19}$$

The symbol $\otimes$ indicates a spatial convolution over all coordinates, while $*$ represents the time convolution. Since diffusion is a linear, additive phenomenon, the total temperature

change to an arbitrary heat source function of space and time is given by the superposition of individual point sources. The response of the system to an instantaneous source of power $\Psi(t) = \delta(t)$, and spatial point sources $S(x, y, z) = \delta(x)\delta(y)\delta(z)$ (being δ the Dirac delta function) is called Green's function or *point impulse response function*. The point impulse response function for a tri-dimensional heat equation is:

$$\delta T_{\text{point}}(x, y, z, t) = \frac{1}{\rho C_P} \frac{1}{(4\pi D_T t)^{3/2}} e^{-(x^2+y^2+z^2)/4D_T t}, t \geq 0 \tag{2.20}$$

In the context of photothermal spectroscopy, we are not directly interested in the temperature or pressure perturbations. Rather, the quantity that is actually measured is the medium density, which changes the refractive index. The temperature is connected to the density of the medium via the volumetric expansion coefficient:

$$\beta = -\frac{1}{\rho}\left(\frac{\partial \rho}{\partial T}\right)_p \tag{2.21}$$

so that by substitution of Eq. (2.21) into Eq. (2.20), one obtains the density point impulse response function:

$$\delta \rho_{\text{point}}(x, y, z, t) = -\frac{\beta}{C_P} \frac{1}{(4\pi D_T t)^{3/2}} e^{-(x^2+y^2+z^2)/4D_T t}, t \geq 0 \tag{2.22}$$

The time and space evolution of the temperature impulse response function is presented in Fig. 2.6(a). In this case, the spatial coordinates have been grouped into a radial coordinate due to the spheric symmetry of the system ($r^2 = x^2+y^2+z^2$). The maximum of the thermal field always lays in the point of the excitation ($r = 0$). As the time increases, the thermal field evens out in space, depending on the thermal diffusivity of the sample D_T. Higher thermal diffusivities induce a faster decay of the thermal field. In Fig. 2.6(b), the distribution of the thermal field is observed for 4 times, after the excitation (which happens at $t = 0$).

2.1.3.2 Pressure wave equation solution

Differently from the diffusive thermal mode, the acoustic mode is more complicated to retrieve, since it doesn't lend well to Fourier inversion. In the Fourier space, the solution reduces to

$$\delta \rho(\mathbf{k}, t) = \frac{\beta}{C_P} e^{-\Gamma_a \mathbf{k}^2 t} \cos(v\mathbf{k}t) \tag{2.23}$$

and the corresponding impulse response function depends on the system geometry.

However, it is interesting to present a quite common solution for this problem, in the case of a Gaussian distributed impulse excitation:

$$H(r, t) = \frac{2Q\delta(t)}{\pi w^2} e^{\frac{-2r^2}{w^2}} \tag{2.24}$$

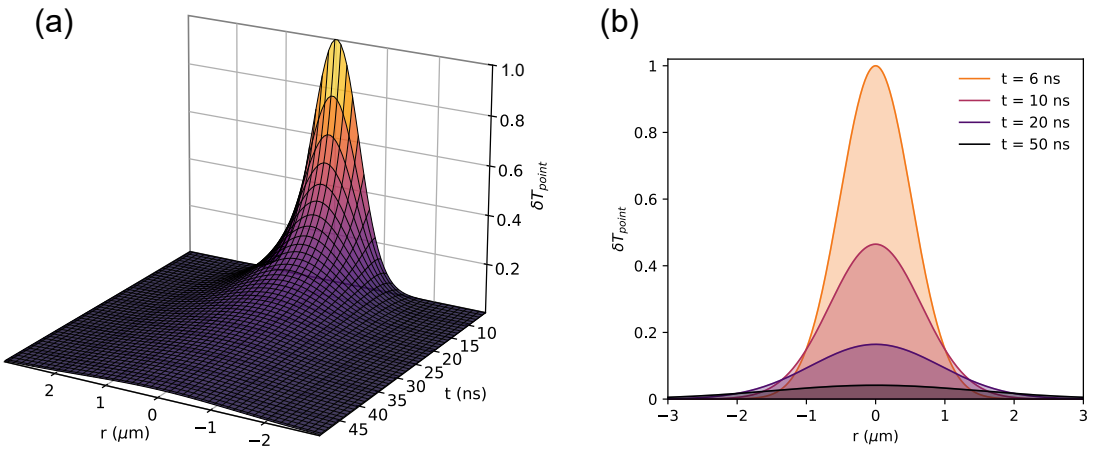

Figure 2.6: (a) Temporal and spatial dependency of the thermal impulse response function, calculated using the thermal diffusivity of air in normal conditions ($D_T = 2.2{\cdot}10^{-5}$ m^2 s^{-1}). (b) Radial dependency of the thermal distribution at 6, 10, 20 and 50 ns after the impulse excitation. A fast decay of the thermal field is observed, while its peak position remains constant.

where Q is the deposited heat, and w is the beam radius. It can be shown [105] that under the assumption of a sufficiently large cylindrical cell of radius b, the solutions of Eq. (2.23) can be expressed as an expansion of zero-order Bessel's functions $J_0(r)$:

$$\delta\rho_{\text{acoustic}}(r,t) = \sum_{j=1}^{\infty} c_j(t) J_0(\nu_j r) \tag{2.25}$$

where $\nu_j = \chi_j/b$, with χ_j being the j-th zero of the zero-order Bessel function ($J_0(\chi_j) = 0$). To solve this problem, the heat source in Eq. (2.24) can also be expanded in terms of zero-order Bessel functions, such that:

$$H(r) = \sum_{i=1}^{\infty} G_i J_0(\nu_i r) \tag{2.26}$$

The time-dependent expansion coefficients are:

$$c_j(t) = \frac{\beta}{C_P} G_j e^{-\nu_j^2 \Gamma_a t} \cos(vt\nu_j) \tag{2.27}$$

$$G_j(t) = \frac{Q}{\pi b^2 J_1(\chi_j)} e^{-\nu_j^2 w^2/8} \tag{2.28}$$

By inserting Eqs. (2.27) and (2.28) into Eq. (2.25), one obtains the density change of the acoustic modes to a Gaussian impulse excitation:

$$\delta\rho_{\text{acoustic}}(r,t) = \frac{\beta Q}{\pi b^2 C_P} \sum_{j=1}^{\infty} \frac{e^{-\nu_j^2 w^2 (1+2t/\tau_\Gamma)/8} \cos(vt\nu_j)}{[J_1(\chi_j)]^2} J_0(\nu_j r) \tag{2.29}$$

where the acoustic attenuation time constant $\tau_\Gamma = w^2/4\Gamma_a$ has been introduced.

2.1.3.3 Combination of acoustic and thermal effects

The overall density change is given by the sum of the impulse response functions for the diffusive and the acoustic mode. The diffusive mode of Eq. (2.22) can be estimated for the Gaussian impulse excitation, giving:

$$\delta\rho_{\text{diffusive}}(r,t) = -\frac{2\beta Q}{\pi C_P w^2(1+2t/t_c)} e^{-2r^2/[w^2(1+2t/t_c)]} \tag{2.30}$$

where $t_c = w^2/4D_T$ is the characteristic thermal decay time. In combination with Eq. (2.29) one obtains:

$$\delta\rho_{\text{impulse}}(r,t) = \delta\rho_{\text{acoustic}}(r,t) + \delta\rho_{\text{diffusive}}(r,t) =$$

$$= \frac{\beta Q}{\pi b^2 C_P} \sum_{j=1}^{\infty} \frac{e^{-\nu_j^2 w^2(1+2t/\tau_\Gamma)/8} \cos(vt\nu_j)}{[J_1(\chi_j)]^2} J_0(\nu_j r) - \frac{2\beta Q e^{-2r^2/[w^2(1+2t/t_c)]}}{\pi C_P w^2(1+2t/t_c)} \tag{2.31}$$

The behavior of the total density change is presented in Fig. 2.7. Panel (a) portrays the radial distribution of the density change, highlighting the two fundamental components: a central depression ($\delta\rho < 0$), caused by the diffusive (thermal) mode, and an outer ring of compression and rarefaction of the medium, which corresponds to the acoustic mode, travelling away from the excitation spot ($r = 0$). As the acoustic wave propagates, the peaks of compression and rarefaction decrease in amplitude for two main reasons: first, the radial propagation causes the energy to distribute over a larger volume (main effect in the picture); second, the acoustic attenuation will reduce the amplitude of the wave as it travels. The acoustic wave travels at the speed of sound v.

This image encapsulates the essence of photoacoustic and photothermal spectroscopies. It shows how, and why, this two phenomena are so closely interlaced, and provides a clear picture of their main differences. First, the rapid separation of the two effects explains why photothermal phenomena are not probed in photoacoustic spectroscopy. The opposite, however, is not true since depending on the geometry of the excitation and probe read-out, photoacoustic phenomena may contribute in the probed refractive index (or density) change. The second main point lies in the magnitude of the two effects. The effects of the thermal field on the density change are much stronger compared to the effects of the pressure. For a long time, the lack of proper tools to measure such effects prevented its use in analytical applications. Recent developments in laser sources and lock-in detection has enabled the advancement of photothermal spectroscopy.

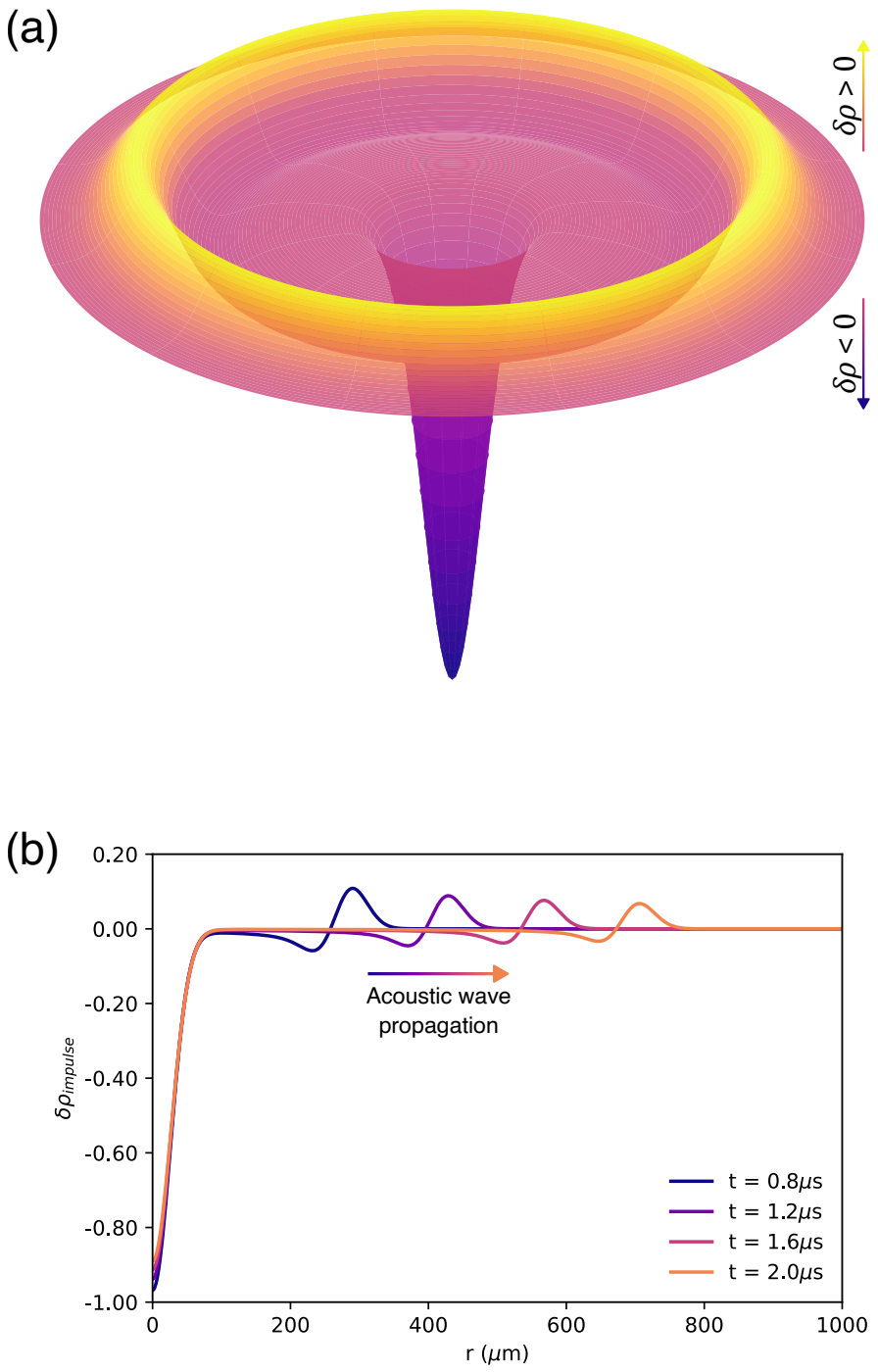

Figure 2.7: (a) Radial distribution of the density change at an instant of 800 ns after the excitation. The negative depression in the center corresponds to the diffusive mode (i.e. the thermal wave), while the ring around the central depression corresponds to the acoustic wave propagating away from the excitation spot. Air parameters at normal condition were used: $\Gamma_a = 1.2{\cdot}10^{-5}$ m^2/s, $D_T = 2.2{\cdot}10^{-5}$ m^2/s, $v = 346$ m/s and a beam waist $w = 50$µm. (b) Representation of the density change as a function of the radial distribution in 4 time frames of 0.8, 1.2, 1.6 and 2.0 µs after the excitation. While the central depression evolves over time, the acoustic wave propagates quickly away at a speed v, and decays in intensity due to acoustic attenuation and expansion over the radial coordinate. Adapted from [88].

2.1.3.4 Modulated excitation fields

A description of the effects induced by modulated excitation fields is relevant since analytical methods exploiting these phenomena such as photothermal and photoacoustic spectroscopies rely on these fields. As previously discussed, phase-sensitive detection is often employed in the detection of periodic signals, greatly simplifying the requirements of the experiment. The general solution, requires the convolution of the spatially and time-dependent source with the impulse response function of the system.

If we neglect the acoustic contribution, for simplicity, the heat diffusion equation has to be solved, leading to the general solution in Eq. (2.19).

Because of its linear nature, we expect to obtain a temperature change composed by a continuous and a periodic component:

$$\delta T(r,t) = \delta T_{cw}(r,t) + \delta T_{osc}(r,t) \tag{2.32}$$

The continuous component arises from the constant deposition of energy from the laser beam into the sample, while the oscillatory term comes from the modulation of the source. The latter is the measured quantity in a lock-in amplifier detection scheme. The scenario of an excitation by a Gaussian intensity distribution is quite common, since high-quality laser beams exhibit a Gaussian spatial distribution of the intensity. Moreover, we can assume a sinusoidal modulation of the intensity, since any other complex modulation can be decomposed into a sum of sine and cosine waves:

$$I(r,t) = I_0 \left[\frac{1+e^{i\omega t}}{2}\right] e^{-2r^2/w^2} = \frac{2P_0}{\pi w^2}\left[\frac{1+e^{i\omega t}}{2}\right] e^{-2r^2/w^2} \tag{2.33}$$

with $P_0/2$ being the average power of the beam, modulated between 0 and P_0. Neglecting heat-diffusion along the excitation axis (for instance in the case of a collimated beam), the thermal change can be written in the form:

$$\delta T(r,t) = \underbrace{\alpha \frac{P_0[1+e^{i\omega t}]}{2}}_{\text{Excitation source}} \; * \; \underbrace{\left[\frac{2}{\rho C_P \pi}\frac{e^{-2r^2/(8D_T t + w^2)}}{8D_T t + w^2}\right]}_{\text{2D-temperature impulse response}} \tag{2.34}$$

where the 2D-temperature impulse response has been obtained as a spatial convolution of the (2D-)point impulse response (formally similar to Eq. (2.20)) and the spatial distribution of the excitation beam. Usually, the cw-component can be neglected since it would be rejected in phase-sensitive detection. By considering only the oscillatory term, the amplitude of such term can be written in the form [106]:

$$\delta T_{osc}(r,t) = \frac{\alpha P_0}{2\pi\rho C_P b^2}\sum_{j=1}^{\infty}\frac{J_0(\nu_j r)}{J_1^2(\chi_j)} e^{-(\chi_j/b)^2 w^2/8}\frac{(\chi_j/b)^2 D_T \sin(\omega t) - \omega\cos(\omega t)}{\omega^2 + (\chi_j/b)^4 D_T^2} \tag{2.35}$$

where the same formalism as in Section 2.1.3.2 has been used, such that χ_j is a zero of the zero-order Bessel function, and b is the dimension of the cell, much larger than the

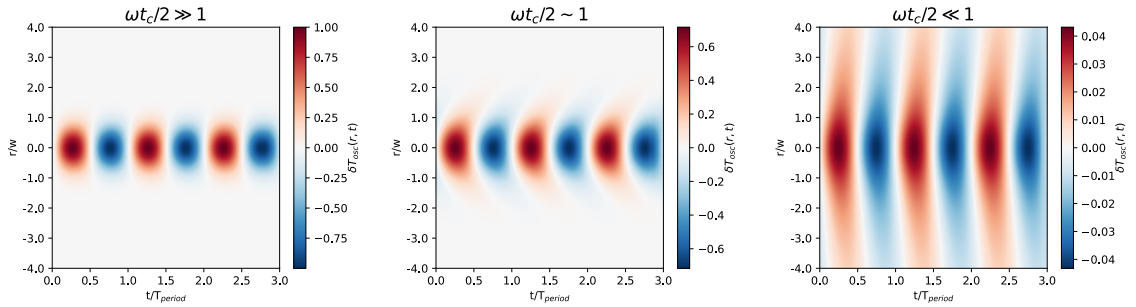

Figure 2.8: Time-evolution of the thermal field for a sinusoidal field along the radial coordinate for different heat-diffusion regimes ($\omega t_c/2 \gg 1$, $\omega t_c/2 \sim 1$, $\omega t_c/2 \ll 1$). In the first regime, the thermal change is mostly localized in the excitation volume. Conversely, for $\omega t_c/2 \ll 1$ the temperature change distributes more rapidly in space, leading to weaker gradients. In the presented scenario, the D_T was changed to span among the different regimes, in which case stronger signals are achieved for localized thermal fields (note the colormap scale).

beam dimension. An example of an oscillatory thermal field is presented in Fig. 2.8 for different thermal diffusivities. It can be seen that the presented scenarios differ quite remarkably: the demarcation line is typically set by the quantity $\omega t_c/2$. If $\omega t_c/2 \gg 1$, the radial thermal diffusion has an insignificant impact on the temperature distribution since the heat is confined within the radius of the excitation beam. Conversely, for $\omega t_c/2 \ll 1$ the radial thermal diffusion broadens the temperature field considerably above the radius of the excitation beam. In Fig. 2.8 these two regimes are explored ($\omega t_c/2 \gg 1$ on the left, $\omega t_c/2 \ll 1$ on the right).

The thermal radial diffusion has a strong implication on the size of the probe beam used to sense the temperature field. In an interferometric approach, the highest sensitivity would be obtained for comparable sizes, such that the probe field experiences the highest phase-shift. Larger probe beams will be less sensitive in probing highly confined thermal fields. It should be noted that, in the overall model hereby presented, mass convection has been neglected for simplicity. However, in a real-case scenario, mass diffusion and the flow direction with respect to the excitation field are additional effects which should be considered in the design of the experiment.

Another fundamental aspect is the dependency between the oscillatory term and the excitation frequency. It has been repeatedly confirmed both experimentally and theoretically that a lowered modulation frequency is beneficial as it increases the photothermal signal. In a simplified description, this relation can be understood by considering that for lower modulation frequencies, the duration of the modulation cycles increases. Hence, prolonged heating and cooling will result in a stronger thermal change, which consequently is detected as an increased measurable temperature difference. A detailed discussion of such dependency is provided in [106]. Such dependency must not be confused with the one presented in Section 2.1.2, which considered the effect of the relaxation rate of the system.

The final dependency that must be discussed is the size of the excitation beam. Even though it is not directly evident from Eq. (2.35), the cell size (b) doesn't influence the amplitude of thermal field if $\omega t_c/2 \gg 1$, since it doesn't reach the cell boundaries. However, it was shown how in this condition, the thermal field is totally localized in the waist of the exciting field. Hence, changing the beam spot size while keeping its power fixed will affect the thermal field, since the same power will spread over a different region. In this case, the observed dependency is quadratic with the reciprocal of the beam radius:

$$\delta T_{osc} \propto \frac{1}{w^2} \tag{2.36}$$

The latter relationship has the implication of enabling sensor miniaturisation, which is widely pursued in modern PTI approaches. It should be kept in mind that affecting the beam waist has an effect on the characteristic diffusion time (t_c), and reducing this value shifts the regime towards $\omega t_c/2 \ll 1$, generating thermal fields where radial diffusion has a large impact. The same discussion applies for the modulation frequency.

It should be remarked that the presented description for intensity modulated fields can also be applied for modulated absorptions. The latter is the case of wavelength modulation spectroscopies presented in Section 1.6.1.2, widely combined with PAS and PTS approaches.

2.1.4 Detection of the photoinduced effects

2.1.4.1 Detecting pressure waves

Pressure waves can be readily detected by means of pressure transducers, such as microphones or mechanical resonators that generate a signal upon deformation. The transducer converts the sound wave into an electrical signal S_{PAS}, proportional to the amplitude of the detected sound wave:

$$S_{\mathrm{PAS}} = R_m \delta p(r_m, \omega) \tag{2.37}$$

where R_m is the microphone responsivity and $\delta p(r_m, \omega)$ is the amplitude of the pressure wave in the microphone position. The form of the pressure-field, as explained in Section 2.1.3, depends on the type and geometry of excitation. A common approach consists in the use of cylindrical geometries, where the modulated excitation by the laser beam is collinear with the axis of the cell. In this case, the symmetry of the problem poses the boundary condition of a vanishing pressure-wave on the cell surface (node). A standing wave is generated within the resonator cell and the microphone must be positioned in an anti-node of the pressure field. A generalized expression of the PAS signal can be given in the following form:

$$S_{\mathrm{PAS}} = C_m \alpha P_{exc} \tag{2.38}$$

where C_m is the cell constant, which represents the sensitivity of the whole PA system and depends upon the properties of the mechanical resonator (volume, Q-factor, geometry), on the frequency and the employed transducer sensitivity, while P_{exc} is the optical power of the excitation source. It is useful to express the resulting signal as a function of the absorption coefficient, which by use of Eq. (1.10) can be expressed in terms of the absorbing analyte concentration (c):

$$S_{\mathrm{PAS}} = C_m c \sigma N_{tot} P_{exc} \tag{2.39}$$

2.1.4.2 Detecting thermal fields with interferometry

The detection of photothermal effects is somewhat more complicated, since the readout is performed via a probe laser, whose properties will affect the photothermal signal. As discussed at the beginning of the chapter, several detection schemes are possible, such as deflection, thermal lensing and interferometric ones. This work will concentrate on the latter aspect.

In photothermal interferometry (PTI), the phase-shift of a probe beam is measured as an intensity change. The phase-shift occurs as the laser passes through a perturbed volume, where the sample has been heated by the excitation beam. The phase of a geometric optics ray passing through the unperturbed sample is given by:

$$\phi = \frac{2\pi}{\lambda} \int\limits_{path} n(x,y,z)\, ds \tag{2.40}$$

with λ being the wavelength of the probe laser and $n(x,y,z)$ the refractive index of the medium. In a sample heated by a Gaussian laser beam, the refractive index exhibits a fluctuation induced by the thermal change:

$$n(r,t) = n_0 + \delta n(r,t) = n_0 + \left(\frac{dn}{dT}\right) \delta T(r,t) \tag{2.41}$$

hence, a phase-shift between the perturbed and unperturbed sample is measured

$$\delta\phi = \frac{2\pi}{\lambda} \left(\frac{dn}{dT}\right) \int\limits_{path} \delta T(r,t)\, ds \tag{2.42}$$

The last equation represents the phase-shift in the case of a single ray. In the most general case, the integral term should be exchanged by a volume-integral which accounts for the spatial distribution of the probe beam:

$$\int\limits_{path} \delta T(r,t)\, ds \quad \xrightarrow[\text{probe distribution}]{\text{integrating over}} \quad \iint\limits_{area} I_P(r_p) \int\limits_{path} \delta T(r_p,s,t)\, ds\, dA \tag{2.43}$$

The integration can be simplified depending on the system geometry, namely the orientation of the probe beam with respect to the thermal field. For collinear beams (excitation

and probe are parallel and overlapped), the optical ray phase shift of Eq. (2.42) becomes

$$\delta\phi \approx \frac{2\pi L}{\lambda}\left(\frac{dn}{dT}\right)\delta T(r,t) \tag{2.44}$$

where L is the interaction pathlength through the sample. It should be noted that for gas samples the thermo-optic coefficient (dn/dT) can be expressed as:

$$\left(\frac{dn}{dT}\right) = \left(\frac{\partial n}{\partial T}\right)_{\rho} + \left(\frac{\partial n}{\partial \rho}\right)_{T}\left(\frac{\partial \rho}{\partial T}\right)_{\rho} \tag{2.45}$$

The first term is the contribution of the refractive index due to the temperature-dependent change in the molar refractivity of the sample. The second term is the density-dependent refractive index change, usually much larger than the former. The density-dependent term can also be cast in terms of the volume expansion coefficient β:

$$\left(\frac{\partial n}{\partial \rho}\right)_{T}\left(\frac{\partial \rho}{\partial T}\right)_{\rho} = -\rho_0\beta\left(\frac{\partial n}{\partial \rho}\right)_{T} \tag{2.46}$$

Further simplifications related to the refractive index of gases in normal pressure conditions ($n_0 \approx 1$) lead to the so called Clausius-Mossotti equation:

$$\left(\frac{dn}{dT}\right) \approx -\frac{n_0 - 1}{T_0} \tag{2.47}$$

where T_0, n_0 being the equilibrium temperature and refractive index of the gas. Finally, Eq. (2.44) can be approximated as

$$\delta\phi \approx -\frac{2\pi L}{\lambda}\left(\frac{n_0 - 1}{T_0}\right)\delta T(r,t) \tag{2.48}$$

The phase-shift is then transduced as a change in intensity by considering the interferometer transfer-function. If we assume a two-arm interferometer (such as a Michelson, Mach-Zehnder or Jamin), the overall intensity measured at the detector will be given by the superposition of the reference (E_r) and sample beam (E_s) amplitudes, with their respective phase-shifts. The two complex amplitudes, passing through the interferometer arms, will read

$$E_r(t) = E_{0,r}e^{i(\omega t + \phi_r)} \tag{2.49}$$

$$E_s(t) = E_{0,s}e^{i(\omega t + \phi_s + \delta\phi(t))} \tag{2.50}$$

where $\phi_{r(s)}$ is the phase accumulated in the propagation within the reference and sample arms, respectively, while $\delta\phi(t)$ is the photothermal phase-shift. The superposition of the amplitudes produces an intensity on a square-law detector:

$$I(t) = |E_r(t) + E_s(t)|^2 = I_r + I_s + 2\sqrt{I_r I_s}\cos(\varphi + \delta\phi(t)) \tag{2.51}$$

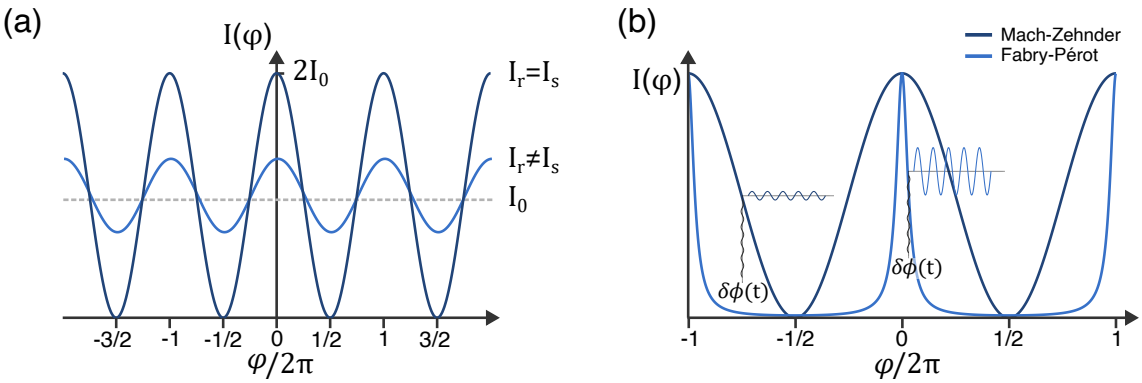

Figure 2.9: (a) Example of a two-beam interference pattern. As the phase retardation between the beams changes, the overall intensity given by the superposition of the beams generates a sinusoidal pattern. (b) Comparison of the interferometric fringes in a Mach-Zehnder and a Fabry-Pérot interferometer. The transduction properties at the quadrature and inflection points are portrayed.

where $I_r + I_s = I_0$ is the input intensity, and $\varphi = \phi_s - \phi_r$ is the phase-shift of the two beams, which accounts for possible retardations introduced by the optical elements. In the case of a perfect beam splitting ($I_s = I_r$), the previous equation reduces to:

$$I(t) = I_0[1 + \cos(\varphi + \delta\phi(t))] \tag{2.52}$$

which correspond to the typical interference pattern of two beams. The contribution of $\delta\phi(t)$ is usually very small, such that it can be considered a perturbation around the phase φ. If this phase is $\varphi = 2n\pi$, constructive interference occurs and the intensity is 4 times the one of the individual beam. Conversely, for phase shifts $\varphi = (2n+1)\pi$ destructive interference is generated. It should be noted that the energy conservation principle is always fulfilled, such that the integral of the intensity over the phase retardation is I_0. In the Mach-Zehnder, Michelson and Jamin interferometers, four waves are produced as a result of double passage of the beam through a beamsplitter. Consequently, two interference patterns (with peak intensity I_0), π-shifted one another are produced. An example of a two-beam interference pattern is provided in Fig. 2.9(a). The highest fringe visibility is produced when perfect beam-splitting is achieved ($I_r = I_s$): however, if the intensities differ, the resulting pattern will tend towards the sum of the two (I_0). The highest sensitivity of the interferometer is achieved in its quadrature point, namely for $\varphi = (n + 1/2)\pi$. Any perturbation of the phase induced by the excitation laser ($\delta\phi(t)$) is transduced as a change in intensity. The AC-component of the intensity is given by:

$$I_{AC}(t) = \cos\left(\frac{\pi}{2} + \delta\phi(t)\right) \approx \delta\phi(t) \tag{2.53}$$

The same considerations apply for the Fabry-Pérot Interferometer (FPI). The interference pattern of an FPI is given as reference in Fig. 2.9(b), in comparison to the pattern of a Mach-Zehnder interferometer. The pattern doesn't follow the $1 + \cos(\varphi)$ relation, but is described by the formula $1/(1 + F\sin^2(\varphi/2))$, where F depends on the mirror reflectivity.

A complete description of the FPI transduction properties is given in Chapter 3. The operation point of highest sensitivity of an FPI is often referred to as *inflection point*. The inflection point of an FPI, doesn't fall at a fixed phase-retardation, but depends on the F-factor. At the inflection point, the AC-component of the intensity will scale as $F \cdot \delta\phi(t)$ [96].

It should be noted that, similarly to Eq. (2.39) in PAS, also the PTS signal scales in the same way:

$$S_{PTS} = K\delta\phi = K\left[-\frac{2\pi L}{\lambda}\left(\frac{n_0 - 1}{T_0}\right)\right]\delta T = K' c\sigma N_{tot} P_{exc} \tag{2.54}$$

where the system's constant have been grouped in K'. In the last decades, novel approaches based on PTI for ultra-sensitive detection have emerged. Various gas cell configurations have been investigated, including those within the laser cavity and those utilising hollow-core optical fibres. The next section will provide a concise review including also the latest advancements in this field.

2.2 Photothermal interferometry: state of the art

2.2.1 Early demonstration

One of the earliest demonstrations of the potential of photothermal interferometry was provided by Davis and Petuchowski [91], who baptized their technique by the name 'Phase Fluctuation Optical Heterodyne' (PFLOH). In PFLOH, a Mach-Zehnder interferometer was employed trace detection of an analyte in a gaseous sample. A schematic of the setup is presented in Fig. 2.10. One arm of the interferometer hosted the gas cell, while the other arm was used as reference. Both probe and excitation beams passed through the sample cell, while the reference was actively kept to the quadrature point with a piezoelectric-mounted optical element to compensate for system's instabilities. With their approach, they demonstrated to be able of detecting changes in the minimum absorption coefficient as low as 10^{-10} cm^{-1}. However, such detection limits were possible due to the very powerful excitation source (Watt level). Only few years later, Campillo et al. [96] realized that by employing a Fabry-Pérot interferometer, the interaction pathlength could have been improved because of the high-finesse of the resonator. In such a configuration, they demonstrated similar sensitivities but with the advantage of higher compactness. In that case, the ultimate detection sensitivity was limited by the system's noise, for instance external acoustic or mechanical noise sources. Hence, increasing the quality of the interferometer would not improve the detection limits of the system.

These first demonstrations could achieve very low detection limits with the aid of powerful pump sources. However, their use outside of laboratory settings is constrained by the presence of bulky and sensitive components. The technological advancement of telecommunication devices, such as diode lasers in the near-infrared, optical fibers and

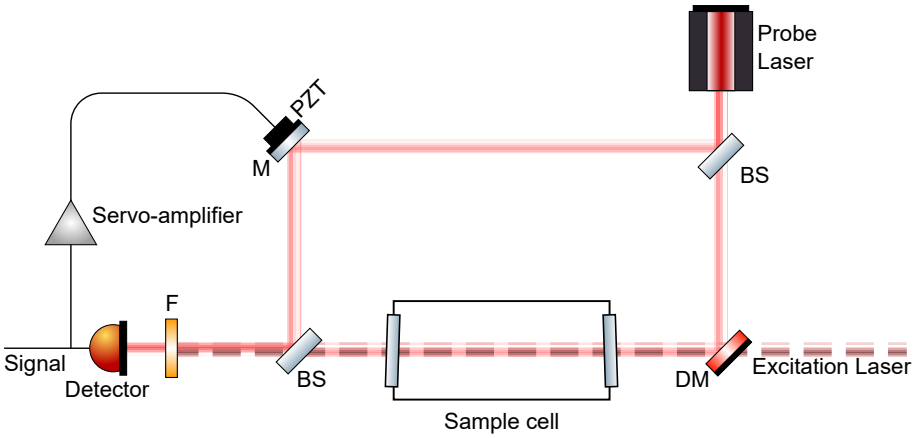

Figure 2.10: Schematic of the PFLOH setup used by Davis et al. [91]. BS, beam-splitter; DM, dichroic mirror; F, filter; M, mirror; PZT, piezo-element.

optical components in this wavelength range facilitated the development of novel sensing schemes.

2.2.2 Fiber based sensors

Optoelectronic components utilized in telecommunications have attained a mature stage and are relatively inexpensive. The coupling of light to optical fibers provides additional benefits in terms of robustness. Most devices are fiber-compatible and even laser sources are nowadays packaged with pigtailed connectors.

Optical fibers are particularly efficient in the telecommunication region, where the absorption losses of -OH impurities in silica limit transparency of the glass. The minimum losses are obtained for the window at 1550 nm, while the lowest dispersion coefficient is achieved around 1310 nm [107]. The rigorous requirements of telecommunication applications do not apply to sensors, where typical fiber lengths are in the order of few meters. However, the tremendous advancement of these technologies has led to lower costs and efficient components, which can be exploited for building innovative sensing schemes. It is not surprising to find that most of the fiber-sensing applications are based on (but not restricted to) 1.3 and 1.5 µm components.

Optical fibers can be used not only for enhanced robustness, but special fibers can also be employed as frameworks to host the analyte gas. This is the case of hollow-core fibers (HCF), which have been extensively employed in PTI arrangements [108]–[111]. A hollow-core fiber presents a hollow cavity which can be engineered to give special transmission properties to the mode propagating in the fiber. By doing so, only a small part of the mode propagates in the solid fiber material. Hollow-core fibers allow transmission in spectral regions otherwise inaccessible due to the glass optical absorption.

The peculiarity of HCF is that they enable light propagation in air even though its refractive index is lower than that of the cladding material. Light guiding in a medium of lower index cannot rely on total internal reflection and it is achieved by optical bandgap

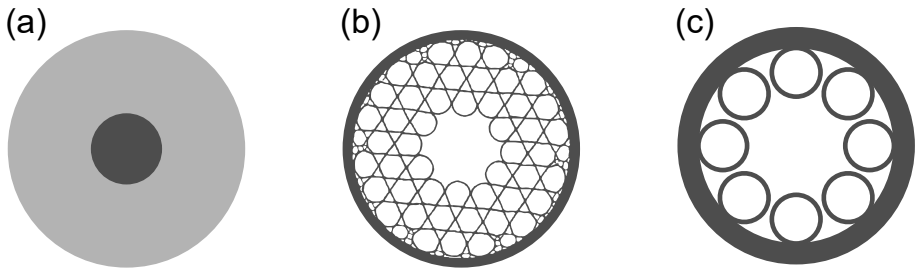

Figure 2.11: (a) Single-cladding optical fiber with higher refractive index core. Examples of (b) a Kagomi photonic crystal fiber and of (c) an antiresonant hollow-core fiber, revolver type.

engineering (in photonic bandgap fibers) which prohibits light propagation in the cladding. An example is given by Kagome fibers: in Kagome hollow-core fibers the cladding is generated by a glass-web of periodic shape. An easier geometry that achieves the same result is based on the antiresonant effect [112]. In antiresonant hollow-core fibers (ARHCF), a simplified geometry of few hollow silica channels is arranged around the hollow core. This technology exploits properly phased reflections from the thin silica layers, in order to confine the mode in the core of the waveguide [113]. Basically, several Fabry-Pérot reflections are exploited to obtain mode confinement. What is actually very relevant is that, the reflection condition of a Fabry-Pérot (as schematically presented in Fig. 2.9(b)) is obtained for a wide-range of wavelengths. Thus, the mode confinement can be engineered for broadband transmission. A comparison of the cross-sectional view of these type of fibers is provided in Fig. 2.11.

The advantage of using HCFs as hosts for the analyte gas comes from the possibility of having both pump and probe beam guided within the same fiber. Hence, the interaction pathlength between the thermal field and the probe laser is enhanced accordingly. Several meters of interaction length can be easily achieved, while the winding of the fiber allows a relatively compact system. The physics of PTI in a HCF is analogous to the one already presented, with the only difference being the measured phase-shift. Rather than measuring a refractive index change in the medium, what is actually measured is the different effective index (n_{eff}) of the probe propagating in the fiber. The fiber can be added within the arm of a fiber-based interferometer, or the reflectivity at the end of the fiber can be used to create a low-finesse Fabry-Pérot interferometer.

In [108], the authors achieved outstanding noise equivalent absorption on the order of 10^{-10} cm^{-1} with a 10m-long HCF. At the same time, dynamic ranges over six orders of magnitude were demonstrated, proving the high versatility of their system.

This work was further advanced by the same authors [110], where a more sensitive transduction scheme based on modal interference between two modes propagating in the HCF was achieved. Each mode will suffer a different phase-shift depending on the mode overlap with the induced thermal field, and the measured phase-shift is given by the difference of the individual modal shifts.

The main drawbacks of such approaches concerns the thermal/fluid dynamic processes of a gas-filled HCF, which is very complex and significantly different from a free-space system. Moreover, since the possibility of collinear propagation requires good transmission properties of the fiber for both pump and probe beam, most of their application is limited to NIR and visible range, were weaker overtone absorptions are targeted. Most recent works employing ARHCF fibers in the mid-infrared are presented in [111], [114], and further works are expected as the technological advancement of ARHCF is still ongoing.

2.2.3 Miniaturized Fabry-Pérot

Another advantageous approach in photothermal interferometry consists in the use of compact Fabry-Pérot interferometers. As described in Section 2.1.3.4, a small pump waist enhances the thermal gradient in the excitation volume enabling sensor miniaturization. This concept has been exploited in crossed beam configuration between a pump and a probe laser coupled to the FPI. The pump laser is focused between the dielectric mirrors of the FPI, and the probe laser is spatially overlapped to the excitation volume. Since the Fabry-Pérot interferometer behaves as an optical resonator, the probe beam is reflected many times within the mirror before exiting the device, and each passage through the excitation volume causes an additional phase-shift.

One of the most appealing aspects of this approach is the inherent miniaturisation capabilities of the FPI. Fabry-Pérot cavities with moderate [115] or high-finesse [116] have been fabricated directly on single-mode fibers by femtosecond laser ablation. Monolithic configurations would be extremely advantageous since they don't require careful alignment of the FPI mirrors. Alternatively, fabrication of concave micro-mirrors on the surface of two optical fibers can generate high-finesse ($\sim 10^5$) cavities [117], [118]. Commercial instruments based on on-fiber Fabry-Pérot resonators as all-optical microphones are already available on the market [119] and their use for photothermal spectroscopy is readily done [120], [121].

Fabry-Pérot enhancement in photothermal interferometry has been widely explored at TU Wien, with the work of Waclawek et al. [97], [122]–[125] and has recently attracted attention from other authors [126]. It was demonstrated that, by employing proper noise-rejection schemes such as balanced detection, extremely low detection limit could be achieved with figures of merit reaching state of the art sensitivities (NNEA $\sim 10^{-9}$ $\mathrm{W\,cm^{-1}\,Hz^{-1/2}}$). This technique was also baptized 'Interferometric Cavity Assisted Photothermal Spectroscopy' (ICAPS) and Chapter 3 is focused on this approach, together with the novelties introduced by this work on the topic.

In conclusion, a multitude of methodologies are available in photothermal interferometry, and it is difficult to identify the superiority of one technique over the others, as they all possess advantages and limitations. Table 2.1 reviews and compares the most recent and effective methods in photothermal interferometry.

Table 2.1: Comparison between state of the art PTI techniques.

Technique	Gas cell	Analyte	Excitation wavelength	NEC	Integration time	Interaction length	Pump Power	α_{min} (cm^{-1})	NNEA ($W\,cm^{-1}\,Hz^{-1/2}$)
2f-WM-PTI[127]	HCF	N_2O	4.46 µm	0.8 ppm	1 sec	25 cm	6 mW	$8.20{\cdot}10^{-05}$	$4.90{\cdot}10^{-07}$
PTI[128]	HC-PBF	C_2H_2	1530.37 nm	10 ppb	100 sec	2 × 28 m	55 mW	$1.17{\cdot}10^{-08}$	$6.41{\cdot}10^{-09}$
2f-WM-PTI[108]	HC-PBF	C_2H_2	1530.37 nm	2 ppb	1 sec	10 m	15.3 mW	$2.30{\cdot}10^{-09}$	$1.15{\cdot}10^{-10}$
MPD-PTS[110]	ARHCF	C_2H_2	1533 nm	68 ppt	1 sec	4.67 m	108 mW	$1.60{\cdot}10^{-11}$	$5.64{\cdot}10^{-11}$
FDM-PTI[129]	ARHCF	H_2O CO_2 CO	1392 nm 2033 nm 4.60 µm	9 ppb 25 ppb 2.7 ppb	1 sec	13 cm	2 mW 200 mW 5 mW	$3.60{\cdot}10^{-09}$	$2.33{\cdot}10^{-09}$
2f-WM-PTI[111]	ARHCF	NO	5.26 µm	11 ppb	144 sec	25 cm	78 mW	$4.19{\cdot}10^{-06}$	$4.29{\cdot}10^{-07}$
2f-WM-PTI[126]	FFPC	CH_4	1651 nm	78 ppb	100 sec	<1 mm	66 mW	$3.00{\cdot}10^{-08}$	$7.06{\cdot}10^{-08}$
ICAPS[125]	FPI	NO	5.26 µm	64 ppb	1 sec	<1 mm	36 mW	$4.80{\cdot}10^{-07}$	$5.70{\cdot}10^{-08}$
ICAPS[123]	FPI	SO_2	7.24 µm	3 ppb	1 sec	<1 mm	200 mW	$7.90{\cdot}10^{-09}$	$4.50{\cdot}10^{-09}$

All the presented techniques used a 1550 nm probe line.
2f-WM, second-harmonic wavelength modulation; **MPD**, mode-phase-difference; **FDM**, frequency-division-multiplexed; **ICAPS**, interferometric cavity assisted photothermal spectroscopy; **(AR)HCF(-PBF)**, (anti-resonant) hollow core fiber (photonic bandgap fiber); **FFPC**, fiber Fabry-Pérot cavity.

Chapter 3

Interferometric cavity assisted photothermal spectroscopy

Interferometric cavity assisted photothermal spectroscopy is one of the many PTI approaches that exploit the Fabry-Pérot interferometers as a transducer for thermally-induced effects.

A peculiarity of ICAPS is the excitation scheme, which is orthogonal with respect to the probe beam. The main reason lies in the spectral transmission of Fabry-Pérot devices, usually limited to a narrow band defined by the employed multi-dielectric coating. Although collinear approaches are possible (as presented for fiber FPIs), they might pose stability problems as the excitation source can be absorbed from the mirrors, producing drifts and a modulated signal potentially indistinguishable from the photothermal one. In orthogonal excitation, on the other hand, the beam can be focused in a tiny spot to trigger stronger photothermal effects, preserving the sensitivity of the technique. Care must be taken to prevent the excitation beam from touching the mirrors, to avoid the aforementioned problems. An additional benefit of orthogonal excitation is the coupling versatility of different excitation sources, potentially opening the path for multi-component analysis. In many cases, the gas volume is enclosed within an air-tight gas cell equipped with optical windows.

The core element of ICAPS is the Fabry-Pérot interferometer, thoroughly described in Section 3.1. Commercial use of FPIs is common for several applications. FPIs are especially used for wavelength filtering: tunable filtering is achieved by changing the separation of the mirrors, or within certain limits, by tilting the interferometer, with a resolving power that depends on the reflectivity of the mirrors. For very high-finesse, the FPI can be used for frequency stabilization of laser sources, with the well known Pound-Drever-Hall method [130].

Another common application is the use of solid crystals, such that the reflective surfaces act as low-quality mirrors of the FPI: in this case, the term *etalon* is also used. Etalons behave as frequency markers and find wide usage in spectroscopic applications.

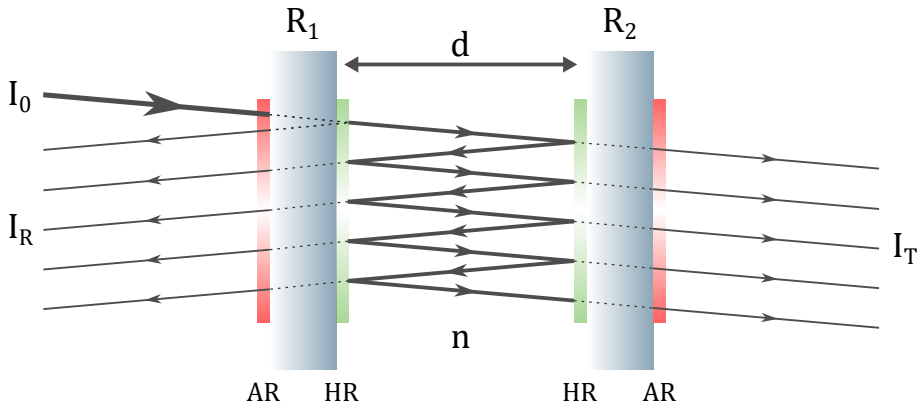

Figure 3.1: Schematic of a Fabry-Pérot interferometer. An anti-reflection coating on the first interface prevents additional reflections, while a high-reflective coating is deposited on the second surface. As a result, multiple partially transmitted and reflected beams are obtained. The coherent superposition of these beams produces constructive or destructive interference, depending on the round-trip phase shift between the multiple reflected beams.

3.1 The Fabry-Pérot Interferometer

In its simplest form, a Fabry-Pérot interferometer consists of two planar mirrors with reflectivities R_1 and R_2, separated by a distance d, as portrayed in Fig. 3.1. Losses generated by scattering and absorption at the mirror surfaces or from the medium itself are neglected. If a monochromatic planar wave of wavelength λ enters the FPI at an incidence angle θ with an intensity I_0 and electric field amplitude E_0, the propagating electromagnetic field will be partially reflected at the first mirror, while the transmitted intensity portion will bounce back and forth between the two mirrors with a portion of light transmitted through the second mirror. At each round-trip within the cavity, the field accumulates a phase-retardation corresponding to

$$\phi = 2knd\cos\theta \tag{3.1}$$

being $k = 2\pi/\lambda$ the vacuum wavevector and n the medium refractive index.

The overall reflected and transmitted amplitudes (E_r and E_t, respectively) of the FPI are given by the superposition of all the waves partially reflected and transmitted at each mirror of the resonator. If r and t are the Fresnel reflection and transmission coefficients of the two mirrors (symmetrical resonator), the reflected and transmitted field are given by:

$$E_r = E_0\left[r - t^2 e^{i\phi}\sum_{n=0}^{\infty}(r^2 e^{i\phi})^n\right] \tag{3.2}$$

$$E_t = -E_0 t^2 e^{i\phi}\sum_{n=0}^{\infty}(r^2 e^{i\phi})^n \tag{3.3}$$

where ϕ is the phase retardation of the field after a cavity round-trip, formerly defined.

The reflected and transmitted intensities are readily obtained by the square modulus of Eqs. (3.2) and (3.3), which normalized to the incident intensity provide reflectance ($\mathcal{R}$) and transmittance ($\mathcal{T}$) of the FPI:

$$\mathcal{R} = \frac{4R\sin^2(\phi/2)}{(1-R)^2 + 4R\sin^2(\phi/2)} = \frac{F\sin^2(\phi/2)}{1 + F\sin^2(\phi/2)} \tag{3.4}$$

$$\mathcal{T} = \frac{(1-R)^2}{(1-R)^2 + 4R\sin^2(\phi/2)} = \frac{1}{1 + F\sin^2(\phi/2)} \tag{3.5}$$

Eqs. (3.4) and (3.5) are often called *Airy formulas*, where $F = 4R/(1-R)^2$ is the *coefficient of finesse*. It can be readily shown that the maximum of transmission is achieved for $\sin^2(\phi/2) = 0$, which corresponds to constructive interference of the transmitted partial amplitudes such that $\phi = 2m\pi$ and $\lambda_{\text{res}} = 2nd\cos\theta/m$. It is more convenient to describe the phenomenon in the frequency domain, such that the resonance frequencies will be a multiple of the mode index (m):

$$\nu_{\text{res}} = \frac{mc}{2nd\cos\theta} \tag{3.6}$$

which corresponds to a comb of equally spaced frequencies (for a non dispersive medium). The separation between the resonance frequencies is called *free spectral range*:

$$\delta\nu_{\text{FSR}} = \frac{c}{2nd\cos\theta} \tag{3.7}$$

The effect of the reflectivity on the transmission and reflection profiles is shown in Fig. 3.2. With low mirror reflectivities the interference pattern resembles a sine-wave with limited fringe visibility: this is often the case of the interface reflectivity obtained between air and dense materials, where the refractive index contrast causes incident beams to be partially reflected. However, as the reflectivity is increased, the interference pattern drastically changes, providing the typical Lorentzian shape of optical resonators.

The full-width at half-maximum (FWHM) of the Airy formulas can be obtained from Eqs. (3.4) and (3.5), giving:

$$\Delta\nu_{\text{FWHM}} = \delta\nu_{\text{FSR}}\frac{2}{\pi}\arcsin\left(\frac{1-R}{2\sqrt{R}}\right) \tag{3.8}$$

However, this definition breaks down at low reflectivities ($R \approx 0.172$) as both Airy functions do not reach 1/2, as shown in Fig. 3.2. The most important descriptor of the FPI as a spectral selector is its *Airy finesse* ($\mathcal{F}$), defined as the ratio between FSR and FWHM, which from Eq. (3.8) gives:

$$\mathcal{F} := \frac{\delta\nu_{\text{FSR}}}{\Delta\nu_{\text{FWHM}}} = \frac{\pi}{2}\left[\arcsin\left(\frac{1-R}{2\sqrt{R}}\right)\right]^{-1} \tag{3.9}$$

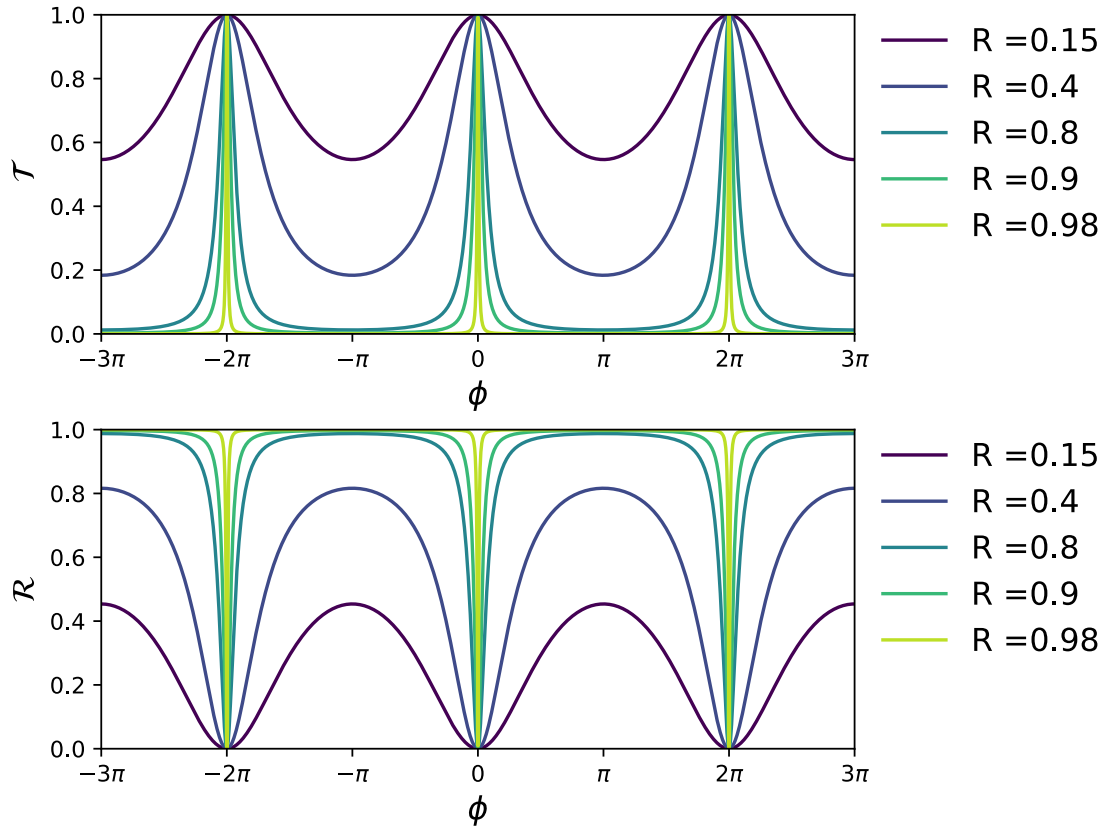

Figure 3.2: Transmittance and reflectance of an FPI as a function of the phase-retardation ϕ for different reflectivities.

In [131], Ismail et al. clarified the main misconceptions around such quantities and demonstrated how those definitions are not suitable for non-scanning applications (fixed FPI separation). A better descriptor of the resonator quality is provided by the spectral line shapes. Each resonance mode can be described by a Lorentz function, whose FWHM depends on the system losses. If we inject photons within the cavity, their characteristic decay time τ_c will be related to the Lorentzian FWHM by:

$$\Delta\nu_{\mathrm{FWHM}'} = \frac{1}{2\pi\tau_c} \tag{3.10}$$

which leads to the Lorentzian Finesse:

$$\mathcal{F} := \frac{\delta\nu_{\mathrm{FSR}}}{\Delta\nu_{\mathrm{FWHM}'}} = \frac{2\pi}{-\ln(R^2)} \tag{3.11}$$

obtained by $\delta\nu_{\mathrm{FSR}} = 1/t_{rt}$, being t_{rt} the photon round-trip time in the cavity, and $\tau_c = -t_{rt}/\ln(R^2)$. In the presence of large mirror losses (low reflectivity), the FWHM will be large enough to produce a partial overlap between the tails of neighboring modes, leading to the sinusoidal-like interference pattern. On the other hand, for sufficiently high reflectivities the full interference pattern will appear as the sum of well separated Lorentzian lines. The advantage of this description lies in the fact that at low reflec-

tivities, both the Lorentzian FWHM and the relative Finesse are still meaningful. For sufficiently high mirror reflectivities ($R > 0.7$), the Airy definition and the Lorentzian one are practically identical.

Both Eqs. (3.9) and (3.11) show the dependency of the finesse on the mirror quality. However, in real-case scenarios the measured finesse might differ substantially from the theoretical one. In general, the total finesse can be expressed as:

$$\frac{1}{\mathcal{F}^2} = \sum_i \frac{1}{\mathcal{F}_i^2} \tag{3.12}$$

where the different terms $\mathcal{F}_i$ give the contributions to the decrease of the finesse caused by the different imperfections of the interferometer. The main contributions that limits the *reflectivity finesse* are:

Surface roughness: indicates the root-mean-square variation of the surface from ideal flatness. Irregularities in the mirror flatness introduce variable phase-shifts which worsen the total finesse. Manufacturer typically indicate this quantity in fractions of λ. Typical values for standard optical components are $\lambda/20$, while high quality surfaces can exceed $\lambda/200$;

Parallelism errors: if the mirrors are not perfectly parallel, variable cavity phase retardations will be encountered across the etalon;

Scatter and Absorption Losses: scatter introduce an additional leakage of light while materials will absorb light during each pass. These losses are usually insignificant if the proper coatings and materials are used.

Aside from fabrication limitations, the finite extent and the collimation properties of the light source has also a strong implication in the resulting interferometric fringe. A common case is the illumination with Gaussian beams.

3.1.1 Gaussian beam illumination

Unlike planar waves which posses a unique propagation vector, the Gaussian beam exhibit a distribution of wavevectors with the main component pointing on the optical axis. A planar wave decomposition of the Gaussian beam would reveal a distribution of propagation vectors mainly contained within the full-angle divergence of the beam. The result is a superposition of planar waves with a different incidence angle on the FPI, which by Eq. (3.1) corresponds to a different phase-retardation.

Several authors [133]–[135] demonstrated the effect of Gaussian beam illumination considering the beam divergence and its incidence angle on the FPI. It was demonstrated that the overall effect is a reduction of the fringe visibility, as well as a break in the symmetry of the interferometric fringes. An example is provided in Fig. 3.3, where a Gaussian beam of variable beam waist is sent normal to a parallel FPI. The model sums

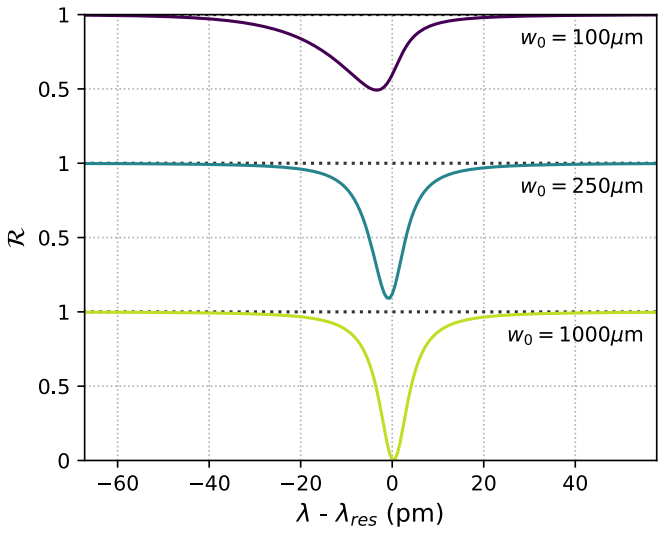

Figure 3.3: Example of Fabry-Pérot illumination with a Gaussian beam of varying beam waist (or divergence) as a function of the wavelength. The simulation was performed for an FPI of 2 mm spacing with reflectivity $R = 0.98$ and resonance wavelength $\lambda_{res} \approx 1550$ nm. Based on the code from [132].

over a sufficient number of reflected waves. The waist position is located on the first mirror, and a detector of infinite extent is assumed. More complete models [135] can evaluate the presence of collection optics (such as single mode fibers), leading to more accurate results.

An important parameter in the practical application of FPI as a transducer is the reflectivity change as a function of the wavelength ($d\mathcal{R}/d\lambda$), since it defines its sensitivity to a phase-change. While the fringe visibility decreases, the increasing asymmetry favours the high-wavelength side of the interferometric fringe, partially mitigating the negative effect on the sensitivity. In Section 2.1.4.2, the impact of the probe beam size on the transduction of photothermal effects has been discussed. In the presence of highly localized thermal fields, optimum probe sizes should be comparable in dimension with the excited volume. In such cases, focused beams might provide improved sensitivity in photothermal sensing. However, by doing so, the coupling efficiency to the FPI is strongly degraded. In general, a trade-off is expected between optimum coupling and efficiency in probing the thermal field. A spherical mirror FPI configuration could provide a double benefit in this sense, by improving the finesse of the resonator, while at the same time focusing the probe beam in a tiny spot between the mirrors, potentially allowing improved PTS sensitivity.

3.2 ICAPS principles

As many other Fabry-Pérot based sensors, the ICAPS technology exploits the resonance frequency dependency on the medium refractive index (RI), given in Eq. (3.6). Tiny changes in the RI can be easily transduced as intensity changes by properly tuning the probe laser to the interferometric fringe. The additional phase-shift ($\delta\phi$) caused by

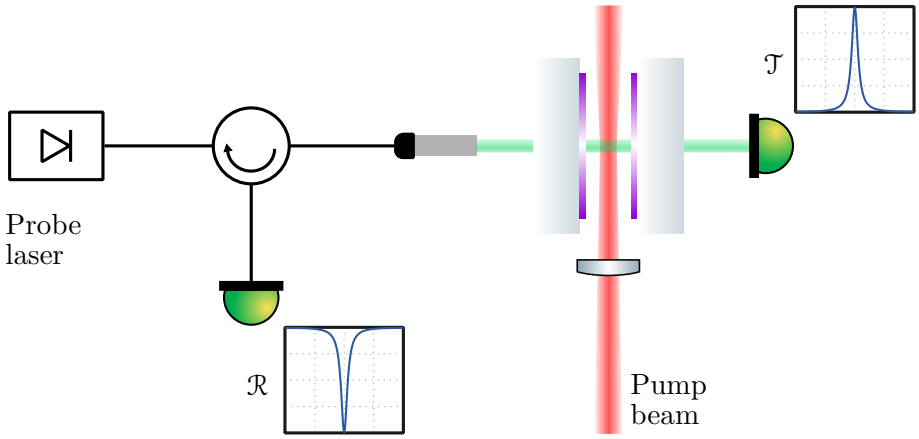

Figure 3.4: Typical arrangement of an ICAPS setup with a fiber-based probe readout line.

the RI perturbation (δn) will be:

$$\delta\phi = \frac{4\pi}{\lambda}\delta n d\cos\theta \tag{3.13}$$

which corresponds to a shift of the resonance wavelength in the spectral domain. This property is frequently employed to quantify RI changes, induced by pressure, temperature, or the FPI filling material itself. In the case of photothermal excitation, the RI perturbation is proportional to the concentration of the analyte, as per Eq. (2.54). Since the perturbation is periodic, phase-sensitive detection can be employed to retrieve both its amplitude and phase. Two fundamental requirements must be fulfilled during an ICAPS experiment:

1. **Spectral tuning to the interferometric fringe**: the sensitivity of the method is affected by the relative detuning between the resonance wavelength (λ_{res}) and the probe laser wavelength (λ_p). Highest linearity and sensitivity are achieved in the vicinity of the *inflection points* (IPs) of the interferometer transfer function, which for a Lorentzian-shaped mode profile fall at $\lambda_p - \lambda_{res} = \pm w/\sqrt{3}$, being w the half-width at half-maximum;

2. **Spatial overlapping with the excitation beam**: the probe beam has to sense the thermal field induced by the excitation source. In many cases, it is convenient to focus the pump beam between the mirror of the FPI. In the Mid-IR, typical waist values can easily reach hundreds of micron, posing a tight tolerance on the vertical probe beam alignment. For instance, a $\lambda = 5$ µm beam focused by a 50 mm lens, produces a beam waist of < 100 µm. Due to the relatively large depths of fields (3 mm) of the pump beam, the lateral displacement (on the same plane of the schematic in Fig. 3.4) does not pose a strict requirement on the horizontal displacement between the probe and the excitation focal point.

A simple fiber-based arrangement of an ICAPS setup is presented in Fig. 3.4. Optical fibers offer a simplified alignment and improve the robustness of the system. Many optical

components such as isolators, circulators, optical detectors and FPIs can be conveniently found in the telecommunication region. The resonance can be detected both in transmission and in reflection, by making use of an optical circulator. More details in the choice of the optical components are given in Section 3.2.1. In this work, the reflected component was investigated due to the inherent advantages of using back-reflected radiation. While being prone to parasitic interferences, the reflection-configuration strongly simplifies the alignment to the cavity. At the optimum alignment condition, the back-reflected beam is automatically aligned to the collimator and is then collected onto the photodetector. The light collected on the detector will produce a voltage signal which can be expressed as:

$$S(\lambda_p, \lambda_{\text{res}}) = P(\lambda_p)R(\lambda_p)[1 - L(\lambda_p, \lambda_{\text{res}})] \tag{3.14}$$

where $P(\lambda_p)$ is the optical power of the probe, as a function of its wavelength, $R(\lambda_p)$ is the detector responsivity, which can be considered a constant in the limited spectral extent of the probe laser and $L(\lambda_p, \lambda_{\text{res}})$ is the Lorentzian transmission function of the resonance. In a generic situation, the latter can be expressed as:

$$L(\lambda_p, \lambda_{\text{res}}) = A\frac{w^2}{w^2 + (\lambda_p - \lambda_{\text{res}})^2} \tag{3.15}$$

where A takes into account the fringe visibility ($0 < A < 1$) of a real-case scenario. The PTS signal is generated as a result of a modulated absorption occurring at frequency ω_{exc} in the filling medium of the air-spaced etalon. Hence, a modulated RI is generated ($n(t) = n_0 + \delta n \sin(\omega_{exc}t)$) which induces an equivalent modulation of the resonance wavelength:

$$\lambda_{\text{res}}(t) = \bar{\lambda}_{\text{res}} + \delta\lambda_t \sin(\omega_{exc}t) \tag{3.16}$$

with $\bar{\lambda}_{\text{res}}$ being the unperturbed resonance wavelength and $\delta\lambda_t = 2\delta n d \cos\theta$ being the thermal modulation depth induced by the modulated absorption.

Similarly to the description presented in Section 1.6.1.2, the detected signal can be expanded as a Taylor series around $\bar{\lambda}_{\text{res}}$, to provide the time-dependent voltage signal at a fixed probe wavelength:

$$S(\lambda_p, \lambda_{\text{res}}(t)) = \sum_{n=0}^{\infty} \frac{1}{n!}[\delta\lambda_t \sin(\omega_{exc}t)]^n \frac{\partial^n S}{\partial \lambda_{\text{res}}^n}\bigg|_{\bar{\lambda}_{\text{res}}} \tag{3.17}$$

The component at the modulation frequency ω_{exc} can be extracted by lock-in amplifier detection. For sufficiently small perturbations ($\delta\lambda_t \to 0$), it corresponds to the first term of the series ($n = 1$) since the contribution of higher order terms can be neglected. If the probe slowly scans across the resonance profile, the demodulated signal will be in the form:

$$S_{1\omega,PTS}(\lambda_p, \bar{\lambda}_{\text{res}}) = -\delta\lambda_t P(\lambda_p)\frac{\partial L}{\partial \lambda_{\text{res}}}\bigg|_{\bar{\lambda}_{\text{res}}} \tag{3.18}$$

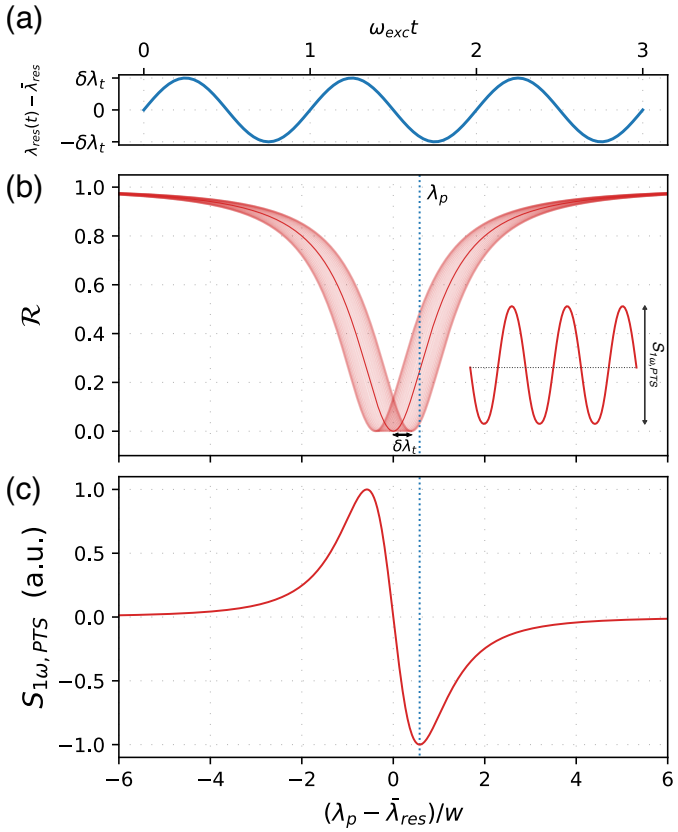

Figure 3.5: Description of the photothermal signal generation in ICAPS. The modulated resonance wavelength (λ_{res}) is detected as a change in reflected intensity. The amplitude of such intensity variation is retrieved upon lock-in amplifier demodulation and corresponds to the PTS signal. The amplitude and its sign depend on the probe wavelength detuning ($\lambda_p - \bar{\lambda}_{\text{res}}$). In dotted line, the probe wavelength at one IP is shown.

In Fig. 3.5, a representation of the photothermal signal generation is presented (assuming a constant $P(\lambda_p)$). The modulated resonance wavelength induces a periodic oscillation of the interferometric fringe, represented in panel (b) as a shaded area around the unperturbed fringe in solid line. The wavelength detuning $\lambda_p - \bar{\lambda}_{\text{res}}$ defines the sensitivity of the thermal transduction. The highest sensitivity is achieved at the IPs, also shown in figure: when the probe is tuned at $\lambda_p - \bar{\lambda}_{\text{res}} = \pm w/\sqrt{3}$, the PTS signal reaches its maximum amplitude. The sign of $S_{1\omega,PTS}$ reflects the phase-shift induced by the slope of the interferometric fringe. Conversely, out of resonance no PTS signal is measured.

3.2.1 Choice of the components

In this section a brief description of the components chosen to set up the ICAPS experiment is given.

3.2.1.1 Probe line for photothermal signal readout

The probe readout line represents a fundamental component of the ICAPS setup. The choice of the optical components starts with the selection of a probe wavelength. From

Eq. (3.13) it is clear that shorter wavelengths are beneficial due to the *compression* of the interferometric transfer function. A minor contribution comes from the dispersion of air refractive index, which increases towards shorter wavelengths.

In the visible and near-IR spectral region most of the necessary optoelectronic components are equally mature. However, fiber-based components are better performing in the telecommunication region. Due to the cost-effectiveness and the availability of fiber-integrated components, the NIR telecom region is the most used for probing applications, as discussed in Section 2.2.

Probe laser. A fundamental component is the probe laser. The first requirement is to ensure that the probe laser does not target any analyte absorption line or of any molecule present in the sample matrix. Secondly, it should be kept in mind that the FPI behaves as a frequency discriminator, meaning that perturbations in the probe's frequency or phase will be detected as a varying reflected intensity of the probe laser. Improving the finesse of the FPI in order to enhance the sensitivity of the system will inevitably enhance also the probe laser noise, keeping unchanged the system performance. In balanced approaches, the laser noise can be compensated via a reference arm, taking full advantage of the improved resonator quality. Several laser sources can be employed as a probe: diode lasers are possibly the cheapest option, and are effective in the way they can be swiftly tuned via bias current injection. However, typical linewidths are in the orders of MHz. Fiber-lasers, instead, offer several advantages at an increased cost: first, narrow-linewidth lasers can achieve linewidths below 1 kHz, meaning that better sensitivities can be attained; they can also be slowly temperature tuned over a larger spectral range compared to diode lasers. Finally, gas lasers such as HeNe sources can also be employed in interferometric approaches, but cannot be tuned in wavelength. Hence, while their application is possible in systems that can be actively compensated (such as the reference arm of a Mach-Zehnder), they are not as attractive in ICAPS, where the fixed mirror separation poses a strong limitation. In principle, temperature or pressure tuning of the cavity would be possible, but such parameters can also affect the PTS signal generation.

Air-spaced interferometer. The second essential component is the Fabry-Pérot interferometer. The requirements can be application sensitive, but the key points to consider are the following:

- **Mirror reflectivity**: defines the *reflectivity finesse*, hence the expected sharpness of the modes. Reflectivities on the order of 0.9 already provide an acceptable finesse of ~ 30. Higher values should be considered critically, as an improved sensitivity implies a reduced linearity.

- **Mirror separation**: the spacing between the mirrors also determines the sensitivity of the method. Having a larger separation compresses the interferometric fringes,

leading to sharper resonance modes. Another benefit of a denser transfer function is the number of accessible resonances, which improves the versatility of the system especially for the narrow tuning range of diode lasers. However, as the separation increases, parallelism errors are more critical and better collimation (e.g. wider beam) is needed. Thus, either larger spot sizes are achieved in the excitation volume, possibly reducing the transduction efficiency, or a worse collimation is chosen, which reduces the fringe visibility, with the same detrimental effect on the system sensitivity. Finally, depending on the application, sufficient space should be allowed for the focused pump laser to pass without touching the mirrors.

Other details should also be considered, especially the material for the spacers, the presence of a wedged optical substrate and deposition of anti-reflection coating on the outer surface. Ultra-low expansion glass (ULE) is a common choice for the spacers, as it provides an extremely stable mirror separation. Anti-reflection coatings and wedged substrates are also often employed to avoid parasitic fringes from reflection at the outer air-substrate interface.

Photodetector. The requirements on the photodetector are not strict, considering that typical optical powers reaching the photosensitive element are sufficient to saturate it. It is beneficial, to operate the system well-above the noise level of the detector, to minimize its influence on the system performance.

3.2.1.2 Excitation source

The choice of the excitation source is strictly dependent on the targeted analyte. The key points to consider for optimal operation are:

- **Line selection**: the selected line defines the strength of the absorption and the produced PTS signal.
- **Excitation power**: high pump powers allow for the generation of stronger thermal gradients. Hence, whenever possible, high power excitation sources are preferred.
- **Beam quality**: the quality of a Gaussian beam is often defined by using the M^2 value. Ideal Gaussian beams in the fundamental mode exhibit $M^2 = 1$, while the presence of higher order transverse modes causes beam degradation, such that $M^2 > 1$. The smallest beam spot by means of lens focusing is achieved for the fundamental mode. Thus, a degraded beam quality corresponds to larger beam spots, resulting in weaker thermal gradients.

3.3 Diode probe laser in ICAPS

In this work, a diode laser was chosen as probe for the ICAPS set-up which had been built within this thesis. Diode lasers are capable of swift wavelength tuning and are

therefore beneficial in applications where fast drifts of the cavity resonance are expected. The resonance wavelength equation provides a clear dependence upon the refractive index and the mirror separation. Both these quantities can be subjected to slow drifts. First, the refractive index has a dependency on the density which is affected by temperature and pressure, and the gas matrix composition. In a real-case application, the gas matrix composition varies as the analyte concentration is modified. Temperature drifts in the environment, that eventually affect the gas cell, are also common.

The system has to counteract those changes in order to keep ICAPS sensor at the inflection point of the resonance mode. For this purpose, locking schemes are employed to allow a continuous correction of the probe wavelength. Diode laser can be tuned via bias current adjustments, simplifying the requirements of the system.

Nevertheless, the inherent variable optical power with the diode current introduces a change in the system response, which has to be taken into consideration. In Fig. 3.6(a), the reflectance transfer function of the interferometer is portrayed. In the scenario of a diode laser coupled to the FPI (Fig. 3.6(b)), the sharpness of the interferometric fringes is influenced by the incident optical power (I_0). This effect is depicted by the light-blue curve which represents the change of reflected intensity with respect to the probe current (dI_R/di). The transduction efficiency of the system, as per Eq. (3.18), is thus affected by the incident intensity and has to be compensated accordingly. As a further complication, the light-current characteristic of the DL causes the IPs to fall at different reflected intensities, which for a Lorentzian shape would be equal to 1/4 of the incident intensity. This is not the case in the described scenario, where the variable optical power of the DL requires the a-priori knowledge of the incident intensity at the IP. This limitation could be circumvented by using a second photodetector that monitors the emitted intensity, at the expense of system simplicity. In some cases, the internal photodiode of diode laser packages can be exploited for such purpose. However, the assumption of an ideal Lorentzian curve does not quite correspond to reality.

An efficient method, investigated in this thesis, consists in a wavelength modulation approach of the probe laser to simultaneously normalize the PTS signal and for the development of a locking scheme to the IP of the interferometric fringe. Normalization and drift compensations ensure a stable readout during the time-frame of the experiment. The modulation of the wavelength can be achieved by current dithering of the DL, such that:

$$i(t) = \bar{\imath} + \delta i \sin(\omega_p t) \tag{3.19}$$

$$\lambda_p(t) = \bar{\lambda}_p + \delta\lambda_p \sin(\omega_p t + \psi) \tag{3.20}$$

where ω_p is the modulation frequency, $\bar{\imath}$ and $\bar{\lambda}_p = \lambda_p(\bar{\imath})$ are the offset current and wavelength, respectively, with modulation depths δi and $\delta\lambda_p$. The probe wavelength can be expressed as a generic polynomial of the current, obtained by spectral characterization of

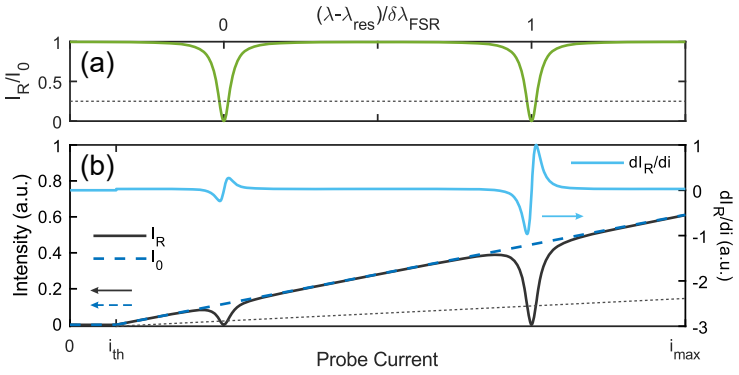

Figure 3.6: (a) Reflectance transfer function of the FPI showing two interference fringes separated by an FSR. (b) Reflected intensity (IR) for a diode probe laser coupled with the FPI, as a function of the injection current. The LI characteristic of the DL is defined by I_0. In light-blue the derivative of the reflected intensity with respect to the probe current (dI_R/di) is portrayed. Two sharp changes are observed in correspondence of the interferometric fringes. In (a) and (b) the gray dotted line represents $1/4$ of the incident intensity and its intersections with the interferometric fringe represent the locations of the IPs. Taken from [124].

the laser source. The modulation depth and current are connected by the tuning coefficient $\delta\lambda_p/\delta i|_{\bar{i}} = \eta(\bar{i})$, while ψ represents the phase delay between the current and the wavelength tuning. The phase delay depends on the laser characteristics and the applied modulation frequency. As the frequency decreases, the phase delay approaches zero [136], [137]. The use of modulation frequencies in the kHz range allows to assumption of a zero-phase delay ($\psi = 0$), which was also confirmed by lock-in detection (absence of a quadrature component signal).

In a similar way as presented for the generation of the photothermal signal (Eq. (3.18)), the system response to a modulated probe interrogation can be modelled. A Taylor expansion of the signal (Eq. (3.14)) around $\bar{\lambda}_p$, assuming a constant λ_{res} leads to:

$$S(\lambda_p(t), \lambda_{\text{res}}) = \sum_{n=0}^{\infty} \frac{1}{n!} [\delta\lambda_p \sin(\omega_p t)]^n \frac{\partial^n S}{\partial \lambda_p^n}\bigg|_{\bar{\lambda}_p} \tag{3.21}$$

Neglecting the higher order terms and demodulating at ω_p, the linear term will correspond to:

$$\begin{aligned} S_{1\omega,p}(\bar{\lambda}_p, \lambda_{\text{res}}) &= \delta\lambda_p \left[\frac{\partial P}{\partial \lambda_p}\bigg|_{\bar{\lambda}_p} [1-L] - P(\bar{i}) \frac{\partial L}{\partial \lambda_p}\bigg|_{\bar{\lambda}_p} \right] \\ &= \delta i \left[\kappa[1-L] - \eta(\bar{i}) P(\bar{i}) \frac{\partial L}{\partial \lambda_p}\bigg|_{\bar{\lambda}_p} \right] \end{aligned} \tag{3.22}$$

where the optical power has been expressed as $P(i) = \kappa(i - i_{th})$, being κ the slope efficiency [mW/mA] and i_{th} the threshold current.

Finally, considering the equality $\partial L/\partial\lambda_p = -\partial L/\partial\lambda_{\text{res}}$, for Lorentzian shaped profiles,

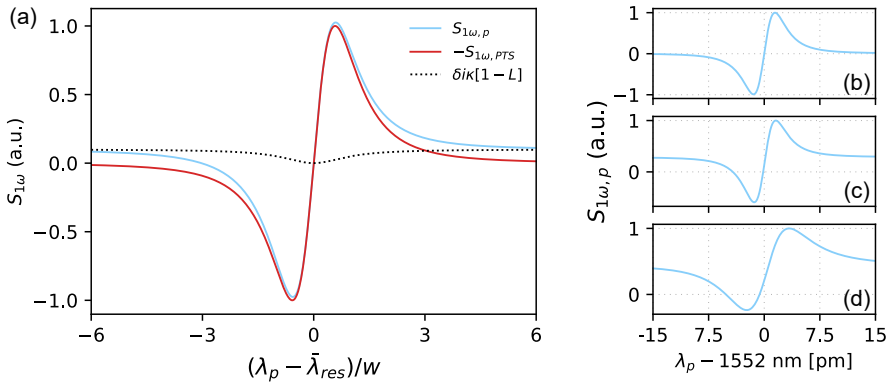

Figure 3.7: (a) Comparison of the transduction properties of the FPI for photothermal excitation ($S_{1\omega,PTS}$, red curve) and system response to probe interrogation ($S_{1\omega,p}$, blue curve) as a function of the probe wavelength detuning from the resonance wavelength in units of w. The scenario has been exaggerated to highlight the difference between the two quantities. In dotted line, the RAM contribution is portrayed. The PTS signal has been inverted for convenience (which practically is achieved by properly setting the lock-in phase). (b-d) Simulated shape of $S_{1\omega,p}$ for DL and cavity values used in this work: (b) $\kappa = 0.13$ mW/mA, $\eta = 3.5$ pm/mA, $P = 50$ mW, $w = 2.5$ pm, (c) $\kappa = 0.13$ mW/mA, $\eta = 1.8$ pm/mA, $P = 1.5$ mW, $w = 2.5$ pm, (d) $\kappa = 0.13$ mW/mA, $\eta = 1.8$ pm/mA, $P = 1.5$ mW, $w = 5$ pm.

one obtains the dependency of both the PTS and the probe interrogation signals as a function of the probe wavelength:

$$S_{1\omega,PTS}(\lambda_p) = \delta\lambda_t P(i)\frac{\partial L}{\partial \lambda_p} \tag{3.23}$$

$$S_{1\omega,p}(\lambda_p) = \underbrace{\delta i\kappa[1-L]}_{\text{RAM contribution}} - \underbrace{\delta i\eta(i)P(i)\frac{\partial L}{\partial \lambda_p}}_{\text{Cavity contribution}} \tag{3.24}$$

A comparison between these two quantities is presented in Fig. 3.7(a). The system response to probe interrogation (Eq. (3.24), presented in blue line) can be decomposed into the sum of two contributions. The first term on the right hand side of the equation, also shown as dotted black line in Fig. 3.7(a), represents a residual amplitude modulation (RAM) contribution of the probe laser, since the wavelength modulation causes an unwanted intensity modulation. The second term is the cavity contribution, which appears in a similar way also in Eq. (3.23). For high finesse cavities, the RAM contribution plays an almost-negligible role with respect to the cavity contribution. An example was given in Fig. 3.6(b), where the RAM contribution appears as a small offset on top of which the cavity contribution appears as sharp peaks.

Assuming typical values for the DL used in this work ($\kappa = 0.13$ mW/mA, $\eta = 3.5$ pm/mA, $P_{\max} = 50mW$) in combination with a resonance of $w = 2.5$ pm, offset values below 1% of the cavity contribution are obtained. If the laser is operated close to the threshold, where the optical power contribution is small compared to the RAM, the offset

can reach even 10% of the cavity contribution. Such scenarios are depicted in Fig. 3.7(b-d), where these parameters have been changed in relation to the cavity sharpness.

In this work, it is proposed to exploit the system response to probe interrogation as a normalization quantity. The aim is to remove any dependency associated to the cavity and the incident power of the probe source. By doing so, a normalized PTS signal is obtained:

$$S_{\text{norm-PTS}} = \frac{S_{1\omega,PTS}}{[S_{1\omega,p} - \delta i\kappa(1-L)]\eta^{-1}(i)} = -\frac{\delta\lambda_t}{\delta i} \tag{3.25}$$

During an experiment, the current modulation depth δi is kept constant, such that the normalized signal scales only with the thermal modulation depth $\delta\lambda_t$, which is absorption dependent. The change in the filling medium refractive index, mirror separation due to thermal expansion and quality of the interferometer (parallelism errors of the mirrors or aging of the dielectric coating) can affect the resonance frequency and/or interferometer performance (finesse). Both lead to a different readout of the photothermal signal, due to the varying optical power. Normalization to the bare optical power, however, does not take into account possible changes in the local slope of the interferometric fringe profile. In contrast, the proposed approach simultaneously compensates for both effects.

At the same time, demodulation at the second harmonic ($2\omega_p$) provides a direct indication of the IPs position through the zero-crossings, allowing for a tight lock of the probe laser to the IP. More details on the locking scheme and the normalization procedure are given in Section 3.5.

3.4 Experimental setup

The experimental setup for the used ICAPS system is presented in Fig. 3.8. As an analyte gas nitric oxide (NO) was selected. Nitric oxide plays a role in the formation of photochemical smog, and it has been recognized as a threatening toxic specie [138]. Nitric oxide is also involved in breath diagnostics, where it has been identified as a biomarker of asthma and inflammatory lung diseases [139]. A distributed feedback quantum cascade laser (DFB-QCL, AdTech Optics) was selected to target the R(6.5) doublet transition of NO falling at 1900.07 cm^{-1}. The QCL was driven through a current driver (Wavelength Electronics, QCL1000), and a sinusoidal dithering was added for performing 2f-WMS. The QCL was temperature stabilized by two thermoelectric coolers (TEC) made of Peltier elements. The beam was focused inside the mirrors of the interferometer by a 50 mm CaF_2 lens. The pump excitation frequency was optimized for $f_{exc} = 312$ Hz, with a modulation depth $\delta\bar{\nu}_{exc} \approx 0.23$ cm^{-1} at a working pressure of 900 mbar, consistent with the operative conditions presented in [111].

The probe readout line was based on polarization maintaining optical fibers in the telecom (1550 nm) region for higher stability. A near-IR fiber-coupled diode laser (Emcore, 1728B-NM-050-31-FC-PM) emitting at 1552 nm was used as probe laser. A low-noise DL

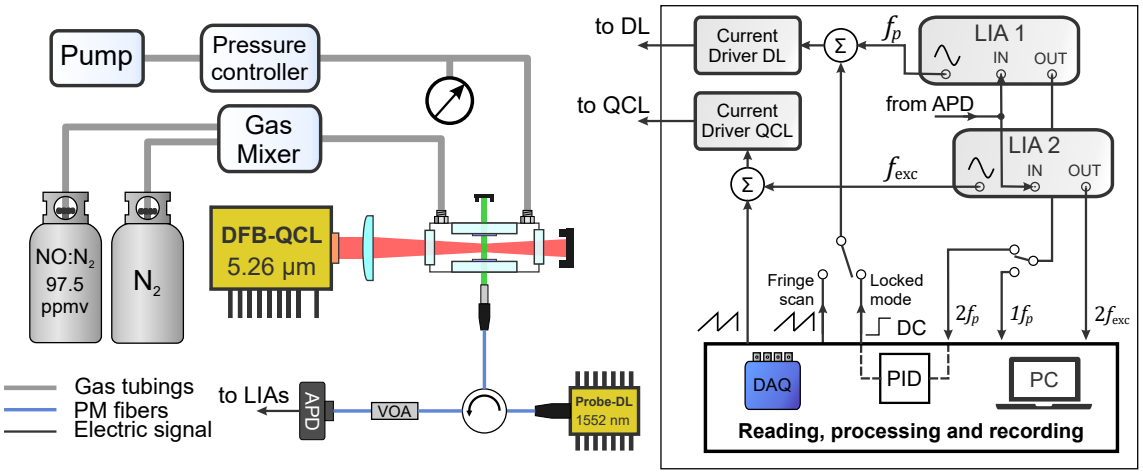

Figure 3.8: Schematic of the experimental setup for an ICAPS measurement. The data acquisition and processing tab comprehends a DAQ system with input/output cards for data recording and processing. Adapted from [124].

Figure 3.9: Picture of the ICAPS gas-cell used in this work, hosting the interferometer.

controller (Koheron, CTK101-B-400) was used for temperature and bias current control. The DL was modulated at a frequency $f_p = 6$ kHz and was selected not to overlap with the excitation frequency. The probe laser was collimated onto the FPI via a fiber-coupled GRIN collimator. The back-reflected intensity was collected by the GRIN-lens and directed by means of an optical circulator (Thorlabs, CIR1550PM-APC) onto an amplified photodetector (APD) (Thorlabs, PDA10CS2). The detector signal was fed to two lock-in amplifiers (Stanford Research Instrument, SR-860). The optical circulator serves also as an optical isolator to reduce optical feedback to the DL. A variable optical attenuator (VOA) was inserted between the circulator and the APD to avoid detector saturation. LIA-1 was used to retrieve the cavity response to probe interrogation, by demodulating at the n-th harmonic of f_p: demodulation at the first harmonic provides $S_{1\omega,p}$, while demodulation at the second harmonic was used for locking purposes. LIA-2 was used to retrieve the PTS signal, demodulating at $2f_{exc}$ to retrieve the 2f-ICAPS signal (which corresponds to $S_{1\omega,PTS}$).

The gas cell was equipped with inlet and outlet connectors to allow flushing of the

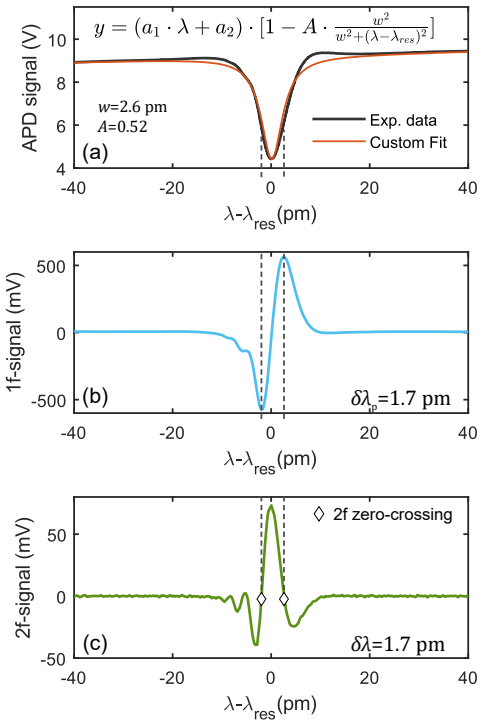

Figure 3.10: (a) Recorded Fabry-Pérot reflection profile obtained via a scan of the probe current and fitting of the observed profile. (b-c) First and second harmonic signal of the system response to probe interrogation: probe current is slowly scanned and sinusoidally modulated with a small modulation depth of $\delta\lambda_p = 1.7$ pm. The zero-crossings coincidence with the IPs position is depicted by the gray-dotted vertical lines. Data published in [124].

target analyte. A certified cylinder with a concentration of 97.5 ppmv (AirLiquide) was used and combined in a gas mixing station with pure nitrogen (N2 5.0) for the preparation of dilutions. A pressure gauge (Keller, LEO 3) and a pressure controller (MKS, 640B) were used to monitor and keep a constant pressure inside the gas cell, while a mini-diaphragm vacuum pump (KNF, N84.3ANDC) was used to allow gas exchange within the gas cell.

The Fabry-Pérot interferometer was installed in a custom-made aluminium gas-cell via a vacuum epoxy, to achieve tight sealing of the gas-cell. The reflectivity of the mirrors was $R = 0.989$, leading to an approximate reflectivity finesse of 280. The spacing of the interferometer was 2 mm, to allow a more versatile tuning between multiple interference fringes. The FPI is constituted by dielectric coatings grown on top of two fused silica substrates, glued together via ultra-lowexpansion glass spacers. The gas cell was temperature stabilized by a Peltier element to improve the interferometer stability.

The reflection profile of the FPI was investigated by tuning the laser across the interferometric fringe in a 20 mA range, corresponding to roughly 80 pm in wavelength, as shown in Fig. 3.10(a). The fringe appears on top of a linear background, arising from the light-current characteristic of the DL, and exhibits a slight asymmetry most likely due to the not-ideal collimation of the laser source in combination with the large FPI spacing.

The experimental data were fitted with a custom function: the linear background parameters (a_1, a_2) were obtained in a separate fitting procedure, excluding the fringe data-points. The Lorentzian parameters resulted in a fringe visibility of $A = 0.52$ and $w = 2.6$ pm. From an FSR = 0.6 nm, an effective Lorentzian finesse of 115 was obtained.

The first and second harmonic signals were obtained upon demodulation at $1f_p$ and $2f_p$. A modulation depth of $\delta\lambda_p = 1.7$ pm ($\delta i = 0.42$ mA) was used, which corresponds to a modulation index $m = \delta\lambda_p/w \approx 0.65$. The small modulation index ensures rejection of the influence of higher-order terms. The distortions of the resonance mode are quite evident in the experimental data and they are observed as shoulders on the low-current tail of the first harmonic signal, or additional lobes in the second harmonic signal. A RAM contribution is observed, which provides an off-resonance offset on the order of 1% of the measured peak value.

The second harmonic signal corresponds to the derivative of the first harmonic, and thus its zero-crossing correspond to the inflection points, as portrayed by the diamonds in Fig. 3.10.

3.5 Locking and normalization schemes

3.5.1 2f-zero crossing locking

The active stabilization of the probe to the fringe IP is fundamental to achieve a stable photothermal signal. The tuning of λ_p can be performed by current or temperature tuning. For real-scenario applications a fast tuning is preferred for a tight lock. In this regard, current tuning appears to be more suitable than temperature tuning [140]. In Fig. 3.11, the key components and the procedural steps of the 2f-zero crossing locking scheme are addressed:

1. The probe laser is dithered and tuned in the proximity of the resonance profile;
2. The photodetector signal is fed to the LIA, which demodulates at $2f_p$;
3. The LIA output signal is used as an error signal for a PID loop. A zero-setpoint is chosen for the PID, which adjusts the probe current to match the zero-crossing.

High-finesse cavities provide an enhanced sensitivity, but they are more susceptible to external noise sources. From Fig. 3.10(c), a locking range of roughly 10 pm can be obtained by the $2f_p$-signal spanning from the first IP to the end of the negative high-wavelength lobe. If the probe is tuned to the second IP, a sudden variation in the mirror separation of $\delta d = 6$ nm is sufficient to shift the resonance mode out of the locking range. Thermal or pressure stresses applied to the interferometer might cause such variation, especially in the case of an interferometer integrated in the cell housing.

For a stable locking procedure, the noise-content in the process variable must be as low as possible. As per Eq. (3.21), the peak value of the 2f-signal scales as $\delta\lambda_p^2$, suggesting that

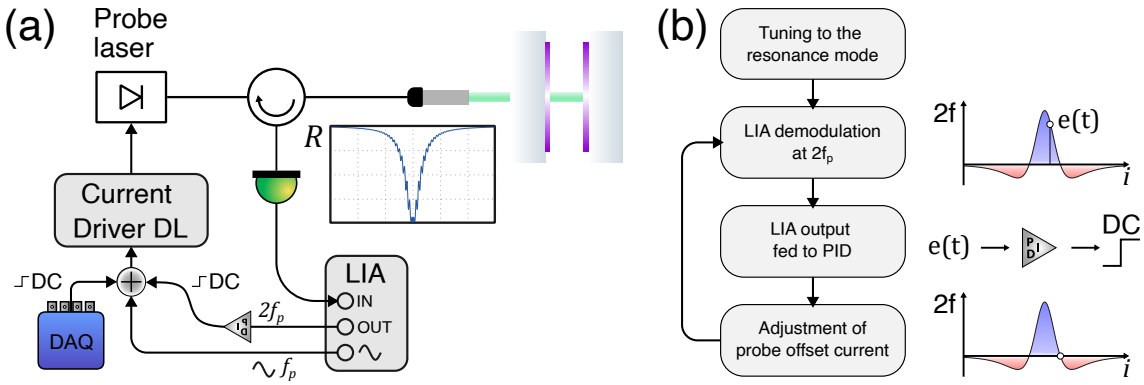

Figure 3.11: (a) Schematic of the components involved in the locking procedure. (b) Diagram of the locking steps: at first, the laser is tuned in proximity of the resonance; the second harmonic signal is used as an error signal for a PID loop, which adjusts the DC-offset of the probe current. By choosing a zero setpoint, the probe is locked to one IP.

huge modulation depths are beneficial. However, there are several limitations to consider. First, such equation is valid in the low modulation index approximation: any further increase (above $m \approx 2.2$) will result in peak signal saturation, while broadening appears even for smaller m-values. The consequence of the profile broadening is also a shift between the *true* IP positions and the zero-crossings of the 2f-profile. Fig. 3.12 summarizes this information: in panel (a), both the broadening and the peak-value scaling (in the inset) with the modulation inset m are portrayed, while panel (b) showcases the zero-crossing deviations from the ideal IP position ($w/\sqrt{3}$).

The most important limitation in the choice of the probe modulation depth is its influence on the PTS signal. The model presented so far in Eqs. (3.23) and (3.24), considered the two separated effects for probe modulation and resonance wavelength modulation. However, in a real ICAPS experiment, these two quantities change simultaneously, such

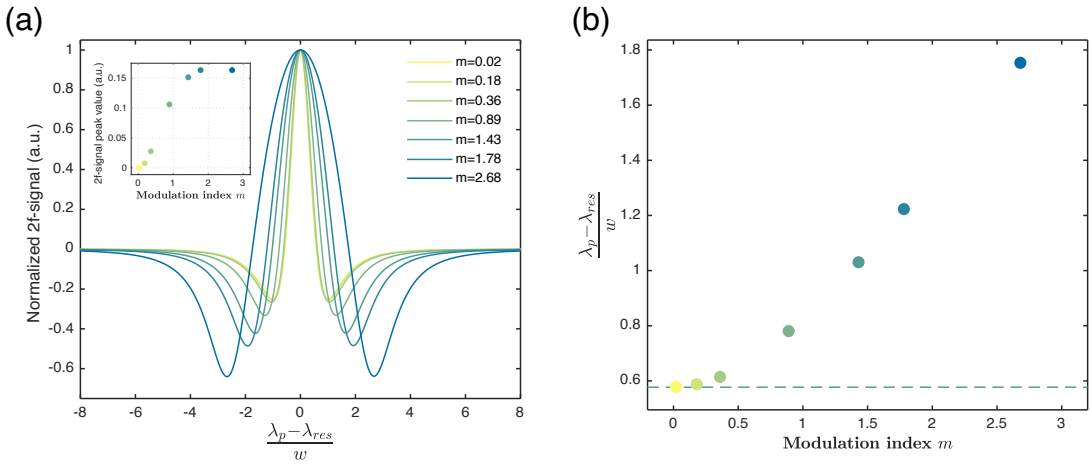

Figure 3.12: (a) Simulation of a 2nd harmonic demodulated signal, by scanning an ideal Lorentzian profile with an increasing modulation index. (b) Shift of the inflection points as an effect of modulation broadening. Dotted line corresponds to the ideal position of the inflection point.

that in theory a mutual influence is to be expected. Usually, the photothermal modulation depths ($\delta\lambda_t$) are much smaller than the probe modulation depths. Hence, the latter have to be kept sufficiently small in order to avoid any interference with the PTS signal. The lower limit is defined by the presence of parasitic interference fringes, which arise from unwanted reflection at the FPI outer surface or any other reflective surface along the probe optical beam path. In this work, modulation indexes $m \approx 0.15$ were sufficient to achieve stable locking. During the ICAPS experiments, the system was locked to the second inflection point since it offered a wider locking-range.

The locking scheme was implemented by feeding the APD signal to LIA-1 and demodulating at $2f_p$. For practical reasons, it is important to keep the time constant of the LIA (ideally below 100 ms) small, to reduce the lag of the demodulated signal employed in the PID-loop. The LIA-1 output was recorded via an input DAQ, and processed in a LabVIEW based PID controller. The PID update rate was kept low (few Hz) in order not to compensate for the photothermal signal. The PID output was sent to the modulation input of the laser driver with an output DAQ, regulating the DC-offset of the probe current to bring the $2f_p$-signal to the zero-crossing.

3.5.2 Normalization procedure

The normalization of the photothermal signal, requires the knowledge of the quantity $[S_{1\omega,p} - \delta i\kappa(1-L)]\eta^{-1}(i)$. The current tuning coefficient ($\eta(i)$) can be obtained via a spectral characterization of the probe laser, which was performed via an FT-IR spectrometer. For the employed DL, as presented in Fig. 3.13, a quadratic polynomial was sufficient to describe the wavelength dependency on the injection current. The quadratic dependency corresponds to a linear behaviour of the current tuning coefficient. Over the full tuning range of the laser source, a wavelength tuning of 1 nm could be achieved at a fixed temperature, with current tuning coefficients ranging between 1.8 to 4 pm/mA.

The RAM contribution in Eq. (3.24) consists of a constant quantity ($\delta i\kappa$) and a detuning-dependent factor ($\delta i\kappa L$). For an ideal interferometric fringe, the last term ranges between 0 (off-resonance) and $\delta i\kappa$ (on-resonance, assuming $A = 1$). Hence, the error that one commits by neglecting the detuning-dependent term is at most $\delta i\kappa$, which as shown before is only a small percentage of the 1f-peak signal. Neglecting this term benefits system simplicity. The quantity $\delta i\kappa$ corresponds to the offset of $S_{1\omega,p}$ and can be obtained with a preliminary analysis. The quantity $[S_{1\omega,p} - \delta i\kappa]\eta^{-1}(i)$ was used as a normalization factor.

Since LIA-1 is used for demodulation at $2f_p$ and does not allow for multiple harmonics demodulation, $S_{1\omega,p}$ was obtained by the DAQ-system via an FFT-analysis of the APD signal performed by the LabView program.

To demonstrate the capability of the sensor to operate in widely distinct operative conditions, the probe current was tuned across one cavity FSR: two fringes were accessible,

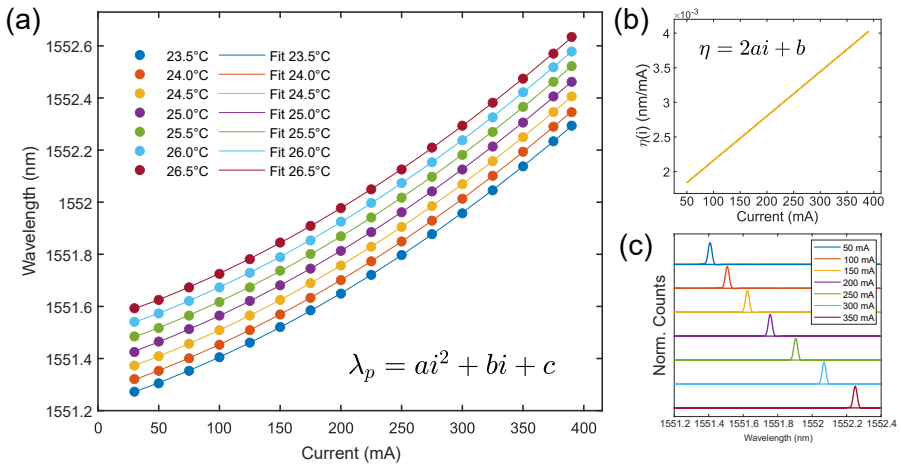

Figure 3.13: FT-IR characterization of the probe laser via a Bruker-Vertex 80v with a spectral resolution of 0.08 cm-1 (19 pm). (a) Emission peak wavelength as a function of injection current for several working temperatures and parabolic fitting (2^{nd} order polynomial) of the experimental data. (b) Current tuning coefficient for the representative temperature of 24.5 °C, obtained from the fitting parameters of panel (a). (c) FT-IR spectra of probe emission for several injection currents at 24.5 °C. Data published in [124].

falling - in the specific conditions - at 108 and 318 mA. Each cavity resonance was scanned by applying a triangular ramp (mHz) to the probe laser current, upon which a sinusoidal modulation was superimposed ($m \approx 0.15$), at a constant laser temperature of 24.5 °C. The probe current modulation depth was chosen not to affect the photothermal readout, and fixed for the whole duration of the experiment. The excitation laser was operated as described in Section 3.4 ($f_{exc} = 312$ Hz and $\delta\bar{\nu}_{exc} \approx 0.23$ cm^{-1}) and its wavelength was tuned to the absorption peak of the NO transition. In this way, a constant PTS excitation at $2f_{exc}$ was generated in the cavity. The gas cell was continuously flushed with a certified concentration of 97.5 ppmv of NO in N_2 at a pressure of 900 mbar. Since the probe was scanned across the cavity mode, LIA-1 was used to demodulate the APD at $1f_p$ (giving $S_{1\omega,p}$), while LIA-2 demodulated the same signal at $2f_{exc}$ (giving $S_{1\omega,PTS}$).

The results of such study are shown in Fig. 3.14. The red curves correspond to the PTS signals, while the blue curves depict the cavity response to probe interrogation after offset removal, in panel (a), and correction with the tuning coefficient, in panel (b). The y-axes scales were chosen to allow a visual overlap of the high-current fringe curves. The trend of the two curves follows the predicted behaviour, demonstrating that the photothermal transduction efficiency follows the interferometric fringe steepness. The only deviation is observed for the left-wing shoulders, possibly due to the non-Lorentzian shape of the resonance profile. Nevertheless, this discrepancy can be neglected since during an ICAPS experiment, the probe laser is tuned to one IP, or, in other words, to the maximum or minimum of the curves. In panel (a) an evident mismatch between the low-current fringe curves can be recognized. It arises from the smaller $\delta\lambda_p$ of lower operating currents, as an

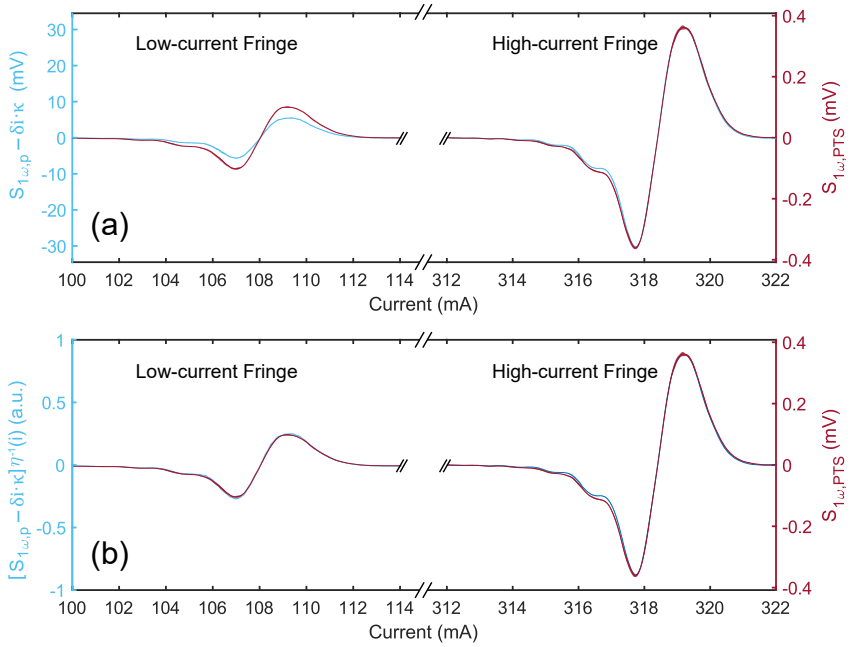

Figure 3.14: In red, the PTS signal as the probe wavelength is scanned across two interferometric fringes via current tuning. In blue, $S_{1\omega,p}$ after (a) offset removal and (b) offset removal and correction via current tuning coefficient. The scaling of the y-axes was chosen to provide a graphical overlap of the high-current fringe curves. The overlap of the two curves in (b) demonstrates that the transduction of the photothermal signal follows the local steepness of the interferometric fringe, as proposed in the theoretical model. Moreover, it proves that the corrected $S_{1\omega,p}$ can be used for normalization purposes. Data published in [124].

effect of the variable current tuning coefficient. The different width (in current units) of the two resonances is a further proof.

The normalization scheme was tested in a real measurement scenario, by actively locking the probe laser to the high-wavelength IP of the two resonances. The locking scheme was applied by retrieving the $2f_p$-signal from LIA-1, while the $1f_p$-signal was obtained by FFT-analysis of the APD-signal as formerly described. The same setup configuration was used, keeping the QCL tuned to the absorption peak.

The raw-2f-WM ICAPS signal is shown together with the normalization quantity $[S_{1\omega,p} - \delta i\kappa]\eta^{-1}(i)$ for the two operative currents in Fig. 3.15(a). The signals in the two scenarios differ by a factor of 3, as a consequence of the different optical power. As shown in Fig. 3.15(b), after normalization the two signals are excellently restored to the same level, removing the dependency of the varying system responsivity. Finally, it is worth noticing that the 1σ noise of the normalized data is comparable for both scenarios. This result indicates that the system's noise is limited by the probe laser's frequency noise and/or by environmental noise since both noise sources by nature are proportionally enhanced by the interferometer as the PTS signal.

The instabilities of the signal for the low-current fringe scenario can be related to the

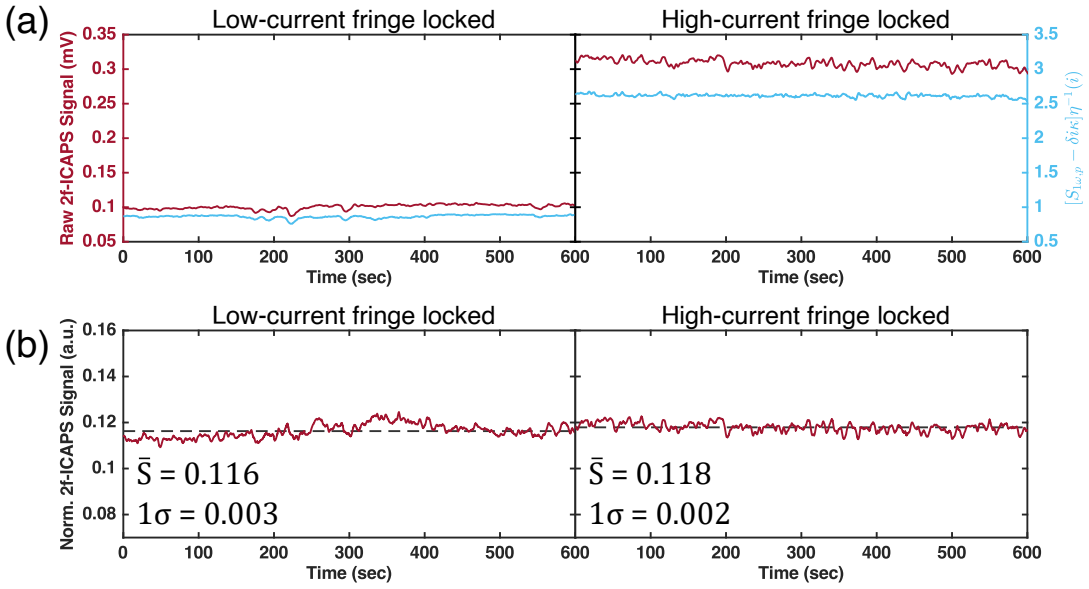

Figure 3.15: (a) Raw 2f-WM ICAPS signal (red curve) together with the normalization factor (blue curve), recorded at the high-current IP for two operative currents of 108 and 318 mA with a fixed concentration of 97.5 ppmv of NO:N_2. The ratio between the red and blue curves provides the normalized 2f-ICAPS signal presented in panel (b). Data published in [124].

noisier cavity signals, which result in lower SNR of the process variable for the PID-locking loop. On the other hand, the drifts observed in the high-current fringe are efficiently compensated by the normalization factor.

3.6 Sensor calibration and limits of detection

The sensor was calibrated for the detection of NO in a concentration range spanning from pure nitrogen up to the certified concentration of 97.5 ppmv NO:N2. The ICAPS measurements were performed by locking the probe laser at the high-current IP. At the same time, a slow triangular ramp (3 mHz) was applied to the QCL injection current to scan its wavelength across the NO absorption line. The APD signal was demodulated by LIA-2 at $2f_{exc}$ to provide the 2f-WM-ICAPS signal, with a time constant of 1 s, corresponding to an equivalent noise bandwidth (ENBW) of $\Delta f_{\mathrm{ENBW}} = 78$ mHz. In Fig. 3.16(a), the spectral scan of the absorption line is shown for several NO concentrations and is compared to the system noise (N_2 only). The low-current tail of the 2f-curve overlaps with a neighboring NO absorption line, falling at 1900.51 cm^{-1} of lower linestrength and depicted in panel (b). Fig. 3.16(c) shows the calibration line of the developed ICAPS sensor. Each datapoint and its error-bars shown in the graph were obtained by mean and standard deviation of four peak values. The standard-deviation of the peaks proved to be comparable with the 1σ sensor noise (recorded for pure N_2), equal to 3.1 µV. The datapoints were fitted with a linear function, providing the calibration line of the sensor. The sensitivity (β) was obtained by the slope of the calibration curve $\beta = 1.4$ µV/ppmv.

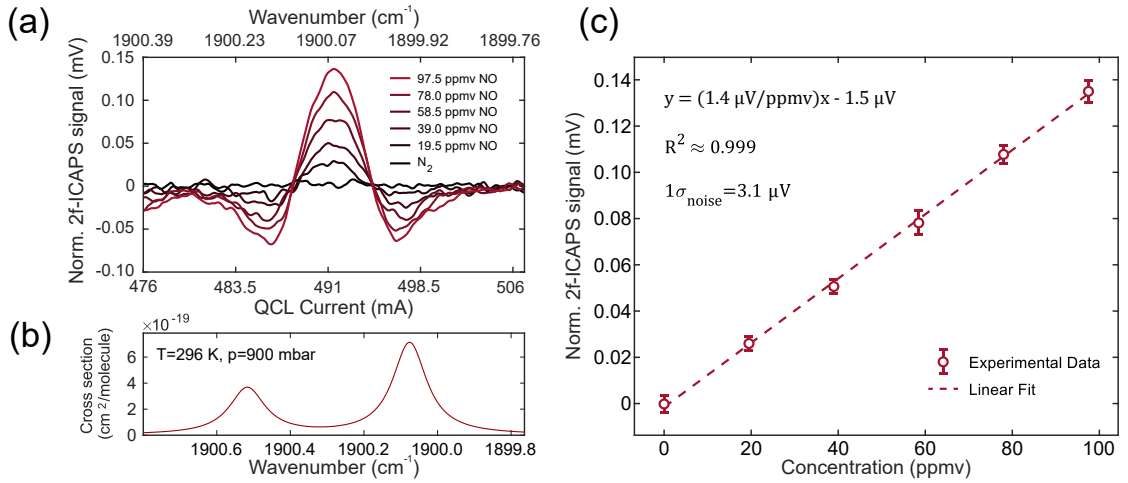

Figure 3.16: (a) Spectral scan of the NO absorption line acquired with a time constant of 1 sec. (b) Simulation from HITRAN database of NO absorption cross section at 900 mbar and 296 K. (c) Calibration line of the NO 2f-ICAPS sensor, obtained as linear fitting of the experimental datapoints. Each datapoint is obtained by averaging four peak values. The normalized signal was scaled back to the amplitude of the 97.5 ppmv peak signal. Data published in [124].

The coefficient of determination ($R^2 \approx 0.999$) proved an excellent linearity over a concentration range of two orders of magnitude. The finesse of the interferometer did not limit the linearity of the sensor. Indeed, the maximum concentration induces a phase shift as little as $\sim 10^{-5}$ rad (as a comparison, the fringe FWHM corresponds to 0.05 rad). At higher concentrations, deviation from linearity would be expected as an effect of direct absorption, i.e. the reduction of the available optical power within the gas cell.

From the sensitivity and the 1σ noise, a NEC (as defined per Eq. (1.42)) of 2 ppmv was achieved, with an ENBW of 78 mHz and an optical excitation power of $\sim$ 30 mW. From the absorption cross-section at 900 mbar ($\sigma_\nu = 7 \cdot 10^{-19}$ cm^2/molecule) calculated by the HITRAN database [18], an $\alpha_{\min} = 3.1 \cdot 10^{-5}$ cm^{-1} and a NNEA $= 3.3 \cdot 10^{-6}$ W cm^{-1} Hz$^{-1/2}$ were obtained, which are comparable to the performance of PTS sensors with similar architectures [97], [111].

3.7 Conclusions

An ICAPS system was developed in combination with a diode laser as a probe. The use of a DL enables fast wavelength tuning to compensate for sensors drifts. However, the inherent intensity modulation that comes with the wavelength tuning results in a changing system responsivity, which has to be compensated for stable operational conditions. The compensation of drifts and system responsivity were both addressed with novel locking and normalization schemes, based on wavelength modulation of the diode laser.

A theoretical model for the photothermal transduction efficiency as a function of the probe detuning from the FP interferometric fringe was proposed. The experimental results

were in excellent agreement with the developed model, proving that the PTS signal follows the enhancement factor provided by the local steepness of the interferometric fringe.

The system was tested in the full current operative range of the probe laser. The recovered PTS signal was correctly scaled back to the same normalized value. This development is crucial for continuous trace gas monitoring using the ICAPS technique together with a probe diode laser. Nevertheless, this method requires the knowledge of the spectral characteristics of the probe laser since the system responsivity is affected by its current tuning coefficient. In this regard, a probe with a linear current tuning characteristic would greatly simplify the normalization process and would not require the constant recording of the probe current, as it was the case for this work.

The system was calibrated for NO detection, and a detection limit of 2 ppmv was achieved with an ENBW of $\Delta f_{\mathrm{ENBW}} = 78$ mHz and an excitation optical power of 30 mW, corresponding to a NNEA of $3.3 \cdot 10^{-6}$ W cm^{-1}Hz$^{-1/2}$. It should be addressed that the figure of merits achieved in this work are far from state of the art. Improvements in detection limit can be achieved by lowering the noise level, e.g. by balanced detection as discussed in [122], [123].

Significant improvements can be achieved by employing a stable resonator, such as spherical mirror cavities. In this case, the stringent requirements of the parallel planes resonator - on the edge of the stability region - are relaxed by the curved mirrors. If system linearity is not a limiting factor, considerably higher finesse values can be achieved with such resonators, while shaping the probe size to smaller beam spots, which is beneficial for the probing of focused excitation beams.

Chapter 4

Long-wavelength Quantum Cascade Lasers

A practical application of quantum cascade lasers was presented in the previous chapter. This chapter will provide an overview of the current state of QCL technology, along with an introduction on the basic principles of these peculiar laser sources.

Historically, the founding principle of QCLs was proposed by Kazarinov and Suris in 1971 [141], who advanced the possibility of achieving gain in *intersubband transitions*. Intersubband transitions take place in periodic structures obtained by repetition of quantum wells and barriers. However, the structure described by Kazarinov and Suris was lacking the *injector* region, which is essential for the operation of quantum cascade lasers. It was only 20 years later, in 1994, that Faist et al. [142] presented the first QCL emitting at 4.6 µm. Few years after, room-temperature (RT) pulsed operation as well as cw-operation at cryogenic temperature were achieved by the same group [143], [144]. The first cw-operation at RT was reported 8 years later [145]. In 2002, a new type of QC devices allowed to explore the terahertz region [146], where numerous applications in imaging and molecular sensing are addressed. In 2004, high-power devices emitting up to 1 W of average power were demonstrated by Evans et al. [147], [148], which opened the route for high-sensitivity optical sensors and wireless communications based on mid-IR radiation.

Many other fundamental breakthrough have been achieved in the last decades comprising:

- **single mode emission**, achieved soon after QCL invention, in 1997 [149], where a first order Bragg grating was used for the selection of the longitudinal mode;
- **external cavity operation** [150], [151], which offers a wide tunability range and is particularly well suited for biological or liquid-phase analysis, where large amide bands can be targeted [152];
- **frequency-comb operation**, first demonstrated in 2012 [47], as discussed in Section 1.6.1.5. Active research is still undergoing in this field, comprising development

of new cavity geometries, such as ring lasers [153] or egg-shaped lasers [154] and methods to achieve stable [155], [156] and spectrally extended comb operation.

- **vertical cavity emission**, is also an important development for low-power consumption devices and high-scalability contexts [157]. Surface emission can be achieved in multiple ways: the most common include second-order Bragg gratings [158], or photonic crystal lasers [159].

The flexibility of the active region designs allowed covering wide spectral ranges with the same material systems. The most impressive results have been achieved for the InGaAs/AlGaAs/InP QCLs, with wall-plug efficiency as high as 27% in pulsed mode and 21% in cw operation [160].

Even though excellent performance was demonstrated, reliable cw-operation at RT is still a technological challenge due to the high threshold power densities which induce self-heating of the devices. Threshold current densities of the best lasers are of the order of 1.5 kA/cm^2. Considering the typical operation voltage, that easily reaches 10 V, standard devices should dissipate tenths of Watts of thermal power. Hence, the heat-extraction capabilities still play a fundamental role in the efficiency of cw-operated sources. In many cases, buried heterostructures obtained by lateral epitaxial regrowth of the semiconductor material helps considerably in removing the excess heat. However, the regrown layer should be highly insulating to avoid current leakage or even device shorting.

The long-wavelength ($\lambda > 10$ µm) region was also explored relatively early, pushing the boundaries of QCL emission up to 19 µm [161]–[163]. At TU Wien [164], emissions up to 23 µm were achieved. However, these initial demonstrations required pulsed operation and cryogenic temperatures, due to the high threshold-current densities. The low optical powers combined with the need of cryogenic cooling, prohibited the use of long-wavelength QCLs for practical applications. The main challenges of long-wavelength devices are briefly described in Section 4.2.

A breakthrough in the development of long-wavelength devices was made at University of Montpellier, where InAs-based technology (also known as antimonide lasers, or Sb-based lasers, due to the common name of semiconductors with a lattice constant compatible with growth on a GaSb substrate and AlSb barriers), allows achieving higher material gain and consequently lower thresholds. The first InAs/AlSb devices emitted around 20 µm [165] and featured threshold current densities of 1.6 kA/cm^2 at 80K. An important development was made by changing the waveguiding approach, from the double metal to dielectric design, which strongly decreased the cavity losses [166]. Single mode emission has been achieved at 17.8 µm, with heat sink temperatures as high as 333K in pulsed mode. Reduction of the doping levels profoundly contributed to diminish the threshold current density at RT [167], bringing it down to 0.73 kA/cm^2 for 3.6 mm-long devices in pulsed operation at RT. CW-operation was also demonstrated in epi-side down mounting up to 20°C near 15.1 µm. The cw regime at RT has been achieved in InAs-based QCLs

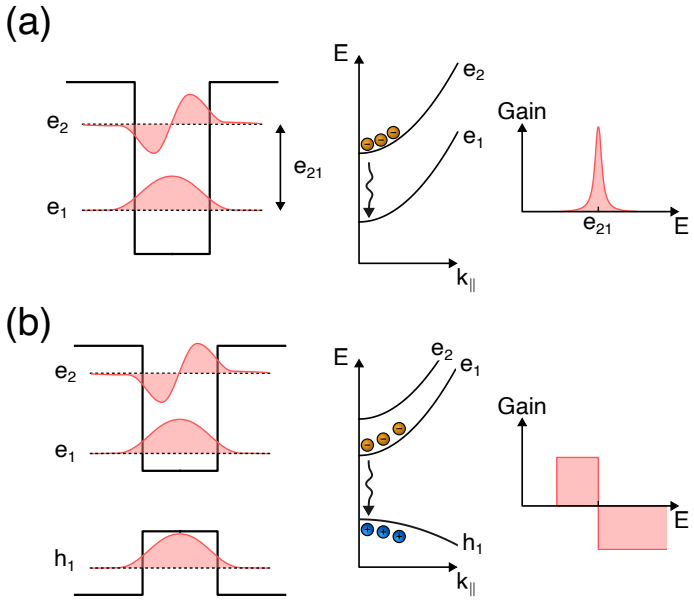

Figure 4.1: Comparison between (a) intersubband and (b) interband transitions. Intersubband transitions occur between confined states in the conduction band, which leads to a narrow gain spectrum. In interband transtions, radiative emission occurs upon recombination of electrons at the bottom of the conduction band and holes in the valence band. The gain medium is transparent below the transition energy, while it becomes lossy on the high-energy side.

at wavelengths up to 17.8 µm [168]. Threshold current density as low as 0.6 kA/cm^2 at 300 K has been recently demonstrated for a 14 µm QCL [169].

The unprecedented performance of antimonide lasers paved the way for optical sensing in the long-wavelength IR, which plays a pivotal role for the detection of BTEX compounds (benzene, toluene, ethylbenzene and xylene). BTEX are representative of the larger class of volatile organic compounds (VOCs) and are used for monitoring air quality in urban areas. High optical power and good beam quality are pre-requisites for optimal performance in sensing systems especially for indirect detection schemes such as photoacoustic and photothermal spectroscopies. The inherent low photon energy of LW radiation limits the optical power output. Several approaches can be used to improve the output power, while preserving the beam quality. Among them, the MOPA (Master Oscillator Power Amplifier) and the tapered laser, have the benefit of increasing the available active volume of the device operating in the fundamental spatial mode, which ensures excellent beam quality. The latter was subject of this work.

4.1 Fundamentals of Quantum Cascade Lasers

Unlike semiconductor diode lasers which rely on interband transitions, quantum cascade lasers exploit intersubband transitions. The scenario is depicted in Fig. 4.1. In a diode laser, the recombination between electrons in the conduction band and holes in the valence band leads to radiative emission, such that the energy of this transition is mainly

defined by the energy gap of the employed material. The resulting gain spectrum is broad as a result of the occupancy of the valence and conduction bands defined by the respective quasi-Fermi levels. The active medium is transparent only on the low-energy side of the gain spectrum and becomes absorptive on the high-energy side. On the other hand, intersubband transitions occur for electrons confined in discrete states within the conduction band. The transition energy is defined by the distance between the electronic states (e2, e1) which can be tailored by modifying the thickness of the quantum well. Another fundamental feature of intersubband transitions is the resulting gain spectrum. The same curvature of the subbands in the confinement plane ($k_{\|}$) leads to very narrow transitions, transparent on both sides of the spectrum. The highest achievable photon energy is ultimately set by the band discontinuity of the materials employed for the quantum wells and barriers.

Since they rely on electronic transitions, QC lasers are *unipolar* devices. The second difference with other semiconductor lasers is their cascaded scheme. The QCL active region contains at least three energy levels required to generate optical gain. The electrons injected in the upper lasing state (e3) emit a photon through a transition to the lower lasing state (e2). The lower lasing state should be quickly depopulated, which can be provided, for instance, by fast scattering to the lowest level involving longitudinal optical (LO) phonons.

The structure described in [141] was missing a fundamental component of modern QC lasers, which is an injector required to transfer electrons from one active region to the next period of the device. The electron transport and injection in the next upper lasing state is achieved by resonant tunneling of electrons. A portion of the injection region is doped to avoid formation of space-charge domains and serves as a reservoir which provides electrons necessary for the device operation. The injector and the active region constitute the building-block of the cascade laser, which is finally obtained via repetition of this unit. Usually, the number of stages N may vary between 10 and 100. Each electron injected is capable of emitting N photons, leading to quantum efficiencies $\eta \gg 1$.

4.1.1 Population inversion condition in QC lasers

The key condition to obtain lasing is the population inversion in the lasing transition. It is useful to draw some general conclusion by considering the simplified system of an active zone composed by 3 energy levels, even though more complex structures such as minibands can be employed. A schematic of the process is presented in Fig. 4.2.

The electrons are injected into the level $n = 3$, while the lasing occurs between levels $n = 3$ and $n = 2$. The injector is assumed to be at a constant population with sheet doping density n_g, aligned with the upper level of the next active region. Assuming a current density J, the electrons will be injected with a rate equal to $\eta_i J/e$, with η_i being the injection efficiency. Scattering processes can induce a transition towards state 2 or 1,

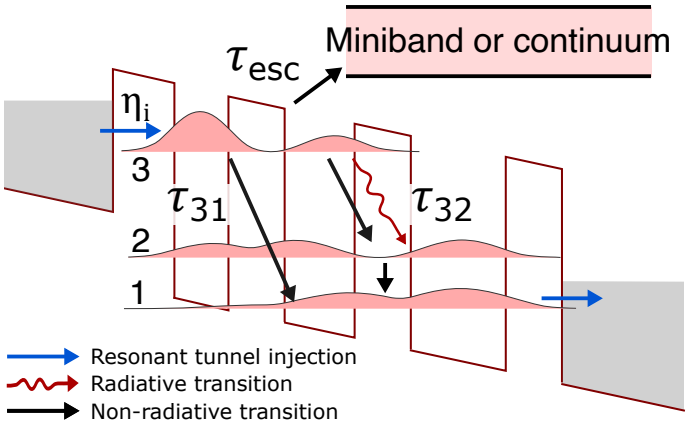

Figure 4.2: Simplified schematic of the processes occurring in the QC active region. Electrons are injected from the injector state into the level $n = 3$. The electrons can follow several paths, such as radiative or non-radiative transition to the level $n = 2$, escape to the continuum or upper energy miniband, or transition towards level $n = 1$. The fast depopulation of the lower lasing state is often provided by the LO-phonon resonance. Finally, the electrons move from level $n = 1$ into the next injector region.

with lifetimes τ_{32},τ_{31}, or can escape to the continuum with a lifetime τ_{esc}. The deactivation rate can be expressed as the sum of these processes:

$$\tau_3^{-1} = \tau_{32}^{-1} + \tau_{31}^{-1} + \tau_{esc}^{-1} \tag{4.1}$$

The level 2 can also be thermally activated depending on the energy difference (Δ) between the Fermi level of the second injector stage and level $n = 2$, such that $n_{2,\mathrm{th}} = n_g \exp(-\Delta/kT)$. Hence, the rate equations for the population of the three levels can be expressed as:

$$\frac{dn_3}{dt} = \frac{\eta_i J}{e} - \frac{n_3}{\tau_3} - S g_c (n_3 - n_2) \tag{4.2}$$

$$\frac{dn_2}{dt} = \frac{n_3}{\tau_{32}} + S g_c (n_3 - n_2) - \frac{n_2 - n_{2,\mathrm{th}}}{\tau_2} \tag{4.3}$$

where S is the photon flux density and g_c the gain cross section. At the steady state ($dn/dt = 0$), below threshold ($S = 0$) the rate equations provide:

$$n_3 = \frac{\eta_i J}{e} \tau_3 \tag{4.4}$$

$$\Delta n = \frac{\eta_i J \tau_3}{e} \left(1 - \frac{\tau_2}{\tau_{32}}\right) - n_{2,\mathrm{th}} \tag{4.5}$$

where $\Delta n = n_3 - n_2$ is the population inversion. The latter requires $\Delta n > 0$, which is valid only if the condition is fulfilled:

$$\tau_2 < \tau_{32} \tag{4.6}$$

In many cases, the thermal backfilling can be considerably reduced by proper engineering of the structure (i.e. by providing an energy separation $\Delta > 100$ meV), such that this term can be dropped. This is equivalent to saying that population inversion can be achieved for whatever value of J, and no transparency current is obtained. It will be shown that, for long-wavelength QC lasers, the thermal back-filling poses some limitations and the transparency current greatly affects the threshold current. Additional contributions to the transparency current will also be considered.

4.1.2 Intersubband transitions and gain

Compared to interband transitions, intersubband ones posses specific selection rules. The gain of the material can be derived by assuming the interaction of a linearly polarized EM-wave ($\mathbf{E}$) and its potential vector ($\mathbf{A}$) and the electronic system. These two quantities can be written in the form:

$$\mathbf{E} = E_0 \boldsymbol{\varepsilon} \cos(\omega t - \mathbf{q} \cdot \mathbf{r}) \tag{4.7}$$

$$\mathbf{A} = -\frac{E_0}{2\omega} \boldsymbol{\varepsilon} \left(e^{i(\omega t - \mathbf{q}\cdot\mathbf{r})} - e^{-i(\omega t - \mathbf{q}\cdot\mathbf{r})} \right) \tag{4.8}$$

where $\boldsymbol{\varepsilon}$ is the polarization vector (perpendicular to $\mathbf{q}$), ω is the pulsation and $\mathbf{q}$ is the wave-vector. The time-dependent Hamiltonian H can be written using the dipolar approximation and the effective mass (m^*) description [170] as:

$$H = -\frac{e}{m^*} \mathbf{A} \cdot \mathbf{p} = \frac{eE_0}{2m^*\omega} (e^{i\omega t} - e^{-i\omega t}) \boldsymbol{\varepsilon} \cdot \mathbf{p} \tag{4.9}$$

being e the elementary charge and $\mathbf{p}$ the electron momentum. From the Fermi golden rule, the rate of the electronic transition between the initial $|i\rangle$ and final $|f\rangle$ states of energies E_i, E_f, respectively, is:

$$W_{if} = \frac{2\pi}{\hbar} \frac{e^2 E_0^2}{4m^{*2}\omega^2} |\langle f| \boldsymbol{\varepsilon} \cdot \mathbf{p} |i\rangle|^2 \delta(E_f - E_i \pm \hbar\omega) \tag{4.10}$$

The term $-\hbar\omega$ and $+\hbar\omega$ correspond to absorption and stimulated emission of the incident photon, respectively. To further expand the transition rate, the wavefunctions of the states are needed. A convenient form comes from Bloch's theorem in periodic potentials:

$$\psi_i(\mathbf{r}) = u_{v_i}(\mathbf{r}) f_i(\mathbf{r}) \tag{4.11}$$

$$f_i(\mathbf{r}) = \frac{1}{\sqrt{S}} e^{i\mathbf{k}_{\parallel i}\cdot\mathbf{r}_\parallel} \chi_i(z) \tag{4.12}$$

where u_{v_i} is the periodic part of the Bloch function which depends on the band-index v_i, $\mathbf{k}_{\parallel i}$ and $\mathbf{r}_\parallel$ are the 2D wavevector and position vector, in the plane of the layers of area S and $\chi_i(z)$ is the envelope function which describes the extension of the electron states in

the heterostructure growth direction.

The matrix element can then be written as:

$$\langle\psi_f|\,\boldsymbol{\varepsilon}\cdot\mathbf{p}\,|\psi_i\rangle = \underbrace{\langle f_f|f_i\rangle\,\langle u_{v_f}|\,\boldsymbol{\varepsilon}\cdot\mathbf{p}\,|u_{v_i}\rangle}_{\text{interband transition}} + \underbrace{\langle u_{v_f}|u_{v_i}\rangle\,\langle f_f|\,\boldsymbol{\varepsilon}\cdot\mathbf{p}\,|f_i\rangle}_{\text{intersubband transition}} \tag{4.13}$$

In an intersubband transition, the band-indexes are the same and $\langle f_f|f_i\rangle = 0$ for $f \neq i$, while $\langle u_{v_f}|u_{v_i}\rangle = 1$ for $v_f = v_i$ and Eq. (4.13) can be simplified giving:

$$\begin{aligned}\langle\psi_f|\,\boldsymbol{\varepsilon}\cdot\mathbf{p}\,|\psi_i\rangle &= \langle f_f|\,\boldsymbol{\varepsilon}\cdot\mathbf{p}\,|f_i\rangle \\ &= \langle\chi_f|\chi_i\rangle\,\frac{1}{S}\int e^{-i\mathbf{k}_{\parallel f}\cdot\mathbf{r}_\parallel}(\varepsilon_x p_x + \varepsilon_y p_y)e^{i\mathbf{k}_{\parallel i}\cdot\mathbf{r}_\parallel}\,dx\,dy \\ &\quad + \delta(\mathbf{k}_{\parallel f} - \mathbf{k}_{\parallel i})\varepsilon_z\,\langle\chi_f|\,p_z\,|\chi_i\rangle\end{aligned} \tag{4.14}$$

The orthogonality of the envelope functions cancels the first term, giving a transition rate in the form:

$$W_{if} = \frac{2\pi}{\hbar}\frac{e^2E_0^2}{4m^{*2}\omega^2}\varepsilon_z^2|\,\langle\chi_f|\,p_z\,|\chi_i\rangle\,|^2\delta(\mathbf{k}_{\parallel f} - \mathbf{k}_{\parallel i})\delta(E_f - E_i \pm \hbar\omega) \tag{4.15}$$

Eq. (4.15) has several important consequences. First, the optical transition can occur only in the presence of an EM-field polarized in the z direction. Fields propagating along this axis cannot induce absorption or stimulated emission. This is the well-known *intersubband polarization selection rule*. A direct consequence is also the inherent TM-polarization of QC lasers light. Second, the optical transitions are vertical ($\Delta\mathbf{k}_\parallel = 0$) and the transition rate is independent on the in-plane wavevector. Finally, the matrix element depends solely on the envelope wavefunction, which can be tailored via band structure engineering.

A more convenient way of expressing Eq. (4.15) makes use of the z dipole moment matrix element, by the equality $\langle\chi_f|\,p_z\,|\chi_i\rangle = im^*\omega\,\langle\chi_f|\,z\,|\chi_i\rangle$, and accounts for the finite width of the transition by a Lorentzian function of half-width at half maximum γ:

$$W_{if} = \frac{\pi e^2E_0^2|\langle z_{if}\rangle|^2}{2\hbar}\frac{\gamma/\pi}{(E_{if} - \hbar\omega)^2 + \gamma^2} \tag{4.16}$$

where $\langle z_{if}\rangle$ is the matrix element ($\langle\chi_f|\,z\,|\chi_i\rangle$). At the maximum the peak of the transition ($E_{if} = \hbar\omega$):

$$W_{if}^{max} = \frac{e^2E_0^2|\langle z_{if}\rangle|^2}{2\gamma\hbar} \tag{4.17}$$

The last quantity is useful in determining the gain of the QCL active region. For an EM wave propagating in the plane of the heterostructure, over an active volume of width w and thickness L_p, the number of photons crossing the structure per unit time is:

$$\phi = \frac{\epsilon_0 ncE_0^2}{2\hbar\omega}wL_p \tag{4.18}$$

with n being the material refractive index and ϵ_0 the vacuum permittivity. In a 3-level system, as the one presented in Section 4.1.1, the variation of the photon flux over a distance dL along the propagation direction is:

$$d\phi = W_{32}^{max} n_3 w dL - W_{32}^{max} n_2 w dL \tag{4.19}$$

being $n_{3(2)} w dL$ the total number of electrons in level 3 (2) in the slice of length dL. The propagation gain is defined by the ratio:

$$G = \frac{d\phi/dL}{\phi} \tag{4.20}$$

which gives, with the aid of Eqs. (4.18) and (4.19):

$$G = \frac{2e^2 \langle z_{32} \rangle^2 \omega}{\varepsilon_0 n c 2\gamma L_p} (n_3 - n_2) \tag{4.21}$$

where the quantity that multiplied the population inversion is the gain peak cross-section g_c. By substitution of Eq. (4.5), neglecting the thermal backfilling of n_2, the propagation gain can be directly connected to the current density:

$$G = gJ \tag{4.22}$$

where g is the gain coefficient:

$$g = \frac{4\pi e \langle z_{32} \rangle^2}{\varepsilon_0 n \lambda 2\gamma L_p} \eta_i \tau_3 \left(1 - \frac{\tau_2}{\tau_{32}}\right) \tag{4.23}$$

Finally, considering the waveguiding effect within the propagation medium, the spatial overlap factor Γ has to be included in the propagation gain:

$$G = \Gamma g J \tag{4.24}$$

The gain is also often expressed in terms of the oscillator strength (f_{32}), a fundamental quantity in the design of active regions:

$$f_{32} = \frac{2m_0 \omega}{\hbar} \langle z_{32} \rangle^2 \tag{4.25}$$

The sum rule for the oscillator strength, derived by the completeness of the eigenstates ($\sum_i |\chi_i\rangle \langle \chi_i| = 1$), gives:

$$\sum_j f_{ij} = m_0/m^* \tag{4.26}$$

which emphasizes the importance of the effective mass in defining the strength of the transition. Sometimes, a scaled oscillator strength $f' = (m^*/m_0) f$ is also used. However, in the latter, the importance of m^* is not evident.

The influence of the effective mass m^* on the gain coefficient is somehow masked in Eq. (4.23). The effective mass has a direct influence on three quantities contained in the gain, namely the transition energy (expressed by the wavelength of the transition λ), the dipole matrix element $\langle z_{32} \rangle^2$ and the lifetime of the excited state τ_3. In a simple quantum well, the energy of the n-th state is $E_n = \pi^2 \hbar^2 n^2 / 2m^* L^2$. Thus, if we keep constant the transition energy but employ a different material system and consequently, we modify the effective mass m^*, also thickness of the well must be changed. The dipole matrix element is also proportional to L, such that $\langle z_{32} \rangle^2 \propto m^{*-1}$. The last contribution comes from the lifetime of the excited state, which can be assumed to be exclusively controlled by the LO phonon scattering. It can be shown that $\tau_3 \propto m^{*-1/2}$. Finally, the dependency of the effective mass on the gain coefficient can be summarized by:

$$g \propto \langle z_{32} \rangle^2 \tau_3 \propto m^{*-3/2} \tag{4.27}$$

which is an extremely important conclusion for the choice of the material system employed in the QC structure. The situation is further complicated by the nonparabolicity of the bands, that makes the effective mass dependent on the energy. A typical approximation in this case comes from Kane's model in a one-band model [171]:

$$m(E) = m^* \left[1 + \frac{E - E_c}{E_g} \right] \tag{4.28}$$

where m^* is the effective mass at the bottom of the conduction band (of energy E_c) and E_g is the effective bandgap. A final consideration relates the bandgap of the materials and their effective mass. Usually, the larger the bandgap and the larger the effective mass. Such considerations are fundamental in the choice of the material system employed in the QC structure.

4.1.3 QCL material systems

Each material system presents its benefits and limitations, which might prevent optimal performances in particular wavelength regions. Regardless of the spectral region of interest, the fundamental requirement for the epitaxial growth of semiconductors is the closeness of the average lattice constant of the QCL structure and the substrate. A list of the most used semiconductors with the electron effective mass, energy bandgap and lattice parameter is provided in Table 4.1.

The most used can be grouped as follows:

1. InGaAs/AlInAs alloys grown on InP;

2. GaAs/AlGaAs family, grown on GaAs substrates;

3. InAs/AlSb compounds, on InAs substrate.

Table 4.1: Properties of the main III-V semiconductors employed in QC structures. The electron effective mass and the bandgap (E_g) in the point Γ are reported. In bold, indirect bandgap materials. Data taken from [172].

Semiconductor	$m^*(\Gamma)/m_0$	E_g^Γ (eV)	Lattice constant (Å)
GaP	**0.13**	**2.886**	5.4505
AlP	**0.22**	**3.63**	5.4672
GaAs	0.067	1.519	5.6533
AlAs	**0.15**	**3.099**	5.6611
InP	0.0795	1.4236	5.8697
InAs	0.026	0.417	6.0583
GaSb	0.039	0.812	6.0959
AlSb	**0.14**	**2.386**	6.1355
InSb	0.0135	0.235	6.4794

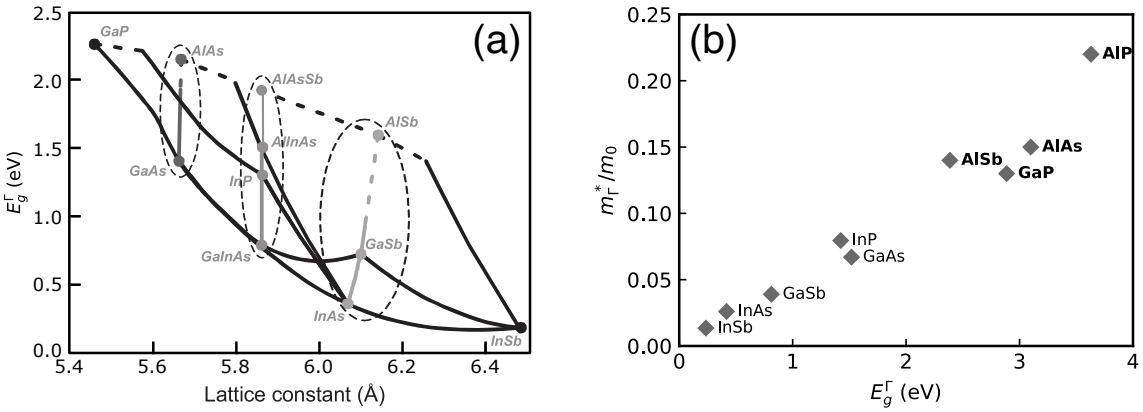

Figure 4.3: (a) III-V semiconductors defined by their lattice constants. Dashed ovals comprise the material systems employed in typical heterostructures. Taken from [170]. (b) Effective mass and energy bandgap of III-V semiconductors presented in Table 4.1.

The InGaAs/AlInAs family was the first to be demonstrated and at the moment are the best-performing solution for QC lasers, in continuous wave comprised between 4.3 µm [173] and 10.3 µm [174] with Watt operation levels. The possibility of InP:Fe lateral regrowth allows the fabrication of buried heterostructures with improved heat dissipation, an important requirement for CW-operation at RT.

GaAs-based QCLs range between 8 µm to the terahertz domain. Typically, in the mid-IR these lasers are less performing than InP-based lasers due to the relatively small useful conduction band offset, and are thus less attractive. However, this technology performs better on the long-wavelength side for purity reasons (inducing less free-electron scattering) and paved the path for THz QCL devices.

Finally, the antimonide compounds comprise InAs, GaSb and AlSb. The most attractive feature of these compounds is the very large band offset $\Delta E_c = 2.1$ eV obtained by employing InAs wells with AlSb barriers. Practically, the presence of intervalley scattering limits the available energy range to about 800 meV, which restricted the emission on the short wavelength side to $\lambda \approx 3$ µm.

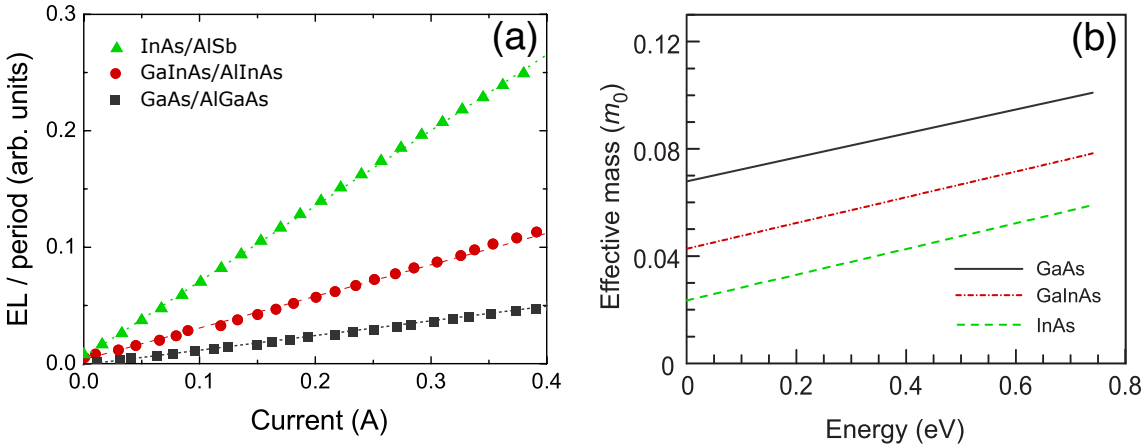

Figure 4.4: (a) III-V semiconductors defined by their lattice constants. Dashed ovals comprise the material systems employed in typical heterostructures. Adapted from [175]. (b) Effect of the band nonparabolicity on the effective mass as a function of the energy. Taken from [170].

Another fundamental advantage of the InAs/AlSb system is the very small effective mass in InAs, connected to its narrow bandgap as depicted in Fig. 4.3(b). In Eq. (4.27) the dependency of the gain on the effective mass was discussed. In [175], such prediction has been experimentally confirmed by electroluminescence on QC structures made of different materials and designed to emit at the same wavelength. The InAs-based samples exhibited the most intense spontaneous emission (Fig. 4.4(a)), demonstrating that the lower effective mass of InAs provided a higher gain compared with other material systems.

The increased gain of InAs provides a clear advantage in the design of QC devices, as the threshold current density can be reduced accordingly especially at long wavelengths. The effect of the band nonparabolicity described by Eq. (4.28) is weaker in this case, because the levels involved in the lasing transition are close to the bottom of the conduction band. The effective mass of GaAs, GaInAs and InAs is shown in Fig. 4.4(b) as a function of the electrons energy.

4.2 Long-wavelength devices

4.2.1 Active region design

Long-wavelength QCLs for the spectral range above 10 µm present some specific features compared with the devices emitting at shorter wavelengths. At first, thicker quantum wells should be employed to reduce the transition energy, which weakens the unwanted interface-related effects. On the other hand, to obtain tunnel coupling between adjacent QWs, thinner barriers have to be designed, especially in the case of the high conduction band offset of AlSb barriers. The barrier layers can be as small as a monolayer, which is half of the lattice constant in zinc-blend structures, or $\sim$ 3 Å. While technologically challenging, such structures were demonstrated by using molecular beam epitaxy growth

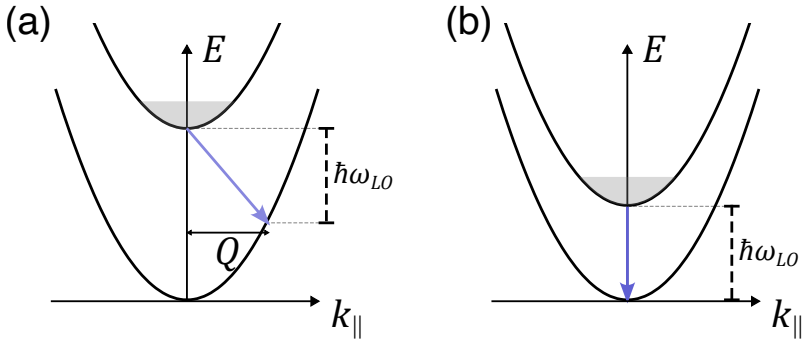

Figure 4.5: Schematic of LO-scattering processes in (a) non-resonant and (b) resonant conditions. The scattering rate is inversely proportional to Q, such that for a resonant transition ($Q \sim 0$) very small lifetimes are achieved.

(MBE) [165], [166].

Another challenge is the rapid decrease of the upper-state lifetime with increasing wavelength. Typically, the upper-state lifetime is set by the LO-phonon scattering and interface-roughness scattering (IFR). The latter depends on the growth quality and reduces the total lifetime of the upper-state. LO-phonon scattering, on the other hand, is a fundamental process which cannot be overcome.

The efficiency of LO-phonon scattering can be obtained by applying Fermi's golden rule, giving a scattering rate:

$$W_{LO} = \frac{m^* e^2 \omega_{LO}}{2\hbar^2 \epsilon_P} \sum_f \int_0^{2\pi} d\theta \frac{I(Q)}{Q} \tag{4.29}$$

being $Q = \sqrt{k_i^2 + k_f^2 - 2k_i k_f \cos(\theta)}$ the momentum exchanged in the scattering process, corresponding to the optical phonon energy $\pm\hbar\omega_{LO}$ and $I(Q)$ the form factor. Eq. (4.29) demonstrates how the LO-scattering rate is much more efficient if the exchanged momentum Q is null. Hence, if the transition is vertical, the scattering rate can be extremely high. This constitute a challenging problem, since by moving towards longer wavelengths, the transition energy (i.e. the subband separation) becomes closer to the LO energy, promoting resonant scattering. This scenario is presented in Fig. 4.5. Such effect is partially compensated by the larger oscillator strengths (due to the larger QWs and small effective mass of InAs), and the reduction of the transition linewidth γ at longer wavelengths.

Maximizing the oscillator strength requires a careful design of the active region structure. The first designs were based on the concept of superlattice active region [162], which optimized the oscillator strength. Active regions of 4 QWs and 3 level resonant-phonon extraction provided values of 70-75 in InAs [167], with corresponding differential gains on the order of 40 cm/kA.

It should be noted that such high gains are achieved in the structures with vertical transitions at very small population inversions. As a consequence, the thermal backfilling ($n_{2,th}$) of the lower lasing state strongly affects the efficiency of the QCL. To reduce its

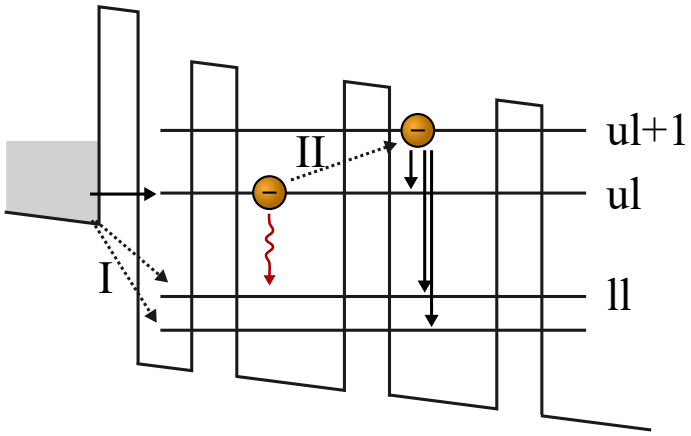

Figure 4.6: Schematic of the leakage processes occurring in a QC structure. Direct injection of electrons in lower states (I) and scattering towards higher energy levels (II) are represented in dashed lines.

negative impact, structures with a wide injector miniband ($\Delta > 100$ meV) are usually employed [176].

The reduction of the doping density is another way to weaken the thermal backfilling but it cannot be pushed too far since it limits the current dynamic range of the device. Both these approaches have been used in [167], where cw-operation was demonstrated at 15 µm up to 400 K.

Another effect to be considered is the leakage current. Leakage currents strongly affect the efficiency of the device as they add to the transparency component in the threshold current density of the device. The latter can be written in the form [176]:

$$J_{th} = \frac{\alpha_m + \alpha_w}{\Gamma g} + J_{bf} + J_{leak} = \frac{\alpha_m + \alpha_w}{\Gamma g} + J_{tr} \tag{4.30}$$

where α_m and α_w are mirror and waveguide losses, while J_{bf} and J_{leak} are the backfilling and the total leakage current densities. The main sources of leakage, presented in Fig. 4.6, are: injection from the last injector state directly into the lower lasing state; scattering of electrons from the upper-lasing state to above-lying subbands. However, this contribution can be significantly reduced by employing proper design of the injector and low doping. The second process allows the electron to escape the upper lasing state towards higher energy levels. Escape to continuum or miniband is also a possibility, depending on the adopted design. For LW-QC lasers, usually large QWs are used and the separation between the upper energy levels cannot be freely increased. Typical values are between the phonon and photon energies, ranging between 30 to 50 meV. Luckily, both LO-scattering and IFR-scattering promote fast return of the electrons from *ul+1* to *ul*, mitigating the overall effect.

To further reduce the leakage components, a diagonal transition scheme can be used, which exploits the vicinity of the injector state to the upper lasing state for an optimized injection.

Table 4.2: Phonon energies expressed in wavelength (µm) for several binary semiconductor compounds at room temperature. Taken from [177].

	LO	TO	2LO	2TO	LO+TO
AlAs	25.0	27.8	12.5	13.9	13.2
AlSb	31.6	33.7	15.8	16.8	16.3
GaAs	34.2	37.3	17.1	18.6	17.8
InP	29.0	32.9	14.5	16.5	15.4
InAs	41.6	46.0	20.8	23.0	21.9

4.2.2 Waveguide considerations

So far the key points concerning the material advantages and precautions in the active region design have been presented. A crucial aspect for optimal laser performance is the waveguide which allows the guided propagation of the EM mode.

A fundamental property of the waveguide are the losses associated with the propagation of the wave. Hence, the transparency of the material composing the waveguide and the active region has to be as high as possible. A fundamental limit comes from phonon resonances which generate the so called Reststrahlen band at about 30-40 µm, a spectral region where lasing is basically prohibited because of the strong absorption of emitted radiation by the lattice vibrations. Table 4.2 summarizes the phonon energies for the main binary semiconductors employed in QCLs. Multi-phonon absorption, while being less intense, strongly affects the transparency of the semiconductors in certain spectral zones at shorter wavelengths. Among the presented materials, InAs provides a good transparency below 20 µm, where 2-phonon LO absorption occurs. This is a further advantage of the InAs family over the others in LW-applications.

Aside from phonon absorption, another loss mechanism which is prevalent in LW-devices is free-carrier scattering, which scales with the concentration of carriers and with λ^2. Doping is the main source of free-carriers in the heterostructure.

The threshold current density, expressed in Eq. (4.30), contains two parameters that can be optimized by waveguide design, namely the confinement factor Γ and the waveguide losses α_w. The confinement factor is defined as the portion of the mode's electric field square modulus confined in the active region, over the total one:

$$\Gamma = \frac{\int_{AR} |E|^2 \, dA}{\int_{-\infty}^{+\infty} |E|^2 \, dA} \tag{4.31}$$

The larger Γ, the higher overlap with the active gain is obtained. The main mechanism for field confinement is defined *index guiding* since the refractive-index discontinuity between the active region and the outer layers (called *cladding layers*) is responsible for mode confinement through total internal reflection. The cladding layers can be obtained by

doping the semiconductor, whose refractive index is lowered by the presence of free-carriers. This comes from the refractive index dependency on the material conductivity, as described by the Drude model. Such waveguide is also defined plasmon-enhanced waveguide [178].

The presence of a doped layer close to the active region would introduce strong losses from free-electron absorption. Thus, low-doped spacer layers are typically employed to separate the mode from the lossy cladding region. Usually a tradeoff between low-loss/low-overlap with thick spacers and high-loss/high-overlap with thin spacers, giving typical values of $\alpha_w \approx 3$ cm^{-1} and $\Gamma \approx 0.5 - 0.6$. Plasmon-enhanced waveguides demonstrated better performances than surface-plasmon or double-metal approaches, where the field is coupled with a metallic layer. The latter are limited by the absorption induced by the metal layer, with typical waveguide losses on the order of $\alpha_w \gtrsim 30$ cm^{-1}.

A final consideration concerns the heat extraction capabilities, which depend on the thermal conductivity of the composing materials. Compared to the InP family, InAs lacks a good thermal conductivity, hence heat accumulation and management are a major concern. The thermal conductivity in the InAs/AlSb active region is strongly anisotropic, reaching a very low value of ~ 3 W/(m K) along the growth direction, and ~ 27 W/(m K) along the lateral direction or in bulk InAs. On the other hand, InP is roughly 2.5 times more conductive, reaching 68 W/(m K). Moreover, InAs technology does not feature lateral regrowth for buried heterostructure, since there are no available insulation techniques.

4.3 State of the art design of 14 µm QCLs

The active region design rules and the waveguide details illustrated so far have been implemented in the realization of QC devices emitting around 14 µm. These wafers were grown as part of the Academic activities carried out at Université de Montpellier and have been processed and characterized within this work for the fabrication of the QC lasers. For such reason, some details on the band-design and the used material are given in this section.

The wafer was grown by molecular beam epitaxy on an InAs substrate in a RIBER 412 solid source machine, equipped with valved cracker cells for the As and Sb using growth rates of 1.0 and 1.5 A/s for AlSb and InAs, respectively. The design was optimized with respect to a previous structure, presented in [167]. The lasing takes place between levels e3 $\rightarrow$ e2, of energy separation 88 meV, corresponding to 14 µm, while the distance between e3 and the upper energy state e4 was increased to 65 meV. Hence, at RT thermal activation depopulates the upper lasing state, while a large part of the promoted electrons returns back to the e3 level, as explained in Section 4.2.1. On the other hand, also the injector width miniband was enlarged to $\Delta = 141$ meV, to reduce the thermal back-filling of e2. Two quantum wells in the middle of the injector region were doped with Si at $n = 8 \cdot 10^{16}$ cm^{-3}. The active zone consists of 45 repetitions of the following layer sequence expressed in Å, starting from the injection

barrier: **26**/41/**1**/62/**1**/67/**2**/66/**2**/64/**6**/64/**6**/62/**6**/59/**9**/58/**10**/57/**11**/56, where AlSb layers are in bold, and the Si-doped layers are underlined.

The active zone is separated from doped cladding layers with Si to $7 \cdot 10^{17}$ cm^{-3} by 3 µm thick undoped InAs spacers. This reduces the mode overlap with the lossy region, due to the free-carrier absorption in the heavily doped cladding layers. The mode overlap with the active region (Γ) and the waveguide losses (α_w) can be estimated to be ~ 0.5 and ~ 3.6 cm^{-1}, respectively, via Finite Element Method (FEM) solver, using COMSOL-multiphysics. Similar simulations are presented later in this work. The band-diagram of such structure is presented in Fig. 4.7 and was simulated via a software developed by Roland Teissier at the Université de Montpellier. This tool computes the electronic band structures by self-consistently solving the coupled Schrödinger-Poisson equations. Among the electronic states, the most relevant are the lasing states (e3, e2) and the upper energy state (e4), which constitutes a parasitic pathway generating losses. The structure is simulated for operative conditions with an electric field of 26 kV/cm. The calculated energy transition e3-e2 corresponds to 85 meV, with a normalized oscillator strength of 50.2. This structure was employed for the fabrication of QCLs presented in [169] and emitting at 14.2 µm, which exhibited an extremely low threshold current density of 0.6 kA/cm^2 at 300 K. A differential gain of 46 cm/kA was also obtained, with a transparency current of $J_{tr} \approx 0.35$ kA/cm^2. The last result, demonstrates that the transparency current is indeed a major component of the threshold current density, and dominates if long cavities or low mirror losses (i.e. treated facets) are considered.

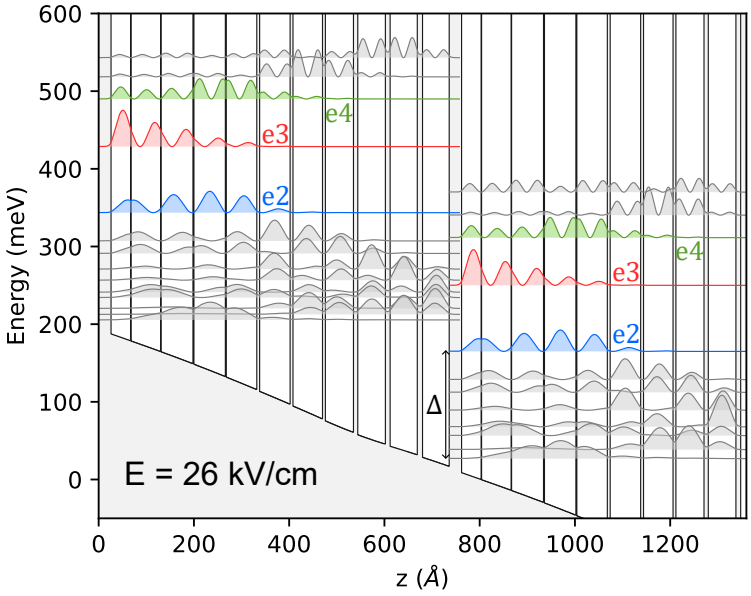

Figure 4.7: Band energy diagram and electronic states (moduli squared), highlighting the upper and lower lasing states e3, e2 and the upper energy level e4, as described in the text.

4.4 Tapered waveguides and tapered lasers

In Chapters 2 and 3, the beneficial influence of the optical power for the photo-excitation of the investigated sample was discussed. Higher optical powers induce stronger thermal effects, which ultimately improves the detection limits of photoacoustic and photothermal approaches. However, with increasing emission wavelength, a fundamental reduction of the available power arises from the reduced photon energy $E = hc/\lambda$.

To counteract the inherent limitations of the LW-region, several approaches can be employed. Clearly, the basic strategy consists in the optimization of the technology in terms of its active region, waveguide properties and heat dissipation, already addressed in the previous section. Secondly, treatment of the facet can improve the outcoupled optical power, by means of an anti-reflection coating on the extracting facet and a high-reflection coating on the opposite one. Such approach was also explored in this work.

A second way concerns the width of the waveguide. Increasing the width of the waveguide has two benefits: first, the reduction of the losses, as the mode penetrates less in the lossy dielectric used for the laser lateral insulation; secondly, and most remarkable, a linear increase of the active volume. However, wider ridge widths might favour higher order transverse mode, which ultimately affect the spectral purity of the device. This is especially important for single-longitudinal mode lasers, where the different effective index between the transverse modes implies, according to the Bragg equation, a different vacuum wavelength. Preserving the spectral quality is mandatory for spectroscopic applications. As a consequence, the ridge width cannot be increased at will.

An approach widely used to achieve high power outputs consists in the amplification of the laser radiation in a semiconductor optical amplifier. Such structure is also referred to as MOPA or *Master Oscillator Power Amplifier*. In the MOPA, the laser cavity and the amplifier region are monolithically integrated within the same chip. This structure is inherently self-aligned and provides a high grade of versatility, since the laser device and the amplifier part are individually pumped. This in needed to achieve the correct operating conditions of the laser cavity, while keeping the amplifier region below the self-lasing condition. The individual pumping of the laser oscillator and the amplifier region allows the optimization of both structures. The geometry of the amplifier section can also be tailored to preserve beam quality, while improving the amplification. A glaring example is a tapered waveguide, schematically shown in Fig. 4.8, which features an increasing ridge width with the position along the waveguide. The tapering of the waveguide should induce an adiabatic expansion of the electric field, which propagates at an angle smaller than the diffraction one.

Historically, tapered waveguides have been introduced to reduce the coupling losses of a field to a narrow waveguide. The inverse-taper structure allows to accept a larger mode, and to shape it into the narrow section of the waveguide. However, in order to operate in an adiabatic regime, the mode should propagate through the taper without undergoing

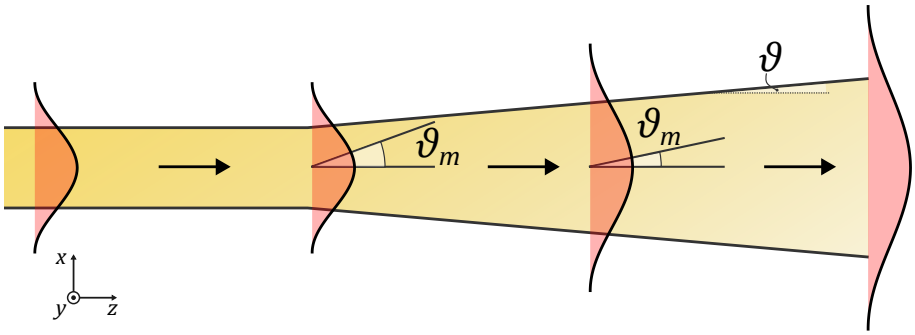

Figure 4.8: Simplified schematic of electric field propagation in a linear tapered waveguide with half taper angle ϑ. The mode diffraction angle, represented with ϑ_m, is a function of the field position within the waveguide and represents the upper limit for ϑ to ensure adiabatic expansion.

mode conversion. Typically this is achieved with a very slow variation of the waveguide width, namely with a narrow taper angle. In [179], [180] Milton & Burns proposed a simple rule to ensure adiabatic operation of a tapered region. According to their proposal, the local half-angle of the taper at to point z along the waveguide should be:

$$\vartheta < \frac{\lambda_0}{2n_{eff}W} \tag{4.32}$$

where λ_0 is the vacuum wavelength, n_{eff} is the effective index of the fundamental mode and W is the local full width of the taper in z. Typically, also the effective index is a function of the width, which however converges to the value of the (ideally) infinitely extended waveguide. This relationship assumes that the field propagates with an angle below the local diffraction angle $\vartheta_m = \lambda_0/2n_{eff}W$. Different tapering functions can be used for this purpose: among them, linear, parabolic and exponential types have been extensively studied [181], [182].

The tapered amplifier offers several advantages over the straight waveguide: first, it provides a larger amplification factor, which scales with its active area, without introducing higher-order modes if properly designed; second, in high-power applications, the field spatial distribution on the wide facet is spread over a larger area reducing the risk of catastrophic optical mirror damage; third, the beam exiting the wide facet will emerge with a narrower diffraction angle, due to the large width of this facet. In some cases, the latter might not pose a real advantage as the output beam will be astigmatic due to the different divergences along the fast and slow axis (y and x in Fig. 4.8). Correction of the astigmatism (i.e. for beam collimation) can be performed with cylindrical lenses, which correct the beam divergence along the vertical and parallel directions.

The alternative approach to MOPAs, consist in the monolithic integration of the waveguide and the amplifier sections in the oscillator cavity. In this sense, the tapered waveguide is employed itself as a laser oscillator. In this case, since lasing necessarily arises also from the tapered region, the narrow straight section acts as a spatial filter for the higher order

modes. The latter exhibit high losses within the narrow ridge, such that their oscillation in the laser cavity is inhibited.

The tapered laser offers a simpler frame compared to a MOPA, at the cost of less versatility. Tapered lasers have been demonstrated in several spectral ranges, for diode lasers, ICLs and QCLs. In the LW-region, tapered lasers emitting up to 10 µm have been reported [183]. In many cases, the limits of such approach lies in the strong inhomogeneities introduced by the asymmetric waveguide. First of all, while a ridge waveguide can be assumed to be at the edge of the stability zone, the tapered cavity acts as an unstable resonator due to the field divergence in the tapered section. Thus, one can assume that upon reflection the beam will continue to diverge and only the central portion of the beam will be allowed to couple back into the ridge section [184]. The 'tails' of the mode will eventually be loss. Moreover, gain, electrical and thermal inhomogeneities can also occur in the waveguide, introducing deviations from the pure adiabatic expansion of the beam. As a consequence, coupling between transverse modes can be achieved, causing asymmetries in the far-field profile of the output beam [185].

In the next chapter, the fabrication results of LW-tapered lasers emitting at 14 µm are presented, along with the electrical, optical and spectral characterization of the devices. Finally, deposition of AR and HR coating and single-mode operation via 1^{st} order Bragg grating is demonstrated.

Chapter 5

Fabrication and characterization of long-wavelength tapered QCLs

In this chapter, the results achieved on the development of long-wavelength tapered lasers are reported. The fabrication process will be discussed at first. It consists in three major steps: the fabrication of the waveguide in the form of a ridge structure, the lateral insulation, which prevents shorting of the device during the final step, the metallization contact deposition. A schematic representation of these steps is provided in Fig. 5.1.

Basically, each step includes a photo-lithographic exposure of the sample, on top of which a proper photo-resist is deposited via spin coating. In photolithography, a photosensitive material is employed to transfer a specific pattern from a hard mask to the sample. The areas not covered by the photomask during exposure to UV-light undergo a chemical reaction which can weaken or strengthen the photosensitive material. In the first case, the resist is defined positive, while in the latter is named negative. This definition comes from the 'polarity' of the pattern transferred to the sample upon development: for a positive resist, the areas exposed to UV-light will be dissolved by the developer, whereas the opposite happens for negative resists. As a consequence, after development the positive resist will present the same pattern as the photomask and in the negative resist the complementary structure is obtained.

For this work, hard masks defining tapered waveguides with full-angles of 0°, 1°, 2° and 3° were designed using the KLayout software and fabricated in LAAS-CNRS. Masks for the three lithographic steps were manufactured, for both positive and negative resists. Each mask was separated in four regions, to have ridges of variable width. Ridge widths of 26 µm, 30 µm, 34 µm and 38 µm were employed in the mask, accounting for the undercut obtained during the wet chemical etching, as explained later in this chapter. In each of these four regions, the four laser types are repeated with a spacing of $\sim$ 450 µm. The base unit for each laser consists in a 5.2mm-long structure, composed by 2.5 mm of ridge section and 2.5 mm of a linear taper section terminated by a 200 µm flat region. The pattern is mirrored and repeated along the waveguide direction.

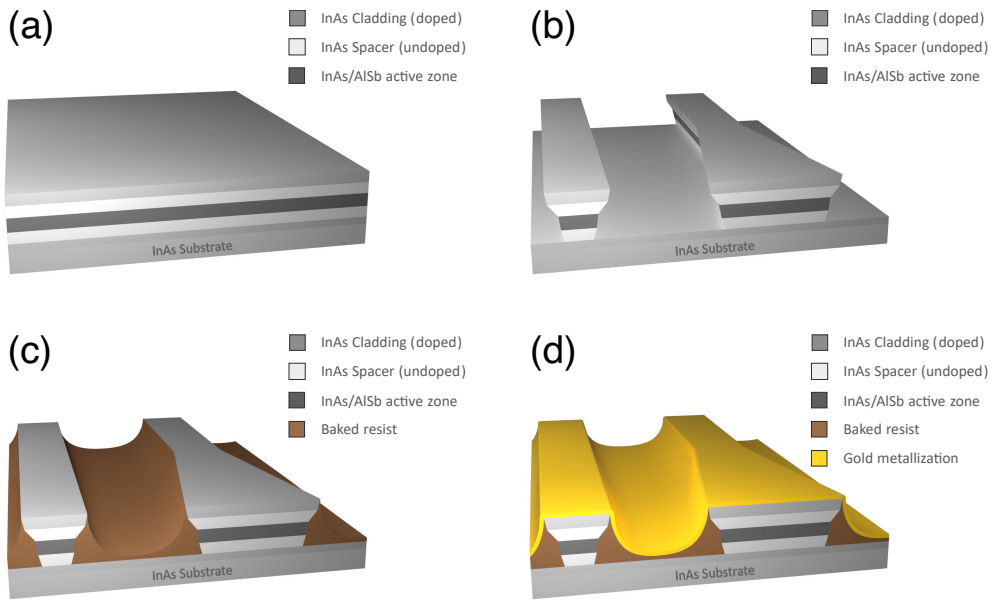

Figure 5.1: Schematic of the QCL fabrication steps. (a) Grown heterostructure, composed by an InAs substrate, and an InAs/AlSb active zone, sandwiched between undoped InAs spacers and doped InAs cladding layers. (b) Mesa etching. (c) Insulation layer. (d) Metallization.

This structure was chosen to provide several taper duty cycles (taper length over the whole resonator length) in the cleaving step of the laser bars, while using a typical resonator length of 3.6mm. A portion of the mask is given in Fig. 5.2(a), where the overlay of the etching, insulation and metallization masks is shown. In Fig. 5.2(b), a picture of the (negative) etching mask is presented.

5.1 Waveguide fabrication

5.1.1 Ridge etching

The process starts by cleaving a piece from the grown 2" wafer. The typical sample size, of the order of 10 mm × 25 mm, is convenient to handle and sufficient to provide a good amount of lasers. The sample is initially cleaned under acetone, ethanol (EtOH), isopropanol (IPA), and deionised water. If residual contamination is present after the cleaning treatment, a low RF power (50 W) Oxygen-Argon reactive ion etching (RIE) can be used.

The sample is baked on a hot-plate at 110 °C to remove residual humidity. Such step is preparative for the photoresist spin coating. The negative resist AZ2020 (MicroChemicals) was used for the deposition of a 3 µm-thick photosensitive layer at 4000 rpm for a time of 30 sec. The resist is pre-baked, prior to UV exposure, for 1 min at 110 °C. The UV exposure was performed with a lithography machine (SUSS MicroTec MJB4 Mask Aligner) under soft-contact configuration. The negative etching mask was used to irradiate

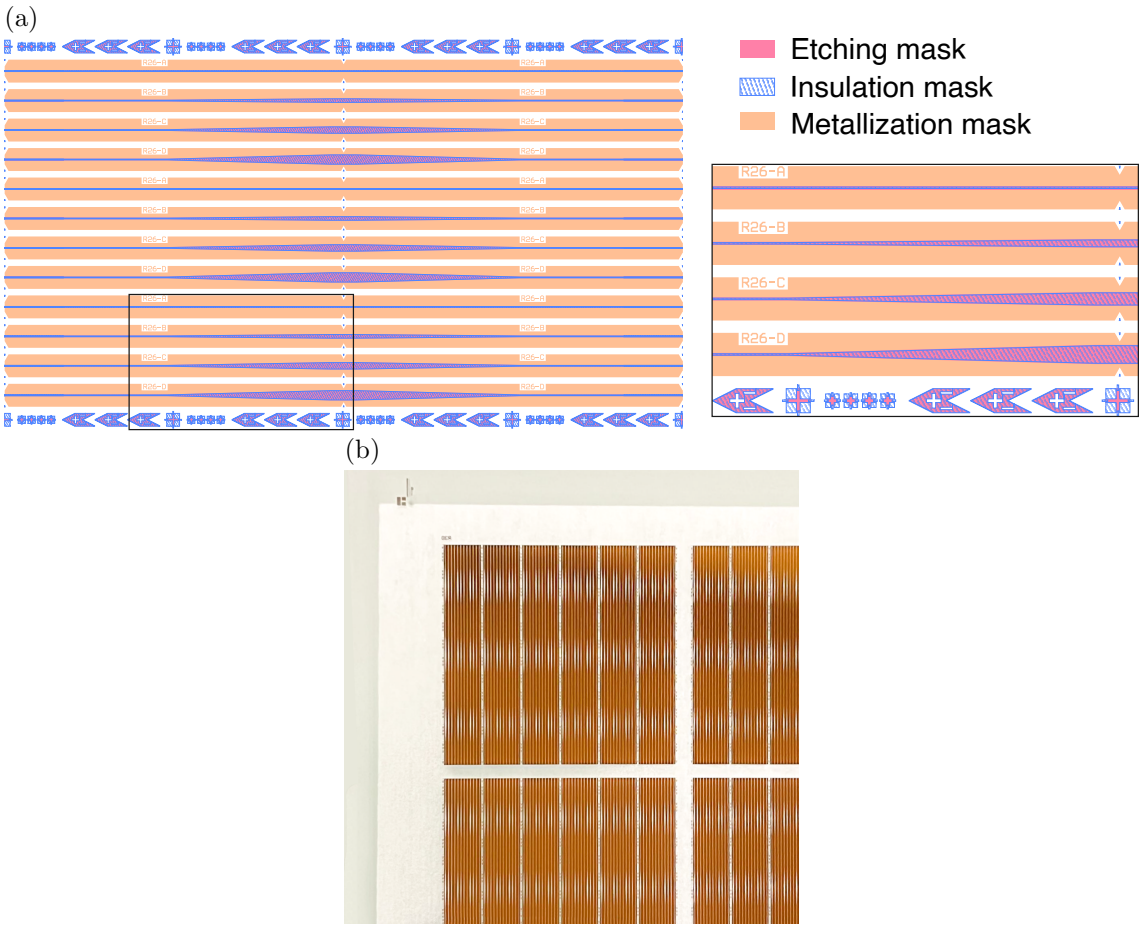

Figure 5.2: (a) Masks used for the tapered laser fabrication. To aid visualization, the etching mask for a positive resist and the insulation mask for a negative resist are shown. Note that insulation and etching mask are identical, apart from a narrower width of the waveguide of few µm, sufficient to obtain the aperture of the insulation on the top of the ridge structure. (b) Photo of the etching mask for a negative photoresist.

only the ridge structures. Negative photoresist usually requires post exposure baking, which was performed at 110 °C for 1 min. This step is essential for the crosslinking mechanism initiated during the exposure. The AZ726 solvent was used as developer, with a development time of 20 sec.

The sample is wet etched in a solution of phosphoric acid, hydrogen peroxide and deionised water (H_3PO_4:H_2O_2:H_2O) in volumetric ratios 2:1:2. The etching rate of such solution is roughly 1 µm/min at room temperature. A deep mesa etching is needed to avoid the lateral spreading of the current, due to the larger in-plane electrical conductivity. Thus, the etching depth should reach at least the bottom cladding layer, which corresponds to a ridge height of circa 12 µm. The different etching rate along the crystallographic directions result in the typical dovetail shape of the ridge. On one side, this shape causes an uneven electric field distribution in the active zone, resulting in a deformation of the energy diagram across the heterostructure. However, the dovetail shape demonstrated to be the most performing [186]. In tapered devices, the sloped sidewalls introduce additional

losses in the form of plasmonic and reflection losses for high-order modes [187], [188], thus favouring the fundamental transverse mode.

A citric acid solution ($C_6H_8O_7$:H_2O, 1:1) is used to reduce the current leakage over the mesa walls. The solution is mixed with hydrogen peroxide (1:1 in volume) and the sample is treated for 5 min. The selective etching of InAs allows to produce an AlSb-rich surface, which limits the side-wall leakage current due to the Al oxidation. The resist is finally stripped in remover PG at a temperature of 80 °C for 60 min, leaving the sample's surface clean from any residual resist. The sample after etching of the mesas is presented in Fig. 5.3(a).

5.1.2 Insulation layer

The next step consists in the insulation of the lateral walls. This process should be performed relatively soon after the mesa etching, to prevent excessive oxidation of the Al-containing QCL active region. As insulation layer, a baked photoresist has been used for the simplicity of the process. This insulation technique is mature and largely employed [169] in the InAs-based technology. Nevertheless, few drawbacks are also present. First, the poor thermal conductivity limits heat extraction, important especially for CW operation. Second, the polymeric nature of the resist induces thermal hysteresis and instabilities when strong thermal cycles are applied to the device.

As a photoresist, the AZ1518 (MicroChemicals) is spin-coated at 4000 rpm for 30 sec. The exposure time was adjusted with respect to the traditional process and increased to 50 sec. The sample is finally developed in AZ726 for 20 sec. An extended exposure time in comparison to the standard process is needed to fully remove the resist on the large taper islands.

The process is terminated by a hard-baking (220 °C for 2 hours), which hardens the polymeric film improving its thermal, chemical and physical stability. The sample after hard-baking is presented in Fig. 5.3(b).

5.1.3 Metallization layer

The top contact metallization is the last photolithographic step of the process. The negative resist AZ2070 (MicroChemicals) is spin coated at 4000 rpm for 30 sec. This resist forms a thick layer of ~ 6 µm, needed for the correct lift-off of the metal layer in the exposed regions of the resist. The resist is pre-baked (110°C for 60 sec) and exposed with the mask in soft-contact mode. An exposure time of 8 sec is used, in combination with a post exposure bake (110°C for 60 sec). The sample is developed in AZ726 for 2 min and 45 sec.

Before the metallization step, a deoxidation process is needed to improve the adhesion of the metallization layer to the sample. Any oxide or organic impurities formed on the sample's surface would prevent proper adhesion of the metallic layer. Deoxidation is

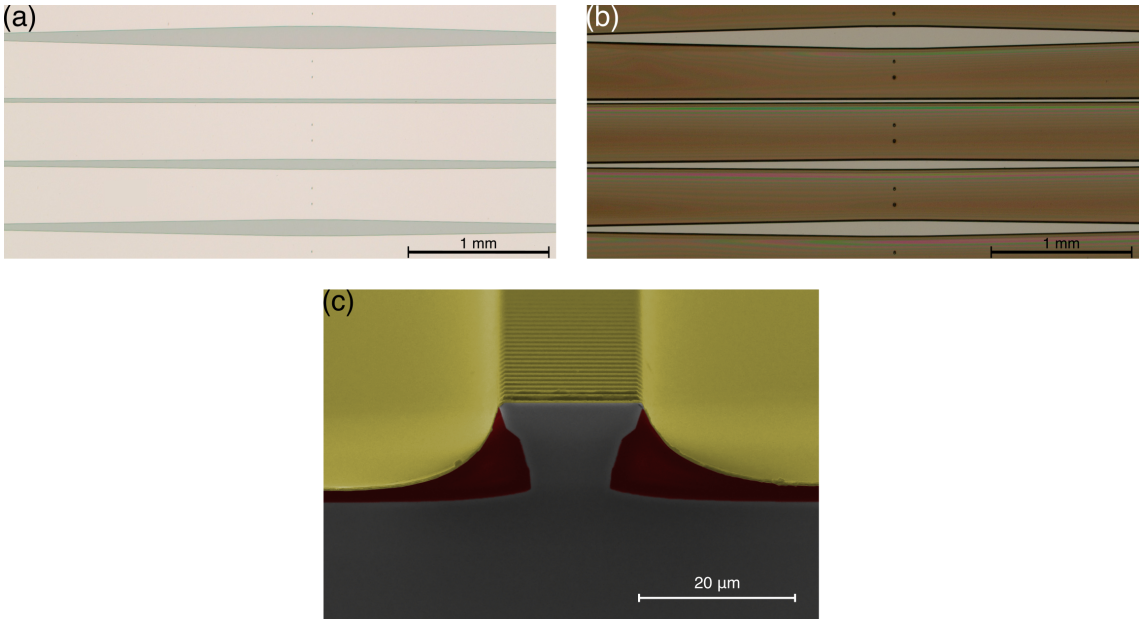

Figure 5.3: Sample after (a) definition of the tapered waveguides and (b) hard-baking of the photoresist. (c) SEM image of the laser facet after the full fabrication process, showing the typical dovetail shape. The picture shows a DFB device, described in Section 5.5.

performed with a solution of HCl:H_2O in ratios 1:4 for 30 seconds.

The sample is transferred to the deposition chamber, kept in ultra-high vacuum. The metal layer is composed by a stack of layers Ti/Au/Cr/Au of thickness 20/200/30/200nm. The Ti layer is used as an adhesion layer to the semiconductor surface, while the Cr layer blocks diffusion of the Indium solder, used to mount the laser bars on the heat sink. The lift-off of the exposed resist is finally performed in acetone.

5.1.4 Mechanical polishing and mounting

Thinning of the substrate is a necessary process to aid the cleavage of the laser bars and the formation of mirror facets. The sample is glued on top of a metallic cylinder using a crystal bond, such that the ridges face the metal surface. The substrate is mechanically polished against SiC paper of variable grits, from P2400 to P4000 for final lapping. The sample is thinned to a thickness of 150 µm. The laser bars are scribed and cleaved in specific points to obtain the expected cavity length and taper duty cycle. The cleaved facets act as mirrors, forming a Fabry-Pérot resonator. The laser facet after the full fabrication process is shown in Fig. 5.3(c). The laser bars can be mounted on Copper heat sink, as shown in Fig. 5.4(a), or further separated into individual lasers.

Single lasers are usually mounted in the epi-side down configuration, such that the ridge is immersed in the Indium solder. This mounting enhances thermal extraction towards the heat sink and is fundamental for correct operation in continuous wave. Conversely, epi-side up mounting is useful when measuring multiple lasers on the same bar.

Finally, gold wires of 50 µm in diameter are manually soldered from the top of the

(a) (b)

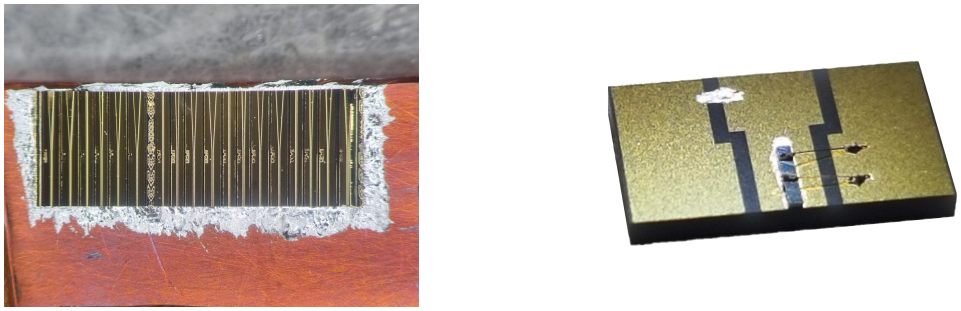

Figure 5.4: (a) Laser bar mounted on top of a Copper submount. (b) Single laser mounted epi-side down on top of a gold-coated AlN submount.

device to a metallized ceramic pad, which will be the first terminal, while the second terminal is the submount itself. In Fig. 5.4(b) a single laser bar mounted on an AlN submount is portrayed.

5.2 Characterization of FP-tapered QCLs

5.2.1 Power enhancement of the tapered cavity

The FP tapered QCLs were characterized in terms of their electrical and optical properties. The devices were mounted in a cryostat (Janis, ST-100) and were biased using a voltage generator (Agilent, E3634A), gated by a pulse generator (Quantum Composers, 9514+ Pulse Generator). A repetition frequency of 12 kHz with a pulse duration of 330 ns was combined with a slow (30 Hz) square wave modulation superimposed via an arbitrary waveform generator (Agilent, 33521A), with a total duty cycle of 0.2%. The emitted radiation was collimated into an FTIR (Bruker, Vertex 70v), using a 2-in. aperture off-axis parabolic (OAP) mirror, with 2-in. focal length. The optical power was collected on the spectrometer's DTGS pyrodetector. Optical power calibrations were carried out using a power meter (Thorlabs, PM100D equipped with a S401C measuring head). For these measurements, lasers driven at 2% duty cycle were placed in front of the sensor without any optics. The maximum collection efficiency was expected.

In Fig. 5.5(a) the light-current-voltage (LIV) curves of representative FP-tapered QCLs are presented. As expected, a scaling of the optical power output with the taper angle can be observed, as the active volume of the laser is increased. Interestingly, the slope efficiency of the tapered lasers appears to be higher than that of the ridge devices. This comes from the different collection efficiency of the optical setup, discussed later in this section. An improvement in the slope efficiency in tapered lasers above 85% of the rollover current was observed. Such behavior happens with a strong change in the optical spectrum, suggesting mode-hopping or mode competition with higher order modes.

As previously discussed, a different collection efficiency is expected as a consequence of the different divergence angle and collection capabilities of the OAP, whose acceptance

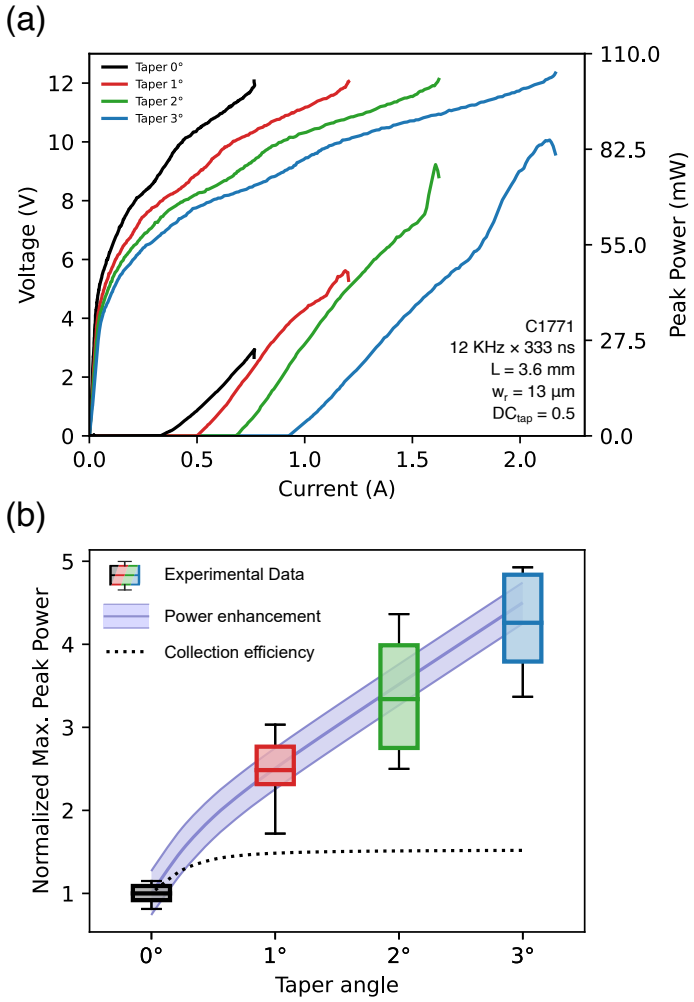

Figure 5.5: (a) LIV curves of the FP-tapered lasers in pulsed operation. The optical power output scales with the taper angle, as the active volume is increased. The peak power scale was calibrated for maximum collection efficiency and does not account for the actual system's collection efficiency. (b) Peak powers of the FP-tapered lasers, normalized to the average peak power of the ridge lasers. In the shaded area, the estimated power enhancement is displayed. In the solid line, the enhancement from a ridge width of 13 µm is shown; lower and upper limits correspond to ±1 µm ridge, respectively. In dotted line, the collection efficiency is shown. Data published in [189].

angle was estimated to be $\alpha = \sin^{-1}(D/2f) = 30°$. The divergence angle of the lasers, in turn, can be estimated from the beam parameter product (BPP) relation [190], [191], as:

$$M^2 = \frac{4\pi}{\lambda}\sigma_0\sigma_\theta \tag{5.1}$$

where λ is the wavelength, M^2 the beam quality factor (with $M^2 = 1$ for an ideal diffracted-limited beam) and $\sigma_{0,\theta}$ are the standard deviation of the near-field spatial intensity distribution and far-field angular intensity distribution. In the assumption of a sinusoidal electric field distribution, the near-field distribution can be expressed as $\sigma_0 \approx 0.18w$, being w the front facet width [192], [193].

In Fig. 5.5(b), the peak power of five devices per type is analysed. The box's horizontal

line represents the mean value, while its limits represent the 1st and 3rd quartiles, and whiskers correspond to the minimum and maximum values of the tested lasers. The experimental data are compared with the expected power enhancement (shaded area), estimated by the active volume increase and the system collection efficiency (dotted line).

The active area enhancement can be simply derived from the tapered geometry as:

$$A_{tap}/A_r = 1 + \frac{L \cdot DC^2 \tan(\vartheta/2)}{w_r}, \quad \text{with} \quad DC = L_{tap}/L \tag{5.2}$$

where A_{tap}/A_r is the active area enhancement with respect to a ridge laser of width w_r and length L (3.6mm in this case), DC is the portion of the taper section over the full cavity length (0.5 for the tested laser bars) and ϑ is the taper full-angle. The collection efficiency, instead, can be estimated assuming a power distribution in the form:

$$P(\theta_x, \theta_y) = P_0 \Phi(\theta_x) \Phi(\theta_y) \tag{5.3}$$

$$\Phi(\theta) = \exp\left[-2\left(\theta/2\sigma_\theta\right)^2\right] \tag{5.4}$$

where θ_x and θ_y are the angular distribution across the two perpendicular axis to the propagation direction and $\sigma_{\theta,x}, \sigma_{\theta,y}$ their standard deviation. It should be noted that in many textbooks, the full beam divergence $\Theta = 4\sigma$ is used. Eq. (5.4) is obtained from the paraxial approximation and the spatial intensity distribution, assuming $\sin(\theta) \approx \theta$. Such distribution is integrated over a cone of half-angle α, more conveniently in polar coordinates:

$$C = \frac{\int_0^{2\pi}\int_0^{\alpha} P(\theta_x, \theta_y)\, \varphi \, d\varphi \, d\phi}{\int_0^{2\pi}\int_0^{\pi/2} P(\theta_x, \theta_y)\, \varphi \, d\varphi \, d\phi} \tag{5.5}$$

$$\text{with} \quad \theta_x = \varphi \cos\phi$$
$$\theta_y = \varphi \sin\phi$$

The fast-axis divergence angle is assumed constant for all the devices and was estimated for a ridge height of 12 µm, which corresponds to $\sigma_{\theta,y} \approx 29.5°$. Thus, the collection efficiency can be calculated for the different taper lasers, by Eq. (5.1) assuming $M^2 = 1$ and retrieving the facet widths in the four cases (13 µm, 45 µm, 70 µm, 108 µm). As it will be shown in Section 5.4, all these assumptions are well supported by experimental findings.

The straight ridge laser features an emission cone comparable to α, such that a collection efficiency of ∼45% is expected. Reducing the slow-axis divergence quickly brings the efficiency close to ∼70% (plateau of the dotted line). Above this point, the power enhancement mainly comes from the active volume increase. The continuous line depicts

Table 5.1: Summary of the main power enhancement features in tapered lasers. The active area enhancement and the collection efficiency are calculated for $L = 3.6$ mm, $DC = 0.5$ and $w_r = 13$ µm. The total enhancement factor is given by the product of the two. In parenthesis, the measured values are compared to the estimated ones.

Taper angle	A_{tap}/A_r	C	Enhancement factor (measured)	
0°	1	42.7%	1	(1)
1°	1.60	67.0%	2.52	(2.48)
2°	2.21	68.3%	3.53	(3.34)
3°	2.81	68.7%	4.52	(4.26)

the optical power enhancement, as described before, for a ridge width of 13 µm (lower and upper boundaries represent ridge widths of ±1 µm, respectively). The experimental data are in good agreement with the expected power enhancement, even if a strong variation from device to device was observed. In conclusion, by neglecting the different collection efficiency, a power enhancement up to 2.8 times (3° taper) was obtained, which agrees well with the active volume enhancement (∼3).

These quantities are summarized in Table 5.1. The power enhancement factor is calculated as the product of the active area and the collection efficiency, normalized to the ridge laser. As it can be seen, the performances seem to deviate from the expected value at larger taper angles. On one side, this could be indicative of a not-ideal behavior, namely non-adiabatic expansion of the beam in the large taper. This can be expected from Eq. (4.32), which implies a maximum facet width of 81 µm for the largest taper angle of 3°. On the other side, the taper facet reaches 108 µm, meaning that according to such relation, non-adiabatic expansion happens in the last 500 µm of the taper.

It should be addressed that in such comparison, the maximum optical powers of the tapered devices were considered. However, the increase in active zone comes with a modification of the cavity geometry, affecting many other parameters such as losses and threshold current density, discussed in the next section. To conclude, while a clear trend was observed and justified, deviations from the presented model can be expected, as these fine parameters have been neglected.

5.2.2 Threshold current density behavior

Another interesting aspect of tapered lasers is the behavior of the threshold current density with the taper angle. It must be noted that the standard expression for threshold current density does not apply to tapered lasers, as it is derived in the assumption of constant waveguide width and photon density independent of the position along the propagation direction [188]. Nevertheless, some general conclusions and insights can be

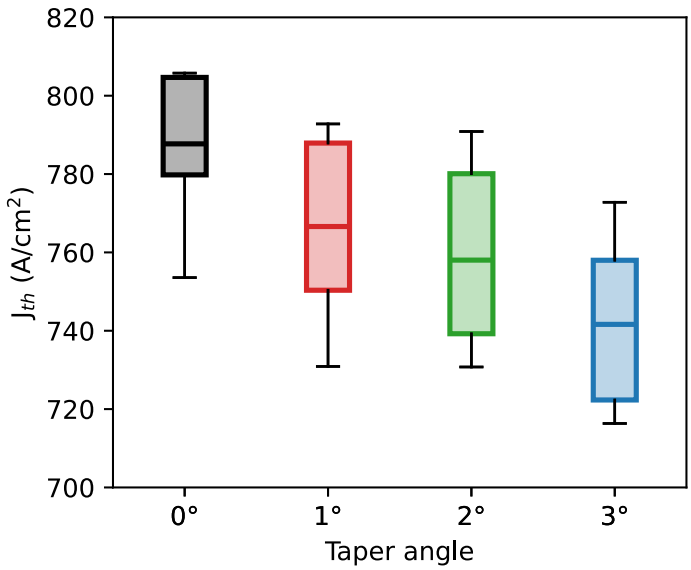

Figure 5.6: Boxplot of the threshold current densities of the FP-tapered lasers presented in Fig. 5.5b. The threshold current density decreases with the taper angle up to 6%. Adapted from [189].

drawn from the analysis of these data.

In Fig. 5.6, the threshold current densities of the same devices presented in Fig. 5.6 are shown. Threshold current densities for straight lasers around 0.8 kA/cm^2 at room temperature were found, in consistence with [169], while values down to 0.74 kA/cm^2 were measured for tapered lasers.

Such behavior has been investigated in similar works [181], [188], [194], [195] and is often explained by the improved mode confinement factor resulting in reduced waveguide losses in the tapered part. Eq. (4.30) provides the dependency of the threshold current density with the waveguide and laser parameters, showing the simultaneous effect of waveguide losses and confinement factor.

To prove this assumption, a mode analysis of the fundamental TM mode for variable ridge widths was performed with the finite element solver of COMSOL multiphysics (mode analysis). The simulation environment was bounded by perfectly matched layers (which behave as perfect absorbers) to prevent the formation of standing waves patterns. The geometry of the waveguide was constructed following the dovetail shape of the ridge, as a consequence of wet etching and is presented in Fig. 5.7. The material stacks and the parameters used in the simulation are presented in Table 5.2. The refractive index and losses cladding layers are obtained from the Drude model, with the knowledge of the doping level. In the spacer and in the active region, the losses have been considered zero, for the low residual doping of the spacers and the transparency condition of the active region. For the latter, the refractive index was obtained as an average over the layers that compose the AR.

Among the calculated modes, the fundamental TM mode was kept and the results are shown in Fig. 5.8. The mode analysis solves the structure providing the complex mode

Table 5.2: Materials and simulation parameters.

Material	**Thickness**	**Refractive index**
Air	/	1 + 0·i
Resist	/	1.6 + 0.1·i
Gold	400 nm	-14 + 81·i [196]
Upper Cladding	3 µm	2.89 + 0.009·i
Spacer	3 µm	3.4 + 0·i
Active Zone	3.6 µm	3.37 + 0·i
Bottom Cladding	2 µm	2.89 + 0.009·i
Substrate	30 µm	1.701 + 0.105·i

effective index $\tilde{n}$. In particular, the real part corresponds to the mode effective index ($\text{Real}(\tilde{n}) = n_{eff}$), which satisfies $\beta = n_{eff}k_0$, being β the propagation constant of the mode in the waveguide and k_0 the vacuum wavevector. The imaginary part corresponds to the extinction coefficient ($\text{Imag}(\tilde{n}) = \kappa$), from which the waveguide absorption coefficient can be determined as:

$$\alpha = \frac{4\pi}{\lambda_0}\kappa \tag{5.6}$$

The waveguide losses decrease as the mode overlap with the lossy lateral insulation layer is reduced. At the same time, the mode overlap in the active region is increased. Both these properties are beneficial for the threshold current density. The tapered lasers are however complex environments. The non-uniformity of the ridge width along the cavity position induces a position-dependent loss and mode overlap. This dependency is portrayed in Fig. 5.9. For the ridge waveguide, the ridge width, mode losses and confinement factor are independent from the cavity position. In the tapered lasers, however, these quantities vary along the position and can be obtained via interpolation of the values retrieved in Fig. 5.8.

As a first approximation, α_w and Γ in the tapered cavity can be obtained as an 'average' over the cavity length, reported in Fig. 5.9. Finally, the threshold current density shift

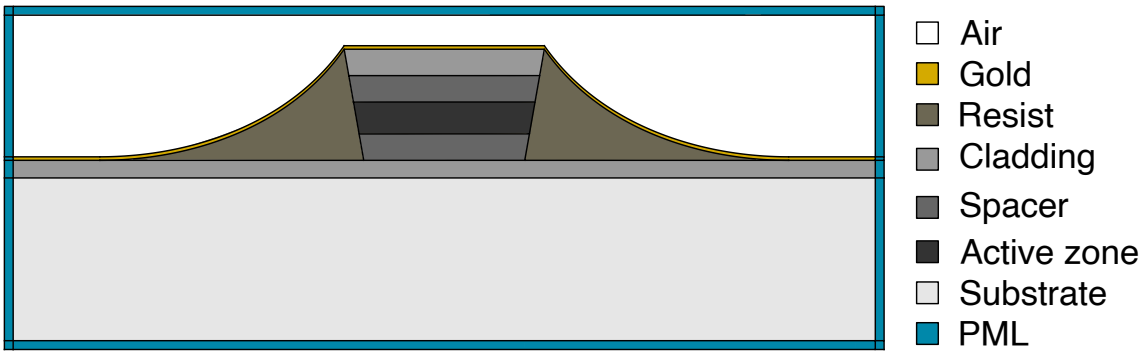

Figure 5.7: Environment of the mode analysis simulation with the simulation domains.

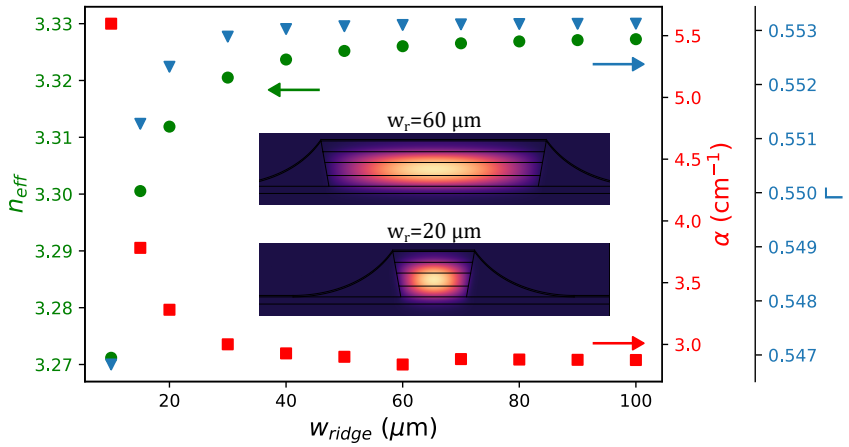

Figure 5.8: Fundamental mode parameters for a parametric sweep of the ridge width.

from the ridge device can be estimated from the variation of α_w and Γ:

$$\delta J_{th} = \frac{\partial J_{th}}{\partial \alpha_w}\delta\alpha_w + \frac{\partial J_{th}}{\partial \Gamma}\delta\Gamma \tag{5.7}$$

with $\delta\alpha_w = \alpha_{x^\circ} - \alpha_{0^\circ}$ and $\delta\Gamma = \Gamma_{x^\circ} - \Gamma_{0^\circ}$. Among the two contributions, the most relevant comes from the waveguide losses.

For the three tapered waveguides, the threshold current densities percentage variations are -2.77%, -3.11% and -3.23% for the 1°, 2° and 3° taper respectively, calculated with respect to a ridge of $w_r = 13$ µm, with $g = 46$ cm/A and $\alpha_m = -\ln R/L$, and $R = 0.29$ the Fresnel reflectivity. On the contrary, the experimental values provided shifts of -3.29%, -4.58% and -6.95%. The values are in fair agreement for the smaller taper angles, but considerably underestimated for the large angle, suggesting that other effects might

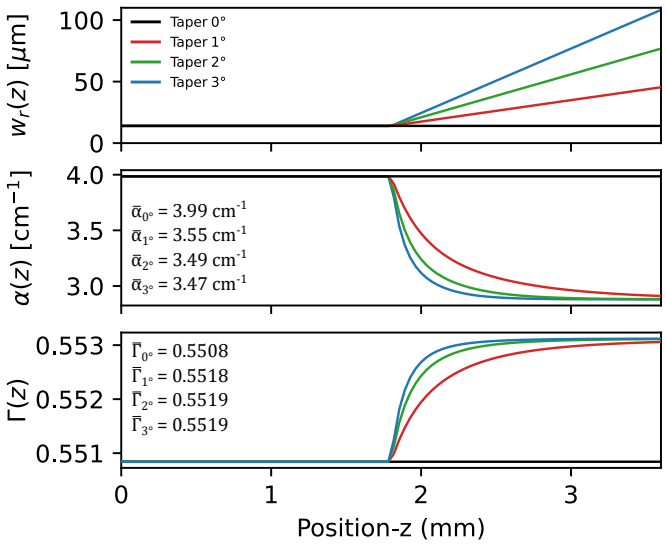

Figure 5.9: Position dependency of w_r, α_w and Γ for the tapered devices. The ridge width in the ridge section was $w_r = 13$ µm.

influence the threshold current density behavior. Additional efforts should be spent to elucidate the deviation observed at larger taper angles.

Two final remarks should be added to complete the discussion. First, adjustments to the ridge width used for the calculation might lead to better agreement with the experimental data, highlighting the strong dependence of the model to the waveguide geometry. For instance, at $w_r = 12$ µm, the percentage shifts are -3.49%, -3.88% and -4.02%. The second point concerns the expected reduction of the tapered facet reflectivity. Since only the central portion of the field can couple back to the cavity, one would expect additional mirror losses, resulting in an increased threshold current, in contradiction with the experimental findings.

As a conclusion, it can be assessed that the influence of the waveguide losses and the confinement factor are evident. However, the deviation at larger taper angles could not be explained with the simplified model hereby presented.

5.3 Coatings deposition

A classical yet effective approach to improve the outcoupled power consists in the deposition of thin dielectric films on the laser facets. Proper facet coatings help to maximize the output from one side, and reduce it from the opposite side, where the energy is eventually lost. Anti-reflection (AR) coatings allow more efficient energy extraction from the cavity, whereas high-reflection (HR) coatings improve the reflectivity of the facet, reducing the cavity losses.

The most advanced AR coatings consist of a series of thin layers, which behave as a narrow passband filter over the designed wavelength region. Such an approach exploits destructive interference of the reflected light, allowing its full transmission. A simplification of this technology is the single quarter-wavelength coating, where a single layer of a dielectric material of thickness $\lambda_n/4$ is used, λ_n being the wavelength in the medium. Application of combined AR/HR coatings allows for further improvement of the slope efficiency and for reduction of the threshold current density compared with only AR-coated devices. Metal deposited on the laser facet is often used as HR coating. To prevent electrical shorting of the device an insulator layer is usually deposited on the facet before its metallization. In order to identify the optimal dielectric thickness (for both AR and HR coatings), the transfer matrix method was used.

5.3.1 Wave-transfer matrix formalism

In the transfer-matrix formalism, the total transmittance and reflectance of a multilayered system is obtained by matrix multiplication of the individual wave-transfer matrices. This method was firstly discussed from Abeles in [197]. Here, we make use of an equivalent notation from Saleh and Teich [198]. The amplitudes of the forward and backward propagating waves at the entrance (U_1^+, U_1^-) and exit (U_2^+, U_2^-) planes of the optical system

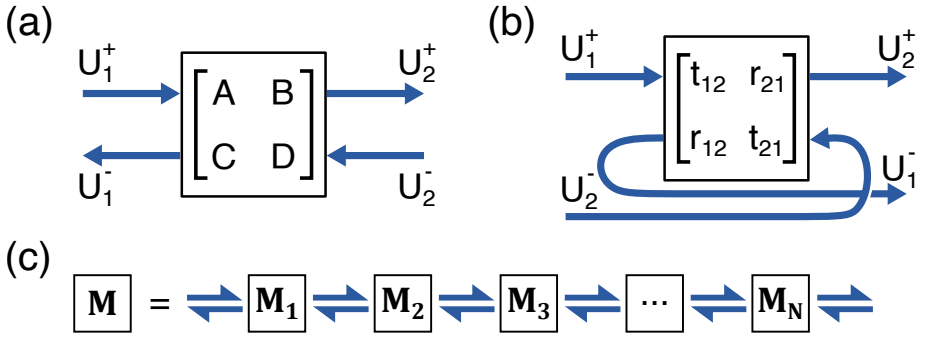

Figure 5.10: Definition of (a) wave-transfer matrix, (b) scatter matrix and (c) multiplication rules of the transfer matrices.

are related by:

$$\begin{bmatrix} U_2^+ \\ U_2^- \end{bmatrix} = \begin{bmatrix} A & B \\ C & D \end{bmatrix} \begin{bmatrix} U_1^+ \\ U_1^- \end{bmatrix} \tag{5.8}$$

where each optical components is identified by an (A, B, C, D) matrix, and the multilayered structure matrix is defined by:

$$\mathbf{M} = \mathbf{M_N} \dots \mathbf{M_2 M_1} \tag{5.9}$$

The transfer-matrix formalism is often combined with the scattering-matrix one, which directly relates the transmitted and reflected waves to the properties of the optical element. The scattering matrix elements have physical significance since they correspond to the forward and backwards transmission and reflection coefficients:

$$\begin{bmatrix} U_2^+ \\ U_1^- \end{bmatrix} = \begin{bmatrix} t_{12} & r_{21} \\ r_{12} & t_{21} \end{bmatrix} \begin{bmatrix} U_1^+ \\ U_2^- \end{bmatrix} \tag{5.10}$$

The drawback of the scatter matrix is that the **S** matrix of cascaded elements is not the product of the **S** matrices of the constituent elements. The relation between the forward and backward propagating amplitudes with the transfer and scattering matrix is provided in Fig. 5.10.

For this reason, the S-matrices of the individual elements (defined by the known transmission and reflection coefficients) are converted into M-matrices, whose multiplication provides the system transfer-function. Finally, from the resulting **M** matrix, the transmission and reflection coefficient can be obtained. The relationship between **S** and **M** is

obtained from manipulation of Eqs. (5.8) and (5.10) as:

$$\mathbf{M} = \frac{1}{t_{21}} \begin{bmatrix} t_{12}t_{21} - r_{12}r_{21} & r_{21} \\ -r_{12} & 1 \end{bmatrix} \tag{5.11}$$

$$\mathbf{S} = \frac{1}{D} \begin{bmatrix} AD - BC & B \\ -C & 1 \end{bmatrix} \tag{5.12}$$

The relevant matrices to solve the system are the scattering matrix for the single dielectric boundary and the propagation through an optical medium, which expressed in terms of their transfer-matrix are respectively given by:

$$\mathbf{M_{1\to 2}} = \frac{1}{2\tilde{n}_2} \begin{bmatrix} \tilde{n}_2 + \tilde{n}_1 & \tilde{n}_2 - \tilde{n}_1 \\ \tilde{n}_2 - \tilde{n}_1 & \tilde{n}_2 + \tilde{n}_1 \end{bmatrix} \tag{5.13}$$

$$\mathbf{M}_{\text{prop}} = \begin{bmatrix} e^{+i\tilde{n}k_0 d} & 0 \\ 0 & e^{-i\tilde{n}k_0 d} \end{bmatrix} \tag{5.14}$$

where $\tilde{n}_1, \tilde{n}_2$ are the complex refractive indexes of the two media ($\tilde{n} = n + i \cdot \kappa$), and d is the propagation length (i.e. the layer thickness for normal incidence). The phase sign in $\mathbf{M}_{\text{prop}}$ depends on the used convention. In this work, the phase has been chosen such that the extinction coefficients (κ) are positive for material absorption. The transfer-matrix for the AR and HR-coating will be:

$$\mathbf{M}_{\text{AR}} = \mathbf{M}_{\mathbf{SiO_2}\to\text{Air}}\mathbf{M}_{\text{prop,}\mathbf{SiO_2}}\mathbf{M}_{\text{AZ}\to\mathbf{SiO_2}}$$
$$\mathbf{M}_{\text{HR}} = \mathbf{M}_{\mathbf{SiO_2}\to\text{Au}}\mathbf{M}_{\text{prop,}\mathbf{SiO_2}}\mathbf{M}_{\text{AZ}\to\mathbf{SiO_2}}$$

Finally, the reflectivity $R = r_{12}r_{12}^*$ is obtained from the knowledge of the calculated

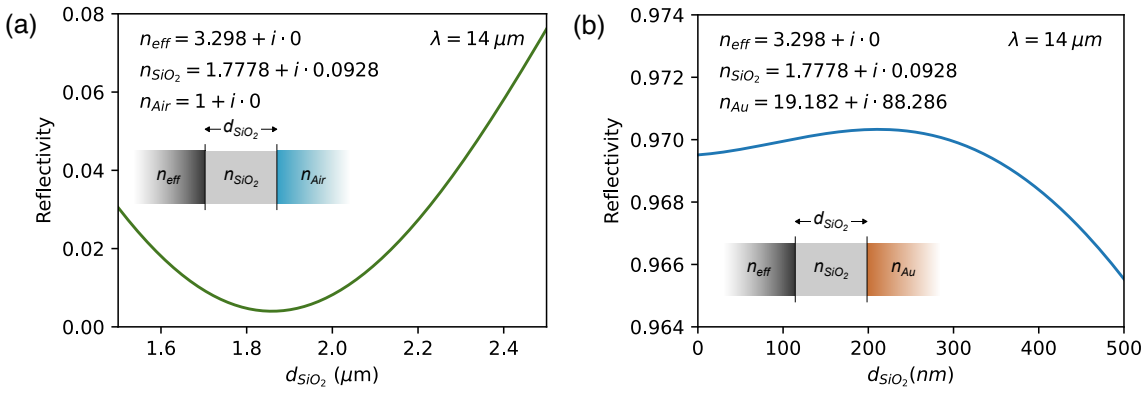

Figure 5.11: Transfer-matrix simulation for (a) an AR-coating and (b) HR-coating. Adapted from [189].

$\mathbf{M_{AR(HR)}}$ elements with the relation $r_{12} = -C/D$.

5.3.2 Coated devices

For both AR and HR coatings, the deposition was performed via sputtering by exposing the laser facet vertically to the sputtered target. The uncoated part of the device was protected with a photoresist (AZ1505, MicroChemical) and the protected zone was lifted-off with acetone cleaning.

The materials choice for the coatings was limited to the available sputtering targets of the sputter deposition machine (SiO_2, Ti and Au). For this reason, silica (SiO_2) was chosen as an AR-layer, even though non-negligible absorptions occur within the thin-film. Transfer-matrix simulations of the two coating stacks are presented in Fig. 5.11. The obtained results might be an over-estimation of the real reflectivity, since diffraction losses were not taken into account.

In a single layer AR-coating, the optimal transmittance is obtained for a layer's refractive index $n = \sqrt{n_0 n_{eff}}$, n_0 being the air refractive index and n_{eff} the mode effective refractive index in the laser waveguide. For silica (SiO_2) at $\lambda_0 = 14$ µm, a refractive index of 1.7778 is found [199], which matches closely with the optimal value of ∼1.81. A SiO_2 layer of ∼1.9 µm was deposited via sputtering on the front facet of two tapered lasers. It is worth noticing that the larger tapered facet supports a fundamental mode with a higher effective refractive index. Hence, the optimal coating refractive index also increases, leading to a worse performance of the AR-coating for constant deposition thickness. However, such variation is less than 100 ppm in reflectivity (or 0.01% reflectivity change), which justifies the choice of depositing the same layer for all devices.

The HR-coating consisted of a bilayer of SiO_2/Au of thickness 220/200nm on the straight part facets. The gold thickness was chosen sufficiently larger than the penetration depth estimated to be around 17 nm.

The LI-curves of the uncoated (as in Fig. 5.5(a)), AR-coated and AR/HR-coated tapered lasers are shown in Fig. 5.12, for the same pulsed operation scheme (330 ns, 12 kHz repetition rate combined with 30 Hz square wave modulation). After AR-coating, the optical power of the lasers significantly increased and the HR coating further improved the slope efficiency dP/dI of the devices. The characteristics of the lasers are summarized in Table 5.3. After AR-coating, the threshold current density increased by about 18% for both devices as an effect of the higher front mirror losses. The HR-coating decreases J_{th} almost to the values of uncoated devices due to the reduced loss of the back mirror.

The effect of the coatings was analysed using Eq. (4.30) for the QCL threshold current density J_{th} including the transparency current J_{tr}. The mirror losses α_m were estimated by $\alpha_m = -\ln(R_F R_B)/2L$, with R_F, R_B being the front and back facet reflectivities. Reflectivity of uncoated facets can be calculated to be 0.29 from the Fresnel equation.

The transparency current, as formerly discussed, accounts mainly for thermal popula-

Table 5.3: Measured quantities for 1° and 3° taper, before and after coating deposition. Threshold current density, slope efficiency and maximum optical powers are compared. Values in square brackets correspond to enhancement factor compared to the uncoated device.

Device	**Quantity**		**Uncoated**	**AR**	**AR/HR**
1° Taper	J_{th}	(kA/cm^2)	0.738	0.865	0.790
	dP/dI	(mW/A)	66 [1]	171 [2.6]	193 [2.9]
	$P_{\max}$	(mW)	48 [1]	163 [3.4]	201 [4.2]
3° Taper	J_{th}	(kA/cm^2)	0.745	0.877	0.772
	dP/dI	(mW/A)	66 [1]	143 [2.2]	165 [2.5]
	$P_{\max}$	(mW)	87 [1]	213 [2.45]	391 [4.5]

tion of the bottom lasing level, which requires additional electron injection to compensate this effect and to preserve the population inversion. In long wavelength QCLs, J_{tr} is the main component of the threshold current. Any change in the facet reflectivity providing a new value of the mirror loss α_{mc} results in a corresponding change in the threshold ΔJ_{th} that can be negative if the reflectivities R_{FC} and/or R_{BC} increase:

$$\Delta J_{th} = \frac{\alpha_{mc} - \alpha_m}{\Gamma g} \frac{1}{2L} = \frac{1}{2L\Gamma g} \ln\left(\frac{R_F R_B}{R_{FC} R_{BC}}\right) \tag{5.15}$$

Let us first consider the effect of only an AR coating. In the tested lasers the AR-coating resulted in a threshold increase of 0.126 and 0.132 kA/cm^2 for the 1° and 3°

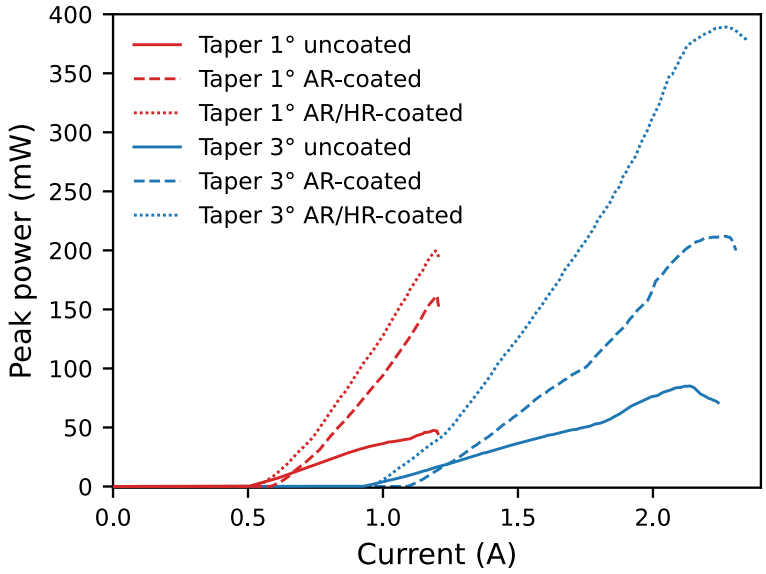

Figure 5.12: LI-curves of the uncoated (continuous line), AR- (dashed line) and AR/HR-coated (dotted line) tapered lasers operated in pulsed mode. Data published in [189].

tapered laser, respectively. Using a value of modal gain $\Gamma g = 23$ cm/kA in Eq. (5.15) we obtain $\Delta J_{th} = 0.126$ kA/cm^2 for the reflectivity of AR-coated facet $R_{FC} = 0.035$. The facet reflectivity can also be found from the slope efficiency of the AR-coated lasers. The portion of generated photons that can escape the laser cavity is defined by the external quantum efficiency:

$$\eta_{\text{ext}} = \frac{\alpha_m}{\alpha_m + \alpha_w} \tag{5.16}$$

In the case of perfect HR coatings on both facets no photon can leave the laser cavity. Inversely, AR coatings improve the light extraction efficiency at the expense of a higher laser threshold produced by the additional loss of photons in the resonator. It is worth noting that in long wavelength QCLs, the threshold increase provoked by the AR coating is less dramatic than at shorter wavelengths. This is mainly due to the high contribution of J_{tr}, which reduces the effect of mirror losses on the threshold current density. Powers of light that leave the resonator through the front (P_F) and back (P_B) facet are related to the facet reflectivities by [200]:

$$\frac{P_F}{P_B} = \sqrt{\frac{R_B}{R_F}}\frac{1-R_F}{1-R_B} = \beta \tag{5.17}$$

from which we obtain $\beta = 1$ for equal reflectivities. Finally, the slope efficiency of the emission through the front facet dP_F/dI, which is related to the reflectivity of both facets, R_F and R_B, can be expressed as:

$$\frac{dP_F}{dI} = \frac{h\nu}{e}\eta_i\frac{P_F}{P_B + P_F}\eta_{\text{ext}} = \frac{h\nu}{e}\eta_i\frac{\beta}{1+\beta}\frac{\alpha_m}{\alpha_m + \alpha_w} \tag{5.18}$$

where $h\nu$ is the photon energy, e is the elementary charge, and η_i is the internal differential efficiency [201]. The last equation gives us a possibility to calculate a ratio of the slope efficiencies of the lasers with different treatment of the facets. In these calculations, waveguide losses $\alpha_w \approx 3.6$ cm^{-1} were used. We compared the initial slope efficiency of the lasers measured from the tapered side just above the threshold (Table 5.3) to avoid the influence of mode competition that can affect the expected linearity of the light-current characteristics. Due to the AR-coatings the slope efficiency of the tested devices increased by 2.6 and 2.2 times for 1° and 3°-tapered lasers, respectively. The reflectivity value of 0.035 obtained from the analysis of the threshold current should result in a smaller increase of 2.1. The observed improvement of the slope efficiency can be achieved if the reflectivity of the AR-coating is in the range 0.01-0.02. On the other hand, with such reflectivity value the threshold current density of the AR-coated QCLs should increase by 0.20-0.16 kA/cm^2, which is considerably larger than the observed shift. It is worth noting that the maximum optical power of the lasers increased even stronger than the initial slope efficiency by a factor of 3.4 for the 1°-tapered device. Application of the HR-coating on the back facets of the AR-coated devices increased the slope efficiency by about 12% whereas the threshold current density decreased almost to the characteristics of the uncoated devices with a shift

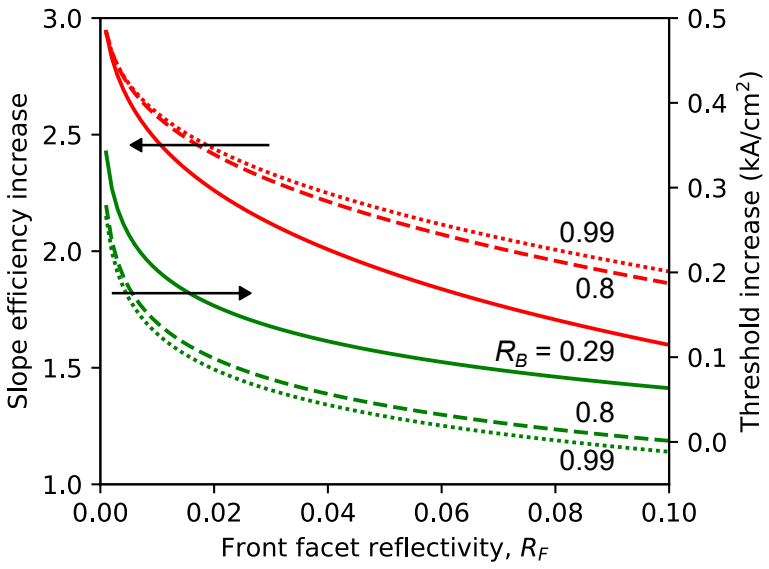

Figure 5.13: Calculated increase in the slope efficiency and threshold current density of coated QCLs as a function of the front facet reflectivity for different values of the back facet reflectivity R_B. The uncoated device is taken as reference (zero threshold current increase and slope efficiency increase of 1). Data published in [189].

of 0.052 and 0.027 kA/cm^2 for 1° and 3°-tapered QCLs, respectively.

The calculated change in the laser characteristics produced by facet coatings is presented in Fig. 5.13 as a function of the front facet reflectivity for uncoated ($R_B = 0.29$) and HR-coated back facets ($R_B = 0.8$ and 0.99). It is interesting to note that HR-coating has no effect on the slope efficiency when the reflectivity of the front facet is low, less than 0.01, because all photons leave the laser cavity through its transparent end and their portion reflecting from the back facet is small. Even for the front facet reflectivities of a few percent both the slope efficiency and the threshold current almost do not change when $R_B > 0.8$. The observed J_{th} shifts of the AR/HR-coated lasers are in fair agreement with the calculated data for a front facet reflectivity of about 0.04 and $R_B > 0.9$. Summarizing the obtained results on AR/HR coating of the tapered QCLs, we should first note the significant increase in the slope efficiency, up to a factor of 2.9 in 1°-tapered lasers, compared with the same uncoated devices. Such improvement can only be obtained when the reflectivity of the front facet is very low, less than 0.01. On the other hand, the observed shifts of the J_{th} after AR and AR/HR coatings correspond to poorer R_F values on the order of 0.04. These data are more consistent as the threshold current is quite reliably measured whereas the slope of the light-current curves can be affected by the spatial mode competition and the collection efficiency of the optical setup. Otherwise, we should admit that the employed approaches are not valid and should be revised to obtain the expected agreement between the RF values obtained by the used methods. For instance, the equations here proposed are valid in the assumption of uniform gain and losses within the length of the cavity [202], which might not be true for complex resonators such

as the tapered waveguide. In support of this supposition, we should also note that the increase in the total emitted power in the AR/HR-coated devices is even larger than the improvement in the initial slope efficiency in comparison with uncoated lasers, reaching a factor of 4 in the 1°-tapered QCLs. The deposition of an AR coating causes only a slight increase in the threshold current density, which is dominated by the transparency current density. The optical power is enhanced by at least 2 times with an AR-coating and up to 4 times with AR/HR coating. The lasers fabricated and studied in this work outperform long-wavelength InAs-based QCLs reported to date in terms of slope efficiency and output optical power.

5.4 Far-Field and beam quality

The far-field patterns of the tapered lasers were measured with the setup presented in Fig. 5.14, built to determine the divergence and beam quality factor along the slow-axis direction. The laser was mounted on top of a rotation stage (Thorlabs, PRMTZ8), aligning its front facet to the rotation axis. The stage was connected to a personal computer and controlled via a custom LabView program. The laser was biased with the same driving scheme as the one presented in Section 5.2.1. The diverging cone of light was collected on a pyrodetector (InfraTec, LIE-332f-#) without interposing any optical element between the laser and the detector element. The pyrodetector with an active element of 1.3 mm diameter was placed at several centimetres from the laser facet. The pyrodetector signal was demodulated via lock-in amplifier (AMETEK, SR7270) and the magnitude was recorded on a personal computer together with the stage position. Filter order and time constant of the lock-in amplifier were adjusted according to the rotation stage speed, in order to optimize the signal-to-noise ratio while keeping the experiment duration reasonably low.

In Fig. 5.15(c-f), the far field profiles for the four laser types are shown. Tapered lasers exhibited narrower far-field patterns in the slow-axis direction, as expected from

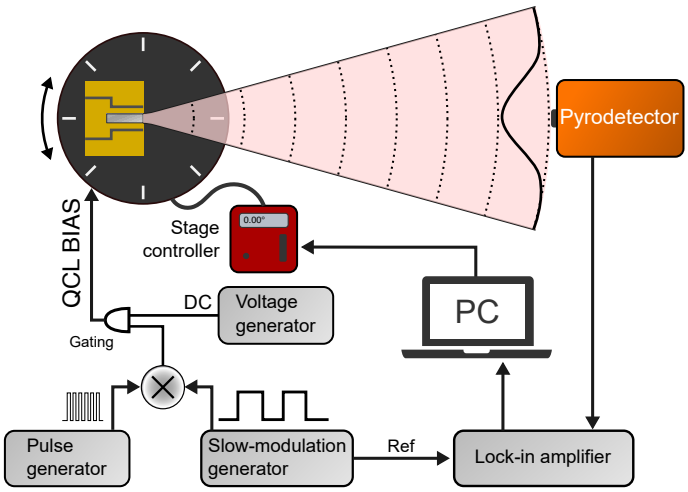

Figure 5.14: Schematic of the setup used for the measurement of the far-field patterns.

the diffraction theory. The spatial-frequency components of a beam propagating along the z-direction can be obtained, under the paraxial approximation, as:

$$P(s) = \int_{-\infty}^{+\infty} E(x) e^{i2\pi s x} dx \tag{5.19}$$

being s the spatial frequency ($2\pi s = k_x = (2\pi\lambda)\sin\theta$), and $E(x)$ the electric field distribution along the slow-axis of the laser facet. The theoretical far-field profiles were calculated from the near-field electric field distributions, obtained via COMSOL simulations. In Fig. 5.15(a) the electric field distribution of the fundamental TM mode in a 14 µm wide waveguide is presented. Analogous simulations were performed for tapered facets, using ridge widths of 45 µm, 70 µm and 108 µm, according to the laser geometry. The electric field distribution along the slow-axis direction was obtained from the simulation (an example is given in Fig. 5.15(b)) and used in Eq. (5.19) to simulate the far-field intensity profile (dots in panels (c-f)), retrieved as the modulus squared of the spatial-frequency distribution. Overall, an excellent agreement between the expected and the experimental far-field patterns was found, proving that nearly ideal Gaussian beam qualities were achieved along the slow-axis.

The beam quality was estimated from the experimental data, using the second order

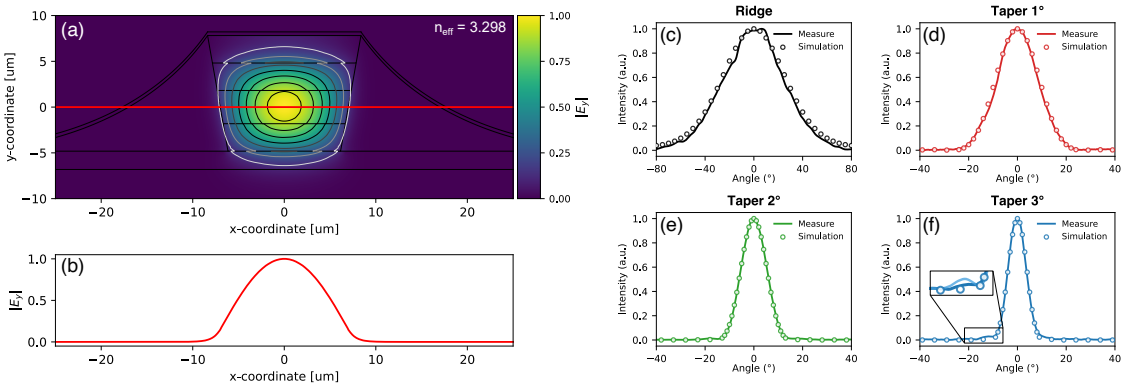

Figure 5.15: (a) Simulation of a ridge waveguide of 14 µm. The electric field's magnitude for the fundamental TM mode is shown. In red, a cutline passing through the center of the active zone. (b) Electric field amplitude along the cutline, used to simulate the far-field intensity presented in (c). (c-f) Far-field angular intensity distribution measured for the four lasers (continuous lines). Overlayed in dots, simulation of the expected far-field for the respective laser. In panel (f), an inset of a side-lobe appearance is shown: in light blue, a far-field measurement at higher bias current ($1.8I_{th}$) is presented. The side-lobe is more pronounced, causing a degradation of the M^2 factor, as shown in Table 5.4. Aside from the side-lobe, no difference with the low bias current measurement was observed. Data published in [189].

Table 5.4: Standard deviation of the angular intensity distribution (σ_θ) and beam quality factor (M^2) for the four types of lasers. The values to the left/right of the arrow correspond to low/high current bias, respectively. If a single value is displayed, identical results were found. The M^2 is calculated according to Eq. (5.1).

Taper angle	σ_θ	$\mathbf{M^2}$
0°	26°	~ 1[a]
1°	8.03°	1.02
2°	5.06° $\rightarrow$ 5.13°	1.07 $\rightarrow$ 1.08
3°	4.23° $\rightarrow$ 4.80°	1.29 $\rightarrow$ 1.46

[a] The quality factor for a narrow ridge suffers from larger near-field distribution errors. This can lead to unphysical values $M^2 < 1$.

momentum (standard deviation) of the angular intensity distribution, defined as:

$$\sigma_\theta^2 = \frac{\int_{-\infty}^{+\infty} (\theta - \bar{\theta})^2 I(\theta) d\theta}{\int_{-\infty}^{+\infty} I(\theta) d\theta} \tag{5.20}$$

being $\bar{\theta}$ the first order momentum (mean) of the distribution. The Gaussian distribution is the probability density distribution with the smallest standard deviation. Thus, any deviation from Gaussian shape, leads to a deviation of the beam quality factor from 1. By using Eq. (5.1) with the knowledge of σ_θ by Eq. (5.20), the beam quality factor can be estimated. The standard deviation of the spatial intensity distribution was approximated from the facet width w_r using the formula $\sigma_0 = 0.18 w_r$. Calculation from the simulated electric field distribution led to similar results. The divergence angle and the beam quality factor for the profiles shown in Fig. 5.15 are presented in Table 5.4. Both were estimated for low ($1.5 I_{th}$) and high bias current ($1.8 I_{th}$), reported in table to the left and right of the arrow, respectively. A degradation of the beam quality was observed at higher currents, as a consequence of side lobes appearance. An example is shown on the left-wing of the intensity distribution of the 3° taper (inset of Fig. 5.15(f)).

5.5 Distributed Feedback Tapered QCLs

The last point to be discussed is the selection of single longitudinal mode emission. Spectroscopic applications require selective targeting of roto-vibrational transitions, to avoid possible interferences from neighboring absorbing lines.

Fabry-Pérot devices allow the oscillation of multiple modes within the gain spectrum of the laser, as an effect of the optical feedback provided by the facet reflectivity. The separation of the longitudinal modes (free spectral range) is defined by the cavity length

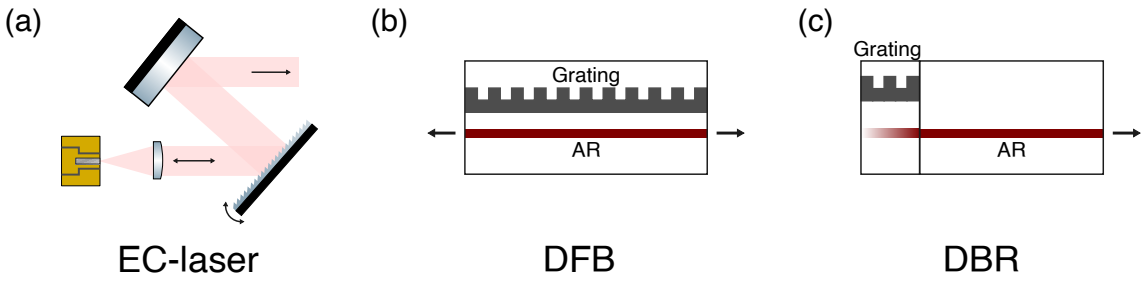

Figure 5.16: Schematic of (a) EC-laser in the Littrow configuration, (b) DFB and (c) DBR lasers.

and the group index of the material, similarly to what was presented in Section 3.1. Thus, FP-lasers find application when wide spectral features are probed and, just like in non-dispersive approaches, the resulting information is 'integrated' over the emission spectrum of the laser source.

Gas-phase spectroscopy requires single longitudinal mode operation which can be attained by introducing wavelength-dependent feedback to the laser cavity. The main approaches used for single mode selection are external cavity (EC) lasers, distributed feedback (DFB) lasers and, similarly, distributed Bragg reflector (DBR) lasers, schematically shown in Fig. 5.16.

In EC-lasers, a grating-coupled system is added to the laser chip to obtain a tunable single-mode source. An EC system is made up of three main elements, the gain element, the collimating lens and the grating which acts as a wavelength filter element within the system. A very common EC system is the Littrow configuration, where the first-order diffracted beam is back coupled into the laser, whereas the zeroth-order beam is collected through an additional mirror. Broad tuning is achieved through the rotation of the grating. The main advantages of this configuration are the increased feedback of the setup and the easier alignment of the optical components. However, care must be taken to avoid misalignment of the grating, while suppression of parasitic Fabry-Pérot interferences must be inhibited with AR-coating on the front-facet of the laser, thus complicating the realization of these sources.

Distributed feedback and distributed Bragg reflectors are monolithic solutions, in which the mode selection occurs by introducing frequency-dependent losses in the laser cavity (DFB) or in its vicinity (DBR). In the DFB laser, the frequency-dependent losses are induced by a grating etched in the semiconductor material, displaced vertically or laterally with respect to the active region. The presence of a corrugation in this layer induces a periodic modulation of the refractive index along the propagation direction of the mode within the cavity. Light propagating in a periodic medium of periodicity Λ is backscattered if the Bragg condition is satisfied $\Lambda = m\lambda_n/2$, being m the diffraction order and λ_n the wavelength in the medium. The scattering, distributed along the active region, provides optical feedback for the selection of the longitudinal mode. As it will be shown, however, two symmetric modes are generated as a consequence of the grating presence in the active

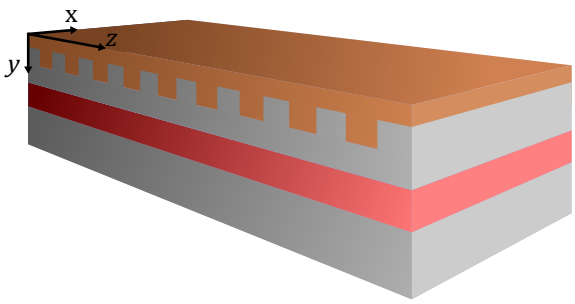

Figure 5.17: Pictorial representation of a DFB-laser with a grating etched on the top cladding of the device.

zone. Conversely, in a distributed Bragg reflector, the Bragg reflection happens near the cavity ends rather than in the active region. For this reason, the light back-scattered by the Bragg reflector selects a single longitudinal mode. The grating is etched outside of the active region and the DBR laser behaves as an FP laser whose mirror reflectivity varies with wavelength. Lasing occurs at the wavelength of highest reflectivity. Historically, DBR lasers developed in parallel with DFB lasers. However, the main limit was that if the unpumped active region material is used to etch the grating at the cavity ends, it will inevitably introduce high losses, compromising the designed reflectivity. If transparent materials are used, instead, the DBR and the active region form two separate waveguides and the transfer of the optical mode becomes the main limitation. In this case, an effective reflectivity is considered by accounting for coupling losses between the two regions.

In this work, DFB-structures were employed for the selection of the longitudinal mode, due to the easiness of the fabrication process. In the next section, the basic principles of the coupled-mode theory for DFB operation are provided.

5.5.1 Coupled-wave theory

The coupled-wave theory of DFB lasers was first introduced by Kogelnik and Shank [203] to describe the propagation of two coupled travelling waves in a periodic structure. In such structure, each travelling wave (forward propagating and backward propagating) injects energy to the wave travelling in the opposite direction as a consequence of the Bragg reflection.

The system can be modelled as a structure in which the refractive index is position dependent along the wave propagation, as in Fig. 5.17. Kogelnik and Shank proposed a general solution by including a complex refractive index, composed by a modulation of both the real (refractive index) and imaginary part (gain coefficient):

$$n(z) = n_{eff} + \frac{\Delta n_{eff}}{2} \cos(2\beta_B z) \tag{5.21}$$

$$\alpha(z) = \alpha + \frac{\Delta \alpha}{2} \cos(2\beta_B z) \tag{5.22}$$

where $\beta_B = \pi/\Lambda$ is the propagation constant at the Bragg condition, Λ is the periodicity of the system and $\Delta n_{eff}, \Delta\alpha$ are the modulations of the real and imaginary part of the complex index. The Bragg condition for a first order grating can be expressed as:

$$\Lambda = \frac{\lambda_B}{2n_{eff}} \tag{5.23}$$

meaning that the periodicity of the system is half of the wavelength in the medium λ/n_{eff}. The corresponding frequency in a homogeneous medium of refractive index n_{eff} is the Bragg frequency $\omega_B = c\beta_B$. The peculiar behavior of the grating is that a wave with such a frequency cannot propagate inside the periodic medium.

To understand the underlying phenomenon, one can start from the behavior of a wave inside an infinite periodic structure, which provides some important results applicable to the finite laser structures. This problem is analogous to the transport of electrons in crystals and shows similar solutions, namely Bloch-waves whose propagation is prohibited in proximity of the Bragg frequency.

It can be shown that at the Bragg condition two modes exist in the structure, with frequencies centred in ω_B and symmetrically separated by the stop-band $\Delta\omega$. This result is schematically shown in Fig. 5.18, which shows the dispersion diagram relating the propagation constant and the frequency of the propagating wave in a 1D-Bragg grating. The dispersion diagram highlights the photonics bandgaps as those regions where no solutions are found.

A simple way to depict this situation is the following: in order to have a mode within the structure at energy ω_B in correspondence of β_B, the effective index should correspond to the average index (n_{eff}). If we consider dielectric layers of equal thickness, such condition happens when the field (whose $\lambda_n = 2\Lambda$ for the Bragg condition) has its antinodes on the discontinuity surface, where it gets partially reflected. This process is so efficient that the wave propagation is completely inhibited and total internal reflection occurs. On contrary, when the antinodes are aligned to the centers of the material layers, the two band-edge modes are obtained. One mode will lie mostly in the high-refractive index material, thus appearing on the high frequency side of the stop-band, while the second mode will lie in the low-refractive index material, corresponding to the low frequency mode. The actual situation is more complicated since there are no such abrupt discontinuities in the etched grating, but the underlying concepts remain the same.

The transmittance of a Bragg grating is also presented in Fig. 5.18, showing the stop-band in correspondence to the Bragg wavelength (ω_B). If properly engineered, this wavelength-dependent transmission can be centred on the gain band of the laser, thus favouring the oscillation of the modes next to the Bragg frequency. The inherent symmetry of the system results in dual-mode emission, with mode separation given by $\Delta\omega$. However, in real devices the symmetry is broken by the presence of the random cleaving position in the periodic medium and by the mirrored facets, which introduce additional

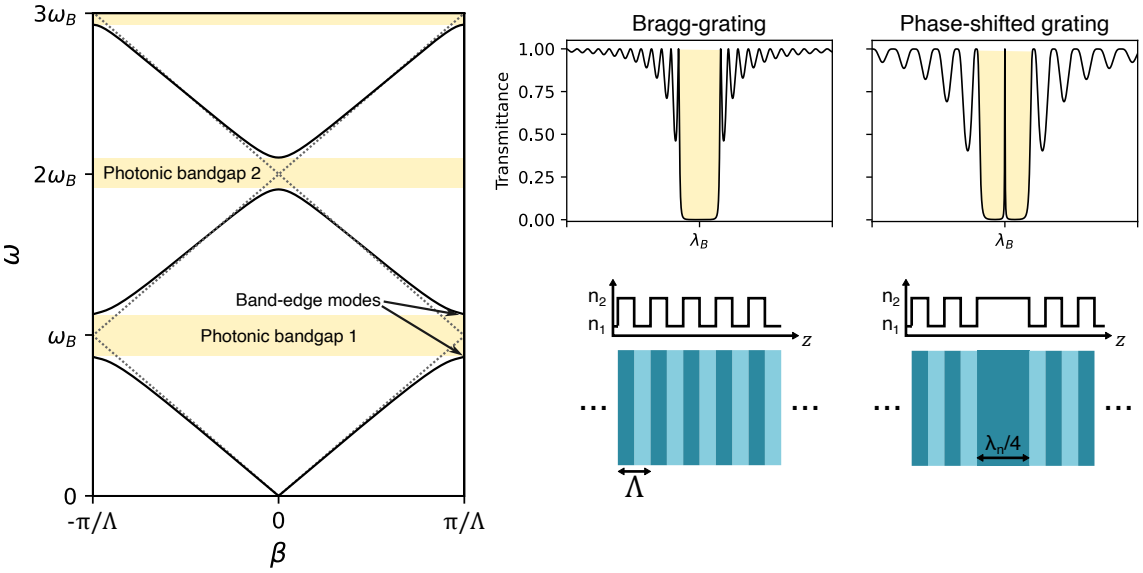

Figure 5.18: On the left, dispersion diagram of an infinitely-extended Bragg grating restricted to the first Brillouin zone. The generation of photonic bandgaps is highlighted, and the band-edge modes are indicated by the arrows. In dotted line, $\omega = c\beta$ is represented, corresponding to the propagation in a homogeneous medium of refractive index $\bar{n} = (n_1 + n_2)/2$, namely in absence of the modulation. On the right, the transmittance of a Bragg-grating and a phase-shifted grating. In the first, the field is fully reflected in the stop-band, hence prohibiting propagation. At the edge of the stop-band, two modes are observed. The phase-shifted grating adds a $\lambda/4$ phase-shifter to introduce a propagation mode in the stop-band, i.e. at the Bragg frequency.

phase-shifts. The breaking of the symmetry gives rise to a high threshold mode in the photonic bandgap. The higher threshold is due to the fact that such mode is mainly localized in the vicinity of the facets. There are however approaches that favour the bandgap mode. This can be achieved either via deposition of AR and HR coating, either by introducing an element that breaks the symmetry of the photonic crystal. The latter is the case of the phase-shifted grating, where a $\lambda/4$ element is used to induce a $\pi/2$ phase shift. The resulting structure, as presented in Fig. 5.18, exhibits a mode in correspondence of the Bragg frequency.

In the model from Kogelnik and Shank, the solution of the system is provided for complex index, as introduced in Eqs. (5.21) and (5.22). They derived a fundamental quantity of the periodic structure, the coupling coefficient κ:

$$\kappa = \frac{\pi \Delta n_{eff}}{2\lambda_B} + \frac{i\Delta\alpha}{4} \tag{5.24}$$

which measures the strength of the backward Bragg scattering. In the general scenario, both Δn_{eff} and $\Delta\alpha$ can participate to the feedback. For what concerns this work, however, the mode selectivity is mainly defined by the index contrast, while the loss contribution introduces a differential gain between the band-edge modes.

Under index coupling condition, the coupling coefficient is directly proportional to the

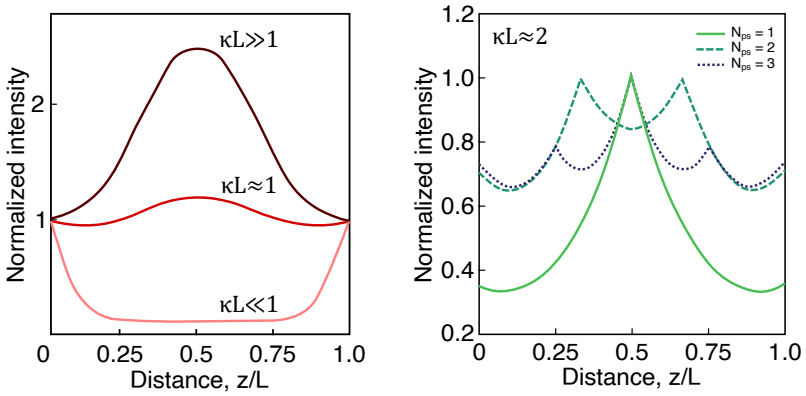

Figure 5.19: On the left, the spatial intensity distribution for several coupling constants is shown. Adapted from [203]. On the right, the same is portrayed in the presence of a variable number of phase-shifters (N_{ps}). Adapted from [204].

index contrast and can be expressed in terms of mode separation by rearranging Eq. (5.24) with $\Delta\alpha \approx 0$:

$$\kappa = \frac{\Delta\omega}{2c} n_{eff} \tag{5.25}$$

The importance of this quantity lies in the dramatic effects that it exerts on the intensity distribution in the laser resonator. Usually, the dimensionless quantity κL is used to describe the spatial distribution of the mode. When the coupling is small ($\kappa L \ll 1$), the device is said to be in undercoupling conditions and the intensity is concentrated at the facet of the device. Conversely, when the coupling is large ($\kappa L \gg 1$), the modal intensity peaks in the center of the device and decays towards the ends (overcoupling condition). The regime in the middle is defined critical coupling, where $\kappa L \approx 1$ and the intensity is more or less uniformly distributed throughout the device. Summarizing, in the undercoupling condition, the field interacts weakly with the grating since most of the energy is localized at the device ends; in the overcoupling condition, the power from the device is less efficiently extracted as a consequence of its strong confinement in the middle of the device; finally, the optimal situation is found in the critical coupling condition. Such effect is portrayed in Fig. 5.19, along with the effect of a phase-shifter in the grating. The beneficial effect of a phase-shifter was already demonstrated in Fig. 5.18, by showing the introduction of a gap-mode. Here, it is interesting to note that in critical coupling conditions, the field is mainly concentrated in the shifter position. This, in turn, results in spatial hole burning with the appearance of side-modes. For this reason, approaches with an increased number of shifters (N_{ps}), equally spaced along the cavity can be employed, to achieve a more homogeneous distribution of the field in the cavity.

In this work, a metallo-dielectric grating was employed, described in more details in the next sections. This configuration has been demonstrated to be an efficient way to discriminate between the symmetric modes of a Bragg grating.

5.5.2 Metallo-dielectric grating

The metallo-dielectric grating is a system composed of a patterned semiconductor-metal interface. It can be readily obtained by etching a grating in the upper-cladding layer of the QC-device, and covering the structure with a metallization layer. This method was proposed by Carras et al. [205]–[207] , who demonstrated the insensitivity of the coupling coefficient to the fabrication uncertainties. Thus, the metallo-dielectric waveguide stands out as a robust and easy method for the fabrication of DFB-QCLs.

The metallo-dielectric waveguide supports two modes satisfying the Bragg condition with different n_{eff}: the semiconductor mode confined under non-etched areas and the metal mode below metallized grating grooves. The semiconductor mode is very similar to the optical mode existing in the QCL waveguide without any grating and its loss does not depend much on the grating geometry. The metal mode with higher loss exhibits anti-crossing behavior as a function of the grating depth due to the surface plasmon resonances generated at the metal-dielectric boundary.

The design of the grating was carried out with the aid of COMSOL simulations, which allow calculating the mode eigenfrequencies, losses and overlap coefficients with the active zone. For the simulation, the same layers and parameters as in Table 5.2 were used. The period of the structure Λ was obtained by using the Bragg reflection condition (Eq. (5.23)) for $\lambda = 14$ µm and n_{eff} obtained by the frontal cross-section simulation proposed in Fig. 5.8.

The COMSOL solver can be used to obtain the dispersion diagram of the structure, by using a Floquet periodicity condition by imposing a variable propagation constant. Usually, a small range around the Bragg propagation constant is sufficient to observe the wanted dispersion diagram. These results are shown in Fig. 5.20, for three different solutions by using a grating height of 0.65 µm. The first two solutions correspond respectively to the semiconductor mode and the plasmonic mode. The third, less relevant solution, corresponds to a higher semiconductor transverse mode, with a field mostly confined in the spacers section.

Since in a DFB the lasing occurs mainly in proximity of the band-edge, the COMSOL solver was set to solve the Helmholtz equation only for such modes by imposing an antiperiodicity condition at the edges of the studied domain. The analysis was conducted for variable grating heights and upper cladding thicknesses. Higher grating heights improve the index contrast between the two modes, while reducing the cladding thickness results in a better interaction of the guided mode with the grating: in both cases, the coupling coefficient is increased. The eigenmodes are expressed in terms of their complex eigenfrequencies $\tilde{\omega} = \omega + i\delta_\omega$, where δ_ω accounts for the mode losses, or more precisely the mode lifetime. Equivalent waveguide propagation losses can be estimated from the relation:

$$\alpha = \frac{2\delta_\omega}{v_g} = \frac{2n_{eff}\delta_\omega}{c} \tag{5.26}$$

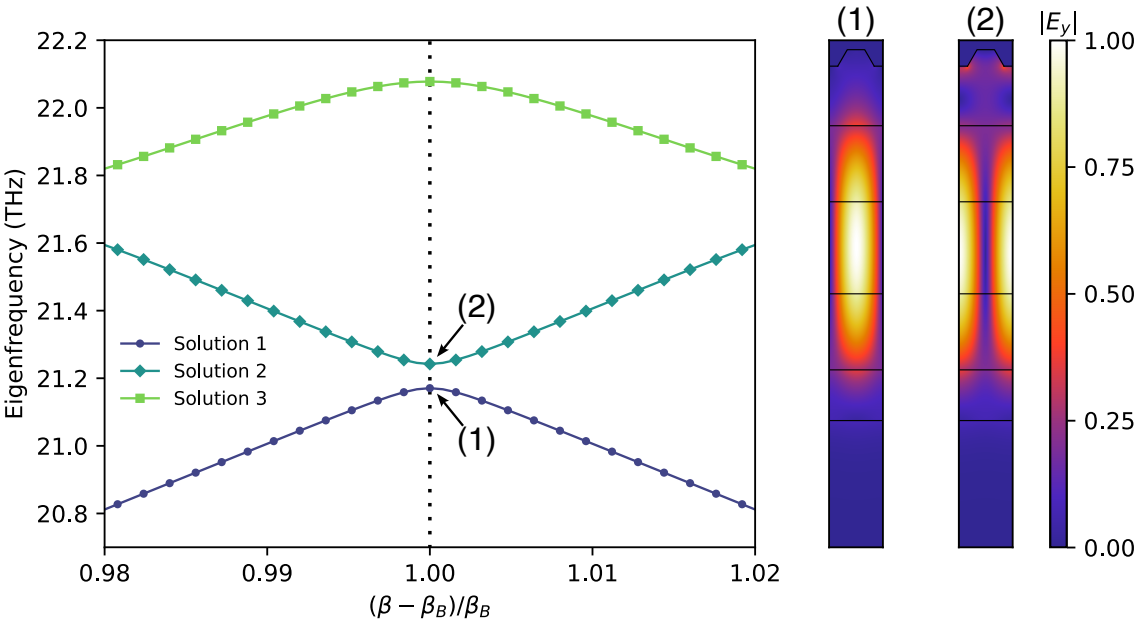

Figure 5.20: On the left, the dispersion diagram of the metallo-dielectric grating, simulated in COMSOL. The propagation vector was changed across the Bragg condition (β_B) to reconstruct the dispersion relation. Indicated in (1) and (2), the semiconductor and the plasmonic mode at the band-edge. The electric field distribution of these modes is shown on the right.

It should be noted that band-edge modes are non-propagating (standing) waves, as the group velocity approaches zero. However, for the sake of the comparison, many authors [205] substitute the group velocity with the phase velocity, leading to the aforementioned formula.

The simulation results are summarized in Fig. 5.21, where the modes eigenfrequencies, losses, confinement factor and the relevant figure of merit χ have been calculated. The latter is expressed as the ratio between the confinement factor Γ and the losses α:

$$\chi = \frac{\Gamma}{\alpha} \tag{5.27}$$

From the analysis of the eigenmode frequencies, the anti-crossing behavior of the plasmonic mode (in blue) is evident. On the other hand, the semiconductor mode eigenfrequency is only slightly affected by the grating height. The same applies for the waveguide losses, which are almost comparable to the non-patterned waveguide ($h_g = 0$). The plasmonic mode however is strongly affected by the coupling with the metal layer, being partly located in the lossy upper cladding layer, thus experiencing higher losses. The differential mode losses are the criterion by which the semiconductor mode can be favoured for lasing, having a lower threshold. However, the threshold gain of the mode, apart from its vicinity to the gain peak of the QCL, depends on the mode overlap coefficient. For this reason, the χ-figure of merit is used.

As previously described, the coupling coefficient κ is a fundamental parameter of the

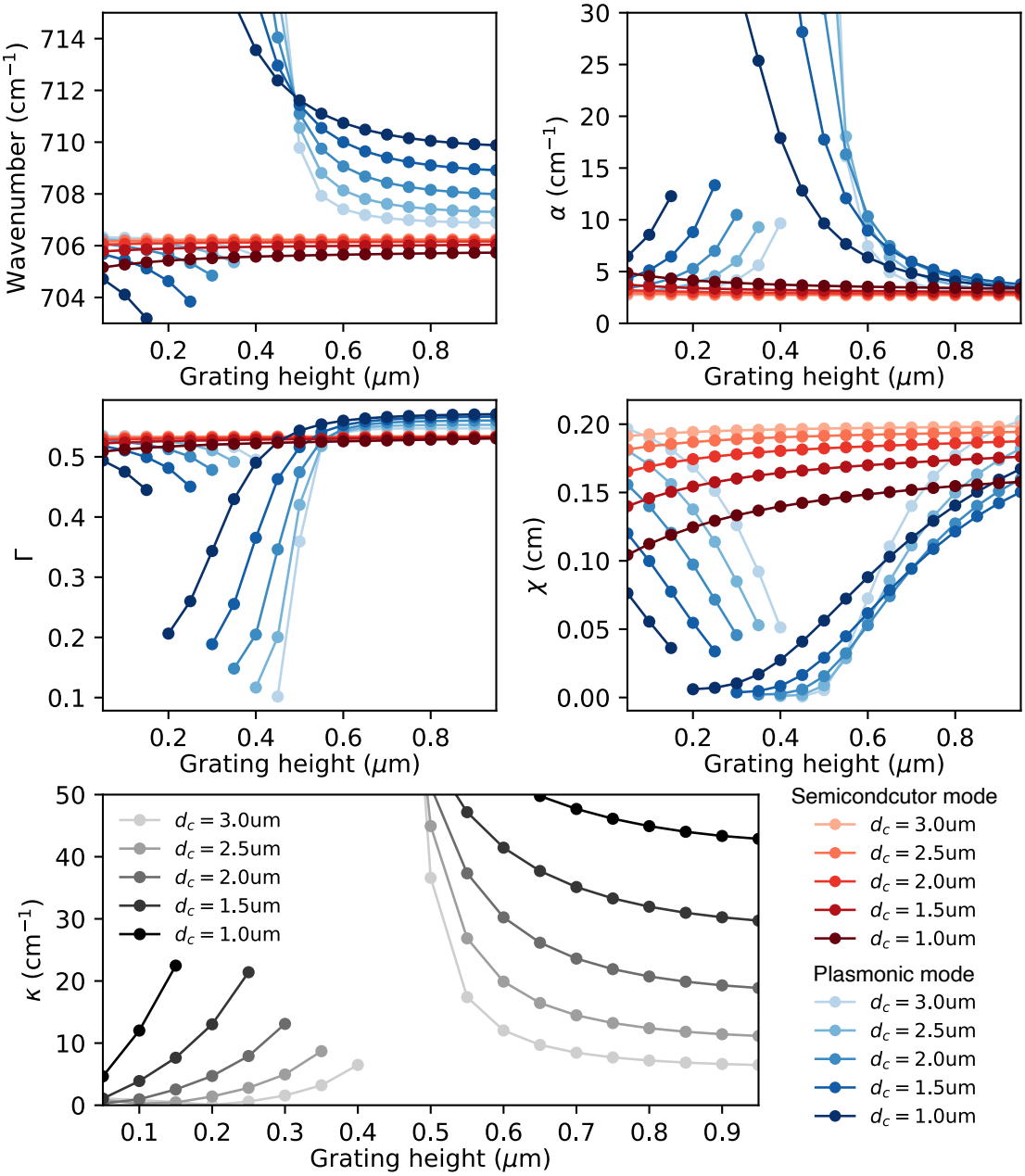

Figure 5.21: Results of the COMSOL simulation for the semiconductor and plasmonic modes for several grating heights and upper cladding thicknesses. Modes' eigenfrequencies, losses, confinement factor and χ-figure of merit. On the bottom, the coupling coefficient of the simulated metallo-dielectric grating.

DFB-laser. This quantity, as per Eq. (5.25), scales with the mode offset. It is convenient to work in a region where κ is less sensitive to fabrication tolerances. Grating heights above 600 nm have minimal influence on the metal mode's frequency, granting more robustness during the fabrication process. It is known that best performances are achieved for the critical coupling condition ($\kappa L \approx 1$), which for the targeted length of 3.6 mm corresponds to $\kappa \sim 3$ cm^{-1}. However, for our devices, experimental evidence demonstrated better mode control under overcoupling condition $\kappa L > 1$ [186].

For the explained reasons, a cladding thickness of 2 µm and a grating height of $\sim$ 700nm

were targeted in the fabrication process, corresponding to an estimated $\kappa \sim 25$ cm^{-1} with a loss contrast of ~ 2 cm^{-1}.

5.5.3 DFB-laser fabrication

The fabrication of a DFB-device does not differ from the process in making a FP-device. However, the preliminary steps consisting in thinning of the cladding and definition of the grating are required.

While the grating periodicity for LW devices reaches ~ 2 µm, the required resolution for fine wavelength selection is on the order of the nm, which is typically not achievable via standard photolithography. A classical approach is based on holographic lithography, which exploits the coherent superposition of two beams to generate an interference pattern of periodicity inferior to the used wavelength. However, such approach does not provide the possibility to simultaneously expose multiple regions of the sample with different periodicity.

An extremely versatile and precise technique which surpasses this limitation is Electron Beam Lithography (EBL). In EBL, an electron beam is accelerated by a strong electric field, reaching energies on the order of $\sim 10-50$ keV, and is focused by a system of magnetic lenses. By doing so, extremely small beam spots (< 10nm) can be achieved, which expose an electron sensitive material. The spot is deflected with the magnetic lenses in a small area (100µm $\times$ 100µm), named *writefield*. Since the DFB patterns are usually larger than the writefield, the sample is moved under the spot with an interferometric stage to expose the whole sample. This can cause stitching errors and requires careful preparation steps (writefield alignment). The pattern that has to be transferred to the sample is provided in the form of a Graphic Design System (GDS) to the computer operating the machine. The pattern is decomposed in adjacent working areas, which are exposed sequentially. The maximum feature of the tapered grating imposed to use a writefiled of 150µm $\times$ 150µm, to avoid stitching lines (running along the cavity direction) to compromise the grating quality. Due to the large size of the sample, the exposure might take many hours. For a faster exposure, the Meander-scan strategy was used, without compromising the quality of the grating. It consists of a continuous writing in a raster pattern, opposed to the line mode, where the writing takes place only when the beam is moving in one direction.

As an electron-sensitive material, AZ2020 (MicroChemicals) was used, diluted in EBR solvent with ratio 10:4 in order to obtain thinner films. The resist thickness has to be sufficiently thin to provide homogeneous exposure of the film, but thick enough to survive the etching step. The resist was spin coated at 6000 rpm for 30 sec. The sample was exposed in a Raith Pioneer Two EBL machine, by using a dose of 13.7 µC/cm^2. The exposure is followed by a post-exposure baking at 110°C for 60 sec and development for 15 sec in AZ726.

The cladding thinning and the etching of the grating are performed via Inductively

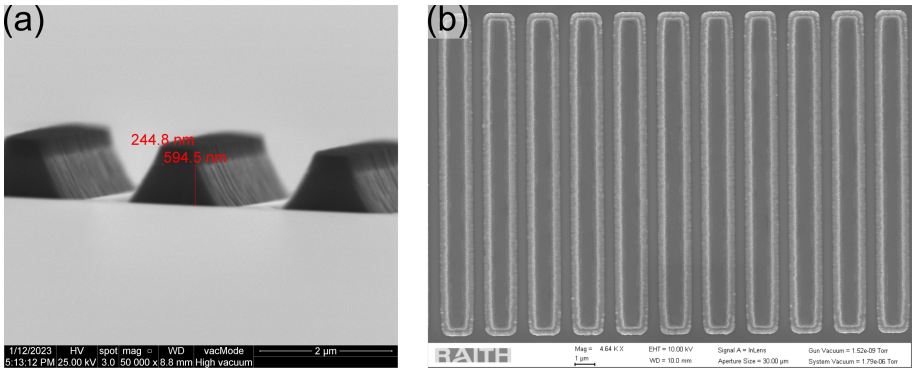

Figure 5.22: Example of a SEM image of the fabricated grating after (a) ICP etching and (b) resist lift-off. The ICP etching results in sloped wall of the grating.

Coupled Plasma (ICP) dry etching (ICP Oxford), with a low RF power of 50 W in Argon environment. Typical etching rates of InAs are 40 nm/min. The etched grating is shown in Fig. 5.22, before (a) and after (b) strip-off of the exposed resist. The ICP etching produces sloped walls in the grating, which were taken into account in the simulation process by using trapezoidal grating elements.

5.5.4 Single-mode tapered QCLs

Devices with grating periodicities Λ of 2070 - 2080 nm were fabricated for all the four tapered types along the full extension of the cavity. A picture of the devices and their cross-section is given in Fig. 5.23. The lasers were characterized in pulsed mode, with a pulse duration of 100 ns to limit intra-pulse heating effects. The light was collimated into an FTIR (Bruker, Vertex 70-v) to record the emission spectra, with a resolution of 0.2 cm^{-1}. The lasers were tested both near the threshold and close to the rollover current, to ensure single mode operation in the whole current range. The frequency emission is demonstrated in Fig. 5.24 for all the device types. Side-mode suppression ratios (SMSR) greater than 20 dB were observed. Interestingly, a peak wavelength of $\lambda \approx 13.89$ µm was obtained for all the devices, which corresponds to an effective index $n_{eff} \approx 3.339$ obtained from the Bragg condition, in good agreement with the cross-section waveguide

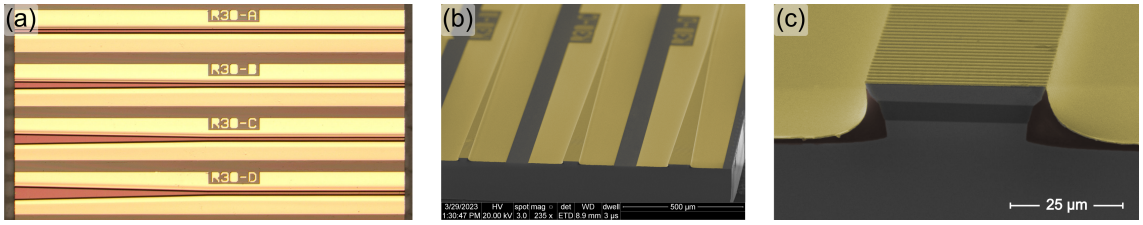

Figure 5.23: (a) Cleaved bar of DFB-Tapered QCLs. Letters from A to D, correspond respectively to 0°, 1°, 2° and 3° taper angle. The orange color comes from the grating diffraction. (b) SEM micrography of the tapered facets (1°, 2° and 3°). (c) Close-up image of the 1° device: in yellow, the metallization layer; in brown, the hard-baked insulation layer; in dark grey, the active zone. Taken from [189].

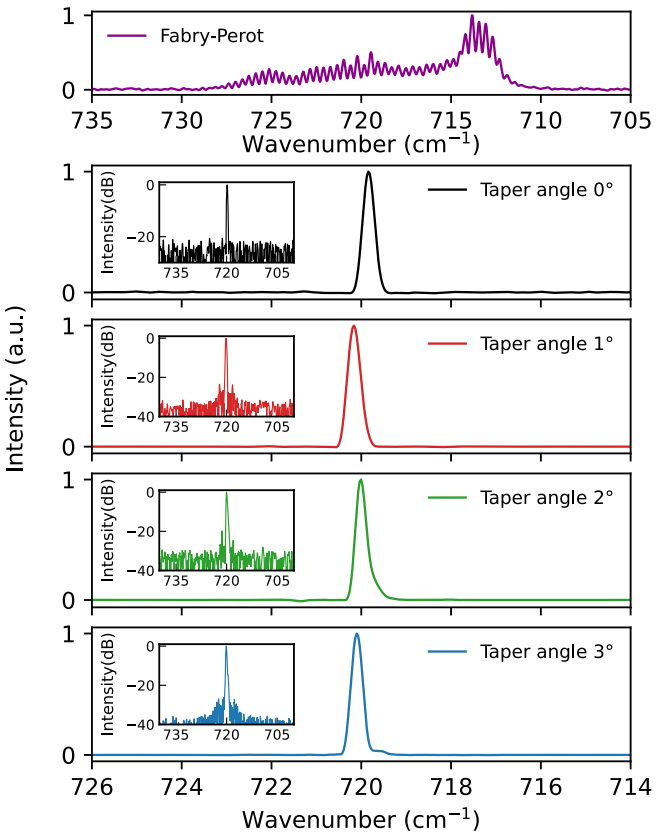

Figure 5.24: FTIR spectra of the DFB-tapered lasers collected at room temperature, compared to the spectrum of a Fabry-Perot device. In the insets, the intensities are shown in logarithmic scale with side-mode suppression ratios greater than 20 dB. Data published in [189].

simulations. It is worth noticing that, even with a constant grating periodicity across the cavity length, a good mode selection was obtained for all devices. One would indeed expect that, in a tapered device, the propagation constant varies along the cavity position, causing a deviation from the Bragg condition. To address this effect in theory, a chirped grating could be employed. However, experimental evidence showed that this adjustment was not required.

The 1° taper was further analysed at several temperatures between 120K and 280K. Emission spectra were collected for bias currents between 300 and 900mA for each temperature, while no prominent change in the spectrum was observed. The results are collected in Fig. 5.25. For clarity, only the highest current measurement has been shown in Fig. 5.25(b). The performed analysis suggests mode-hop free tunability in the whole range. The respective LIV curves are portrayed in Fig. 5.25(a). A tuning coefficient of $\eta_T = -0.058$ cm^{-1}/K was obtained by fitting the peak wavenumber with the temperature.

The same device was tested in CW operation, in a limited temperature range. Thermal management is still an undergoing problem considering the large device area and the electric power dissipation of these devices. In particular, heat extraction might become a problem in the tapered area, where a large heat accumulation is expected. Heat dissipation

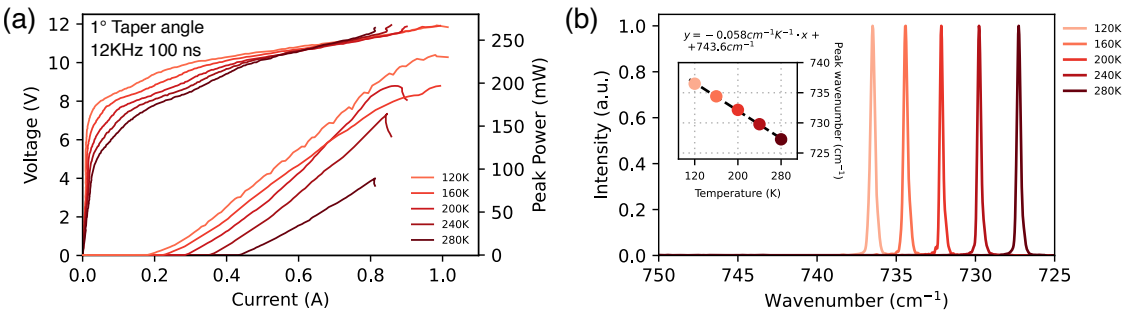

Figure 5.25: (a) LIV curves of a 1° tapered laser under pulsed operation (12kHz 100 ns). (b) Temperature tuning between 120K and 280K. Only the spectra for the highest current of each temperature has been kept. Data published in [189].

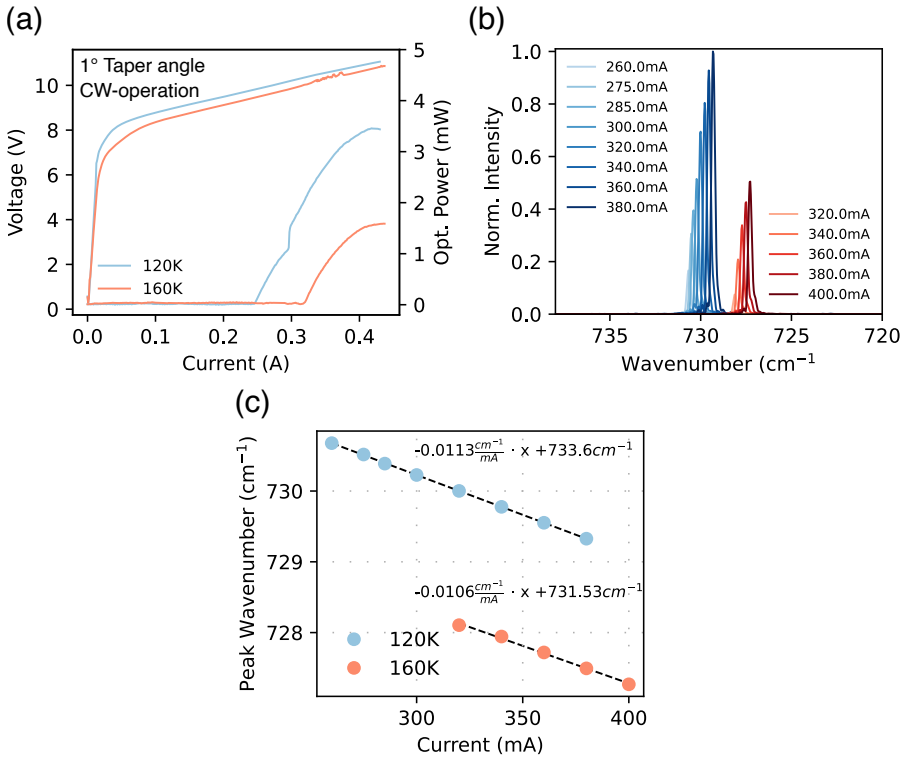

Figure 5.26: (a) LIV curves of the 1° tapered laser under CW operation. (b) Current tuning at two different temperatures and (c) corresponding peak wavelengths. A linear tuning was observed for both temperatures with similar tuning coefficients.

simulations were beyond the scope of this work, but would constitute a necessary next step. In Fig. 5.26, the results for the CW-operation are portrayed. The device was operated for a heat-sink temperature of 120K and 160K. A kink in the LI curve at 120K is observed, which might indicate a change in the transverse mode distribution, since it is not reflected in the spectrum. Thermal lensing effects can be expected in the tapered region under cw-operation, causing a modification of the far-field profile and a change in the measured power. The current tuning appeared linear over the whole current range, as demonstrated in panels (b) and (c). Similar current tuning coefficients were obtained

for the two temperatures, on the order of $\eta_i \simeq -0.011$ cm^{-1}/mA. Optical powers on the order of ~ 4 mW were extracted from a single untreated facet.

Optimization of the coupling coefficient is mandatory to enhance the outcoupled power, while retaining single-mode operation. At the same time, coating depositions as demonstrated in Section 5.3 are expected to provide an additional enhancement factor.

5.6 Conclusions

This chapter was devoted to the study of tapered devices as a possible solution to improve the inherent lack of optical power of long-wavelength devices. The work aimed to demonstrate an increased power output in pulsed operation without sacrificing beam quality of the laser beam.

The tapered lasers provided a power improvement consistent with their larger active zone. The largest taper angle was able to provide an optical power almost ~ 3 times larger than the ridge device, with a nearly Gaussian far-field intensity distribution and reduced beam divergences, as low as $\sim$4.2°. The threshold current density behavior was analysed, suggesting that the lower waveguide losses in the taper section might be the main source of the negative shift observed in comparison with ridge devices.

The deposition of thin coatings proved to be an easy and efficient way to improve the outcoupled power from the tapered facet, even with the use of SiO_2 which exhibits non-negligible losses in the LW region. The major achievement, together with the improved power output, is the demonstration of the relatively small increase in threshold current. As the latter is largely dominated by the transparency current, the increased mirror losses introduced by the AR-coating represent an acceptable trade-off for higher power output. Coated devices could achieve peak powers in pulsed operation on the order of 400 mW, outperforming InAs-based LW-QCLs reported to date.

Finally, single frequency operation was demonstrated for all the tapered devices, by using a first-order Bragg grating. The fabrication was guided by COMSOL simulations, which allow computing the most important parameters of the DFB-structure. Spectral characterization of the devices revealed SMSRs in excess of 20 dB, a typical metric for qualifying a laser as single mode. CW-operation was tested and observed even for long-tapered devices. Optimization of the coupling coefficient and efficient heat dissipation strategies are fundamental future steps to fully leverage on the larger gain area provided by the tapered waveguide.

Chapter 6

Long-wavelength QCLs sensing

This conclusive chapter is devoted to showcase the capabilities of InAs-based LW-QCLs for sensing in the fingerprint region. The LWIR region plays a pivotal role for the detection of BTEX compounds (benzene, toluene, ethylbenzene and xylene). BTEX are representative of the larger class of volatile organic compounds (VOCs) and are used for monitoring air quality in urban areas. The vibrational structure of these aromatic molecules is not as simple as for diatomic molecules. In benzene (C_6H_6), for example, there are a total of 30 vibrational modes, which can be reduced for the molecular symmetry to 10 degenerate vibrational modes. Among them, only two, indicated with A_{2u} and E_{1u} are IR-active. The first corresponds to the out-of-plane vibration, falling at 673 cm^{-1}, while the second to stretching and bending of the C-H bonds, generating three separate bands at 1038 cm^{-1}, 1484 cm^{-1}, 3048 cm^{-1} [208]. As represented in Fig. 6.1, the out-of-plane vibration is typically very strong as it involves a strong dipole moment variation, producing an absorption cross-section at the peak almost 2 order of magnitudes higher than the corresponding peaks in the mid-IR. The same considerations apply for the substituted aromatic rings of toluene and xylene. The second advantage in the LW-region is the small overlapping of the absorption features with little to none environmental contribution, allowing the identification of regions were no overlap is found for selective sensing of these species.

Classically, these species have been monitored exploiting the absorption bands at 1500 cm^{-1} and 3000 cm^{-1}, compensating the lower absorption cross-sections with more sophisticated approaches such as multi-pass absorption or cavity enhanced techniques [209], [210].

The fingerprint region, where also strong fundamental vibrations of aromatic substances lie, have been for long ignored due to the lack of bright sources. Few demonstrations used difference frequency generation to access the LW-region [212]. Advances in interband cascade lasers are pushing their limits towards higher wavelengths. However, the most recent demonstrations are limited to cryogenic temperatures and pulsed operation [26], which is not attractive for spectroscopic applications. On the other hand,

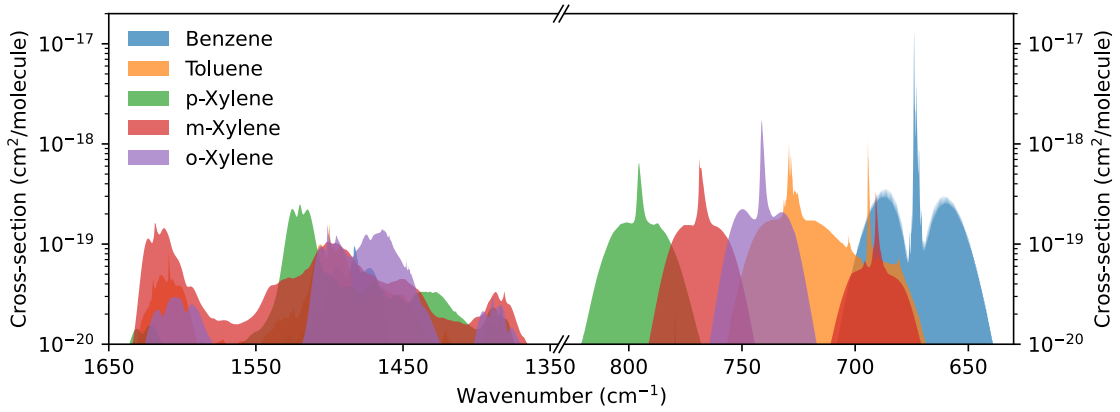

Figure 6.1: Cross-sections of the gaseous BTEX compounds at ambient pressure and room temperature conditions, taken from the PNNL-IR database [211].

the technological maturity of InAs-based LW-QCLs, which emerged in the last decade, allowed the first demonstrations of BTEX detection in the fingerprint region, with less complicated methods based on photoacoustic sensing (QEPAS and CEPAS) [213], [214].

The employment of LW-QCLs in the ICAPS technology, presented in Chapter 3, would be extremely attractive, as small sensing volumes can be combined with the high-sensitivity of the method. However, some preliminary considerations are needed to estimate the feasibility of the LW-ICAPS technology in the context of this work.

First, the excitation optical powers of LW-QCLs can be on the order of few mW, in contrast with the tenths or hundreds of mW of typical mid-IR QCLs. Consequently, the produced photothermal signals will scale accordingly with the available excitation power. Milliwatt powers are usually sufficient to produce detectable PTS signals, depending on the noise level of the system. Indeed, in a first approximation, by assuming the same performance of the ICAPS system for benzene detection (NNEA of $\sim 3{\cdot}10^{-6}$ W cm^{-1}Hz$^{-1/2}$), a limit of detection on the single-ppm digit should be achievable for 1 mW of optical power and 78 mHz of ENBW. Nevertheless, the gas-cell employed in Chapter 3 was equipped with CaF_2 windows, which completely extinguishes radiation above 11 µm, prohibiting the coupling of any LW-source.

Secondly, the tapered-QCLs presented in Chapter 5 feature an emission centred around 720 cm^{-1}. In this spectral range, only broad tails of toluene's fundamental absorption can be found, resulting in a strong loss of sensitivity. The tailoring of the grating periodicity is needed to shift the emission towards the characteristic absorptions of the BTEX compounds.

In order to showcase the potential of the LW-sources, classical absorption spectroscopy based on a multipass cell approach was investigated. The laser used in this demonstration was a straight ridge device, based on an active region design similar to the one presented in Chapter 5. The laser emission was tailored to target 674 cm^{-1} and was provided by the Université de Montpellier.

6.1 LW-sensing of CO_2 and C_6H_6

6.1.1 QCL characteristics

The spectral and optical characterization of the LW-QCL employed for CO_2 and C_6H_6 detection are presented in Fig. 6.2. The characterization, as for the devices described in the previous chapter, were performed on an FTIR (Bruker, Vertex 70v), with the laser cooled with LN_2 in a cryostat. The measurements were performed in CW-operation, aiming for the highest operational temperature (around 268K). It is important that the laser operates at temperatures accessible to Peltier elements, typically above 250K for reliable temperature control. The spectral tuning reveals roughly a current tuning coefficient of $\eta_i = -0.005$ cm^{-1}/mA, with emissions in the range 676.5 - 677.3 cm^{-1}.

The setup realized for the spectroscopic measurements requires a more convenient mounting of the laser. The latter was hosted in an aluminium box, equipped with a KBr optical window. Such material grants an extended transmittance (up to 26 µm), but is hygroscopic and can be damaged at high humidity content. For this reason, the humidity level of the system has to be kept under control, for instance by dry air flushing. Moreover, it is of uttermost importance to keep the humidity inside the laser box under control, especially at temperatures below 0°C. Condensation of water on top of the cold laser facet might end up damaging the laser device when it is turned on. For this reason, the lid of the box was equipped with inlet/outlet connectors to flush or evacuate the laser chamber.

The AlN submount, on top of which the QCL is soldered in epi-side down configuration, was thermally contacted with a silicon-based paste to a copper heat sink. The latter is kept at controlled temperature via a Peltier element and the temperature is monitored via a Pt100 sensor. The temperature stability was managed via a TEC controller (TEC-1091, Meerstetter). The hot-side of the Peltier was cooled via water-recirculation on the bottom of the aluminium box.

The LI curve was acquired by keeping the laser at constant temperature (260K) with water-cooling to 17°C and Peltier cooling of the laser chip. The fastly diverging beam was collimated by a ZnSe plano-convex lens of 25mm focal length and the optical power of the collected beam was measured by a large area power meter (SOLO2, Gentec-EO).

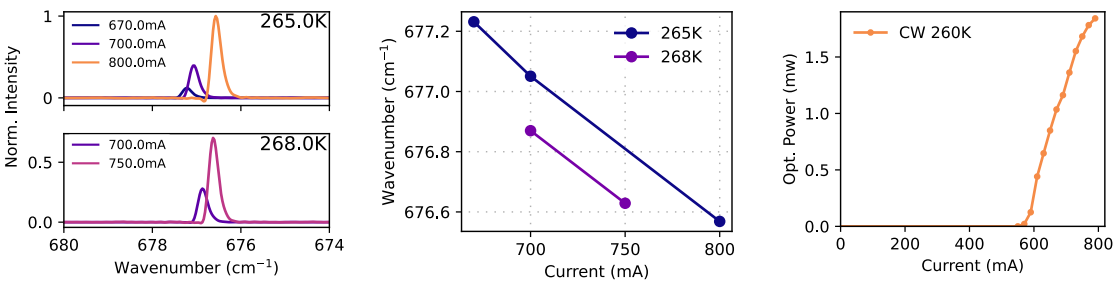

Figure 6.2: Spectral and optical characterization of the employed QCL.

6.1.2 Experimental setup

The experimental setup realized for the gas sensing measurements is presented in Fig. 6.3. The arrangement for the laser box was already discussed in the previous section. The collimated laser beam was coupled to a circular multipass cell (Sensirion, IRcell S15) with the aid of a green alignment laser diode (Thorlabs) and a flippable mirror. The multipass cell features a gold-coated segmented inner surface, meaning that the inner circular surface is machined to obtain a series of spherical mirrors, which compensate the beam divergence as it undergoes multiple (86) reflections. The beam covers a maximum pathlength of $\sim$ 1512 cm. The cell was used in this highest pathlength configuration, to ensure the highest sensitivity.

The gas cell was equipped with ZnSe optical windows, with commercial AR-coatings, optimized for the region 8-12 µm. While not being designed for the LW-region, such coating provides $\sim$ 85% transmittance according to the producer, which is a good trade-off between performance and cost.

Aside from the laser, the other fundamental component is the photodetector. The mid-IR scene is mainly dominated by the highly sensitive mercury-cadmium-telluride (MCT) detectors, most of which can operate under Peltier cooling without the stringent requirements of LN2 cooling. MCT feature an unmatched specific detectivity (D*, [cm $Hz^{1/2}$/W]) which can achieve 10^{10} cm $Hz^{1/2}$/W for sensing elements centred in the mid-IR. Nevertheless, MCT detectors optimized for the LW-IR exhibit a strong drop in D* of almost 2 orders of magnitude. As an example, at 14 µm the detectivity drops to $5 \cdot 10^8$ cm $Hz^{1/2}$/W, requiring 4 stages of thermoelectric cooling [215].

Secondly, the dynamic range of these detectors is typically very limited and requires

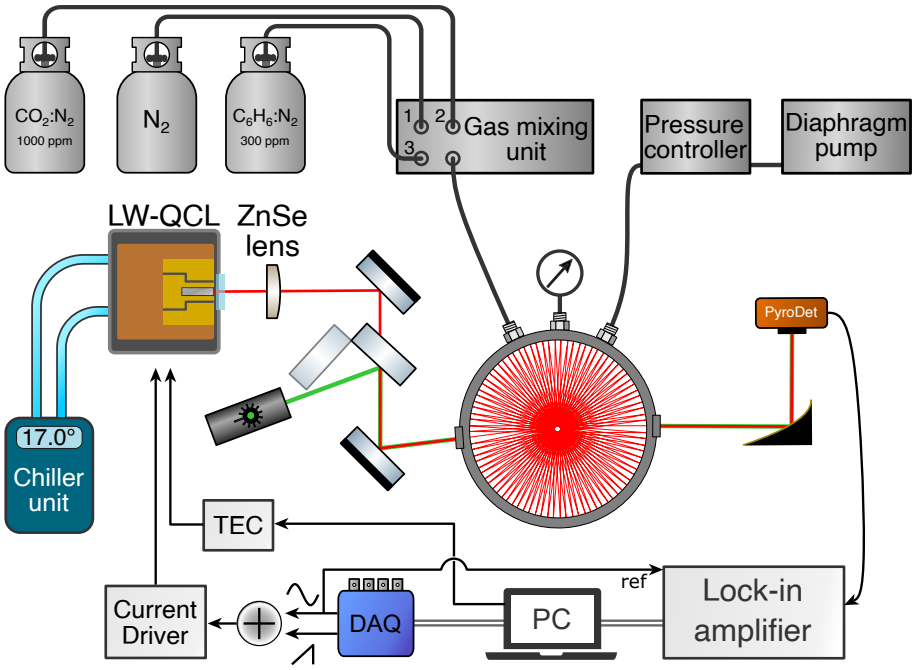

Figure 6.3: Experimental setup used for the detection of CO_2 and C_6H_6 in the LW-region.

expedients to reduce the impinging optical power, such as neutral density filters, to avoid non-linearities in the signal.

Finally, these detectors are generally very expensive compared to others. An affordable and broadband alternative are pyrodetectors. In particular, a novel pyrodetector (Laser-Components, PR01) was employed, which possesses a peak detectivity on the order of $5 \cdot 10^8$ cm $\mathrm{Hz}^{1/2}$/W. Pyrodetectors convert a change in temperature due to the absorption of light into a voltage signal. Hence, these detectors require a modulated intensity for detection and DC-power levels can not be detected. Moreover, due to the slow thermal dynamics, the responsivity of these devices drops with frequency (in the specific case, with a -3dB cutoff at 8 kHz), limiting the frequency operative range. Nevertheless, it is still sufficient to perform WMS, as will be shown in the results section. The signal extracted from the pyrodetector was fed to a LIA (Stanford Instruments, SR860), from which the 2f-WMS signal was recorded on a personal laptop.

The gas cell comes equipped with inlet/outlet connectors and a third one connected to a pressure gauge (Keller, LEO 3). The gas system relied on a gas mixing unit (MCQ, GB100) which accepts three input channels and outputs the gas mixture with the wanted mixing ratios at a constant mass flow. The outlet of the cell was connected to a pressure controller (MKS, 640B) and a mini-diaphragm pump (KNF, N84.3ANDC).

The laser parameters and the operational gas pressure were chosen to allow a clear separation of the absorption lines, minimizing cross-response.

6.1.3 Line selection

The knowledge of the emission range is fundamental to predict the possible interfering absorption features arising from atmospheric gases. A survey scan of the laser across its current operative range (550-800 mA) is shown in Fig. 6.4. Among the atmospheric contaminants, only CO_2 plays a relevant role and can be easily detected at its environmental concentration, which at the time of this work amounted to $\sim$ 420 ppm. Water absorption is not really relevant, as the involved cross-sections are 5 orders of magnitude lower than those of CO_2. Even at high relative humidity conditions, they do not exhibit any overlapping. The correct assignment of the peaks is shown in Fig. 6.4, by comparing the database information (top panel) with a 2f-WMS measurement performed at atmospheric concentrations (bottom panel).

Two side peaks (677.3 cm^{-1} and 678 cm^{-1}) of lower cross-section $\sigma \sim 3 \cdot 10^{-19}$ cm^2/molecule were revealed together with an intense line at 677.6 cm^{-1} of $\sigma \sim 7 \cdot 10^{-18}$ cm^2/molecule. Two additional lines were identified, one of which comes from the less abundant isotope $^{13}CO_2$ at 677.85 cm^{-1}.

The abundant presence of CO_2 in the atmosphere poses a limitation to the system performance, as the optical pathlength between the laser and the gas-cell can introduce a non-negligible absorption. Such effect is represented in Fig. 6.5, where the transmittance

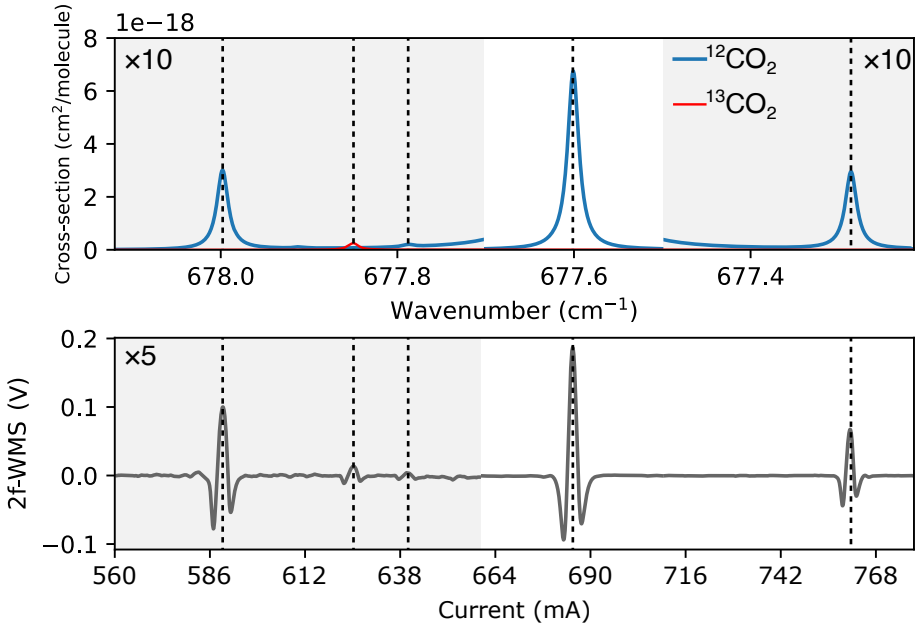

Figure 6.4: Line assignment from HITRAN simulation at 100 mbar, compared to the 2f-WMS measurement of ambient CO_2. The shaded areas have been scaled to improve the visibility. The different peak response of the sensor comes from the linear power output of the laser with the current.

of the overall system has been simulated for ambient and gas-cell contributions. The pathlength in air was roughly $\sim$ 50cm, while it was $\sim$ 1512cm in the multipass cell. In the simulation, a concentration of 10 ppm was considered for the multipass cell (at $p = 100$ mbar), and 420 ppm for the environmental concentration (at atmospheric pressure). In these conditions, the pressure broadening of the intense line induces an overlap with the neighboring lines. More importantly, it reduces the transparency window of the system.

The existing IR-databases (such as HITRAN and PNNL) for benzene absorption cross-section are restricted to specific pressure and temperature conditions. In most cases,

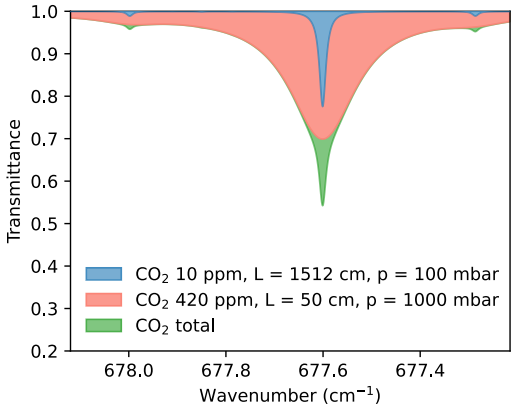

Figure 6.5: HITRAN simulation of CO_2 absorption within the multipass cell at reduced pressure, and in ambient air for 50 cm of optical pathlength. In green, the sum of the two contributions.

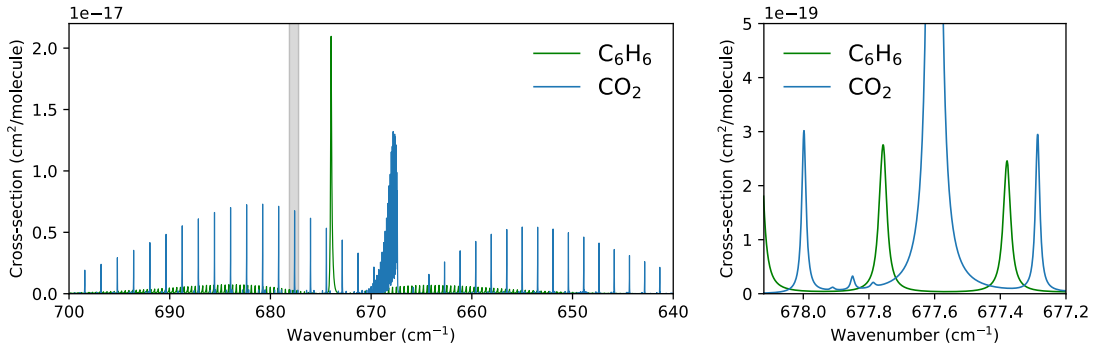

Figure 6.6: On the left, simulation of the absorption cross-sections at 100 mbar and 296K for CO_2 (HITRAN database) and C_6H_6 (Geisa database). The grey shaded area shows the tuning range of the QCL is portrayed. On the right, a zoomed view of the targeted lines.

such information is available at ambient pressure and temperature (as shown in Fig. 6.1). However, this information does not encompass reduced pressure scenarios, as for this work.

An incomplete line list of benzene transitions is contained in the GEISA database [216], which includes pressure broadening parameters. With the knowledge of these quantities, it is possible to simulate a spectrum of the benzene cross-section at custom pressure values, as presented in Fig. 6.6. The simulation used Lorentzian lineshapes with a linewidth defined by the air-pressure broadening. Two peaks were found accessible to the QCL source (shaded area in the left panel of Fig. 6.6), located at 677.38 cm^{-1} and 677.76 cm^{-1}. According to the GEISA database, the first peak is generated by the overlap of 9 closely spaced transitions of similar intensity, while for the second 10 transitions participate to the formation of the peak.

To avoid any interference effect, the setup was enclosed in a box and flushed with N_2 during the duration of the experiment. The selected lines for CO_2 detection were the intense line at 677.6 cm^{-1} and the weaker line at 677.3 cm^{-1} to extend the linearity of the measurement. The line for benzene detection was the one falling at 677.38 cm^{-1}.

6.1.4 Benzene sample preparation

The apparatus used for the preparation of the Benzene sample is presented in Fig. 6.7. The benzene sample was prepared by vacuum evaporation of 100 µL of pure Benzene (>99.5%, Carl Roth) into two interconnected 5L tanks (Festo), previously purged with N_2 and evacuated with a pump. The sample was injected with a syringe through a Swagelok male tube fitting, suitably adapted with a gas chromatography septum (Agilent). The system air tightness was tested to ensure minimum leakages during the injection process. The injection part was cut off of the system with a ball valve after the introduction of the sample in the vacuum environment. The gas tank was further filled with N_2 up to a pressure of 9 bars, resulting in an estimated concentration of 300 ppm C_6H_6:N_2. Such value was estimated from the moles contained in the 100 µL, assuming a molar density at room

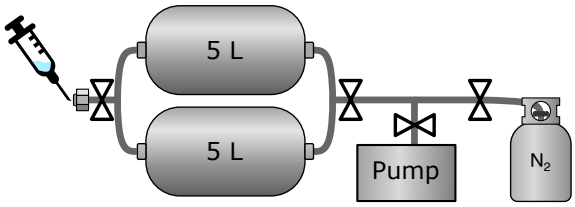

Figure 6.7: Schematic of the apparatus for benzene sample preparation.

temperature of 11.185 mol/L. These moles result in a partial pressure of ∼2.7 mbar, which over the total 9 bars define the estimated volumetric concentration. Uncertainties in the sampling volume, manometer readings and injection efficiency might introduce deviations from the estimated value.

6.2 Calibration curves

6.2.1 CO_2 detection

The calibration of the system usually requires a preliminary step, namely the optimization of the operational parameters such as modulation frequency and modulation depth. The optimization of the signal starts from the choice of of the laser operative parameters. In 2f-WMS, the amplitude of the signal scales with the optical power of the source. Hence, high powers are beneficial to minimize the detector noise contribution. The correct combination of temperature and current aids to achieve optimal conditions. The laser heat-sink temperature was stabilized to -13°C with the inner Peltier element.

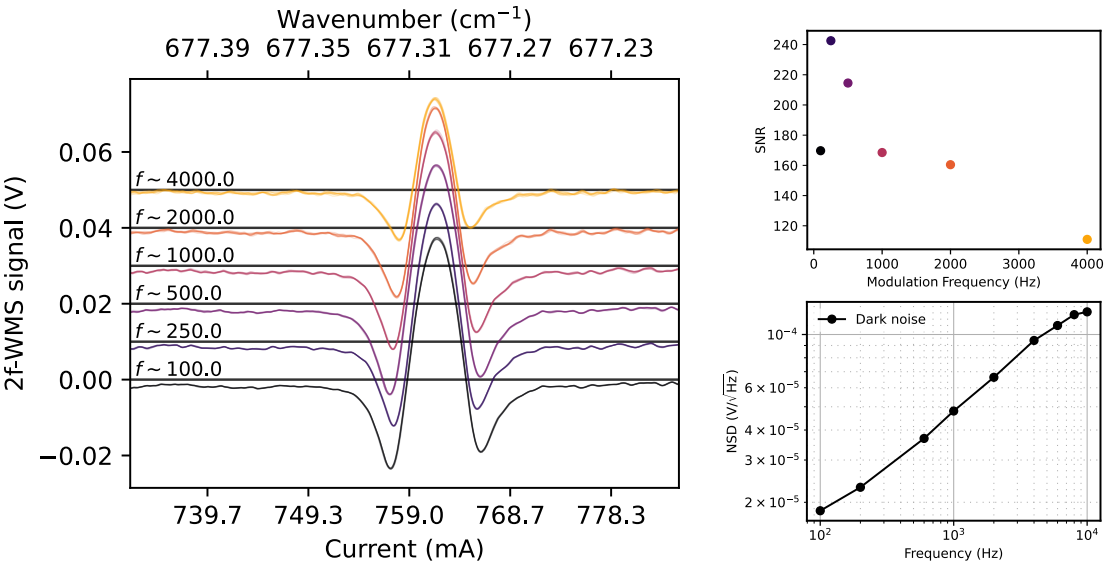

Figure 6.8: On the left, the effect of the modulation frequency on the system performance is shown. For each frequency, a set of 10 curves is overlayed. On the top right, the SNR was calculated from the peak average over the standard deviation of the peak values. On the bottom right, the noise spectral density of the pyrodetector was measured with the LIA for several frequencies.

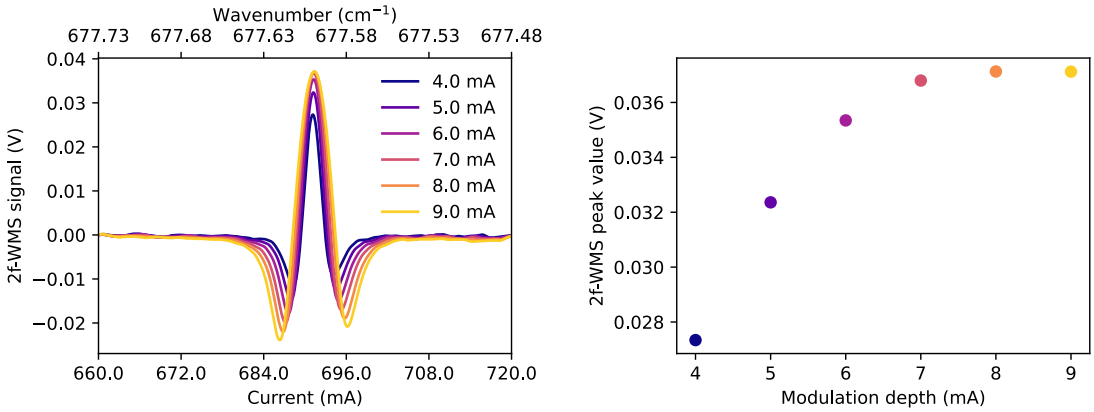

Figure 6.9: Effect of the modulation depth on the signal amplitude. The highest signal is achieved for 8mA of sinusoidal dithering (peak-to-zero).

The advantage of modulation techniques lies in the possibility of reducing the technical noise of the system, which usually decays with 1/f. Nevertheless, when working with a pyrodetector, one has to take into account the responsivity and the noise-characteristic of this special detector. In Fig. 6.8, the effect of the modulation frequency on the signal amplitude is portrayed. The analysis was performed on the weak peak at 677.3cm^{-1}, being less sensitive to CO_2 ambient concentration. It is evident how at higher modulation frequencies, the amplitude of the signal drops as a result of the reduced pyrodetector responsivity. Moreover, at the second-harmonic the extracted signal corresponds to the double of the employed modulation frequency (hence, the 4kHz modulation corresponds to the 8kHz cutoff frequency). Together with the drop in responsivity, an increase in the noise spectral density is observed, further compromising the performance at high frequencies. The noise spectral density was measured with the lock-in amplifier by recording the noise trace over several minutes using the same bandwidth employed for the experiment (ENBW = 3.125 Hz, at τ = 30ms, 3rd order filter).

The SNR was estimated by considering the average peak value over its standard deviation, used as an indication of the system noise. Better performances were found at 260Hz, due to the reduced noise level introduced by the detector. In Fig. 6.9, the typical effect of the modulation amplitude is portrayed, with optimized modulation depths of 8 mA. In this case, the high linestrength peak was analysed while flushing the system for the duration of the experiment.

After finding the optimal operation parameters, the system was calibrated with a variable concentration of CO_2. The certified concentration of 1000ppm CO_2:N_2 was mixed with pure N_2 with the gas blender to obtain dilutions. For the intense line, very little concentrations were needed and the gas mixer was operated on its lower limit, where larger blending errors are expected.

The presence of multiple peaks in the emission range of the QCL allows to use the intense line for high-sensitivity and the weak line for extended linearity. The linearity is

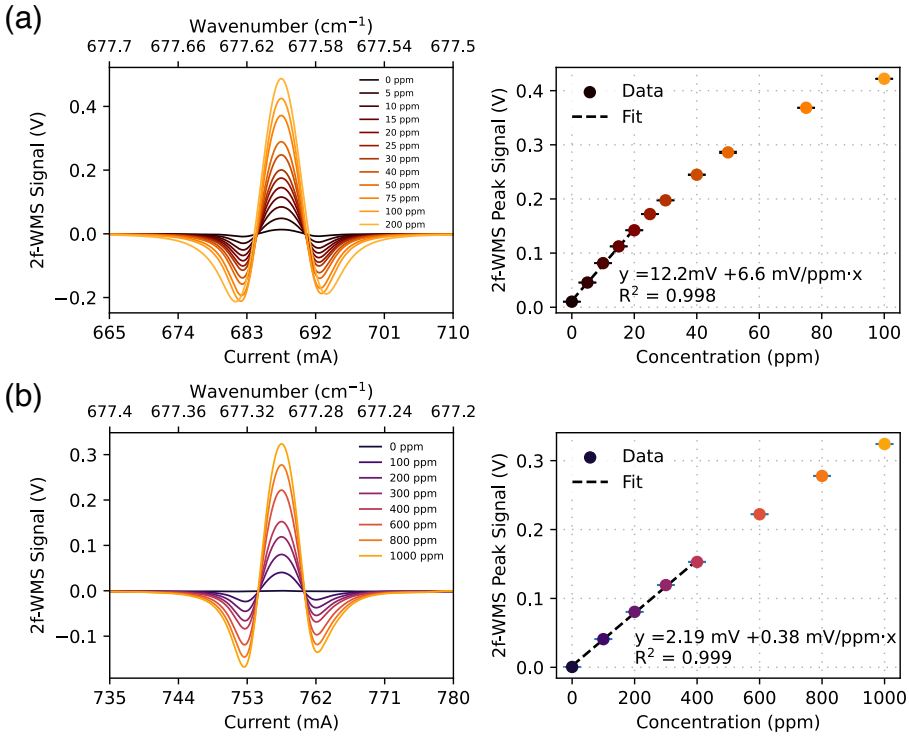

Figure 6.10: Calibration curves for (a) the intense peak at 677.6cm^{-1} and (b) the weak peak at 677.3cm^{-1}.

a weak point of WMS-approaches, as the line peak is measured from the transmittance, which is non-linear with the concentration by its nature.

The calibration curves for CO_2 detection are portrayed in Fig. 6.10. As expected, the high-intensity line exhibited a limited linear range (up to 20 ppm) above which a quadratic behavior with negative concavity is observed. The linear fitting was limited to this concentration level, with a sensitivity of 6.6 mV/ppm. A large background (nominal 0 ppm) was observed, which was attributed to the non-ideal behavior of the gas blender. The instrument requires the valve opening of the used channels. When only N_2 was flushed, a residual contamination with peak value of $\sim$ 3 mV was found, as a contribution of both the atmospheric and the gas-cell paths. The latter was used for background correction. However, when opening the CO_2 channel at null flow (0 ppm in the graph), the background signal presented in the calibration curve arose.

The noise can be estimated by calculating the standard deviation of the signal across the covered spectrum. Pure N_2 measurement was performed, leading to $\sigma = 0.06$mV and a noise equivalent concentration of NEC = 9 ppb (LOD = 27 ppb). The noise level is quite comparable to the dark noise of the pyrodetector, which at $f = 520$ Hz is roughly 0.06mV (NSD $\times \sqrt{\Delta f} \sim 3.5 \cdot 10^{-5} \cdot \sqrt{3.125}$ V). From the knowledge of the absorption cross-section, the minimum absorption coefficient and the noise equivalent absorption can be calculated, resulting in $\alpha_{\min} = 1.6 \cdot 10^{-7}$cm^{-1} and NEA $= 8.8 \cdot 10^{-8}$cm^{-1} Hz$^{-1/2}$, respectively.

The noise traces, presented in Fig. 6.11, reveal the contribution of interferometric fringes, which arise from the non-ideal coupling of the laser to the multipass-cell. Also

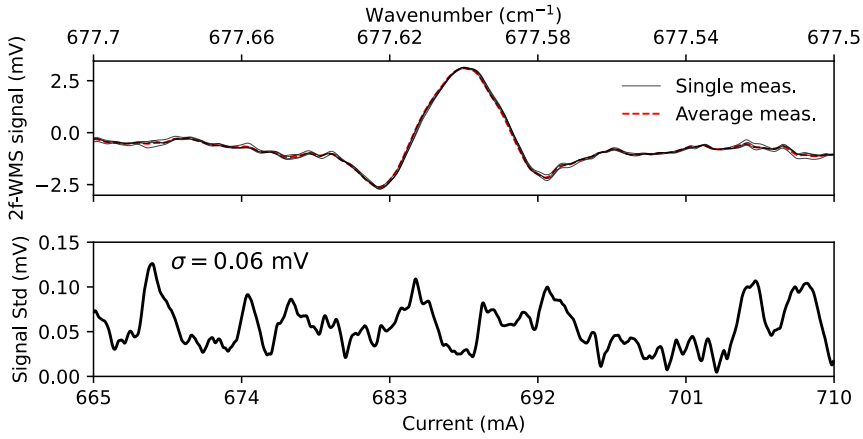

Figure 6.11: Individual and average background measurement (pure N_2), showing a residual CO_2 contamination. The standard deviation of the noise traces for each current value is shown on the bottom, being reasonably similar over the whole spectrum.

the non-optimal AR-coating can have an influence. However, the fringes are stable over the time-scale of the experiment and can be removed by proper background subtraction. Further discussion on the topic is provided in the long-term stability analysis.

6.2.2 C_6H_6 detection

The vibrational structure of benzene appears very complex and the line information are not available. The most important resources are IR-databases (HITRAN, PNNL and GEISA [216]), which contain spectra of the molecule in particular pressure and temperature conditions (as shown in Fig. 6.1). However, precise line information are not readily available and an investigation of the possible influence of the pressure broadening was needed. In Figs. 6.12 and 6.13, the benzene lines were probed at 30, 50, 100 and 150 mbar, adapting the modulation depth accordingly. Compared to the simple case of CO_2, where individual lines can be resolved, in C_6H_6 multiple closely spaced lines overlap giving 'broad' features, whose behavior is difficult to predict. In particular, from the performed investigation it resulted that better performances are achieved at 50 mbar and 150 mbar. High pressures are risky in the sense that pressure broadening of the neighbouring CO_2 lines can introduce unwanted overlap. For consistency with the CO_2 calibration, the 100 mbar pressure was chosen at slight expense of the achieved sensitivity.

The calibration curve, portrayed in Fig. 6.14, was obtained by diluting the prepared 300 ppm tank with pure N_2. The calibration curve appeared linear over the whole concentration range, with a sensitivity of 0.3 mV/ppm, that resulted in a NEC = 200ppb from the noise level of $\sigma = 0.07$mV. In the calibration curve, the positive peak observed at ~ 755mA corresponds to a carbon dioxide contamination which was introduced during the sample preparation. To rule out the possibility of cross-sensitivity between the two substances, and in particular of CO_2 presence in benzene detection, the two gases were mixed through the gas blender. The influence of benzene towards CO_2 detection - aside

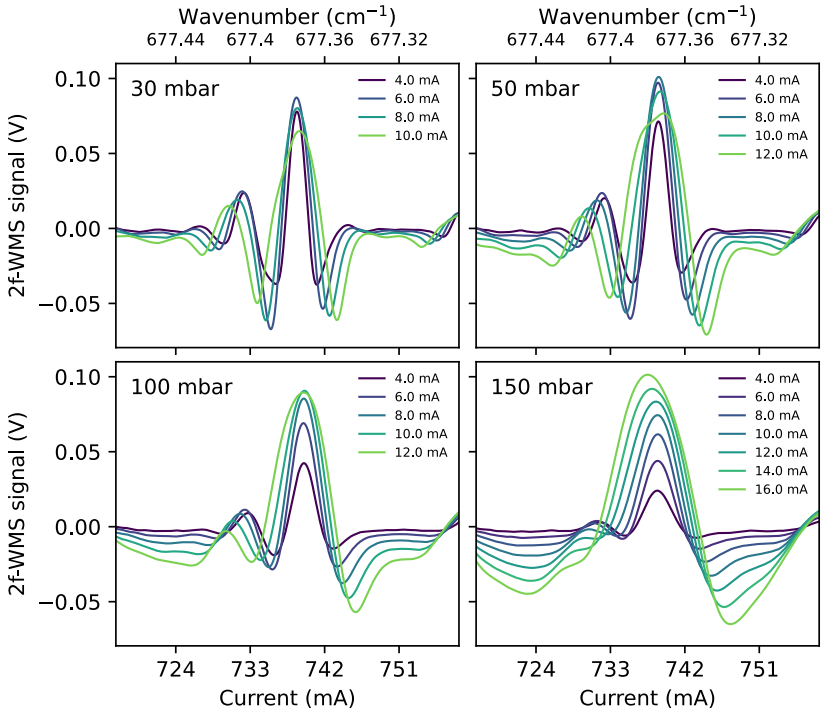

Figure 6.12: Effect of pressure broadening and modulation depth on the benzene spectrum.

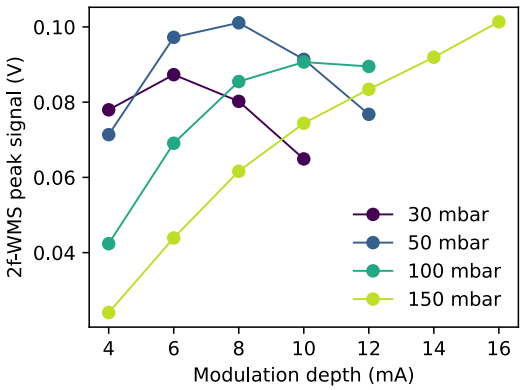

Figure 6.13: Identification of the optimal pressure and modulation depth configuration.

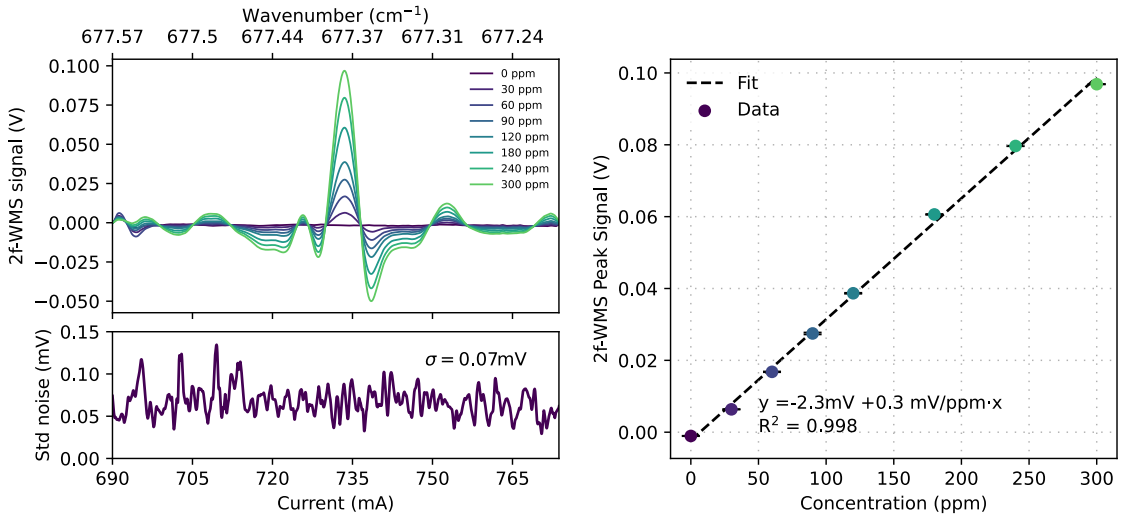

Figure 6.14: 2f-WMS spectra of the benzene lines together with the noise level of the system and calibration curve of the benzene analyser.

from being less plausible due to their ambient concentrations and line intensities - was not investigated as the two substances were contemporary present in the benzene sample.

6.3 Cross-sensitivity

In order to verify minimum cross-sensitivity of the sensor's response, variable mixing ratios for the mixture C_6H_6:CO_2:N_2 were tested. At a fixed concentration of benzene, the sensor's response with addition of CO_2 or N_2 was compared to observe the direct influence of the CO_2 interference. As shown in Fig. 6.15, the benzene peaks in the two conditions are perfectly comparable, aside for the highest CO_2 concentration of 400ppm, where a 1% deviation was observed. The 2f-absorption peak value shifts negatively in the presence of CO_2, as a tail of the negative lobe overlaps with benzene lines. This deviation is almost

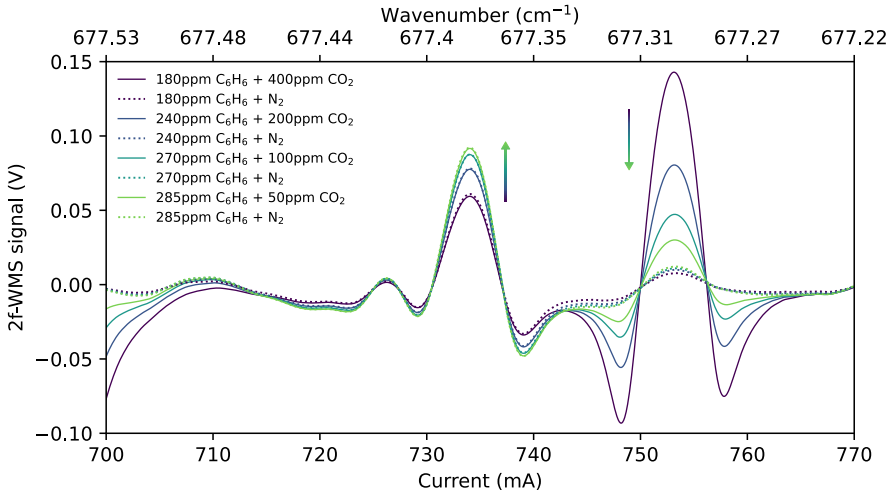

Figure 6.15: Analyser response at different C_6H_6:CO_2:N_2 mixing ratios.

negligible considering its extent and does not affect the linearity of the system, confirming the selectivity of the chosen lines. At higher carbon dioxide concentrations a larger impact is expected, which can be mitigated by reducing the system's pressure.

6.4 Long-term stability

The limits of detection presented for the system suggest that the limiting noise source lies in the pyrodetector dark current, which was strongly reduced by operating at low modulation frequencies. In principle, averaging over longer time scales should reduce the amount of noise captured by the lock-in amplifier. This is equivalent to using a narrower low-pass filter in the demodulation process to capture a smaller portion of the NSD distribution. Such an assumption is only valid if the system is stable over the long integration time. To assess the long-term stability of the system an Allan-deviation analysis was carried out (cfr. Section 1.7.2).

Such analysis was performed on benzene by scanning a short region around the peak position with a frequency of 0.5Hz. The maximum concentration of 300ppm C_6H_6 was used, due to limitations introduced by the gas blender. The mixer uses a channel selected by the user (generally the N_2 one) for balancing of the total flow. This is done internally by the instrument with a PID-loop, which introduces oscillations in the measurement. To avoid such problem, only one channel must be used, resulting in the maximum concentration.

In Fig. 6.16, the results of such investigation are shown. On the top left is the first time trace of the benzene peak against the tuning current, while a spectrogram of the individual spectra recorded over time is shown just below. The spectra, recorded for

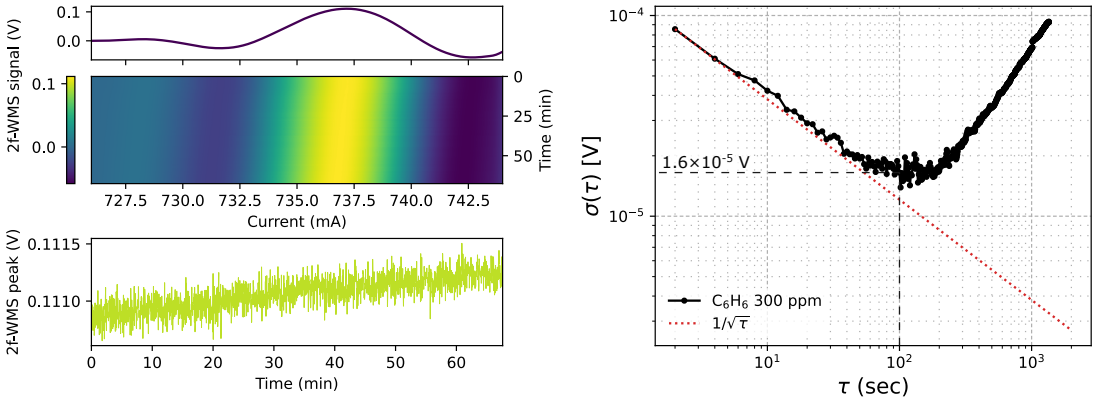

Figure 6.16: Long-term stability assessment of the system. On the top left, a spectrogram of the benzene spectra over 70 minutes of acquisition. The first scan is provided as reference on top. On the bottom, the peak values over time show a slow drift consistent with a line shift. The drift limits the longest integration time as demonstrated by the Allan deviation plot on the right. Optimum integration times are achieved at 100 sec, where the noise level drops from $8.5 \cdot 10^{-5}$V to $1.6 \cdot 10^{-5}$V, corresponding to a reduction of the noise level by a factor 5.3.

almost 70 minutes, reveal a constant drift of the peak position, most likely due to a thermal drift of the QCL. Accordingly, a slow drift of the peak signal is observed over time, as depicted on the bottom left. Slow drifts affect the rightmost part of the Allan plot, as the integration over larger times results in an even wider spread of the integrated datapoints. Hence, drifts in the signal limit the maximum integration time constants. This effect is clearly shown in the Allan deviation of the peak values, which exhibit a minimum at $\sim$ 100sec before rising as a consequence of the observed slow drift. The first part of the Allan deviation demonstrates that the dominating noise source is white in nature, since $\sigma \propto 1/\sqrt{\tau}$. With integration times of 100sec, the system noise is reduced by a factor of ~ 5.3 leading to a lower detection limit of $\mathrm{NEC}_{100s} = 40$ppb for C_6H_6. It is reasonable to assume that a similar improvement in the noise would happen also for the case of CO_2, for which a $\mathrm{NEC}_{100s} = 1.7$ppb is obtained.

Finally, it should be noted that in this analysis, lock-in time constants of 30ms were used, with ramp frequencies of 0.5Hz, setting a measurement duty cycle to 1.5%. The measurement duty cycle has the effect of 'lifting' the Allan curve upwards, as less samples are available for averaging [82]. The measurement duty cycle was limited by the communication speed between the LIA and the computer. An optimized communication protocol, built-in lock-in amplifiers or the use of longer integration times would certainly benefit the enhancement of noise rejection.

6.5 Conclusions

In this chapter a spectroscopic demonstration on the capabilities of LW-QCLs was given on the example of carbon dioxide and benzene detection. The system was based on an InAs-based QCL emitting at $\sim 677\mathrm{cm}^{-1}$, housed in a custom-made aluminium box. The laser beam was collimated externally with a high-acceptance ZnSe lens and the beam was coupled to a circular multipass cell. A pyrodetector was employed to measure the light exiting the multipass cell.

The system provided noise equivalent concentrations of 9ppb for CO_2 for the intense line and 200ppb for C_6H_6, assuming a prepared sample concentration of 300ppm. From the CO_2 line parameter and the employed ENBW (3.125Hz), the two metrics of $\alpha_{\min} = 1.6 \cdot 10^{-7}\mathrm{cm}^{-1}$ and $\mathrm{NEA} = 8.8 \cdot 10^{-8}\mathrm{cm}^{-1}\,\mathrm{Hz}^{-1/2}$ were derived. The ENBW can be further reduced to improve the noise rejection. Such assumption was confirmed by an Allan deviation analysis, for which a stability up to 100 seconds of integration time was observed. At 100sec integration time, the detection limits could be reduced by a factor of 5. The observed slow drift, most likely connected to the laser or its driving electronics, was the main cause of instability. Temperature compensation of the laser chip might help in reducing the observed drift. At the same time, the influence of the laser optical power cannot be ruled out. In that sense, different approaches such as 2f/1f normalization should remove this instability.

Finally, it was demonstrated how selective identification of the two species can be achieved by working at reduced pressure, favouring line separation. At the operative pressure of 100 mbar, the influence of ambient concentration CO_2 (400ppm) affected the benzene response by only 1%.

In conclusion, a laser source capable of targeting the main absorption of benzene would certainly benefit, and is expected to improve the limits of detections by almost two orders of magnitude.

Summary and perspectives

Continued advances in lasers, and in particular mid-IR sources are driving the development of novel, highly effective sensor systems designed for rapid and rugged trace gas detection. Laser-based sensor systems present numerous benefits over traditional methods, including rapid and non-invasive measurement, minimal matrix interference, and high sensitivity, making them an ideal tool for gas sensing. The most widespread approaches for laser-based gas sensing are based on the measurement of the intensity transmitted by the sample after absorption. Trace gas detection is then achieved by maximizing the optical pathlength interaction with the sample, by means of multipass cells or cavity enhanced techniques. Despite the high-sensitivity of the method, the need of a larger interaction volume increases the time needed to homogeneously fill the gas cell, compromising real-time monitoring. In this regard, a thoughtful design of the gas cell can aim towards the optimization of the optical pathlength-to-volume ratio. Circular multipass cells, also used in this dissertation, for instance, are designed according to this criterion.

Direct absorption techniques, however, do not fully leverage the high brilliance of laser sources, as the typical optical powers are sufficient to saturate photodetectors such that optical filters are needed. In contrast to direct approaches, indirect sensing approaches measure the effects generated upon photon absorption, taking full advantage of the high optical powers of lasers. Photoacoustic spectroscopy can be considered the ancestor of indirect approaches, since it was first employed back in 1880 using the sun as radiation source. The advent of lasers not only surged this field, but opened the path for novel detection techniques, which remained unexplored for the lack of proper sensing tools. It is the case for photothermal spectroscopy, in which thermal fields generated in proximity of the excitation field can be probed by employing a second laser source.

Photothermal approaches typically measure the way light is affected by the perturbed medium density, exploiting the direct connection between density and refractive index. Any density change will be reflected in a perturbation of the medium refractive index. Deflection, thermal lensing and interferometric sensing approaches are the most used. The latter measure the phase cumulated by the probe radiation while passing through the perturbed medium with the phase of an unperturbed beam. Such phase-shift is conveniently measured as an intensity change on top of a photodetector. The phase-shift is enhanced in the case of Fabry-Pérot interferometers by a factor proportional to its finesse,

which defines the average number of reflections occurring in such resonant cavity. The potential of a compact FPI for rugged gas sensing was successfully demonstrated in this work through the development of an Interferometric Cavity Assisted Photothermal Spectroscopy (ICAPS) system. In real-case scenario applications, changes in the gas matrix composition, temperature and pressure have to be actively compensated, as these would compromise the reliability of the sensor readout. A possible solution is given by fast tunable probe laser sources, such as laser diodes. A convenient normalization and locking approach were developed and demonstrated in the whole current tuning range of the DL. The benefit of this approach lies in the possibility of normalizing the sensor's response by the quality of the interferometer. The real-time investigation of the FPI, addressed by wavelength modulation of the probe source, serves as a reference for the PTS signal. The effect of the probe detuning from the resonance conditions was demonstrated experimentally, providing a close adherence to the presented model. With such a system, detection limits on the single-digit ppm concentration range were obtained for NO, corresponding to normalized noise equivalent absorptions of $3.3 \cdot 10^{-6}$ $\mathrm{W\,cm^{-1}Hz^{-1/2}}$. Considerable improvements can be envisioned with balanced detection approaches, where a reference beam can be employed for efficient rejection of the common mode noise by differential lock-in amplification. Based on the experience gained in this dissertation, it is suggested that future developments should pay particular attention to the design and construction of the gas cell housing the FPI. Proper arrangements, designed to relax the stresses applied on the FPI optical substrates can strongly improve stability towards the environmental temperature and the differential pressure between outer and inner environments. Furthermore, a stable optical cavity composed by curved mirrors can provide a double benefit: on one side, it would greatly improve the finesse of the FPI, at cost of a reduced linearity; on the other side, proper mode matching of the probe beam would allow a reduced beam waist between the mirrors. In turn, this would ensure the sensing of the spatial volume where the highest thermal gradients are generated, thereby improving the sensitivity of the method. In the next years, further advances in the field are expected, especially towards system integration due to the inherent miniaturization potential of FPIs.

A promising application of PTS concerns sensing using long-wavelength sources, where the efficiency of MCT detectors drops considerably. However, along with the performance of the PTS technique, high-performing laser sources are also needed. The InAs-based quantum cascade lasers, thanks to the small effective electron mass of InAs, closed the gap between mid-IR and the inaccessible Reststrahlen band, demonstrating LW continuous-wave operation even at room temperature. The pursuit of enhanced optical powers is a common objective, since in most applications it enables higher performance. This thesis built on recent advances on LW-sources, pushing the boundaries of the extracted optical powers. Tapered laser cavities were designed and fabricated within this dissertation with the aim to improve the QCL active volume while preserving excellent beam quality. The results obtained on tapered lasers demonstrated an optical power scaling consistent

with the active zone increase. Enhancements up to a factor of 3 were observed in pulsed operation for the largest taper angle of 3°. At the same time, the far-field distribution was measured to assess the beam quality factor (M^2). The slow-axis beam divergences approached the diffraction-limited value, providing almost ideal Gaussian intensity distribution with highly reduced divergence angles compared with the ridge laser. Angular standard deviations as small as 4.2° were obtained, with $M^2 \approx 1$. The threshold current density behavior was also investigated, suggesting that the reduced waveguide losses in the taper section might be responsible for the negative threshold current shift.

Thin film coatings are also a viable solution to improve the extracted optical power. Their combination with LW-devices and tapered lasers was demonstrated in this work, providing a considerable improvement of the slope efficiency (up to a factor of 4.5). Maximum peak powers on the order of 400 mW were obtained for a 3° taper, treated with both AR and HR coating deposition. Coincidentally, the threshold current density was not drastically degraded, as it is dominated by the transparency component. The deposition of a HR coating almost completely compensated for the detrimental effect of the single AR coating on the threshold current.

The selection of a single longitudinal mode is typically required in gas phase spectroscopic applications. In Fabry-Pérot devices, many longitudinal modes can oscillate within the gain spectrum of the active medium, resulting in multi-mode operation. The spectral selection was performed by a first-order Bragg grating, achieving side-mode suppression ratios in excess of 20 dB for all the tapered devices. CW-operation is still an ongoing challenge for tapered devices, due to the high dissipated electrical power. Future optimization steps include a careful choice of the device length, duty cycle of the tapered section and strategies for improved heat extraction capabilities, to mitigate the heat generated in the active zone. Nevertheless, preliminary results were demonstrated for shortened devices with few mW power outputs in uncoated devices.

Trace sensing in the LWIR was one of the driving reasons behind LW-QCL development. In particular, monitoring of volatile organic compounds, often represented by the subclass of BTEX, is gaining attention over the last decade. Highly sensitive detection in the LWIR is possible due to the strong absorption cross-sections occurring in this spectral range, with the additional advantage of high selectivity due to the small cross-sensitivity with atmospheric species. A sensor system based on a LW-QCL was built to showcase the capabilities of these devices. The laser was stabilized at -13°C, readily done by Peltier cooling. In combination with a circular multipass cell for improved sensitivity, detection limits as low as 9ppb and 200ppb were achieved for CO_2 and C_6H_6, respectively, with an ENBW of 3.125 Hz. The noise equivalent absorption was estimated to be $\sim 8.8 \cdot 10^{-8}$ $\mathrm{cm^{-1}\,Hz^{-1/2}}$ on a 15 m optical pathlength. The long-term stability of the sensor system revealed that with an optimal integration time of 100 s the aforementioned detection limits would be improved by a factor of 5.

Despite the good limits of detection achieved with the direct absorption method, it

would be attractive to demonstrate the coupling of LW-sources with the ICAPS technology. In addition, a QCL capable of targeting benzene's fundamental absorption at 674 cm^{-1} is expected to improve the detection limits by almost two orders of magnitude.

References

[1] M. Lackner, "TUNABLE DIODE LASER ABSORPTION SPECTROSCOPY (TDLAS) IN THE PROCESS INDUSTRIES – A REVIEW," *Reviews in Chemical Engineering*, vol. 23, no. 2, Jan. 2007. DOI: 10.1515/REVCE.2007.23.2.65.

[2] S. Schilt, L. Thévenaz, M. Niklès, L. Emmenegger, and C. Hüglin, "Ammonia monitoring at trace level using photoacoustic spectroscopy in industrial and environmental applications," *Spectrochimica Acta Part A: Molecular and Biomolecular Spectroscopy*, vol. 60, no. 14, pp. 3259–3268, Dec. 2004. DOI: 10.1016/j.saa.2003.11.032.

[3] B. Henderson, A. Khodabakhsh, M. Metsälä, I. Ventrillard, F. M. Schmidt, D. Romanini, G. A. D. Ritchie, S. Te Lintel Hekkert, R. Briot, T. Risby, N. Marczin, F. J. M. Harren, and S. M. Cristescu, "Laser spectroscopy for breath analysis: Towards clinical implementation," *Applied Physics B*, vol. 124, no. 8, p. 161, Aug. 2018. DOI: 10.1007/s00340-018-7030-x.

[4] Z. Du, S. Zhang, J. Li, N. Gao, and K. Tong, "Mid-Infrared Tunable Laser-Based Broadband Fingerprint Absorption Spectroscopy for Trace Gas Sensing: A Review," *Applied Sciences*, vol. 9, no. 2, p. 338, Jan. 18, 2019. DOI: 10.3390/app9020338.

[5] B. Schwarz, P. Reininger, D. Ristanić, H. Detz, A. M. Andrews, W. Schrenk, and G. Strasser, "Monolithically integrated mid-infrared lab-on-a-chip using plasmonics and quantum cascade structures," *Nature Communications*, vol. 5, no. 1, p. 4085, Jun. 6, 2014. DOI: 10.1038/ncomms5085.

[6] A. Yu. Luk'yanov and M. A. Novikov, "The sensitivity of thermal-lens and phase-shift (interferometric) techniques in photothermal spectroscopy: A comparative study," *Technical Physics*, vol. 45, no. 11, pp. 1470–1474, Nov. 2000. DOI: 10.1134/1.1325032.

[7] D. Smith and P. Španěl, "The challenge of breath analysis for clinical diagnosis and therapeutic monitoring," *The Analyst*, vol. 132, no. 5, pp. 390–396, 2007. DOI: 10.1039/B700542N.

[8] I. Manisalidis, E. Stavropoulou, A. Stavropoulos, and E. Bezirtzoglou, "Environmental and Health Impacts of Air Pollution: A Review," *Frontiers in Public Health*, vol. 8, p. 14, Feb. 20, 2020. DOI: 10.3389/fpubh.2020.00014.

[9] "Ambient air pollution: A global assessment of exposure and burden of disease." (), [Online]. Available: https://www.who.int/publications-detail-redirect/9789241511353 (visited on 02/19/2024).

[10] O. A. R. US EPA. "Criteria Air Pollutants." (Apr. 9, 2014), [Online]. Available: https://www.epa.gov/criteria-air-pollutants (visited on 02/19/2024).

[11] *Directive 2008/50/EC of the European Parliament and of the Council of 21 May 2008 on ambient air quality and cleaner air for Europe*, Sep. 18, 2015.

[12] P. Q. Tranchida, M. Zoccali, and L. Mondello, "High-speed GC-MS," in *Hyphenations of Capillary Chromatography with Mass Spectrometry*, Elsevier, 2020, pp. 109–132, ISBN: 978-0-12-809638-3. DOI: 10.1016/B978-0-12-809638-3.00003-X.

[13] M. Van Deursen, J. Beens, H.-G. Janssen, P. Leclercq, and C. Cramers, "Evaluation of time-of-flight mass spectrometric detection for fast gas chromatography," *Journal of Chromatography A*, vol. 878, no. 2, pp. 205–213, May 2000. DOI: 10.1016/S0021-9673(00)00300-9.

[14] J. Hodgkinson and R. P. Tatam, "Optical gas sensing: A review," *Measurement Science and Technology*, vol. 24, no. 1, p. 012 004, Jan. 1, 2013. DOI: 10.1088/0957-0233/24/1/012004.

[15] P. T. Moseley, "Solid state gas sensors," *Measurement Science and Technology*, vol. 8, no. 3, p. 223, Mar. 1997. DOI: 10.1088/0957-0233/8/3/003.

[16] N. Yamazoe and K. Shimanoe, "Receptor Function and Response of Semiconductor Gas Sensor," *Journal of Sensors*, vol. 2009, pp. 1–21, 2009. DOI: 10.1155/2009/875704.

[17] E. Roueff, H. Abgrall, P. Czachorowski, K. Pachucki, M. Puchalski, and J. Komasa, "The full infrared spectrum of molecular hydrogen," *Astronomy & Astrophysics*, vol. 630, A58, Oct. 2019. DOI: 10.1051/0004-6361/201936249.

[18] I. Gordon, L. Rothman, C. Hill, R. Kochanov, Y. Tan, P. Bernath, M. Birk, V. Boudon, A. Campargue, K. Chance, B. Drouin, J.-M. Flaud, R. Gamache, J. Hodges, D. Jacquemart, V. Perevalov, A. Perrin, K. Shine, M.-A. Smith, J. Tennyson, G. Toon, H. Tran, V. Tyuterev, A. Barbe, A. Császár, V. Devi, T. Furtenbacher, J. Harrison, J.-M. Hartmann, A. Jolly, T. Johnson, T. Karman, I. Kleiner, A. Kyuberis, J. Loos, O. Lyulin, S. Massie, S. Mikhailenko, N. Moazzen-Ahmadi, H. Müller, O. Naumenko, A. Nikitin, O. Polyansky, M. Rey, M. Rotger, S. Sharpe, K. Sung, E. Starikova, S. Tashkun, J. V. Auwera, G. Wagner, J. Wilzewski, P. Wcisło, S. Yu, and E. Zak, "The HITRAN2016 molecular spectroscopic database," *Journal of Quantitative Spectroscopy and Radiative Transfer*, vol. 203, pp. 3–69, Dec. 2017. DOI: 10.1016/j.jqsrt.2017.06.038.

[19] M. Šimečková, D. Jacquemart, L. S. Rothman, R. R. Gamache, and A. Goldman, "Einstein A-coefficients and statistical weights for molecular absorption transitions in the HITRAN database," *Journal of Quantitative Spectroscopy and Radiative Transfer*, vol. 98, no. 1, pp. 130–155, Mar. 2006. DOI: 10.1016/j.jqsrt.2005.07.003.

[20] T. G. Mayerhöfer, S. Pahlow, and J. Popp, "The Bouguer-Beer-Lambert Law: Shining Light on the Obscure," *ChemPhysChem*, vol. 21, no. 18, pp. 2029–2046, Sep. 15, 2020. DOI: 10.1002/cphc.202000464.

[21] J. B. Tatum, "The interpretation of intensities in diatomic molecular spectra," vol. 14, p. 21, Mar. 1967. DOI: 10.1086/190149.

[22] R. H. Dicke, "The Effect of Collisions upon the Doppler Width of Spectral Lines," *Physical Review*, vol. 89, no. 2, pp. 472–473, Jan. 15, 1953. DOI: 10.1103/PhysRev.89.472.

[23] A. T. Ramsey and L. W. Anderson, "Pressure Shifts in the 23Na Hyperfine Frequency," *The Journal of Chemical Physics*, vol. 43, no. 1, pp. 191–194, Jul. 1, 1965. DOI: 10.1063/1.1696452.

[24] W. W. Bewley, C. L. Canedy, C. S. Kim, M. Kim, C. D. Merritt, J. Abell, I. Vurgaftman, and J. R. Meyer, "Continuous-wave interband cascade lasers operating above room temperature at $\lambda = 4.7$-5.6 µm," *Optics Express*, vol. 20, no. 3, p. 3235, Jan. 30, 2012. DOI: 10.1364/OE.20.003235.

[25] L. Li, H. Ye, Y. Jiang, R. Q. Yang, J. C. Keay, T. D. Mishima, M. B. Santos, and M. B. Johnson, "MBE-grown long-wavelength interband cascade lasers on InAs substrates," *Journal of Crystal Growth*, vol. 425, pp. 369–372, Sep. 2015. DOI: 10.1016/j.jcrysgro.2015.02.016.

[26] J. A. Massengale, Y. Shen, R. Q. Yang, S. D. Hawkins, and J. F. Klem, "Long wavelength interband cascade lasers," *Applied Physics Letters*, vol. 120, no. 9, p. 091 105, Feb. 28, 2022. DOI: 10.1063/5.0084565.

[27] A. N. Baranov and R. Teissier, "Quantum Cascade Lasers in the InAs/AlSb Material System," *IEEE Journal of Selected Topics in Quantum Electronics*, vol. 21, no. 6, pp. 85–96, Nov. 2015. DOI: 10.1109/JSTQE.2015.2426412.

[28] B. S. Williams, "Terahertz quantum-cascade lasers," *Nature Photonics*, vol. 1, no. 9, pp. 517–525, Sep. 2007. DOI: 10.1038/nphoton.2007.166.

[29] C. Gmachl, F. Capasso, D. L. Sivco, and A. Y. Cho, "Recent progress in quantum cascade lasers and applications," *Reports on Progress in Physics*, vol. 64, no. 11, pp. 1533–1601, Nov. 1, 2001. DOI: 10.1088/0034-4885/64/11/204.

[30] M. Gehrtz, E. A. Whittaker, and G. C. Bjorklund, "Quantum-limited laser frequency-modulation spectroscopy," *Journal of the Optical Society of America B*, vol. 2, no. 9, p. 1510, Sep. 1, 1985. DOI: 10.1364/JOSAB.2.001510.

[31] J. M. Supplee, E. A. Whittaker, and W. Lenth, "Theoretical description of frequency modulation and wavelength modulation spectroscopy," *Applied Optics*, vol. 33, no. 27, p. 6294, Sep. 20, 1994. DOI: 10.1364/AO.33.006294.

[32] J. Reid and D. Labrie, "Second-harmonic detection with tunable diode lasers - Comparison of experiment and theory," *Applied Physics B Photophysics and Laser Chemistry*, vol. 26, no. 3, pp. 203–210, Nov. 1981. DOI: 10.1007/BF00692448.

[33] R. Arndt, "Analytical Line Shapes for Lorentzian Signals Broadened by Modulation," *Journal of Applied Physics*, vol. 36, no. 8, pp. 2522–2524, Aug. 1965. DOI: 10.1063/1.1714523.

[34] G. Gervasoni, M. Carminati, and G. Ferrari, "FPGA-based lock-in amplifier with sub-ppm resolution working up to 6 MHz," in *2016 IEEE International Conference on Electronics, Circuits and Systems (ICECS)*, Monte Carlo, Monaco: IEEE, Dec. 2016, pp. 117–120, ISBN: 978-1-5090-6113-6. DOI: 10.1109/ICECS.2016.7841146.

[35] M. Andersson, L. Persson, T. Svensson, and S. Svanberg, "Flexible lock-in detection system based on synchronized computer plug-in boards applied in sensitive gas spectroscopy," *Review of Scientific Instruments*, vol. 78, no. 11, p. 113 107, Nov. 1, 2007. DOI: 10.1063/1.2813346.

[36] "Principles of Lock-in Detection | Zurich Instruments." (), [Online]. Available: https://www.zhinst.com/europe/en/resources/principles-of-lock-in-detection (visited on 06/07/2024).

[37] W. Demtröder, *Laser Spectroscopy*. Berlin, Heidelberg: Springer Berlin Heidelberg, 2008, ISBN: 978-3-540-73415-4 978-3-540-73418-5. DOI: 10.1007/978-3-540-73418-5.

[38] G. C. Bjorklund, "Frequency-modulation spectroscopy: A new method for measuring weak absorptions and dispersions," *Optics Letters*, vol. 5, no. 1, p. 15, Jan. 1, 1980. DOI: 10.1364/OL.5.000015.

[39] P. Martín-Mateos and P. Acedo, "Heterodyne phase-sensitive detection for calibration-free molecular dispersion spectroscopy," *Optics Express*, vol. 22, no. 12, p. 15 143, Jun. 16, 2014. DOI: 10.1364/OE.22.015143.

[40] P. Martín-Mateos, J. Hayden, P. Acedo, and B. Lendl, "Heterodyne Phase-Sensitive Dispersion Spectroscopy in the Mid-Infrared with a Quantum Cascade Laser," *Analytical Chemistry*, vol. 89, no. 11, pp. 5916–5922, Jun. 6, 2017. DOI: 10.1021/acs.analchem.7b00303.

[41] Z. Wang, K.-P. Cheong, M. Li, Q. Wang, and W. Ren, "Theoretical and Experimental Study of Heterodyne Phase-Sensitive Dispersion Spectroscopy with an Injection-Current-Modulated Quantum Cascade Laser," *Sensors*, vol. 20, no. 21, p. 6176, Oct. 29, 2020. DOI: 10.3390/s20216176.

[42] H. Zhang, T. Wu, Q. Wu, W. Chen, C. Ye, M. Wang, M. Zhu, and X. He, "Methane detection with a near-infrared heterodyne phase-sensitive dispersion spectrometer at a stronger frequency modulation using direct injection-current dithering," *Optics Express*, vol. 31, no. 15, p. 25 070, Jul. 17, 2023. DOI: 10.1364/OE.495581.

[43] G. Wysocki and D. Weidmann, "Molecular dispersion spectroscopy for chemical sensing using chirped mid-infrared quantum cascade laser," *Optics Express*, vol. 18, no. 25, p. 26 123, Dec. 6, 2010. DOI: 10.1364/OE.18.026123.

[44] M. Nikodem, D. Weidmann, and G. Wysocki, "Chirped laser dispersion spectroscopy with harmonic detection of molecular spectra," *Applied Physics B*, vol. 109, no. 3, pp. 477–483, Nov. 2012. DOI: 10.1007/s00340-012-5060-3.

[45] S. Lindner, J. Hayden, A. Schwaighofer, T. Wolflehner, C. Kristament, M. González-Cabrera, S. Zlabinger, and B. Lendl, "External Cavity Quantum Cascade Laser-Based Mid-Infrared Dispersion Spectroscopy for Qualitative and Quantitative Analysis of Liquid-Phase Samples," *Applied Spectroscopy*, vol. 74, no. 4, pp. 452–459, Apr. 2020. DOI: 10.1177/0003702819892646.

[46] A. Dabrowska, S. Lindner, A. Schwaighofer, and B. Lendl, "Mid-IR dispersion spectroscopy – A new avenue for liquid phase analysis," *Spectrochimica Acta Part A: Molecular and Biomolecular Spectroscopy*, vol. 286, p. 122 014, Feb. 2023. DOI: 10.1016/j.saa.2022.122014.

[47] A. Hugi, G. Villares, S. Blaser, H. C. Liu, and J. Faist, "Mid-infrared frequency comb based on a quantum cascade laser," *Nature*, vol. 492, no. 7428, pp. 229–233, Dec. 2012. DOI: 10.1038/nature11620.

[48] H. Choi, L. Diehl, Z.-K. Wu, M. Giovannini, J. Faist, F. Capasso, and T. B. Norris, "Gain Recovery Dynamics and Photon-Driven Transport in Quantum Cascade Lasers," *Physical Review Letters*, vol. 100, no. 16, p. 167 401, Apr. 24, 2008. DOI: 10.1103/PhysRevLett.100.167401.

[49] J. Hayden, M. Geiser, M. Gianella, R. Horvath, A. Hugi, L. Sterczewski, and M. Mangold, "Mid-infrared dual-comb spectroscopy with quantum cascade lasers," *APL Photonics*, vol. 9, no. 3, p. 031 101, Mar. 1, 2024. DOI: 10.1063/5.0159042.

[50] C. Silvestri, X. Qi, T. Taimre, K. Bertling, and A. D. Rakić, "Frequency combs in quantum cascade lasers: An overview of modeling and experiments," *APL Photonics*, vol. 8, no. 2, p. 020 902, Feb. 1, 2023. DOI: 10.1063/5.0134539.

[51] P. Jouy, J. M. Wolf, Y. Bidaux, P. Allmendinger, M. Mangold, M. Beck, and J. Faist, "Dual comb operation of $\lambda \sim 8.2$ µm quantum cascade laser frequency comb with 1 W optical power," *Applied Physics Letters*, vol. 111, no. 14, p. 141 102, Oct. 2, 2017. DOI: 10.1063/1.4985102.

[52] M. Gianella, A. Nataraj, B. Tuzson, P. Jouy, F. Kapsalidis, M. Beck, M. Mangold, A. Hugi, J. Faist, and L. Emmenegger, "High-resolution and gapless dual comb spectroscopy with current-tuned quantum cascade lasers," *Optics Express*, vol. 28, no. 5, p. 6197, Mar. 2, 2020. DOI: 10.1364/OE.379790.

[53] M. Beiser, N. Opačak, J. Hillbrand, G. Strasser, and B. Schwarz, "Engineering the spectral bandwidth of quantum cascade laser frequency combs," *Optics Letters*, vol. 46, no. 14, p. 3416, Jul. 15, 2021. DOI: 10.1364/OL.424164.

[54] G. Villares, J. Wolf, D. Kazakov, M. J. Süess, A. Hugi, M. Beck, and J. Faist, "On-chip dual-comb based on quantum cascade laser frequency combs," *Applied Physics Letters*, vol. 107, no. 25, p. 251 104, Dec. 21, 2015. DOI: 10.1063/1.4938213.

[55] B. Hinkov, F. Pilat, L. Lux, P. L. Souza, M. David, A. Schwaighofer, D. Ristanić, B. Schwarz, H. Detz, A. M. Andrews, B. Lendl, and G. Strasser, "A mid-infrared lab-on-a-chip for dynamic reaction monitoring," *Nature Communications*, vol. 13, no. 1, p. 4753, Aug. 13, 2022. DOI: 10.1038/s41467-022-32417-7.

[56] Y.-H. Lee, R. G. Maus, B. W. Smith, and J. D. Winefordner, "Laser-Induced Fluorescence Detection of a Single Molecule in a Capillary," *Analytical Chemistry*, vol. 66, no. 23, pp. 4142–4149, Dec. 1, 1994. DOI: 10.1021/ac00095a005.

[57] H. Kronemayer, W. Bessler, and C. Schulz, "Gas-phase temperature imaging in spray systems using multi-line NO-LIF thermometry," *Applied Physics B*, vol. 81, no. 8, pp. 1071–1074, Dec. 2005. DOI: 10.1007/s00340-005-1986-z.

[58] M. L. Viengerov, "New method of gas analysis based on tyndall-roentgen optoacoustic effect," *Doklady Akademii Nauk SSSR*, vol. 19, no. 687, p. 8, 1938.

[59] E. L. Kerr and J. G. Atwood, "The Laser Illuminated Absorptivity Spectrophone: A Method for Measurement of Weak Absorptivity in Gases at Laser Wavelengths," *Applied Optics*, vol. 7, no. 5, p. 915, May 1, 1968. DOI: 10.1364/AO.7.000915.

[60] C. F. Dewey, R. D. Kamm, and C. E. Hackett, "Acoustic amplifier for detection of atmospheric pollutants," *Applied Physics Letters*, vol. 23, no. 11, pp. 633–635, Dec. 1, 1973. DOI: 10.1063/1.1654774.

[61] R. D. Kamm, "Detection of weakly absorbing gases using a resonant optoacoustic method," *Journal of Applied Physics*, vol. 47, no. 8, pp. 3550–3558, Aug. 1, 1976. DOI: 10.1063/1.323153.

[62] A. Miklós, P. Hess, and Z. Bozóki, "Application of acoustic resonators in photoacoustic trace gas analysis and metrology," *Review of Scientific Instruments*, vol. 72, no. 4, pp. 1937–1955, Apr. 1, 2001. DOI: 10.1063/1.1353198.

[63] X. Zhao, M. Guo, D. Cui, C. Li, H. Qi, K. Chen, F. Ma, J. Huang, G. Zhang, and J. Zhao, "Multi-pass Differential Photoacoustic Sensor for Real-Time Measurement of SF_6 Decomposition Component H_2S at the ppb Level," *Analytical Chemistry*, vol. 95, no. 21, pp. 8214–8222, May 30, 2023. DOI: 10.1021/acs.analchem.3c00003.

[64] J. Hayden, B. Baumgartner, J. P. Waclawek, and B. Lendl, "Mid-infrared sensing of CO at saturated absorption conditions using intracavity quartz-enhanced photoacoustic spectroscopy," *Applied Physics B*, vol. 125, no. 9, p. 159, Sep. 2019. DOI: 10.1007/s00340-019-7260-6.

[65] Y. Pan, L. Dong, H. Wu, W. Ma, L. Zhang, W. Yin, L. Xiao, S. Jia, and F. K. Tittel, "Cavity-enhanced photoacoustic sensor based on a whispering-gallery-mode diode laser," *Atmospheric Measurement Techniques*, vol. 12, no. 3, pp. 1905–1911, Mar. 25, 2019. DOI: 10.5194/amt-12-1905-2019.

[66] S. Schilt and L. Thévenaz, "Wavelength modulation photoacoustic spectroscopy: Theoretical description and experimental results," *Infrared Physics & Technology*, vol. 48, no. 2, pp. 154–162, Jun. 2006. DOI: 10.1016/j.infrared.2005.09.001.

[67] Z. Wang, Q. Nie, H. Sun, Q. Wang, S. Borri, P. De Natale, and W. Ren, "Cavity-enhanced photoacoustic dual-comb spectroscopy," *Light: Science & Applications*, vol. 13, no. 1, p. 11, Jan. 5, 2024. DOI: 10.1038/s41377-023-01353-6.

[68] J. T. Friedlein, E. Baumann, K. A. Briggman, G. M. Colacion, F. R. Giorgetta, A. M. Goldfain, D. I. Herman, E. V. Hoenig, J. Hwang, N. R. Newbury, E. F. Perez, C. S. Yung, I. Coddington, and K. C. Cossel, "Dual-comb photoacoustic spectroscopy," *Nature Communications*, vol. 11, no. 1, p. 3152, Jun. 19, 2020. DOI: 10.1038/s41467-020-16917-y.

[69] A. A. Kosterev, Yu. A. Bakhirkin, R. F. Curl, and F. K. Tittel, "Quartz-enhanced photoacoustic spectroscopy," *Optics Letters*, vol. 27, no. 21, p. 1902, Nov. 1, 2002. DOI: 10.1364/OL.27.001902.

[70] T. Milde, M. Hoppe, H. Tatenguem, M. Mordmüller, J. O'Gorman, U. Willer, W. Schade, and J. Sacher, "QEPAS sensor for breath analysis: A behavior of pressure," *Applied Optics*, vol. 57, no. 10, p. C120, Apr. 1, 2018. DOI: 10.1364/AO.57.00C120.

[71] B. Li, C. Feng, H. Wu, S. Jia, and L. Dong, "Calibration-free mid-infrared exhaled breath sensor based on BF-QEPAS for real-time ammonia measurements at ppb level," *Sensors and Actuators B: Chemical*, vol. 358, p. 131 510, May 2022. DOI: 10.1016/j.snb.2022.131510.

[72] V. Spagnolo, P. Patimisco, S. Borri, G. Scamarcio, B. E. Bernacki, and J. Kriesel, "Part-per-trillion level SF_6 detection using a quartz enhanced photoacoustic spectroscopy based sensor with single-mode fiber-coupled quantum cascade laser excitation," *Optics Letters*, vol. 37, no. 21, p. 4461, Nov. 1, 2012. DOI: 10.1364/OL.37.004461.

[73] Y. He, Y. Ma, Y. Tong, X. Yu, and F. Tittel, "HCN ppt-level detection based on a QEPAS sensor with amplified laser and a miniaturized 3D-printed photoacoustic detection channel," *Optics Express*, vol. 26, p. 9666, Apr. 16, 2018. DOI: 10.1364/OE.26.009666.

[74] P. Patimisco, G. Scamarcio, F. Tittel, and V. Spagnolo, "Quartz-Enhanced Photoacoustic Spectroscopy: A Review," *Sensors*, vol. 14, no. 4, pp. 6165–6206, Mar. 28, 2014. DOI: 10.3390/s140406165.

[75] A. Sampaolo, P. Patimisco, M. Giglio, A. Zifarelli, H. Wu, L. Dong, and V. Spagnolo, "Quartz-enhanced photoacoustic spectroscopy for multi-gas detection: A review," *Analytica Chimica Acta*, vol. 1202, p. 338 894, Apr. 2022. DOI: 10.1016/j.aca.2021.338894.

[76] Y. Yin, D. Ren, C. Li, R. Chen, and J. Shi, "Cantilever-enhanced photoacoustic spectroscopy for gas sensing: A comparison of different displacement detection methods," *Photoacoustics*, vol. 28, p. 100 423, Dec. 2022. DOI: 10.1016/j.pacs.2022.100423.

[77] J. Suchánek, P. Janda, M. Dostál, A. Knížek, P. Kubát, P. Roupcová, P. Bitala, V. Nevrlý, and Z. Zelinger, "Photoacoustic spectroscopy with mica and graphene micro-mechanical levers for multicomponent analysis of acetic acid, acetone and methanol mixture," *Microchemical Journal*, vol. 144, pp. 203–208, Jan. 2019. DOI: 10.1016/j.microc.2018.08.034.

[78] K. Liu, Y. Cao, G. Wang, W. Zhang, W. Chen, and X. Gao, "A novel photoacoustic spectroscopy gas sensor using a low cost polyvinylidene fluoride film," *Sensors and Actuators B: Chemical*, vol. 277, pp. 571–575, Dec. 2018. DOI: 10.1016/j.snb.2018.09.037.

[79] H. Lhermet, T. Verdot, A. Teulle, A. Berthelot, A. Gliere, B. Desloges, F. Souchon, M. Fournier, J.-M. Fedeli, and J.-G. Coutard, "Micro-Photoacoustic Cell with Integrated Microphone for Sub-Ppm Gas Sensing," in *2019 20th International Conference on Solid-State Sensors, Actuators and Microsystems & Eurosensors XXXIII (TRANSDUCERS & EUROSENSORS XXXIII)*, Berlin, Germany: IEEE, Jun. 2019, pp. 68–71, ISBN: 978-1-5386-8104-6. DOI: 10.1109/TRANSDUCERS.2019.8808295.

[80] W. Trzpil, J. Charensol, D. Ayache, N. Maurin, R. Rousseau, A. Vicet, and M. Bahriz, "A silicon micromechanical resonator with capacitive transduction for enhanced photoacoustic spectroscopy," *Sensors and Actuators B: Chemical*, vol. 353, p. 131 070, Feb. 2022. DOI: 10.1016/j.snb.2021.131070.

[81] Daniel. MacDougall, W. B. Crummett, and . Et Al., "Guidelines for data acquisition and data quality evaluation in environmental chemistry," *Analytical Chemistry*, vol. 52, no. 14, pp. 2242–2249, Dec. 1, 1980. DOI: 10.1021/ac50064a004.

[82] P. Werle, R. Mücke, and F. Slemr, "The limits of signal averaging in atmospheric trace-gas monitoring by tunable diode-laser absorption spectroscopy (TDLAS)," *Applied Physics B Photophysics and Laser Chemistry*, vol. 57, no. 2, pp. 131–139, Aug. 1993. DOI: 10.1007/BF00425997.

[83] P. Werle, "Accuracy and precision of laser spectrometers for trace gas sensing in the presence of optical fringes and atmospheric turbulence," *Applied Physics B*, vol. 102, no. 2, pp. 313–329, Feb. 2011. DOI: 10.1007/s00340-010-4165-9.

[84] A. G. Bell, "LXVIII. Upon the production of sound by radiant energy," *The London, Edinburgh, and Dublin Philosophical Magazine and Journal of Science*, vol. 11, no. 71, pp. 510–528, Jan. 1881. DOI: 10.1080/14786448108627053.

[85] J. P. Gordon, R. C. C. Leite, R. S. Moore, S. P. S. Porto, and J. R. Whinnery, "Long-Transient Effects in Lasers with Inserted Liquid Samples," *Journal of Applied Physics*, vol. 36, no. 1, pp. 3–8, Jan. 1965. DOI: 10.1063/1.1713919.

[86] E. A. McLean, L. Sica, and A. J. Glass, "INTERFEROMETRIC OBSERVATION OF ABSORPTION INDUCED INDEX CHANGE ASSOCIATED WITH THERMAL BLOOMING," *Applied Physics Letters*, vol. 13, no. 11, pp. 369–371, Dec. 1968. DOI: 10.1063/1.1652475.

[87] P. R. Longaker and M. M. Litvak, "Perturbation of the Refractive Index of Absorbing Media by a Pulsed Laser Beam," *Journal of Applied Physics*, vol. 40, no. 10, pp. 4033–4041, Sep. 1969. DOI: 10.1063/1.1657139.

[88] S. Bialkowski, N. G. C. Astrath, M. Proskurnin, and S. Bialkowski, *Photothermal Spectroscopy Methods* (Chemical Analysis), Second edition. Hoboken, NJ: Wiley, 2019, 1 p., ISBN: 978-1-119-27908-2 978-1-119-27909-9.

[89] J. Hodgkinson, M. Johnson, and J. P. Dakin, "Photothermal detection of trace optical absorption in water by use of visible-light-emitting diodes," *Applied Optics*, vol. 37, no. 31, p. 7320, Nov. 1, 1998. DOI: 10.1364/AO.37.007320.

[90] C. C. Davis and S. J. Petuchowski, "Phase fluctuation optical heterodyne spectroscopy of gases," *Applied Optics*, vol. 20, no. 14, p. 2539, Jul. 15, 1981. DOI: 10.1364/AO.20.002539.

[91] C. C. Davis, "Trace detection in gases using phase fluctuation optical heterodyne spectroscopy," *Applied Physics Letters*, vol. 36, no. 7, pp. 515–518, Apr. 1980. DOI: 10.1063/1.91590.

[92] G. Ricchiuti, A. Dabrowska, D. Pinto, G. Ramer, and B. Lendl, "Dual-Beam Photothermal Spectroscopy Employing a Mach–Zehnder Interferometer and an External Cavity Quantum Cascade Laser for Detection of Water Traces in Organic Solvents," *Analytical Chemistry*, vol. 94, no. 47, pp. 16 353–16 360, Nov. 29, 2022. DOI: 10.1021/acs.analchem.2c03303.

[93] G. Ricchiuti, L. Riedlsperger, A. Dabrowska, E. Rosenberg, L. O'Faolain, and B. Lendl, "Mid-Infrared Photothermal Spectroscopy for the Detection of Caffeine in Beverages," *Sensors*, vol. 24, no. 6, p. 1974, Mar. 20, 2024. DOI: 10.3390/s24061974.

[94] J. Stone, "Measurements of the Absorption of Light in Low-Loss Liquids," *Journal of the Optical Society of America*, vol. 62, no. 3, p. 327, Mar. 1, 1972. DOI: 10.1364/JOSA.62.000327.

[95] J. Stone, "Thermooptical Technique for the Measurement of Absorption Loss Spectrum in Liquids," *Applied Optics*, vol. 12, no. 8, p. 1828, Aug. 1, 1973. DOI: 10.1364/AO.12.001828.

[96] A. J. Campillo, S. J. Petuchowski, C. C. Davis, and H.-B. Lin, "Fabry–Perot photothermal trace detection," *Applied Physics Letters*, vol. 41, no. 4, pp. 327–329, Aug. 15, 1982. DOI: 10.1063/1.93524.

[97] J. P. Waclawek, V. C. Bauer, H. Moser, and B. Lendl, "2f-wavelength modulation Fabry-Perot photothermal interferometry," *Optics Express*, vol. 24, no. 25, p. 28 958, Dec. 12, 2016. DOI: 10.1364/OE.24.028958.

[98] P. M. Morse, K. U. Ingard, and K. U. Ingard, *Theoretical Acoustics*, Repr., 1. Princeton University Press ed. Princeton, NJ: Princeton University Press, 1986, 927 pp., ISBN: 978-0-691-02401-1 978-0-691-08425-1.

[99] A. Miklós, "Acoustic Aspects of Photoacoustic Signal Generation and Detection in Gases," *International Journal of Thermophysics*, vol. 36, no. 9, pp. 2285–2317, Sep. 2015. DOI: 10.1007/s10765-015-1875-6.

[100] X. Yin, L. Dong, H. Zheng, X. Liu, H. Wu, Y. Yang, W. Ma, L. Zhang, W. Yin, L. Xiao, and S. Jia, "Impact of Humidity on Quartz-Enhanced Photoacoustic Spectroscopy Based CO Detection Using a Near-IR Telecommunication Diode Laser," *Sensors*, vol. 16, no. 2, p. 162, Jan. 27, 2016. DOI: 10.3390/s16020162.

[101] V. Spagnolo, A. A. Kosterev, L. Dong, R. Lewicki, and F. K. Tittel, "NO trace gas sensor based on quartz-enhanced photoacoustic spectroscopy and external cavity quantum cascade laser," *Applied Physics B*, vol. 100, no. 1, pp. 125–130, Jul. 2010. DOI: 10.1007/s00340-010-3984-z.

[102] R. A. Rooth, A. J. L. Verhage, and L. W. Wouters, "Photoacoustic measurement of ammonia in the atmosphere: Influence of water vapor and carbon dioxide," *Applied Optics*, vol. 29, no. 25, p. 3643, Sep. 1, 1990. DOI: 10.1364/AO.29.003643.

[103] A. A. Kosterev, L. Dong, D. Thomazy, F. K. Tittel, and S. Overby, "QEPAS for chemical analysis of multi-component gas mixtures," *Applied Physics B*, vol. 101, no. 3, pp. 649–659, Nov. 2010. DOI: 10.1007/s00340-010-4183-7.

[104] J. Hayden, B. Baumgartner, and B. Lendl, "Anomalous Humidity Dependence in Photoacoustic Spectroscopy of CO Explained by Kinetic Cooling," *Applied Sciences*, vol. 10, no. 3, p. 843, Jan. 24, 2020. DOI: 10.3390/app10030843.

[105] J. A. Sell, *Photothermal Investigations of Solids and Fluids*. Boston: Academic Press, 1989, ISBN: 978-0-12-636345-6.

[106] U. Radeschnig, A. Bergmann, and B. Lang, "Optimization of the optical path length amplitude for interferometric photothermal gas and aerosol sensing considering advection: A theoretical study," *Journal of Applied Physics*, vol. 135, no. 9, p. 094 501, Mar. 7, 2024. DOI: 10.1063/5.0184357.

[107] T. Miya, Y. Terunuma, T. Hosaka, and T. Miyashita, "Ultimate low-loss single-mode fibre at 1.55 µm," *Electronics Letters*, vol. 15, no. 4, p. 106, 1979. DOI: 10.1049/el:19790077.

[108] W. Jin, Y. Cao, F. Yang, and H. L. Ho, "Ultra-sensitive all-fibre photothermal spectroscopy with large dynamic range," *Nature Communications*, vol. 6, no. 1, p. 6767, Apr. 13, 2015. DOI: 10.1038/ncomms7767.

[109] M. Nikodem, K. Krzempek, G. Dudzik, and K. Abramski, "Hollow core fiber-assisted absorption spectroscopy of methane at 34 µm," *Optics Express*, vol. 26, no. 17, p. 21 843, Aug. 20, 2018. DOI: 10.1364/OE.26.021843.

[110] P. Zhao, Y. Zhao, H. Bao, H. L. Ho, W. Jin, S. Fan, S. Gao, Y. Wang, and P. Wang, "Mode-phase-difference photothermal spectroscopy for gas detection with an anti-resonant hollow-core optical fiber," *Nature Communications*, vol. 11, no. 1, p. 847, Feb. 12, 2020. DOI: 10.1038/s41467-020-14707-0.

[111] K. Krzempek, P. Jaworski, P. Kozioł, and W. Belardi, "Antiresonant hollow core fiber-assisted photothermal spectroscopy of nitric oxide at 5.26 µm with parts-per-billion sensitivity," *Sensors and Actuators B: Chemical*, vol. 345, p. 130 374, Oct. 2021. DOI: 10.1016/j.snb.2021.130374.

[112] M. A. Duguay, Y. Kokubun, T. L. Koch, and L. Pfeiffer, "Antiresonant reflecting optical waveguides in SiO2-Si multilayer structures," *Applied Physics Letters*, vol. 49, no. 1, pp. 13–15, Jul. 7, 1986. DOI: 10.1063/1.97085.

[113] W. Belardi, "Design and Properties of Hollow Antiresonant Fibers for the Visible and Near Infrared Spectral Range," *Journal of Lightwave Technology*, vol. 33, no. 21, pp. 4497–4503, Nov. 1, 2015. DOI: 10.1109/JLT.2015.2477775.

[114] K. Zheng, H. Bao, W. Luo, F. Liu, F. Chen, H. Liao, S. Zhao, S. Jiang, C. Zheng, H. L. Ho, S. Gao, and W. Jin, "Hollow-core fiber-based mid-infrared photothermal spectroscopy for multi-component gas sensing," *IEEE Journal of Selected Topics in Quantum Electronics*, pp. 1–6, 2024. DOI: 10.1109/JSTQE.2024.3388522.

[115] T. Wei, Y. Han, H.-L. Tsai, and H. Xiao, "Miniaturized fiber inline Fabry-Perot interferometer fabricated with a femtosecond laser," *Optics Letters*, vol. 33, no. 6, p. 536, Mar. 15, 2008. DOI: 10.1364/OL.33.000536.

[116] C. Saavedra, D. Pandey, W. Alt, H. Pfeifer, and D. Meschede, "Tunable fiber Fabry-Perot cavities with high passive stability," *Optics Express*, vol. 29, no. 2, p. 974, Jan. 18, 2021. DOI: 10.1364/OE.412273.

[117] A. Muller, E. B. Flagg, J. R. Lawall, and G. S. Solomon, "Ultrahigh-finesse, low-mode-volume Fabry–Perot microcavity," *Optics Letters*, vol. 35, no. 13, p. 2293, Jul. 1, 2010. DOI: 10.1364/OL.35.002293.

[118] D. Hunger, T. Steinmetz, Y. Colombe, C. Deutsch, T. W. Hänsch, and J. Reichel, "A fiber Fabry–Perot cavity with high finesse," *New Journal of Physics*, vol. 12, no. 6, p. 065 038, Jun. 28, 2010. DOI: 10.1088/1367-2630/12/6/065038.

[119] S. Preißer, B. Fischer, and N. Panzer, "Listening to Ultrasound with a Laser: A new way to measure ultrasound waves by optical means," *Optik & Photonik*, vol. 12, no. 5, pp. 22–25, Dec. 2017. DOI: 10.1002/opph.201700031.

[120] P. Breitegger, B. Lang, and A. Bergmann, "Intensity Modulated Photothermal Measurements of NO_2 with a Compact Fiber-Coupled Fabry–Pérot Interferometer," *Sensors*, vol. 19, no. 15, p. 3341, Jul. 30, 2019. DOI: 10.3390/s19153341.

[121] D. Pinto, H. Moser, J. P. Waclawek, S. Dello Russo, P. Patimisco, V. Spagnolo, and B. Lendl, "Parts-per-billion detection of carbon monoxide: A comparison between quartz-enhanced photoacoustic and photothermal spectroscopy," *Photoacoustics*, vol. 22, p. 100 244, Jun. 2021. DOI: 10.1016/j.pacs.2021.100244.

[122] J. P. Waclawek, C. Kristament, H. Moser, and B. Lendl, "Balanced-detection interferometric cavity-assisted photothermal spectroscopy," *Optics Express*, vol. 27, no. 9, p. 12 183, Apr. 29, 2019. DOI: 10.1364/OE.27.012183.

[123] J. P. Waclawek, H. Moser, and B. Lendl, "Balanced-detection interferometric cavity-assisted photothermal spectroscopy employing an all-fiber-coupled probe laser configuration," *Optics Express*, vol. 29, no. 5, pp. 7794–7808, Mar. 1, 2021. DOI: 10.1364/OE.416536.

[124] D. Pinto, J. P. Waclawek, S. Lindner, H. Moser, G. Ricchiuti, and B. Lendl, "Wavelength modulated diode probe laser for an interferometric cavity-assisted photothermal spectroscopy gas sensor," *Sensors and Actuators B: Chemical*, vol. 377, p. 133 061, Feb. 2023. DOI: 10.1016/j.snb.2022.133061.

[125] G. Malvicini, J. P. Waclawek, D. Pinto, H. Moser, S. Iadanza, K. Gradkowski, L. O'Faolain, and B. Lendl, "Balanced-detection interferometric cavity-assisted photothermal spectroscopy via collimating fiber-array integration," *Sensors and Actuators B: Chemical*, vol. 412, p. 135 766, Aug. 2024. DOI: 10.1016/j.snb.2024.135766.

[126] K. Krzempek, P. Jaworski, L. Tenbrake, F. Giefer, D. Meschede, S. Hofferberth, and H. Pfeifer, "Photothermal gas detection using a miniaturized fiber Fabry-Perot cavity," *Sensors and Actuators B: Chemical*, vol. 401, p. 135 040, Feb. 2024. DOI: 10.1016/j.snb.2023.135040.

[127] Z. Li, Z. Wang, F. Yang, W. Jin, and W. Ren, "Mid-infrared fiber-optic photothermal interferometry," *Optics Letters*, vol. 42, no. 18, p. 3718, Sep. 15, 2017. DOI: 10.1364/OL.42.003718.

[128] Y. Lin, F. Liu, X. He, W. Jin, M. Zhang, F. Yang, H. L. Ho, Y. Tan, and L. Gu, "Distributed gas sensing with optical fibre photothermal interferometry," *Optics Express*, vol. 25, no. 25, p. 31 568, Dec. 11, 2017. DOI: 10.1364/OE.25.031568.

[129] F. Chen, S. Jiang, H. L. Ho, S. Gao, Y. Wang, and W. Jin, "Frequency-Division-Multiplexed Multicomponent Gas Sensing with Photothermal Spectroscopy and a Single NIR/MIR Fiber-Optic Gas Cell," *Analytical Chemistry*, vol. 94, no. 39, pp. 13 473–13 480, Oct. 4, 2022. DOI: 10.1021/acs.analchem.2c02599.

[130] R. W. P. Drever, J. L. Hall, F. V. Kowalski, J. Hough, G. M. Ford, A. J. Munley, and H. Ward, "Laser phase and frequency stabilization using an optical resonator," *Applied Physics B Photophysics and Laser Chemistry*, vol. 31, no. 2, pp. 97–105, Jun. 1983. DOI: 10.1007/BF00702605.

[131] N. Ismail, C. C. Kores, D. Geskus, and M. Pollnau, "Fabry-Pérot resonator: Spectral line shapes, generic and related Airy distributions, linewidths, finesses, and performance at low or frequency-dependent reflectivity," *Optics Express*, vol. 24, no. 15, p. 16 366, Jul. 25, 2016. DOI: 10.1364/OE.24.016366.

[132] H. Varu, "The optical modelling and design of Fabry Perot Interferometer sensors for ultrasound detection," Ph.D. dissertation.

[133] E. Nichelatti and G. Salvetti, "Spatial and spectral response of a Fabry–Perot interferometer illuminated by a Gaussian beam," *Applied Optics*, vol. 34, no. 22, p. 4703, Aug. 1, 1995. DOI: 10.1364/AO.34.004703.

[134] P. La Penna, A. Di Virgilio, M. Fiorentino, A. Porzio, and S. Solimeno, "Transmittivity profile of high finesse plane parallel Fabry–Perot cavities illuminated by Gaussian beams," *Optics Communications*, vol. 162, no. 4-6, pp. 267–279, Apr. 1999. DOI: 10.1016/S0030-4018(99)00063-2.

[135] D. M. Marques, J. A. Guggenheim, R. Ansari, E. Z. Zhang, P. C. Beard, and P. R. T. Munro, "Modelling Fabry-Pérot etalons illuminated by focussed beams," *Optics Express*, vol. 28, no. 5, p. 7691, Mar. 2, 2020. DOI: 10.1364/OE.382526.

[136] H. Li, G. B. Rieker, X. Liu, J. B. Jeffries, and R. K. Hanson, "Extension of wavelength-modulation spectroscopy to large modulation depth for diode laser absorption measurements in high-pressure gases," *Applied Optics*, vol. 45, no. 5, p. 1052, Feb. 10, 2006. DOI: 10.1364/AO.45.001052.

[137] J. Liu, J. Jeffries, and R. Hanson, "Wavelength modulation absorption spectroscopy with 2 f detection using multiplexed diode lasers for rapid temperature measurements in gaseous flows," *Applied Physics B*, vol. 78, no. 3-4, pp. 503–511, Feb. 2004. DOI: 10.1007/s00340-003-1380-7.

[138] B. Weinberger, "The Toxicology of Inhaled Nitric Oxide," *Toxicological Sciences*, vol. 59, no. 1, pp. 5–16, Jan. 1, 2001. DOI: 10.1093/toxsci/59.1.5.

[139] M. R. McCurdy, A. Sharafkhaneh, H. Abdel-Monem, J. Rojo, and F. K. Tittel, "Exhaled nitric oxide parameters and functional capacity in chronic obstructive pulmonary disease," *Journal of Breath Research*, vol. 5, no. 1, p. 016 003, Mar. 1, 2011. DOI: 10.1088/1752-7155/5/1/016003.

[140] S. T. Sanders, D. W. Mattison, J. B. Jeffries, and R. K. Hanson, "Rapid temperature tuning of a 14-µm diode laser with application to high-pressure H_2O absorption spectroscopy," *Optics Letters*, vol. 26, no. 20, p. 1568, Oct. 15, 2001. DOI: 10.1364/OL.26.001568.

[141] R. F. Kazarinov and R. Suris, "Possible amplification of electromagnetic waves in a semiconductor with a superlattice," *Soviet Physycs. Semiconductors*, vol. 5, pp. 707–709, Oct. 1971.

[142] J. Faist, F. Capasso, D. L. Sivco, C. Sirtori, A. L. Hutchinson, and Alfred Y. Cho, "Quantum cascade laser," *Science (New York, N.Y.)*, vol. 264, no. 5158, pp. 553–556, 1994. DOI: 10.1126/science.264.5158.553.

[143] J. Faist, F. Capasso, C. Sirtori, D. L. Sivco, J. N. Baillargeon, A. L. Hutchinson, S.-N. G. Chu, and A. Y. Cho, "High power mid-infrared (λ ~5 µm) quantum cascade lasers operating above room temperature," *Applied Physics Letters*, vol. 68, no. 26, pp. 3680–3682, Jun. 24, 1996. DOI: 10.1063/1.115741.

[144] C. Sirtori, J. Faist, F. Capasso, D. L. Sivco, A. L. Hutchinson, S. N. G. Chu, and A. Y. Cho, "Continuous wave operation of midinfrared (7.4–8.6 µm) quantum cascade lasers up to 110 K temperature," *Applied Physics Letters*, vol. 68, no. 13, pp. 1745–1747, Mar. 25, 1996. DOI: 10.1063/1.116654.

[145] M. Beck, D. Hofstetter, T. Aellen, J. Faist, U. Oesterle, M. Ilegems, E. Gini, and H. Melchior, "Continuous Wave Operation of a Mid-Infrared Semiconductor Laser at Room Temperature," *Science*, vol. 295, no. 5553, pp. 301–305, Jan. 11, 2002. DOI: 10.1126/science.1066408.

[146] R. Köhler, A. Tredicucci, F. Beltram, H. E. Beere, E. H. Linfield, A. G. Davies, D. A. Ritchie, R. C. Iotti, and F. Rossi, "Terahertz semiconductor-heterostructure laser," *Nature*, vol. 417, no. 6885, pp. 156–159, May 2002. DOI: 10.1038/417156a.

[147] A. Evans, J. S. Yu, J. David, L. Doris, K. Mi, S. Slivken, and M. Razeghi, "High-temperature, high-power, continuous-wave operation of buried heterostructure quantum cascade lasers," *Applied Physics Letters*, vol. 84, no. 3, pp. 314–316, Jan. 19, 2004. DOI: 10.1063/1.1641174.

[148] A. Evans, J. S. Yu, S. Slivken, and M. Razeghi, "Continuous-wave operation of $\lambda \sim$4.8µm quantum-cascade lasers at room temperature," *Applied Physics Letters*, vol. 85, no. 12, pp. 2166–2168, Sep. 20, 2004. DOI: 10.1063/1.1793340.

[149] J. Faist, C. Gmachl, F. Capasso, C. Sirtori, D. L. Sivco, J. N. Baillargeon, and A. Y. Cho, "Distributed feedback quantum cascade lasers," *Applied Physics Letters*, vol. 70, no. 20, pp. 2670–2672, May 19, 1997. DOI: 10.1063/1.119208.

[150] R. Maulini, M. Beck, J. Faist, and E. Gini, "Broadband tuning of external cavity bound-to-continuum quantum-cascade lasers," *Applied Physics Letters*, vol. 84, no. 10, pp. 1659–1661, Mar. 8, 2004. DOI: 10.1063/1.1667609.

[151] A. Hugi, R. Maulini, and J. Faist, "External cavity quantum cascade laser," *Semiconductor Science and Technology*, vol. 25, no. 8, p. 083 001, Aug. 2, 2010. DOI: 10.1088/0268-1242/25/8/083001.

[152] A. Schwaighofer, M. R. Alcaráz, C. Araman, H. Goicoechea, and B. Lendl, "External cavity-quantum cascade laser infrared spectroscopy for secondary structure analysis of proteins at low concentrations," *Scientific Reports*, vol. 6, no. 1, p. 33 556, Sep. 16, 2016. DOI: 10.1038/srep33556.

[153] B. Meng, M. Singleton, M. Shahmohammadi, F. Kapsalidis, R. Wang, M. Beck, and J. Faist, "Mid-infrared frequency comb from a ring quantum cascade laser," *Optica*, vol. 7, no. 2, p. 162, Feb. 20, 2020. DOI: 10.1364/OPTICA.377755.

[154] I. Heckelmann, M. Bertrand, A. Dikopoltsev, M. Beck, G. Scalari, and J. Faist, "Quantum walk comb in a fast gain laser," *Science*, vol. 382, no. 6669, pp. 434–438, Oct. 27, 2023. DOI: 10.1126/science.adj3858.

[155] L. Consolino, M. Nafa, F. Cappelli, K. Garrasi, F. P. Mezzapesa, L. Li, A. G. Davies, E. H. Linfield, M. S. Vitiello, P. De Natale, and S. Bartalini, "Fully phase-stabilized quantum cascade laser frequency comb," *Nature Communications*, vol. 10, no. 1, p. 2938, Jul. 3, 2019. DOI: 10.1038/s41467-019-10913-7.

[156] J. Hillbrand, M. Bertrand, V. Wittwer, N. Opačak, F. Kapsalidis, M. Gianella, L. Emmenegger, B. Schwarz, T. Südmeyer, M. Beck, and J. Faist, "Synchronization of frequency combs by optical injection," *Optics Express*, vol. 30, no. 20, p. 36 087, Sep. 26, 2022. DOI: 10.1364/OE.456775.

[157] A. V. Babichev, E. S. Kolodeznyi, A. G. Gladyshev, D. V. Denisov, G. V. Voznyuk, M. I. Mitrofanov, N. Yu. Kharin, V. Yu. Panevin, S. O. Slipchenko, A. V. Lyutetskii, V. P. Evtikhiev, L. Ya. Karachinsky, I. I. Novikov, N. A. Pikhtin, and A. Yu. Egorov, "Surface Emitting Quantum-Cascade Ring Laser," *Semiconductors*, vol. 55, no. 7, pp. 591–594, Jul. 2021. DOI: 10.1134/S106378262107006X.

[158] C. Pflügl, M. Austerer, W. Schrenk, S. Golka, G. Strasser, R. P. Green, L. R. Wilson, J. W. Cockburn, A. B. Krysa, and J. S. Roberts, "Single-mode surface-emitting quantum-cascade lasers," *Applied Physics Letters*, vol. 86, no. 21, p. 211 102, May 23, 2005. DOI: 10.1063/1.1929070.

[159] R. Colombelli, K. Srinivasan, M. Troccoli, O. Painter, C. F. Gmachl, D. M. Tennant, A. M. Sergent, D. L. Sivco, A. Y. Cho, and F. Capasso, "Quantum Cascade Surface-Emitting Photonic Crystal Laser," *Science*, vol. 302, no. 5649, pp. 1374–1377, Nov. 21, 2003. DOI: 10.1126/science.1090561.

[160] M. S. Vitiello, G. Scalari, B. Williams, and P. De Natale, "Quantum cascade lasers: 20 years of challenges," *Optics Express*, vol. 23, no. 4, p. 5167, Feb. 23, 2015. DOI: 10.1364/OE.23.005167.

[161] G. Scamarcio, C. Gmachl, F. Capasso, A. Tredicucci, A. L. Hutchinson, D. L. Sivco, and A. Y. Cho, "Long-wavelength interminiband Fabry-Pérot and distributed feedback quantum cascade lasers," *Semiconductor Science and Technology*, vol. 13, no. 11, pp. 1333–1339, Nov. 1, 1998. DOI: 10.1088/0268-1242/13/11/019.

[162] A. Tredicucci, C. Gmachl, F. Capasso, D. L. Sivco, A. L. Hutchinson, and A. Y. Cho, "Long wavelength superlattice quantum cascade lasers at $\lambda \simeq 17$ µm," *Applied Physics Letters*, vol. 74, no. 5, pp. 638–640, Feb. 1, 1999. DOI: 10.1063/1.123026.

[163] A. Tredicucci, C. Gmachl, M. C. Wanke, F. Capasso, A. L. Hutchinson, D. L. Sivco, S.-N. G. Chu, and A. Y. Cho, "Surface plasmon quantum cascade lasers at $\lambda \sim 19$ µm," *Applied Physics Letters*, vol. 77, no. 15, pp. 2286–2288, Oct. 9, 2000. DOI: 10.1063/1.1316768.

[164] J. Ulrich, J. Kreuter, W. Schrenk, G. Strasser, and K. Unterrainer, "Long wavelength (15 and 23 µm) GaAs/AlGaAs quantum cascade lasers," *Applied Physics Letters*, vol. 80, no. 20, pp. 3691–3693, May 20, 2002. DOI: 10.1063/1.1481236.

[165] M. Bahriz, G. Lollia, P. Laffaille, A. Baranov, and R. Teissier, "InAs/AlSb quantum cascade lasers operating near 20 µm," *Electronics Letters*, vol. 49, no. 19, pp. 1238–1240, Sep. 2013. DOI: 10.1049/el.2013.2412.

[166] D. Chastanet, A. Bousseksou, G. Lollia, M. Bahriz, F. H. Julien, A. N. Baranov, R. Teissier, and R. Colombelli, "High temperature, single mode, long infrared (λ = 17.8 µm) InAs-based quantum cascade lasers," *Applied Physics Letters*, vol. 105, no. 11, p. 111 118, Sep. 15, 2014. DOI: 10.1063/1.4895763.

[167] A. N. Baranov, M. Bahriz, and R. Teissier, "Room temperature continuous wave operation of InAs-based quantum cascade lasers at 15 µm," *Optics Express*, vol. 24, no. 16, p. 18 799, Aug. 8, 2016. DOI: 10.1364/OE.24.018799.

[168] H. Nguyen Van, Z. Loghmari, H. Philip, M. Bahriz, A. Baranov, and R. Teissier, "Long Wavelength (λ > 17 µm) Distributed Feedback Quantum Cascade Lasers Operating in a Continuous Wave at Room Temperature," *Photonics*, vol. 6, no. 1, p. 31, Mar. 21, 2019. DOI: 10.3390/photonics6010031.

[169] K. Kinjalk, D. A. Díaz-Thomas, Z. Loghmari, M. Bahriz, R. Teissier, and A. N. Baranov, "InAs-Based Quantum Cascade Lasers with Extremely Low Threshold," *Photonics*, vol. 9, no. 10, p. 747, Oct. 10, 2022. DOI: 10.3390/photonics9100747.

[170] R. Paiella, Ed., *Intersubband Transitions in Quantum Structures* (McGraw-Hill Nanoscience and Technology Series). New York: McGraw-Hill, 2006, 431 pp., ISBN: 978-0-07-145792-7.

[171] C. Sirtori, F. Capasso, J. Faist, and S. Scandolo, "Nonparabolicity and a sum rule associated with bound-to-bound and bound-to-continuum intersubband transitions in quantum wells," *Physical Review B*, vol. 50, no. 12, pp. 8663–8674, Sep. 15, 1994. DOI: 10.1103/PhysRevB.50.8663.

[172] I. Vurgaftman, J. R. Meyer, and L. R. Ram-Mohan, "Band parameters for III–V compound semiconductors and their alloys," *Journal of Applied Physics*, vol. 89, no. 11, pp. 5815–5875, Jun. 1, 2001. DOI: 10.1063/1.1368156.

[173] J. Yu, A. Evans, S. Slivken, S. Darvish, and M. Razeghi, "Short wavelength (λ ∼4.3 µm) high-performance continuous-wave quantum-cascade lasers," *IEEE Photonics Technology Letters*, vol. 17, no. 6, pp. 1154–1156, Jun. 2005. DOI: 10.1109/LPT.2005.846568.

[174] Feng Xie, C. Caneau, H. P. Leblanc, D. P. Caffey, L. C. Hughes, T. Day, and Chung-en Zah, "Watt-Level Room Temperature Continuous-Wave Operation of Quantum Cascade Lasers With λ >10 µm," *IEEE Journal of Selected Topics in Quantum Electronics*, vol. 19, no. 4, pp. 1 200 407–1 200 407, Jul. 2013. DOI: 10.1109/JSTQE.2013.2240658.

[175] E. Benveniste, A. Vasanelli, A. Delteil, J. Devenson, R. Teissier, A. Baranov, A. M. Andrews, G. Strasser, I. Sagnes, and C. Sirtori, "Influence of the material parameters on quantum cascade devices," *Applied Physics Letters*, vol. 93, no. 13, p. 131 108, Sep. 29, 2008. DOI: 10.1063/1.2991447.

[176] "State-of-the-Art Mid-Infrared QCLs: Elastic Scattering, High CW Power, and Coherent-Power Scaling," in *Mid-Infrared and Terahertz Quantum Cascade Lasers*, D. Botez and M. A. Belkin, Eds., 1st ed., Cambridge University Press, Jun. 30, 2023, pp. 41–101, ISBN: 978-1-108-55206-6 978-1-108-42793-7. DOI: 10.1017/9781108552066.003.

[177] D. Botez and M. A. Belkin, Eds., *Mid-Infrared and Terahertz Quantum Cascade Lasers*, 1st ed. Cambridge University Press, Jun. 30, 2023, ISBN: 978-1-108-55206-6 978-1-108-42793-7. DOI: 10.1017/9781108552066.

[178] C. Sirtori, P. Kruck, S. Barbieri, H. Page, J. Nagle, M. Beck, J. Faist, and U. Oesterle, "Low-loss Al-free waveguides for unipolar semiconductor lasers," *Applied Physics Letters*, vol. 75, no. 25, pp. 3911–3913, Dec. 20, 1999. DOI: 10.1063/1.125491.

[179] A. Milton and W. Burns, "Mode coupling in optical waveguide horns," *IEEE Journal of Quantum Electronics*, vol. 13, no. 10, pp. 828–835, Oct. 1977. DOI: 10.1109/JQE.1977.1069240.

[180] W. K. Burns, A. F. Milton, and A. B. Lee, "Optical waveguide parabolic coupling horns," *Applied Physics Letters*, vol. 30, no. 1, pp. 28–30, Jan. 1, 1977. DOI: 10.1063/1.89199.

[181] K. Pierscinski, A. Kuzmicz, D. Pierscinska, G. Sobczak, M. Sakowicz, P. Gutowski, K. Janus, K. Chmielewski, and M. Bugajski, "Optimization of Cavity Designs of Tapered AlInAs/InGaAs/InP Quantum Cascade Lasers Emitting at 4.5 µm," *IEEE Journal of Selected Topics in Quantum Electronics*, vol. 25, no. 6, pp. 1–9, Nov. 2019. DOI: 10.1109/JSTQE.2019.2948500.

[182] H. Abiri, S. Farzaneh, A. Bakhtazad, and M. H. Rahnavard, "Optimization of tapering profile in IC-DFB and DBR lasers," presented at the Symposium on Integrated Optoelectronics, R. H. Binder, P. Blood, and M. Osinski, Eds., San Jose, CA, Jul. 14, 2000, p. 862. DOI: 10.1117/12.391494.

[183] F. Wang, S. Slivken, and M. Razeghi, "High-brightness LWIR quantum cascade lasers," *Optics Letters*, vol. 46, no. 20, p. 5193, Oct. 15, 2021. DOI: 10.1364/OL.442213.

[184] J. N. Walpole, "Semiconductor amplifiers and lasers with tapered gain regions," *Optical and Quantum Electronics*, vol. 28, no. 6, pp. 623–645, Jun. 1996. DOI: 10.1007/BF00411298.

[185] R. Blanchard, T. S. Mansuripur, B. Gökden, N. Yu, M. Kats, P. Genevet, K. Fujita, T. Edamura, M. Yamanishi, and F. Capasso, "High-power low-divergence tapered quantum cascade lasers with plasmonic collimators," *Applied Physics Letters*, vol. 102, no. 19, p. 191 114, May 13, 2013. DOI: 10.1063/1.4806985.

[186] Z. Loghmari, "Lasers à cascades quantiques InAs / AlSb au-delà de 10µm : Émission mono-fréquence et génération du THz par différence de fréquences," Ph.D. dissertation, 2019.

[187] X. Huang, Y. Chiu, W. O. Charles, and C. Gmachl, "Ridge-width dependence of the threshold of long wavelength ($\lambda \approx$14 µm) quantum cascade lasers with sloped and vertical sidewalls," *Optics Express*, vol. 20, no. 3, p. 2539, Jan. 30, 2012. DOI: 10.1364/OE.20.002539.

[188] B. Gökden, T. S. Mansuripur, R. Blanchard, C. Wang, A. Goyal, A. Sanchez-Rubio, G. Turner, and F. Capasso, "High-brightness tapered quantum cascade lasers," *Applied Physics Letters*, vol. 102, no. 5, p. 053 503, Feb. 4, 2013. DOI: 10.1063/1.4791557.

[189] D. Pinto, D. Dìaz-Thomas, Z. Loghmari, K. Kinjalk, R. Teissier, M. Bahriz, B. Lendl, and A. Baranov, "Long wavelength distributed feedback tapered quantum cascade lasers," *Optics Express*, May 16, 2024. DOI: 10.1364/OE.521039.

[190] A. E. Siegman, "New developments in laser resonators," in *Optical Resonators*, vol. 1224, SPIE, Jun. 1, 1990, pp. 2–14. DOI: 10.1117/12.18425.

[191] G.-i. Hatakoshi, "Analysis of Beam Quality Factor for Semiconductor Lasers," *Optical Review*, vol. 10, no. 4, pp. 307–314, Jul. 2003. DOI: 10.1007/s10043-003-0307-1.

[192] P. Rauter, S. Menzel, A. K. Goyal, B. Gökden, C. A. Wang, A. Sanchez, G. W. Turner, and F. Capasso, "Master-oscillator power-amplifier quantum cascade laser array," *Applied Physics Letters*, vol. 101, no. 26, p. 261 117, Dec. 24, 2012. DOI: 10.1063/1.4773377.

[193] P. Rauter, S. Menzel, B. Gokden, A. K. Goyal, C. A. Wang, A. Sanchez, G. Turner, and F. Capasso, "Single-mode tapered quantum cascade lasers," *Applied Physics Letters*, vol. 102, no. 18, p. 181 102, May 6, 2013. DOI: 10.1063/1.4804261.

[194] L. Nähle, J. Semmel, W. Kaiser, S. Höfling, and A. Forchel, "Tapered quantum cascade lasers," *Applied Physics Letters*, vol. 91, no. 18, p. 181 122, Oct. 29, 2007. DOI: 10.1063/1.2805628.

[195] Y. Li, J. Wang, N. Yang, J. Liu, T. Wang, F. Liu, Z. Wang, W. Chu, and S. Duan, "The output power and beam divergence behaviors of tapered terahertz quantum cascade lasers," *Optics Express*, vol. 21, no. 13, p. 15 998, Jul. 1, 2013. DOI: 10.1364/OE.21.015998.

[196] M. N. Polyanskiy, *Refractive index database*, Accessed on 2023-09-21.

[197] F. Abelès, "Recherches sur la propagation des ondes électromagnétiques sinusoïdales dans les milieux stratifiés: Application aux couches minces," *Annales de Physique*, vol. 12, no. 5, pp. 596–640, 1950. DOI: 10.1051/anphys/195012050596.

[198] B. E. A. Saleh and M. C. Teich, *Fundamentals of Photonics* (Wiley Series in Pure and Applied Optics), Third edition. Hoboken, NJ: Wiley, 2019, 2 pp., ISBN: 978-1-119-50687-4.

[199] J. Kischkat, S. Peters, B. Gruska, M. Semtsiv, M. Chashnikova, M. Klinkmüller, O. Fedosenko, S. Machulik, A. Aleksandrova, G. Monastyrskyi, Y. Flores, and W. Ted Masselink, "Mid-infrared optical properties of thin films of aluminum oxide, titanium dioxide, silicon dioxide, aluminum nitride, and silicon nitride," *Applied Optics*, vol. 51, no. 28, p. 6789, Oct. 1, 2012. DOI: 10.1364/AO.51.006789.

[200] M. Ettenberg, H. S. Sommers, H. Kressel, and H. F. Lockwood, "CONTROL OF FACET DAMAGE IN GaAs LASER DIODES," *Applied Physics Letters*, vol. 18, no. 12, pp. 571–573, Jun. 15, 1971. DOI: 10.1063/1.1653545.

[201] S. J. Jang, C. I. Yeo, J. S. Yu, and Y. T. Lee, "Performance improvement by metal–dielectric HR coating in laterally coupled DFB laser with metal surface gratings," *Applied Physics B*, vol. 100, no. 3, pp. 553–558, Sep. 2010. DOI: 10.1007/s00340-010-4104-9.

[202] K. Petermann, *Laser Diode Modulation and Noise*. Dordrecht: Springer Netherlands, 1988, ISBN: 978-0-7923-1204-8 978-94-009-2907-4. DOI: 10.1007/978-94-009-2907-4.

[203] H. Kogelnik and C. V. Shank, "Coupled-Wave Theory of Distributed Feedback Lasers," *Journal of Applied Physics*, vol. 43, no. 5, pp. 2327–2335, May 1972. DOI: 10.1063/1.1661499.

[204] G. P. Agrawal, J. E. Geusic, and P. J. Anthony, "Distributed feedback lasers with multiple phase-shift regions," *Applied Physics Letters*, vol. 53, no. 3, pp. 178–179, Jul. 18, 1988. DOI: 10.1063/1.100166.

[205] A. De Rossi, M. Carras, and D. J. Paul, "Low-Loss Surface-Mode Waveguides for Terahertz Si–SiGe Quantum Cascade Lasers," *IEEE Journal of Quantum Electronics*, vol. 42, no. 12, pp. 1233–1238, Dec. 2006. DOI: 10.1109/JQE.2006.883496.

[206] M. Carras and A. De Rossi, "Photonic modes of metallodielectric periodic waveguides in the midinfrared spectral range," *Physical Review B*, vol. 74, no. 23, p. 235 120, Dec. 26, 2006. DOI: 10.1103/PhysRevB.74.235120.

[207] M. Carras, M. Garcia, X. Marcadet, O. Parillaud, A. De Rossi, and S. Bansropun, "Top grating index-coupled distributed feedback quantum cascade lasers," *Applied Physics Letters*, vol. 93, no. 1, p. 011 109, Jul. 7, 2008. DOI: 10.1063/1.2950086.

[208] M. Preuss and F. Bechstedt, "Vibrational spectra of ammonia, benzene, and benzene adsorbed on Si (001) by *first principles* calculations with periodic boundary conditions," *Physical Review B*, vol. 73, no. 15, p. 155 413, Apr. 11, 2006. DOI: 10.1103/PhysRevB.73.155413.

[209] J. D. Jeffers, C. B. Roller, K. Namjou, M. A. Evans, L. McSpadden, J. Grego, and P. J. McCann, "Real-Time Diode Laser Measurements of Vapor-Phase Benzene," *Analytical Chemistry*, vol. 76, no. 2, pp. 424–432, Jan. 1, 2004. DOI: 10.1021/ac0345392.

[210] M. Mhanna, G. Zhang, N. Kunnummal, and A. Farooq, "Cavity-Enhanced Measurements of Benzene for Environmental Monitoring," *IEEE Sensors Journal*, vol. 21, no. 3, pp. 3849–3859, Feb. 1, 2021. DOI: 10.1109/JSEN.2020.3026981.

[211] S. Sharpe, R. Sams, and T. Johnson, "The PNNL quantitative IR database for infrared remote sensing and hyperspectral imaging," in *Applied Imagery Pattern Recognition Workshop, 2002. Proceedings.*, Washington, DC, USA: IEEE Comput. Soc, 2002, pp. 45–48, ISBN: 978-0-7695-1863-3. DOI: 10.1109/AIPR.2002.1182253.

[212] M. K. Shakfa, M. Mhanna, H. Jin, D. Liu, K. Djebbi, M. Marangoni, and A. Farooq, "A mid-infrared diagnostic for benzene using a tunable difference-frequency-generation laser," *Proceedings of the Combustion Institute*, vol. 38, no. 1, pp. 1787–1796, 2021. DOI: 10.1016/j.proci.2020.06.382.

[213] J. Karhu, H. Philip, A. Baranov, R. Teissier, and T. Hieta, "Sub-ppb detection of benzene using cantilever-enhanced photoacoustic spectroscopy with a long-wavelength infrared quantum cascade laser," *Optics Letters*, vol. 45, no. 21, p. 5962, Nov. 1, 2020. DOI: 10.1364/OL.405402.

[214] D. Ayache, W. Trzpil, R. Rousseau, K. Kinjalk, R. Teissier, A. N. Baranov, M. Bahriz, and A. Vicet, "Benzene sensing by Quartz Enhanced Photoacoustic Spectroscopy at 14.85 µm," *Optics Express*, vol. 30, no. 4, p. 5531, Feb. 14, 2022. DOI: 10.1364/OE.447197.

[215] "HgCdTe (MCT) Photoconductive Detector PCI-4TE-14," VIGO Photonics. (), [Online]. Available: https://vigophotonics.com/product/pci-4te-14/ (visited on 05/27/2024).

[216] T. Delahaye, R. Armante, N. Scott, N. Jacquinet-Husson, A. Chédin, L. Crépeau, C. Crevoisier, V. Douet, A. Perrin, A. Barbe, V. Boudon, A. Campargue, L. Coudert, V. Ebert, J.-M. Flaud, R. Gamache, D. Jacquemart, A. Jolly, F. Kwabia Tchana, A. Kyuberis, G. Li, O. Lyulin, L. Manceron, S. Mikhailenko, N. Moazzen-Ahmadi, H. Müller, O. Naumenko, A. Nikitin, V. Perevalov, C. Richard, E. Starikova, S. Tashkun, Vl. G. Tyuterev, J. Vander Auwera, B. Vispoel, A. Yachmenev, and S. Yurchenko, "The 2020 edition of the GEISA spectroscopic database," *Journal of*

Molecular Spectroscopy, vol. 380, p. 111 510, Jul. 2021. DOI: 10.1016/j.jms.2021.111510.

List of publications

Peer-reviewed Publications

1. D. Pinto, H. Moser, J. P. Waclawek, S. Dello Russo, P. Patimisco, V. Spagnolo, and B. Lendl, "Parts-per-billion detection of carbon monoxide: A comparison between quartz-enhanced photoacoustic and photothermal spectroscopy," *Photoacoustics*, vol. 22, p. 100 244, Jun. 2021, ISSN: 22135979. DOI: 10.1016/j.pacs.2021.100244

2. G. Ricchiuti, A. Dabrowska, D. Pinto, G. Ramer, and B. Lendl, "Dual-Beam Photothermal Spectroscopy Employing a Mach–Zehnder Interferometer and an External Cavity Quantum Cascade Laser for Detection of Water Traces in Organic Solvents," *Analytical Chemistry*, vol. 94, no. 47, pp. 16 353–16 360, Nov. 29, 2022, ISSN: 0003-2700, 1520-6882. DOI: 10.1021/acs.analchem.2c03303

3. D. Pinto, J. P. Waclawek, S. Lindner, H. Moser, G. Ricchiuti, and B. Lendl, "Wavelength modulated diode probe laser for an interferometric cavity-assisted photothermal spectroscopy gas sensor," *Sensors and Actuators B: Chemical*, vol. 377, p. 133 061, Feb. 2023, ISSN: 09254005. DOI: 10.1016/j.snb.2022.133061

4. G. Malvicini, J. P. Waclawek, D. Pinto, H. Moser, S. Iadanza, K. Gradkowski, L. O'Faolain, and B. Lendl, "Balanced-detection interferometric cavity-assisted photothermal spectroscopy via collimating fiber-array integration," *Sensors and Actuators B: Chemical*, vol. 412, p. 135 766, Aug. 2024, ISSN: 09254005. DOI: 10.1016/j.snb.2024.135766

5. D. Pinto, D. Dìaz-Thomas, Z. Loghmari, K. Kinjalk, R. Teissier, M. Bahriz, B. Lendl, and A. Baranov, "Long wavelength distributed feedback tapered quantum cascade lasers," *Optics Express*, May 16, 2024, ISSN: 1094-4087. DOI: 10.1364/OE.521039

6. K. Kinjalk, F. Paciolla, B. Sun, A. Zifarelli, G. Menduni, M. Giglio, H. Wu, L. Dong, D. Ayache, D. Pinto, A. Vicet, A. N. Baranov, P. Patimisco, and A. Sampaolo, "Highly Selective and Sensitive Detection of Volatile Organic Compounds using Long Wavelength InAs-based Quantum Cascade Lasers through Quartz Enhanced Photoacoustic Spectroscopy," *Applied Physics Reviews*, Jun. 2024. DOI: 10

.1063/5.0189501

Conference Proceedings

1. M. Giglio, A. Sampaolo, P. Patimisco, D. Pinto, G. Menduni, A. Elefante, S. D. Russo, F. Sgobba, A. Zifarelli, F. K. Tittel, and V. Spagnolo, "Quartz-enhanced photoacoustic spectroscopy of methane isotopologues," in *Photonic Instrumentation Engineering VIII*, vol. 11693, International Society for Optics and Photonics, Mar. 5, 2021, p. 116930I. DOI: 10.1117/12.2578149

2. D. Pinto, K. Kinjalk, A. Meguekam, M. Bahriz, and A. N. Baranov, "Tapered quantum cascade lasers in the long-wavelength mid-infrared region," in *Quantum Sensing and Nano Electronics and Photonics XIX*, M. Razeghi, G. A. Khodaparast, and M. S. Vitiello, Eds., San Francisco, United States: SPIE, Mar. 15, 2023, p. 90, ISBN: 978-1-5106-5965-0 978-1-5106-5966-7. DOI: 10.1117/12.2649669

3. D. Pinto, J. Waclawek, S. Lindner, H. Moser, G. Ricchiuti, and B. Lendl, "Highly sensitive and rugged gas optical detection via interferometric cavity-assisted photothermal spectroscopy," in *Photonic Instrumentation Engineering X*, Y. Soskind and L. E. Busse, Eds., San Francisco, United States: SPIE, Mar. 8, 2023, p. 30, ISBN: 978-1-5106-5961-2 978-1-5106-5962-9. DOI: 10.1117/12.2648273

4. G. Ricchiuti, A. Dabrowska, D. Pinto, G. Ramer, and B. Lendl, "Mid-IR photothermal sensing of liquids for trace analysis," in *Photonic Instrumentation Engineering X*, Y. Soskind and L. E. Busse, Eds., San Francisco, United States: SPIE, Mar. 8, 2023, p. 32, ISBN: 978-1-5106-5961-2 978-1-5106-5962-9. DOI: 10.1117/12.2649811